



THE HONG KONG
POLYTECHNIC UNIVERSITY

香港理工大學

Pao Yue-kong Library

包玉剛圖書館

Copyright Undertaking

This thesis is protected by copyright, with all rights reserved.

By reading and using the thesis, the reader understands and agrees to the following terms:

1. The reader will abide by the rules and legal ordinances governing copyright regarding the use of the thesis.
2. The reader will use the thesis for the purpose of research or private study only and not for distribution or further reproduction or any other purpose.
3. The reader agrees to indemnify and hold the University harmless from and against any loss, damage, cost, liability or expenses arising from copyright infringement or unauthorized usage.

IMPORTANT

If you have reasons to believe that any materials in this thesis are deemed not suitable to be distributed in this form, or a copyright owner having difficulty with the material being included in our database, please contact lbsys@polyu.edu.hk providing details. The Library will look into your claim and consider taking remedial action upon receipt of the written requests.

FEMTOSECOND BROADBAND TIME-RESOLVED
FLUORESCENCE AND TRANSIENT ABSORPTION
STUDY ON METHYL-4-DIMETHYLAMINO BENZOATE
AND PHENYLENEETHYNYLENE GOLD(I) COMPLEXES

CHAN TSZ LEUNG

Ph.D

The Hong Kong Polytechnic University

2016

The Hong Kong Polytechnic University

Department of Applied Biology and Chemical Technology

Femtosecond Broadband Time-resolved Fluorescence
and Transient Absorption Study on Methyl-4-
dimethylaminobenzoate and Phenyleneethynylene
Gold(I) Complexes

CHAN Tsz Leung

A Thesis Submitted in Partial Fulfillment of the Requirements for the Degree of
Doctor of Philosophy

July 2015

CERTIFICATE OF ORIGINALITY

I hereby declare that this thesis is my own work and that, to the best of my knowledge and belief, it reproduces no material previously published or written, nor material that has been accepted for the award of any other degree or diploma, except where due acknowledgement has been made in the text.

----- (*Signed*)

----- CHAN Tsz Leung (*Name of student*)

Abstract

Photo-induced intramolecular charge transfer (ICT) and luminescence are among the most significant processes in nature and have ample applications in chemistry, biology, and development of new materials. Methyl-4-dimethylaminobenzoate (DMABME) is a prototype molecule showing the ICT while a series of gold(I) oligo-phenyleneethynylene (PE) complexes provide rare example exhibiting ligand controlled luminescence upon photo-excitation. In spite of the interest and previous studies on these two types of systems, fundamental processes and factors governing the ICT in DMABME and the luminescence from the gold(I) PE complexes have remained unclear. With a purpose to address these issues, this thesis is conducted by integrating a range of time-resolved spectroscopic methods which combines the broadband time-resolved emission with transient absorption in timescale ranging seamlessly from femtosecond to hundreds microseconds for DMABME and the gold(I) PE complexes with excitation at varied selected wavelengths and solvent conditions. The study provides direct evidence for determining dynamics and deactivation pathways of the overall cascades of photo-excited DMABME and gold(I) PE complexes.

The study of DMABME in acetonitrile provides unequivocal evidence for a common origin of $L_a \pi\pi^*$ nature for both the ICT state and its precursor the locally excited state. Comparison of the time-resolved processes observed for DMABME in acetonitrile and in methanol unveils a remarkable effect of solvent hydrogen bonding (H-bonding) in altering strongly the dynamics and pathway of the excited state deactivation. It is identified for the first time that, in the protic

solvent methanol, the H-bonding between solute and solvent promotes formation of an H-bonded ICT state which in turn opens up an effective channel of internal conversion to the ground state not available in acetonitrile.

The time-resolved studies on gold(I) complexes containing oligo(*p*-PE), oligo(*m*-PE), and oligo(*o*-PE) ligands allow direct observation of the intersystem crossing (ISC) from emitting excited singlet to triplet state as well as to identify unambiguously the pathways for luminescence from these complexes. The results showed that, for the gold(I) oligo(*p*-PE) complexes, the rate of ISC is controlled largely by the extent of π -conjugation of the PE ligand in the excited singlet state. With an increase of ligand π -conjugation, the ISC rate drops by several orders of magnitude leading to a dramatic increase of the lifetime of prompt fluorescence (PF). This challenges the conventional view of heavy atom prompted ISC in luminescent transition metal complexes. Moreover, it is found that all the complexes investigated exhibit dual emission with the low energy component due to the phosphorescence from emitting triplet state and the high energy component the fluorescence, composed of PF and very long living delayed fluorescence produced through triplet-triplet annihilation (TTA) from the emitting triplet state. The efficiency of TTA is observed to vary with both the PE ligand length and the substitution pattern of the ligand, contributing a key factor for the varied luminescence behaviours displayed by these complexes.

The work presented in this thesis demonstrates the power of time-resolved spectroscopy in unravelling the elementary steps and key factors for the dynamics and pathways of excited state processes. The results enable clearer pictures to be obtained for clarifying controversies on the ICT of the *para* donor-

acceptor compounds and for a better understanding of the photophysics of luminescent gold(I) complexes which should prove useful in applications such as photo-catalysis and design of organic light-emitting diodes.

Publications Arising from the Thesis

1. Chan, C. T. L.; Cheng, C. C. W.; Ho, K. Y. F.; Kwok, W. M. “*Femtosecond broadband time-resolved fluorescence and transient absorption study of the intramolecular charge transfer state of methyl 4-dimethylaminobenzoate*” *Phys. Chem. Chem. Phys.* **2011**, *13*, 16306-16313.
2. Lu, W.; Kwok, W. M.; Ma, C.; Chan, C. T. L.; Zhu, M. X.; Che, C. M. “*Organic triplet excited states of gold(I) complexes with oligo(o- or m-phenyleneethynylene) ligands: conjunction of steady state and time-resolved spectroscopic studies on exciton delocalization and emission pathways*” *J. Am. Chem. Soc.* **2011**, *133*, 14120-14135.
3. Ma, C.; Chan, C. T. L.; Kwok, W. M.; Che, C. M. “*Ligand π -conjugation dictated intersystem crossing in phenyleneethynylene gold(I) complexes*” *Chem. Sci.* **2012**, *3*, 1883-1892.

Acknowledgements

First and foremost, I would like to take this opportunity to thank my supervisor, Dr. Wai-Ming Kwok, for giving me the opportunity to work in his laboratory and for his marvelous guidance, valuable advice and discussion.

I devote my sincere thanks to Dr. Chensheng Ma for her generous help and enormous contribution to the thesis. I want to thank my groupmates, Dr. Chan-Wut Cheng, Dr. Yat-Fung Ho and Ms. Chau-Ting Chan for the helpful discussions and advice. Many thanks go to all the members of the Department of Applied Biology and Chemical Technology for their support and assistance.

I would like to offer my special thanks to the research group of Prof. Chi-Ming Che of the University of Hong Kong for the collaboration on the research project of oligo-gold(I) PE complexes.

Last but not least, may I express my deepest appreciation to my family and friends for their understanding and encouragement throughout my period of study.

Table of Contents

Certificate of Originality	i
Abstract	ii
Publications Arising from the Thesis	v
Acknowledgements	vi
Table of Contents	vii
List of Figures	xv
List of Tables	xxiv
List of Abbreviations	xxv
Chapter 1 Introduction	1
1.1 Overview of the Interaction of Matter with Light	1
1.2 The Radiative and Non-Radiative Energy Dissipating Pathways	5
1.3 Background of the Photo-Induced Intramolecular Charge Transfer Reaction of DMABZs	10
1.4 Background of the Hydrogen-Bonding Effects on DMABZs	15
1.5 Background of the Intersystem Crossing Rate of Oligo-gold(I) PE Complexes	17

1.6	Background of the Luminescence Properties of Oligo-gold(I) PE Complexes	21
1.7	References	26
Chapter 2 Experimental Methodologies		36
2.1	Introduction to Pump-Probe Spectroscopy	36
2.2	Time-Resolved Spectroscopic Techniques	38
2.2.1	Background of time-resolved spectroscopy	38
2.2.1.1	Background of fs-TRF spectroscopy	39
2.2.1.2	Background of fs-TA spectroscopy	41
2.2.1.3	Background of ns-TA and ns-TRE spectroscopy	43
2.2.2	Femtosecond laser source	47
2.2.2.1	Oscillator	49
2.2.2.2	Ultrafast Ti:sapphire amplifier	51
2.2.2.3	Wavelength conversion	54
2.2.3	Femtosecond broadband time-resolved fluorescence spectroscopy	55
2.2.4	Femtosecond broadband time-resolved fluorescence anisotropy ...	59
2.2.5	Femtosecond broadband transient absorption spectroscopy	61

2.2.6	Nanosecond time-resolved emission spectroscopy	65
2.2.7	Nanosecond broadband transient absorption measurement	68
2.3	Steady State Measurements	69
2.3.1	Steady state absorption measurement	69
2.3.2	Steady state fluorescence measurement	69
2.3.3	Fluorescence quantum yield measurement	70
2.4	Spectra Calibration and Data Analysis	72
2.5	Sample Information and Materials	76
2.6	References	78
Chapter 3	Ultrafast Broadband Time-Resolved Study on the Excited States of Methyl-4-dimethylaminobenzoate in Acetonitrile	80
3.1	Results	80
3.1.1	Steady state absorption and fluorescence spectroscopy	80
3.1.2	Femtosecond time-resolved fluorescence spectroscopy	82
3.1.3	Femtosecond time-resolved fluorescence anisotropy spectroscopy	85
3.1.4	Femtosecond to microsecond transient absorption spectroscopy ...	88

3.1.5	Deactivation cascade for photo-excited DMABME in acetonitrile	94
3.2	Discussion	95
3.2.1	The ICT reaction and electronic origination of ¹ LE and ¹ ICT states of DMABME in acetonitrile	95
3.2.2	Comparison in excited state dynamics between DMABME and DMABA and DMAAP	99
3.2.3	Implication for practical application	100
3.3	References	101
Chapter 4	Ultrafast Broadband Time-Resolved Spectroscopic Study on Solvent Hydrogen Bonding Effect in Excited State Dynamics of Methyl-4-dimethylaminobenzoate	106
4.1	Results	106
4.1.1	Steady state absorption and fluorescence spectroscopy	106
4.1.2	Femtosecond time-resolved fluorescence in methanol	109
4.1.3	Femtosecond time-resolved fluorescence anisotropy in methanol	113
4.1.4	Femtosecond time-resolved fluorescence in deuterated methanol	115
4.1.5	Femtosecond transient absorption spectroscopy	118

4.2	Discussion	121
4.2.1	Solvent effect on the dynamics of ICT reaction	122
4.2.2	H-bonding effect on the decay dynamics of charge transfer state	123
4.2.3	Overall deactivation pathway for photo-excited DMABME in methanol	125
4.2.4	Implication of solvent H-bonding effect on the practical application of DMABME type of molecules	126
4.3	References	128

Chapter 5 Ultrafast Broadband Time-Resolved Study on the Excited States of Selected Phenyleneethynylene Gold (I) Complexes: Ligand π -Conjugation Controlled Intersystem Crossing ... 132

5.1	Results	132
5.1.1	Excited state dynamics of monomeric gold(I) PE complex	132
5.1.1.1	Femtosecond time-resolved fluorescence and transient absorption study	132
5.1.1.2	Nanosecond time-resolved emission study	138
5.1.2	Excited state dynamics of oligo(<i>p</i> -PE) and gold(I) oligo(<i>p</i> -PE) complex	142

5.1.2.1	Femtosecond time-resolved fluorescence and transient absorption study	142
5.1.2.2	Nanosecond time-resolved emission study	149
5.1.3	Excited state dynamics of oligo(<i>m</i> -PE) and gold(I) oligo(<i>m</i> -PE) complex	156
5.1.3.1	Femtosecond time-resolved fluorescence and transient absorption study	156
5.2	Discussion	160
5.2.1	Comparison of the spectral and temporal evolution character of oligo(<i>p</i> -PE) and gold(I) oligo(<i>p</i> -PE) complex	160
5.2.2	Comparison of the spectral and temporal evolution character of oligo(<i>m</i> -PE) and gold(I) oligo(<i>m</i> -PE) complex	164
5.2.3	General remarks on the photophysics of gold(I) PE complexes ...	167
5.2.4	Implication of the excited state dynamics of gold(I) oligo(PE) complexes	169
5.3	References	172
Chapter 6	Ultrafast Broadband Time-Resolved Study on Selected Gold (I) oligo(o- or m-phenyleneethynylene) Complexes: Substitution Dependent Luminescence Dynamics and Pathway	177

6.1	Results	177
6.1.1	Time-resolved fluorescence study of gold(I) oligo(<i>o</i> - or <i>m</i> -PE) complexes	177
6.1.2	Femtosecond transient absorption study of gold(I) oligo(<i>o</i> - or <i>m</i> -PE) complexes	183
6.1.3	Nanosecond time-resolved emission study of gold(I) oligo(<i>o</i> - or <i>m</i> -PE) complexes	191
6.2	Discussion	197
6.2.1	Emission pathways of gold(I) oligo(<i>o</i> - or <i>m</i> -PE) complexes	197
6.2.2	Comparison of the emission property of gold(I) oligo(<i>o</i> - or <i>m</i> -PE) complexes	199
6.2.3	General features of the excited states of gold(I) oligo(<i>o</i> - or <i>m</i> -PE) complexes	201
6.3	References	202
Chapter 7	Conclusions	206
Appendix	212
	Supplementary Figures	212

Supplementary Program Code for the Computer Control in ns-TA Measurement	221
Other Publications	222

List of Figures

Figure 1.1	Jablonski diagram of some radiative and non-radiative processes available to a photo-excited molecule	2
Scheme 1.1	Structures of the studied and related compounds	11
Scheme 1.2	Structure of the gold(I)-PE complexes and the corresponding free ligands	19
Scheme 1.3	Chemical structures of selected oligo(<i>o</i> -PE) and oligo(<i>m</i> -PE) gold(I) complexes	23
Scheme 2.1	Schematic presentation for pump-probe spectroscopic technique	37
Scheme 2.2	Schematic diagram for the principle of fs-TRF measurement ...	40
Scheme 2.3	Schematic diagram for the principle of fs- and ns-TA measurement	43
Scheme 2.4	Schematic diagram for the principle of ns-TRE measurement ...	45
Scheme 2.5	Schematic layout of the ultrafast laser system	48
Scheme 2.6	Schematic diagram of the Micra oscillator cavity	50
Scheme 2.7	Schematic diagram of stretcher, compressor and regenerative amplifier (RGA) in the Ti:sapphire amplifier	53
Scheme 2.8	Schematic diagram for Kerr-gated fs-TRF and fs-TRFA spectrometer	56

Scheme 2.9	Schematic diagram for the fs-TA experimental setup	62
Scheme 2.10	Schematic diagram for the ns-TRE experimental setup	67
Scheme 2.11	Schematic diagram showing the fs-TA data at sub-ps delay time before (a) and after (b) the GVD correction	73
Figure 3.1	Steady state UV-visible absorption (red) and 280 nm excited fluorescence (blue) spectra of DMABME in acetonitrile. The inset shows the molecular structure and the polarization directions for the $S_0 \rightarrow L_a$ and $S_0 \rightarrow L_b$ transitions	81
Figure 3.2	Broadband time-resolve fluorescence spectra of DMABME in acetonitrile recorded at 0-5 ps (a) and 5-5000 ps (b) after 280 nm excitation. The inset in (a) shows the isosbestic point observed as temporal evolution of the spectra	83
Figure 3.3	Experimental (\circ , Δ) and fitted (—) kinetic decay profiles of TRF (a) and TA (b) at indicated wavelengths for 280 nm excited DMABME in acetonitrile. The insets show the decay profiles at longer decay time up to ~ 6 ns	85
Figure 3.4	Broadband time-resolved fluorescence anisotropy spectra of DMABME in acetontirile recorded at 0.5, 5, 50 ps after 280 nm excitation	87
Figure 3.5	Broadband transient absorption of DMABME in acetonitrile recorded at 0-100 ps (a), 100-6000 ps (b), 5-250 ns (c) and 5-	

	1000000 ns (d) after 280 nm ((a) and (b)) or 266 nm ((c) and (d)) excitation	90
Figure 3.6	Experimental (\circ , Δ) and fitted (—) kinetic of ns-TA at 310 nm and 430 nm with 266 nm excitation of DMABME in acetonitrile under open air condition (a) and purged with nitrogen gas (b)	92
Scheme 3.1	Proposed deactivation pathways for photo-excited DMABME in acetonitrile	94
Figure 4.1	Steady state UV-visible absorption (red) and normalized 280 nm excited fluorescence (blue) spectra recorded for DMABME in methanol (solid line) and acetonitrile (dotted line)	107
Figure 4.2	Temporal evolution of broadband time-resolved fluorescence spectra of DMABME recorded at 0-5 ps (a) and 5-500 ps (b) in methanol after 280 nm excitation. The inset in (a) shows magnified spectra revealing an isosbestic point at ~ 480 nm; The inset in (b) shows dynamic shift of ^1ICT emission maximum as a function of time. $\nu_{\text{max}}^{\text{ICT}}$ corresponds to $\lambda_{\text{max}}^{\text{ICT}}$ in unit of wavenumber	111
Figure 4.3	Experimental (\circ , Δ) and fitted (—) time profiles of (a) TRF and (b) TA at indicated wavelengths for 280 nm excited DMABME in methanol. The insets show the decay profiles at longer timescale up to ~ 1 ns	113

Figure 4.4	Femtosecond broadband time-resolved fluorescence anisotropy spectra of DMABME recorded in methanol at 0.5, 5, 50 ps after 280 nm excitation	115
Figure 4.5	Femtosecond broadband time-resolved fluorescence spectra of DMABME recorded at 0-20 ps in CH ₃ OD (a) and CD ₃ OD (b) after 280 nm excitation. The insets show temporal evolution of TRF spectra at longer time delay from 5 ps to 700 ps after the photo-excitation	117
Figure 4.6	Comparison of normalized experimental (○, Δ, □) and fitted (—) TRF time profile at ~560 nm of 280 nm excited DMABME in CH ₃ OH (red), CH ₃ OD (green) and CD ₃ OD (blue). The insets show the decay profiles at ~360 nm (○) and ~560 nm (Δ, □) in CH ₃ OD and CD ₃ OD at the early delay times	118
Figure 4.7	Femtosecond broadband transient absorption spectra of DMABME in methanol recorded at 0-20 ps (a) and 20-6000 ps (b) after excitation at 280 nm. The inset in (b) compares TA spectra recorded at 6 ns after excitation in acetonitrile (red) and methanol (blue)	119
Scheme 4.1	Proposed deactivation pathways for photo-excited DMABME in methanol	125
Figure 5.1	Broadband time-resolve fluorescence (a) and transient absorption (b) spectra of 1a in acetonitrile recorded at indicated time delays	

	after excitation at 280 nm. The inset shows the spectra recorded at late times after the excitation	134
Figure 5.2	Experimental (\circ , Δ) and fitted (—) decay profiles of fs-TRF (a) and fs-TA (b) at indicated wavelengths obtained with 280 nm excitation of 1a in acetonitrile. The inset shows the decay profiles at longer delay time after the excitation	136
Figure 5.3	ns-TRE spectra recorded after 280 nm excitation of 1a in deoxygenated acetonitrile recorded at indicated time delays. The inset shows the experimental (\circ) and fitted (—) phosphorescence (Phos) kinetic trace obtained for 1a in deoxygenated acetonitrile	138
Scheme 5.1	Dynamics and major deactivation pathways proposed for 1a in acetonitrile after 280 nm excitation	140
Figure 5.4	Broadband time-resolve fluorescence (a) and transient absorption (b) spectra of 2a in acetonitrile recorded at indicated time delays after excitation at 280 nm. The insets show the early time delay of the spectra	143
Figure 5.5	Experimental (\circ , Δ) and fitted (—) decay profiles of fs-TRF (a) and TA (b) at indicated wavelengths obtained with 280 nm excitation of 2a in acetonitrile. The insets show the decay profiles at the early delay times	145
Figure 5.6	Broadband time-resolve fluorescence (a) and transient absorption (b) spectra of 2b in acetonitrile recorded at indicated time delays	

	after excitation at 280 nm. The insets show the early time delay of the spectra	147
Figure 5.7	Experimental (\circ , Δ) and fitted (—) decay profiles of fs-TRF (a) and TA (b) at the indicated wavelengths obtained with 280 nm excitation of 2b in acetonitrile. The insets show the decay profiles at early delay times	149
Figure 5.8	ns-TRE spectra recorded after 280 nm excitation of 2a in deoxygenated acetonitrile recorded at indicated time delays. The inset shows the comparison of spectra obtained at the indicated delay times from fs-TRF (red line) and ns-TRE (blue line) measurement of 2a in deoxygenated acetonitrile after 280 nm excitation	151
Figure 5.9	Experimental (\circ , Δ) and fitted (—) phosphorescence (Phos) and delayed fluorescence (DF) kinetic traces of 2a obtained from ns-TRE with 280 nm excitation in deoxygenated acetonitrile	152
Scheme 5.2	Dynamics and major deactivation pathways proposed for 2a and 3a in acetonitrile after 280 nm excitation	154
Figure 5.10	Broadband time-resolve fluorescence (a) and transient absorption (b) spectra of 3b in acetonitrile recorded at indicated time delays after excitation at 280 nm. The inset shows the early time delay of the spectra	156
Figure 5.11	Experimental (\circ , Δ) and fitted (—) kinetic time profiles of fs-TRF ((a), (c)) and TA ((b), (d)) at indicated wavelengths obtained with	

	280 nm excitation of 3a ((a), (b)) and 3b ((c), (d)) in acetonitrile. The insets show the decay profiles at early delay times	158
Scheme 5.3	Schematic representation of the torsional disordered (a) and the planar (b) structure of the oligo(<i>p</i> -PE) chromophore in 2a and 2b	162
Figure 6.1	Broadband time-resolve fluorescence spectra of 1 (a), 2 (b) and 3 (c) recorded at indicated time delays in acetonitrile after excitation at 280 nm. The insets show comparisons between fs-TRF recorded at ~50 ps (solid line) and ns-TRE recorded at ~3 μs (dotted line) after the excitation	179
Figure 6.2	Experimental (○, Δ) and fitted (—) decay profiles of TRF at indicated wavelengths obtained after 280 nm excitation of 1 (a), 2 (b) and 3 (c) in acetonitrile. The insets show the decay profiles at long decay times after the excitation	182
Figure 6.3	Broadband transient absorption of 1 ((a) and (b)), 2 (c) and 3 (d) in acetonitrile recorded at indicated delay times after excitation at 280 nm. The insets show the spectral evolution at long delay times after the photo-excitation	184
Figure 6.4	Normalized experimental (○, Δ) and fitted (—) kinetic time profiles obtained from TA at selected wavelengths of 1 (a), 2 (b) and 3 (c) in acetonitrile after 280 nm excitation. The insets show	

	the corresponding temporal evolution at late delay times after the photo-excitation	187
Figure 6.5	Broadband time-resolved emission spectra of 1 (a), 2 (b) and 3 (c) recorded at indicated decay times in deoxygenated acetonitrile with nitrogen purging after 280 nm excitation. The insets show the magnified spectra corresponding to the delayed fluorescence of the respective system	192
Figure 6.6	Normalized experimental (\circ , Δ) and fitted (—) phosphorescence (Phos) and delayed fluorescence (DF) kinetic traces obtained for 1 (a), 2 (b) and 3 (c) after 280 nm excitation in deoxygenated acetonitrile	194
Scheme 6.1	Proposed deactivation and emission pathways for oligo(PE) gold(I) complexes 1 , 2 and 3 in acetonitrile after 280 nm excitation	197
Figure S1	Steady state UV-visible absorption (red) and normalized 280 nm excited fluorescence (blue) spectra recorded for DMABEE in acetonitrile	212
Figure S2	Broadband transient absorption of DMABEE in acetonitrile recorded at 0-100 ps (a) and 100-6000 ps (b) after 280 nm excitation	213
Figure S3	Experimental (\circ , Δ) and fitted (—) kinetic decay profiles of TA at indicated wavelengths for 280 nm excited DMABEE in	

	acetonitrile. The inset shows the decay profiles at longer decay time up to ~6 ns	214
Figure S4	Steady state UV-visible absorption (red) and normalized 280 nm excited fluorescence (blue) spectra recorded for DMABEE in methanol	215
Figure S5	Broadband transient absorption of DMABEE in methanol recorded at 0-20 ps (a) and 20-6000 ps (b) after 280 nm excitation	216
Figure S6	Experimental (\circ , Δ) and fitted (—) kinetic decay profiles of TA at indicated wavelengths for 280 nm excited DMABEE in methanol. The inset shows the decay profiles at longer decay time up to ~1 ns	217
Figure S7	Steady state UV-visible absorption (red) and normalized 280 nm excited fluorescence (blue) spectra recorded for 1a (a), 2a (b) and 3a (c) in acetonitrile. The insets show the magnified view of the fluorescence spectra	218
Figure S8	Steady state UV-visible absorption (red) and normalized 280 nm excited fluorescence (blue) spectra recorded for 1b (a), 2b (b) and 3b (c) in acetonitrile	219
Figure S9	Steady state UV-visible absorption (red) and normalized 280 nm excited fluorescence (blue) spectra recorded for 1 (a), 2 (b) and 3 (c) in acetonitrile. The insets show the magnified view of the fluorescence spectra	220

List of Tables

Table 3.1	Photophysical parameters obtained for DMABME and DMABEE in acetonitrile	82
Table 4.1	Photophysical parameters obtained for DMABME and DMABEE in acetonitrile and methanol	108
Table 5.1	Spectral parameters of 1a – 3a and 2b – 3b	137
Table 6.1	Spectral parameters of 1 – 3	181

List of Abbreviations

¹ ICT	Intramolecular charge transfer state
¹ LE	Locally excited state
¹ MLCT	Singlet metal-to-ligand charge transfer state
³ MLCT	Triplet metal-to-ligand charge transfer state
³ $\pi\pi^*$	$\pi\pi^*$ natured triplet state
³ T ₁	Triplet
[TEE]H ₄	Tetraethynylethene
A	Acceptor
AC	Aromatic carbonyl
BS	Beam splitter
CaF ₂	Calcium fluoride
CCD	Charge-coupled device
CH ₃ CN	Acetonitrile
CT	Charge transfer
D	Donor
DF	Delayed fluorescence
dinap	2,2'-bis(diphenylphosphino)-1,1'-binaphthyl
DMA	Dimethylamino
DMAAP	4-dimethylaminoacetophenone
DMABA	4-dimethylaminobenzaldehyde
DMABEE	Ethyl-4-dimethylaminobenzoate
DMABME	Methyl-4-dimethylaminobenzoate
DMABN	4-dimethylaminonitrile

DMABZ	4-dimethylaminobenzoate
DSS	Dynamic Stokes' shift
ΔE	Energy difference
ΔL	Difference in optical path
Δt	Time between the pump and the probe / Temporal delay
E_1	Low energy level
E_2	Higher energy level
ESA	Excited state absorption
ε	Molar absorptivity
ε_{\max}	Molar absorptivity maximum
FC	Franck-Condon
fs	Femtosecond
GB	Ground state bleaching
GVD	Group velocity dispersion
h	Planck's constant
H-bonding	Hydrogen bonding
IC	Internal conversion
ICCD	Intensified charge-coupled device
ICT	Intramolecular charge transfer
I_{LE}/I_{ICT}	Intensity ratio of 1LE to 1ICT state emission
IR	Infra-red
IRF	Instrument response function
ISC	Intersystem crossing
k_f	Radiative rate of fluorescence
k_{ISC}	ISC rate

k_q	Quenching rate
k_r	Radiative rate
LC	Ligand centred
LE	Locally excited
LE/ICT	LE to ICT
λ	Wavelength
λ_{\max}	Wavelength maximum
MCP	Microchannel plate
Nd:YLF	Neodymium Yttrium Lithium Fluoride
Nd:YVO ₄	Neodymium Yttrium orthovanadate
ns	Nanosecond
OLED	Organic light-emitting diode
OPA	Optical parametric amplifier
PCy ₃	Tricyclohexylphosphine
PE	Phenyleneethynylene
PF	Prompt fluorescence
Phos	Phosphorescence
PICT	Planarized intramolecular charge transfer
ps	Picosecond
r	Anisotropy
RGA	Regenerative amplifier
S/N	Signal-to-noise
SDG	Synchronization and delay generator
SE	Stimulated emission
S ₀	Electronic ground state

S_1	Lowest electronically excited singlet state
S_n	Upper electronically excited singlet state
SOC	Spin-orbit coupling
TA	Transient absorption
Ti:sapphire	Titanium:sapphire
TICT	Twisted intramolecular charge transfer
TRE	Time-resolved emission
TRF	Time-resolved fluorescence
TRFA	Time-resolved fluorescence anisotropy
TTA	Triplet-triplet annihilation
T_1	Lowest electronically excited triplet state
T_n	Upper electronically excited triplet state
τ_r	Radiative lifetime
UV	Ultraviolet
VR	Vibrational relaxation
WLC	White-light continuum
μs	Microsecond
ν	Frequency
Φ_e	Overall emission yield
Φ_f	Fluorescence quantum yield
Φ_{ISC}	Intersystem crossing yield
Φ_{PF}	Prompt fluorescence quantum yield
Φ_{R}	Radiative yield

Chapter 1 Introduction

1.1 Overview of the Interaction of Matter with Light

To understand how light interacts with molecular system, we should first consider that light consists photons, each of which has a quantum of energy proportional to its frequency (ν). Absorption of photon by a molecule occurs when the photon has exactly the amount of energy that matches the energy difference (ΔE) between a low (E_1) and a higher (E_2) energy level of the molecule, leading the molecule to excite from the low to the high electronic state. This process is called electronic transition and can be described by the equation below:

$$\Delta E = E_2 - E_1 = h\nu$$

Where h is the Planck's constant

Electronic transition is an instantaneous process where the Franck-Condon principle applies. Due to the large difference (by ~ 1000 times) in mass between a proton and an electron, the motions of nuclei are usually much slower ($10^{-13} - 10^{-14}$ s) compared to that of the electrons ($10^{-15} - 10^{-16}$ s).^{1,2} As a consequence, the absorption of photons by a molecule can only initiate an abrupt jump of the electrons from one electronic orbital to another without changes in the positions of the more massive nuclei in the molecular entity and its environments.^{1,2}

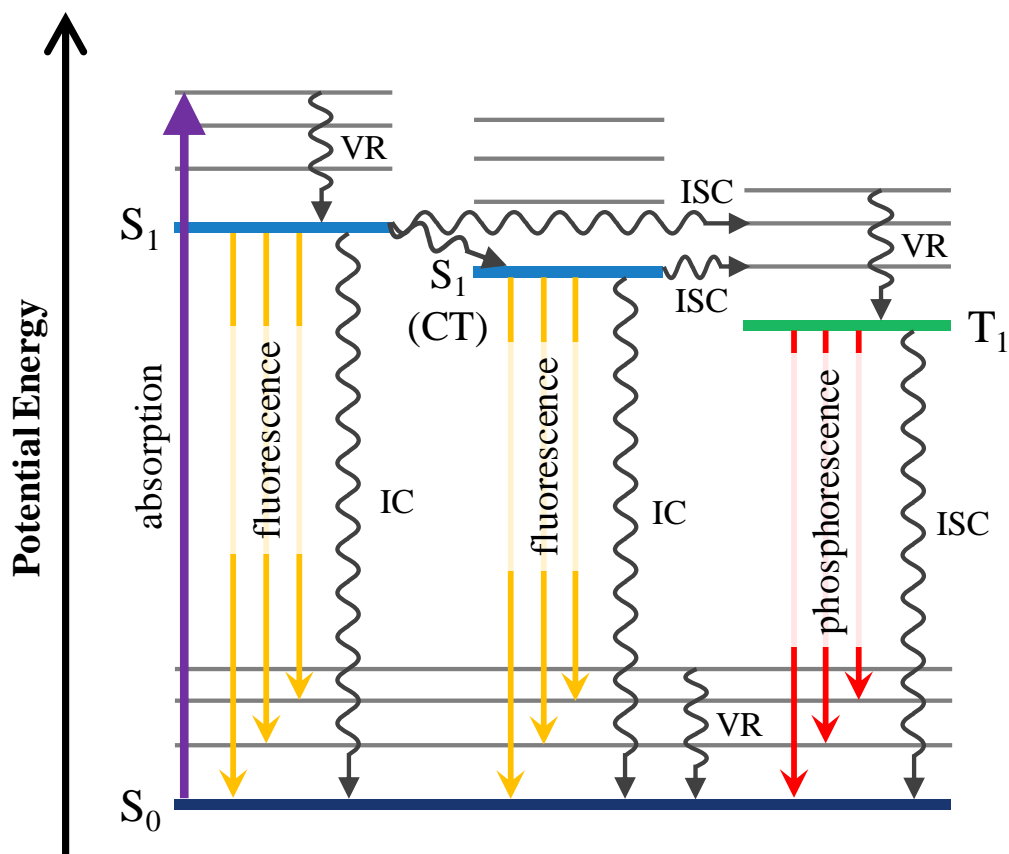


Figure 1.1 Jablonski diagram of some radiative and non-radiative processes available to a photo-excited molecule. Radiative and non-radiative transitions are indicated in straight and wavy arrows respectively. (VR = vibrational relaxation; IC = internal conversion; ISC = intersystem crossing; CT: charge transfer state)

After absorbing the photon, the molecule may dissipate the energy it gained through various possible pathways as outlined in Figure 1.1 using the Jablonski diagram.^{1,2} In the figure, the vertical axis represents the potential energy of the system. In this diagram, only the electronic levels corresponding to the ground state (S_0), the lowest electronically excited singlet state (S_1) and lowest electronically excited triplet state (T_1) of the molecule are shown. The

upper electronically excited singlet (S_n) and triplet (T_n) states are not included in the figure, for most of the photophysical processes concerned in this thesis take place from the lowest excited state. This is so even when the system is subjected to high energy excitation that produces the higher energy S_n state, the S_n to S_1 relaxation is ultrafast, usually happens in femtosecond (fs) timescale, before the onset of most photophysical and photochemistry processes.

The diagram in Figure 1.1 depicts radiative and non-radiative decay pathways between the different excited states and between the excited states and the S_0 . In brief, the commonly encountered radiative pathways in both the absorption or emission processes are:

- (i) Spin-allowed singlet-singlet absorption of photons ($S_0 + h\nu \rightarrow S_1$);
- (ii) Spin-forbidden singlet-triplet absorption of photons ($S_0 + h\nu \rightarrow T_1$);
- (iii) Spin-allowed singlet-singlet emission, called fluorescence ($S_1 \rightarrow S_0 + h\nu$);
- (iv) Spin-forbidden triplet-singlet emission, called phosphorescence ($T_1 \rightarrow S_0 + h\nu$);

On the other hand, the non-radiative processes are:

- (v) Spin-allowed conversions between states of the same spin, called internal conversion (IC) (e.g. $S_1 \rightarrow S_0 + \text{heat}$);

(vi) Spin-forbidden conversions between excited states of different spin (e.g. $S_1 \rightarrow T_1 + \text{heat}$) or between the triplet and the ground state (e.g. $T_1 \rightarrow S_0 + \text{heat}$), called intersystem crossing (ISC).

(vii) Non-radiative decay along the singlet manifold and relaxes to an electronic state having a charge transfer (CT) character, called CT state.

1.2 The Radiative and Non-Radiative Energy Dissipating Pathways

Upon ultraviolet (UV) excitation (purple upward arrow in Figure 1.1), the molecule in the S_0 is promoted to the S_1 . Promptly after the excitation, the S_1 molecule, normally in the vibrationally excited states, first undergoes vibrational relaxation (VR) to lose the excess vibrational energy to the surrounding and relaxes to the lowest vibrational energy level of S_1 . After this, the vibrationally “relaxed” S_1 molecule may deactivate back to the S_0 via a number of relaxation pathways. It can decay back to the S_0 radiatively and this gives out the singlet-singlet ($S_1 \rightarrow S_0$ here) luminescence called fluorescence (orange downward arrows in Figure 1.1). This radiative transition occurs between states of the same multiplicity, is spin-allowed and proceeds at the rate of $\sim 10^6 - 10^9 \text{ s}^{-1}$.¹⁻⁴

The S_1 molecule can also take the non-radiative channel to convert into the S_0 , a process called IC, the non-radiative counterpart of the radiative transition between the states with the same multiplicity. Unlike the very rapid IC from the S_n to S_1 ($S_n \rightarrow S_1$), the rate of IC from S_1 to S_0 ($S_1 \rightarrow S_0$) is usually much slower since the rate of IC is controlled largely by the difference in energy between the correlated state, while the energy difference between the S_1 and S_0 , in many cases, is much larger than that between the S_n and S_1 . The very rapid $S_n \rightarrow S_1$ IC actually accounts for the negligible fluorescence from the upper excited states and the fact that the major contribution of fluorescence in the steady state spectrum is from the S_1 state of the molecule.

Besides, the molecule in the photo-initiated S_1 state can relax non-radiatively along the singlet coordinate and formed the CT state (Figure 1.1).

One of the most commonly formed CT states is the intramolecular CT (ICT) state which its formation is favoured when an electron donating and accepting group is linked together in a molecular entity. In this regard, a large fraction of electronic charge is transferred from the electron donor to the electron acceptor. As a result, positive charge is developed at the donor site and at the same time negative charge can be seen at the acceptor moiety. Similar to the photo-initiated S_1 state, the CT or ICT state can also take the radiative or the non-radiative channel to the S_0 via fluorescence or IC respectively.

Besides IC and fluorescence, for the molecule in S_1 state or relaxed singlet CT state can also change its state of spin and converts from the singlet manifold into the triplet manifold, a process known as ISC (the horizontal wavy arrows in Figure 1.1). ISC is a spin-forbidden process due to non-radiative transition between states of different spin multiplicity. Generally, the rate of ISC is governed by the spin-orbit coupling (SOC) and the energy difference between the precursor singlet and the successor triplet state. The rate of ISC varies from $\sim 10^6 \text{ s}^{-1}$ in aromatic hydrocarbon to $\sim 10^{10} - 10^{11} \text{ s}^{-1}$ in molecules containing “heavy atoms”.¹⁻⁴ The much faster rate of ISC displayed by the “heavy atom” containing molecules is considered to arise due to increased SOC induced by the heavy atom. This is mostly observed with transition metal containing systems where the enhancement of SOC is considered to be proportional to the atomic number of the metal ion, the so-called “heavy atom effect”.¹⁻³

After the ISC, the nascent T_1 molecule may perform VR dissipating the excess vibrational energy prior to other relaxation processes. Then, the vibrationally “relaxed” T_1 may depopulate back to the S_0 through radiative or

non-radiative channel. The radiative decay produces emission named phosphorescence and the non-radiative process called ISC. Phosphorescence (the red downward arrows in Figure 1.1) is due to the radiative transition between states of different multiplicity and proceeds in a much slower rate than that of fluorescence due to spin-forbidden nature of this transition. For the similar reason, the rate of non-radiative $T_1 \rightarrow S_0$ ISC is also much slower, and thus the lifetime of the T_1 is normally very long ranging from 10^{-4} to 10^2 s under deoxygenated condition. This is in contrast to the singlet natured excited state which normally has lifetime in the 10^{-6} to 10^{-9} s.¹⁻⁴

It is worth noting that, apart from the fluorescence emitted from the photo-excited singlet state, the so-called prompt fluorescence (PF), there is in some cases “delayed fluorescence” (DF) arising due to re-populated of the singlet state from the triplet ($T_1 \rightarrow S_1$) after the $S_1 \rightarrow T_1$ ISC. Such $T_1 \rightarrow S_1$ re-population can take place through two possible mechanisms.

One is thermal activation and the other the triplet-triplet annihilation (TTA).¹⁻³ The process of thermal activation induced DF is also called the triplet-to-singlet up-conversion. In this case, the repopulated S_1 and therefore the DF features a lifetime which is nearly identical to the lifetime of the T_1 .^{1,2,5-8} DF given by this mechanism mostly occurs in molecules possessing small singlet-triplet energy gap, such as benzophenone and fluorescein.¹⁻³

On the other hand, TTA proceeds when two triplet state molecules collide and “annihilate” each other, producing one molecule in the higher energy S_1 and the other in the lower energy S_0 (i.e., $T_1 + T_1 \rightarrow S_1 + S_0$). With this mechanism, the re-populated S_1 and thus the DF displays lifetime that is about half of the

lifetime of the T_1 .^{1,2,5,6} It is clear that, to distinguish the mechanism leading to the DF, an effective method is to measure and make comparison of the lifetime displayed by the DF and the phosphorescence from triplet state. The mechanism of thermal activation is implied by nearly identical in the lifetime of DF and phosphorescence; while the TTA mechanism expects the lifetime of DF being about half of the phosphorescence lifetime.^{1,2,5,6,9,10}

In order to investigate the overall deactivation cascade of photo-excited system, time-resolved methods based on various spectroscopic techniques have been applied widely to directly probe the dynamics and spectral feature of the transient excited states. In this thesis, a combined application of fs broadband time-resolved fluorescence (fs-TRF) and fs transient absorption (fs-TA) in conjunction with nanosecond (ns) transient absorption (ns-TA) and ns time-resolved emission (ns-TRE) was used to characterize the excited state pathways and the corresponding relaxation dynamics of two types of molecular systems: one is the typical donor-acceptor (D-A) molecules 4-dimethylaminobenzoates (DMABZs) and the other a series of gold(I) metal complexes containing the oligo-phenyleneethynylene (PE) ligands.

DMABZs can be recognized as pure organic molecules while oligo-gold(I) PE complexes can be classified as organometallic compounds. Although they belong to different molecular categories, they both facilitate ISC owing to the carbonyl substitution on the aromatic scaffold in DMABZs and the SOC induced by the heavy metal ion centre in oligo-gold(I) PE complexes respectively. Nevertheless, their respective excited state dynamics and the factors governing their excited state behaviour are still largely unexplored. As a result,

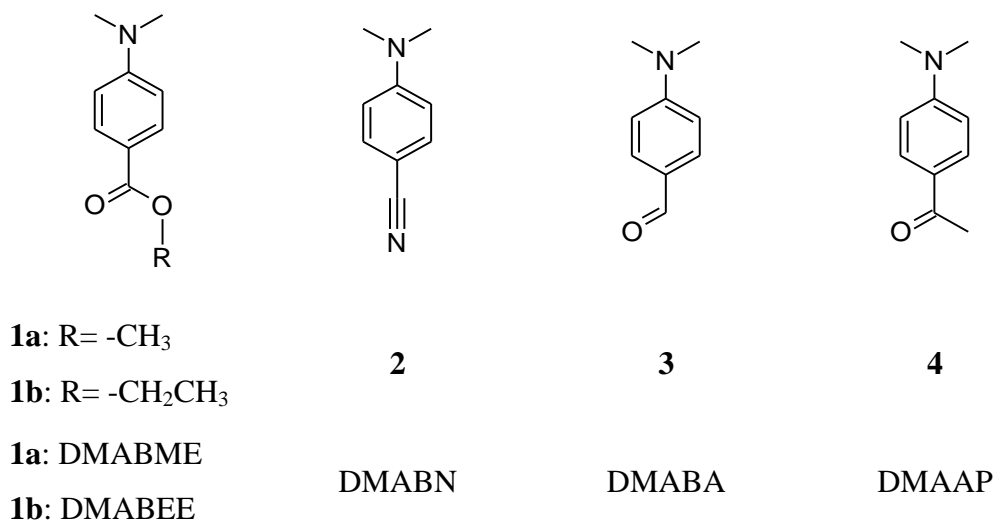
methyl-4-dimethylaminobenzoate (DMABME) is selected as a representative of DMABZs. Its corresponding deactivation cascade in acetonitrile and the competing ICT reaction with respect to ISC are first presented in Chapter 3. The result acts as a paradigm to represent the deactivation pattern for *para*-amino substituted aromatic carbonyl compounds. Furthermore, by comparing the spectral and temporal features of DMABME in methanol *versus* in acetonitrile in Chapter 4, the role of the solvent hydrogen bonding (H-bonding) effect on the dynamics and pathways of the excited state decay can be revealed.

On the other hand, for the oligo-gold(I) PE complexes, the excited state dynamics upon the incorporation of heavy gold(I) metal ion into the PE ligand, together with the effect of ligand π -conjugation in promoting and controlling the ISC rate of the complex is depicted in Chapter 5. Moreover, in Chapter 6, the ligand length and substitution pattern dependent excited state dynamics governing the dual emission character of the oligo-gold(I) PE complexes is presented.

1.3 Background of the Photo-Induced Intramolecular Charge Transfer Reaction of DMABZs

In the recent decades, the excited states of DMABZs have been intensively studied because of the fundamental interest in photo-induced ICT^{11,12} and the practical application of these type of compounds as active ingredients in the UVB sunscreens.¹³⁻¹⁵ Having the dimethylamino as electron donor and the benzoate moiety the electron acceptor group, this type of compound has been considered as model system for study of various aspects of the ICT reaction occurring in the singlet excited state.^{11,12,16-19} Like the prototype D-A molecule 4-dimethylaminonitrile (DMABN, **2** in Scheme 1.1) in polar solvent,^{11,12} these so-called ester analogues of **2** exhibit dual fluorescence induced by the ICT reaction from the initial locally excited (LE) to the ICT state.

A large number of literature studies have been revealed for a substantially higher ICT reactivity for the ester analogues than **2**. In contrast to the little involvement of ICT of **2** in non-polar solvent, the ICT fluorescence has been reported for the esters in aliphatic hydrocarbon solvents.^{11,16} Recently, fs studies reported a ~1 ps ICT time constant for ethyl-4-dimethylaminobenzoate (DMABEE, **1b** in Scheme 1.1) in acetonitrile,^{20,21} much faster than the ~5 ps ICT time reported for **2** in the same solvent.²²⁻²⁵ Although the increase in the ICT rate has been attributed to the stronger electron affinity of the alkoxy-carbonyl group in **1** than that of the cyano in **2**,^{11,16} the details of the ICT pathway for the ester analogue have remained unclear. There have been different views regarding the ICT reaction, in particular the precise electronic nature of the LE state.^{20,21,26}



Scheme 1.1 Structures of the studied and related compounds.

Like the other *para*-substituted benzene derivatives, the lowest energy absorption band of DMABZs is composed of two close lying $\pi\pi^*$ transitions corresponding to the S_0 to L_a and S_0 to L_b in Platt's notation.^{11,12,27} The two transitions are both in-plane polarized but with the polarization direction perpendicular to each other. The L_a polarization is parallel to the long molecular axis while that of the L_b along the short axis. Therefore, the L_a state has inherently the ICT character and can be more stabilized than the L_b by increasing the donor and/or acceptor strength or the solvent polarity.^{11,26} As a result, the difference in energy (ΔE) between the L_a and L_b and even the relative ordering of the two states can be varied by changing the donor/acceptor or polarity of solvent. It is now well accepted that, for **2** at the Franck-Condon (FC) region, the energy of L_a is higher than L_b irrespective of the solvent property, *i.e.*, the L_a is corresponding the S_2 state while the L_b the S_1 state.^{11,26,28} The ICT of **2** is therefore an adiabatic process proceeding with the L_b as precursor to the ICT state which is L_a in parentage.^{11,16,26,29,30}

For **1** in the gas phase, the energy of the L_a is still higher than that of L_b at the FC region but having a reduced ΔE when compared to that of **2** due to the increased strength in the A group, which is benzoate in **1** and benzonitrile in **2**.^{11,31,32} However, steady state fluorescence anisotropy studies²⁶ and some theoretical calculations²⁷ suggested that the ordering in FC of the L_a and L_b state could be reversed in the solution phase, implying that solvent plays an important role in varying the energies of the two states.^{11,16} In this regard, the well known twisted ICT (TICT) model^{11,12} states that the L_b/L_a vibronic mixing presents in **2** is no longer existed in the deactivation cascade of **1** and the related carbonyl analogous, 4-dimethylaminobenzaldehyde (DMABA) and 4-dimethylaminoacetophenone (DMAAP) (**3** and **4** in Scheme 1.1). Within this context, the ICT in DMABZs occurs entirely on the $L_a(S_1)$ hyperpotential energy surface and the kinetics is controlled mainly by entropy activation relevant to such as the rearrangement of the molecular structure.^{11,20,26}

There is however a different view in the so-called planarized ICT (PICT) or state coupling model which questions the L_a versus L_b energy inversion in the FC region.^{11,20,21,26} This model assumes that the order of energy level in the FC region (i.e., $S_1(L_b)$ and $S_2(L_a)$) is retained in DMABZs as in **2** and proposes that, in solution, the ICT reaction occur through the same pathway in the two types of D-A molecules.^{19,21} It also suggests that the reduced ΔE in **1** may facilitate the vibronic mixing between L_b and L_a and is responsible for the faster ICT in **1b** than in **2**. As a consequence, a question remains concerning the character of 1LE state of DMABZs: does the LE feature a L_b character as suggested by the state coupling model or in the L_a character proposed by the TICT model?

In addition to the nature of the LE state, the excited state process of **1** is also complicated by ISC which brings the excited state population from the singlet to the triplet manifold. This is so because **1** bears the carbonyl group attached to the phenyl ring and it is widely known aromatic carbonyl (AC) compound usually features a high ISC efficiency and a very rapid ISC rate.^{1,2} For instance, a nearly unitary ISC efficiency has been reported for AC compounds such as benzophenone and acetophenone; and ISC time constant of several to tens ps for *p*-aminobenzophenone and *p*-hydroxyphenacyl phosphates,³³⁻³⁵ which is comparable to the ICT time reported for **1b**.^{20,21} Therefore, for **1**, ISC is expected to be an important competing process to quench not only the radiative process but also the ICT reaction in the solution phase.

From experiments on closely related **3** and **4** (Scheme 1.1) found that the photo-populated $\pi\pi^*$ state decays rapidly (~ 2 ps time constant) leading to formation of both the ICT state and a $\pi\pi^*$ natured triplet (3T_1) state in acetonitrile.³⁶ Taking into account that the DMABZs type of molecules are used as ingredient in sunscreen products and that the 3T_1 of AC compounds like DMABZs is capable of sensitizing DNA to yield potentially harmful photolesions for the onset of skin cancer,³⁶⁻³⁹ information on the 3T_1 state produced after absorption of UV radiation in molecules as **1** would have important implication for sunscreen safety and for assessing the appropriateness of these compounds as the sunscreen ingredient. In short, the deactivation cascade of UV-excited DMABZs has remained largely unclear in the literature and little is known for certain about the dynamics and formation efficiency of the 3T_1 state.

To help address these issues, broadband fs-TA, fs-TRF anisotropy (fs-TRFA), fs-TRF, and ns-TA spectroscopy were used to study excited state dynamics of DMABME (**1a** in Scheme 1.1) in the solution phase. The data obtained are depicted in Chapter 3 and these provide a direct and comprehensive characterization of the dynamics and spectral signatures for the LE, ICT and the 3T_1 states of **1a** in acetonitrile. The results presented on one hand provide a compelling evidence for clarifying the up to now uncertain LE state electric origin, and on the other hand reveal a clearer picture for the ICT reaction as well as the competing pathway of ISC leading to formation of the 3T_1 state.

1.4 Background of the Hydrogen-Bonding Effects on DMABZs

Besides the excited state dynamics and spectral characteristics, the dual emission of **1a** (Scheme 1.1) is of great interest due to its sensitivity to the property of environment.¹¹ It is known that the dual emission arises due to the photo-induced ICT reaction with the blue component from the LE state and the red component from the ICT state. The structural conformation of the ICT state of this molecule has been under extensive debates, recent experimental study provides strong evidence supporting the TICT model.^{11,26,32,40-42}

On the other hand, the dual emission of its analogues such as **2** and **3** have been demonstrated to be highly solvent polarity dependent.^{11,43,44} For instance in **2**, only LE fluorescence is observed in non-polar solvents; while in polar solvents, the long wavelength ICT fluorescence appears. Upon increasing the solvent polarity, the relative intensity of the red-shifted ICT emission grows in accompanied with a decrease in the intensity of the blue LE fluorescence. Besides, the solvent polarity influence can be reflected from the strong solvatochromic red shift of the ICT fluorescence band maximum and the decrease in the ratio of LE to ICT (LE/ICT) emission intensity.^{11,43} Based on the correlation of the intrinsic emission character (the LE/ICT emission intensity ratio or the ICT emission band maximum) with respect to the surrounding micro-environment, this kind of prototype is capable to serve as a probe to indicate the polarity change in the solvent environment or identify the target compound when it is tethered to a sensing unit.⁴⁵⁻⁴⁷

Giving the potential application of dual emission compounds as the environmental sensor, it is important to understand in detail the influence of

solvent on the emission property of these compounds.^{48,49} Unfortunately, how precisely the interaction between the molecule and surrounding solvents may affect the excited state dynamics and therefore the emission property is largely unexplored for DMABZs type of molecules, to the best of our knowledge. Having explored the excited state deactivation pathway for **1a** in polar aprotic acetonitrile (Chapter 3), we present in Chapter 4 our time-resolved study on the deactivation cascade of **1a** in polar protic solvent methanol to elucidate the effect of solvent, in particular the H-bonding property of solvent, on the deactivation pathway.

It is relevant to note that literature studies have found that for a substantial number of dual emission ICT molecules, including the best known **2**, the intensity ratio of the blue to red emission component, the red emission maximum and the overall emission quantum yield vary significantly in aprotic *versus* in protic solvent.^{11,23,50} For instance, the ICT band emission quantum yield drops from 0.030 to 0.017 and the ICT red emission shifts from ~480 nm (20800 cm⁻¹) in acetonitrile to ~508 nm (19700 cm⁻¹) in methanol.⁵¹ The drastic drop in the emission quantum yield was attributed to the H-bonding formation between the ICT state and solvent molecules in protic solvent, which on the other hand does not occur in the aprotic solvent.^{23,51-53} The H-bonding opens up an additional deactivation channel, which is the IC, for the deactivation of the ICT state to the S₀. In Chapter 4, results obtained from broadband fs-TA and fs-TRF studies are presented for a clearer picture on how the H-bonding may affect the excited state dynamics and the overall deactivation pathway of **1a**.

1.5 Background of the Intersystem Crossing Rate of Oligo-gold(I) PE Complexes

ISC is of fundamental importance for transition metal complexes, its efficiency plays a pivotal role in a wide range of applications of the transition metal complexes, including light-harvesting antennae for solar energy conversion, new materials for luminescence sensing, photo-imaging and optoelectronic devices, *etc.*⁵⁴⁻⁵⁶ Despite of its spin-forbidden nature, the ISC in many luminescent metal complexes proceed at very high rate, surpasses the spin-allowed relaxation pathway(s) such as the radiative decay and nonradiative IC of the excited singlet state to the S_0 .

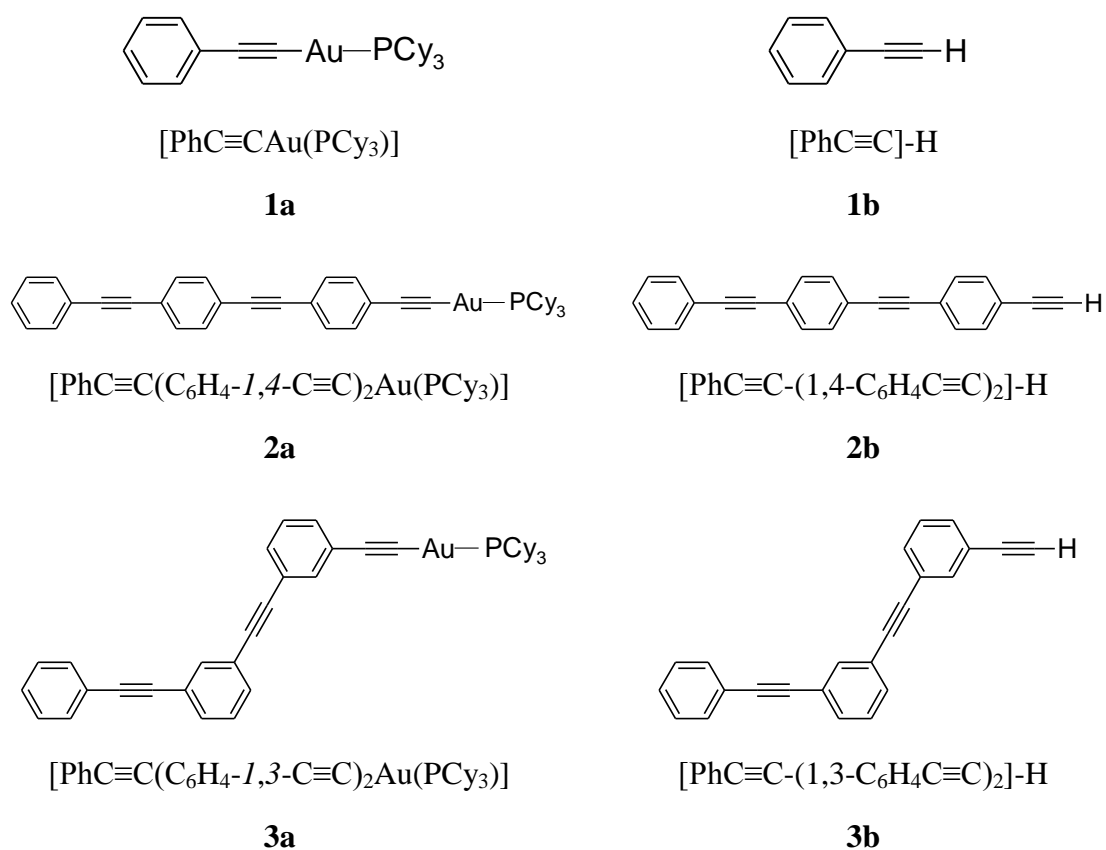
Indeed, recent ultrafast time-resolved studies found that ISC in a number of d-block metal complexes takes place in ultrafast timescale ($< \sim 1$ ps) with a close to unitary yield of the triplet state, leading to a limited contribution of PF from the photo-populated singlet excited states.⁵⁷⁻⁶¹ As a result, a widely accepted model nowadays considers that most of the functional roles exhibited by transition metal complexes are derived from the triplet excited states, as the precursor singlet states are quenched by the rapid ISC at a very early stage before they are significantly involved in the photophysical and/or photochemical processes. The prompt ISC in transition metal complexes has long been attributed to the “heavy-atom effect”^{1,2,54,56} which is expected to facilitate spin crossover by SOC with the efficiency proportional to increase in the atomic number of the metal ion.

However, recent investigations have observed evidences questioning this simplistic correlation and proposed that additional factors may also influence the

ISC and therefore the kinetics of excited state dynamics. Taking the less heavier Fe(II)-diimine complex as an example, it shows formation of the triplet metal-to-ligand charge transfer state ($^3\text{MLCT}$) in <20 fs after photo-excitation,⁶⁰ however, both $[\text{Cu}(\text{diimine})_2]^+$ and $[\text{Pt}(\text{dinap})_2]^+$ (dinap = 2,2'-bis(diphenylphosphino)-1,1'-binaphthyl) feature a relatively long-lived singlet metal-to-ligand charge transfer state ($^1\text{MLCT}$) excited state with ~ 15 and ~ 3 ps lifetime respectively.⁶² The relatively slow ISC in the later two systems was considered to arise due to a reduction in the state mixing between the $^1\text{MLCT}$ and $^3\text{MLCT}$ owing to excited state structural distortion in these complexes.

Furthermore, a series of Rh(III) complexes anchoring 2,5-bis(arylethynyl) rhodacyclopentadienes were reported to display very long-lived and intense fluorescence (fluorescence lifetime = 1.2-3.0 ns, fluorescence quantum yield, $\Phi_f = \sim 0.3-0.7$), in contrast to the minor involvement and ultra-short-lived PF reported for the many other 4d or 5d metal complexes.⁶³ Similarly, anomalous intense fluorescence ($\Phi_f = \sim 0.22$) has also been observed with a tetranuclear gold(I) complexes $[\text{TTE}](\text{AuPCy}_3)_4$ ($[\text{TEE}]\text{H}_4$ = tetraethynylethene, PCy_3 = tricyclohexylphosphine),⁶⁴ despite the involvement of four “heavy atom” gold(I) in the complex.⁶⁵ Until now, little is known for certain on the precise factor(s) governing the rate of ISC in transition metal complexes as well as on the nature, the onset and exact timescale of the ISC.

To help address these issues, in Chapter 5, we present a combined study using broadband fs-TA coupled with fs-TRF^{5,6,41} and ns-TRE spectroscopy^{5,6} to investigate a series of gold(I)-PE complexes **1a-3a** and the corresponding ligand systems (**2b-3b**). The structures of these molecules are depicted in Scheme 1.2.



Scheme 1.2 Structure of the gold(I)-PE complexes and the corresponding free ligands.

Complexes **1a-3a** were selected because they display the interesting PE ligand length (**1a** vs **2a/3a**) and substitution pattern (**2a** vs **3a**) dependent dual emission behavior and the large difference in the emission quantum efficiency which is ~0.66 in **2a** ~0.12 in **3a** and ~0.08 in **1a**.^{6,66} Unlike the parent complex **1a**, complexes **2a** and **3a** both exhibit dual emission made of DF and phosphorescence from the singlet $\pi\pi^*$ ($^1\pi\pi^*$) and triplet $\pi\pi^*$ ($^3\pi\pi^*$) manifold of the oligo(*p*- and *m*-PE) ligand. The $^1\pi\pi^*$ to $^3\pi\pi^*$ emission intensity ratio in **2a** appears to be much larger than in **3a**. Besides, both **2a** and **3a** display also dual

emission at low temperature (77K) due to the phosphorescence and DF with lifetime in microsecond timescale.⁶

With the common Au(PCy₃)⁺ moiety in **1a-3a**, these complexes can be considered as excellent models for study of the role of PE ligand on the excited state dynamics and the emission properties of the respective systems.⁵⁷⁻⁶² On the other hand, it is noted that most of the metal complexes studied in literature by ultrafast spectroscopy feature ISC from the ¹MLCT natured singlet state to the ³MLCT natured triplet state. However, metal complexes having ISC from the ligand centred (LC) excited singlet state to the LC excited triplet state are sparsely studied by ultrafast time-resolved measurements and their excited state cascades have remained largely unexplored. In this regard, complexes **1a-3a** present prototype system for investigating the role of metal on the ISC which occurs between excited states where the excitations rest largely upon the ligand systems.

To help achieving this goal and also to examine the effect of gold(I) on the electronic properties of the π -conjugated and cross-conjugated *p*- and *m*-PE ligand, comparative fs-TA and fs-TRF experiments were also conducted on the corresponding metal-free oligo(PE) ligands **2b** and **3b** (Scheme 1.2). By monitoring the spectral evolution of the excited state spectra, our work provides direct and quantitative evidences for characterizing the dynamics and elementary steps for the emission pathways of **1a-3a**.

1.6 Background of the Luminescence Properties of Oligo-gold(I) PE Complexes

Gold(I) complexes bearing p -PE(n) (n = repeat number of the PE unit) ligand have been of great interest for their attractive properties in electron conductivity, charge-transporting and photo- and electro-luminescence associated with the electron delocalization along the π -conjugated PE backbones. Comparing to the p -PE analogues which have a linear shape and serve as molecular wires, the oligo- and poly- (o - and m -PE) counterparts are less studied as optoelectronic materials.⁶⁷ Recent researches on the oligo(o -PE) and oligo(m -PE) based foldamers⁶⁸ and light-harvesting dendrimers with m -PE components⁶⁹ have revived interest in these conjugated or cross-conjugated oligomers and polymers. Despite the oligo(o -PE) and oligo(m -PE) compounds are capable to form a folded or cyclic structure, the o - and m -PE fragments are rarely introduced as connectors or spacers for connecting two metal centres⁷⁰ while their *para*-substituted analogues have been extensively used for this purpose.⁷¹

Recently, there has been intense interest in developing high performance organic light-emitting diodes (OLEDs) by harvesting both the singlet and triplet excitons of π -conjugated oligomers and polymers.⁷² The expected gain in efficiency is based on the assumption that in organic materials, the excitons formed upon combination of the holes and electrons are in the ratio of one singlet to three triplets, and therefore emissive triplet excitons would lead to improved efficiency of OLEDs.⁷³

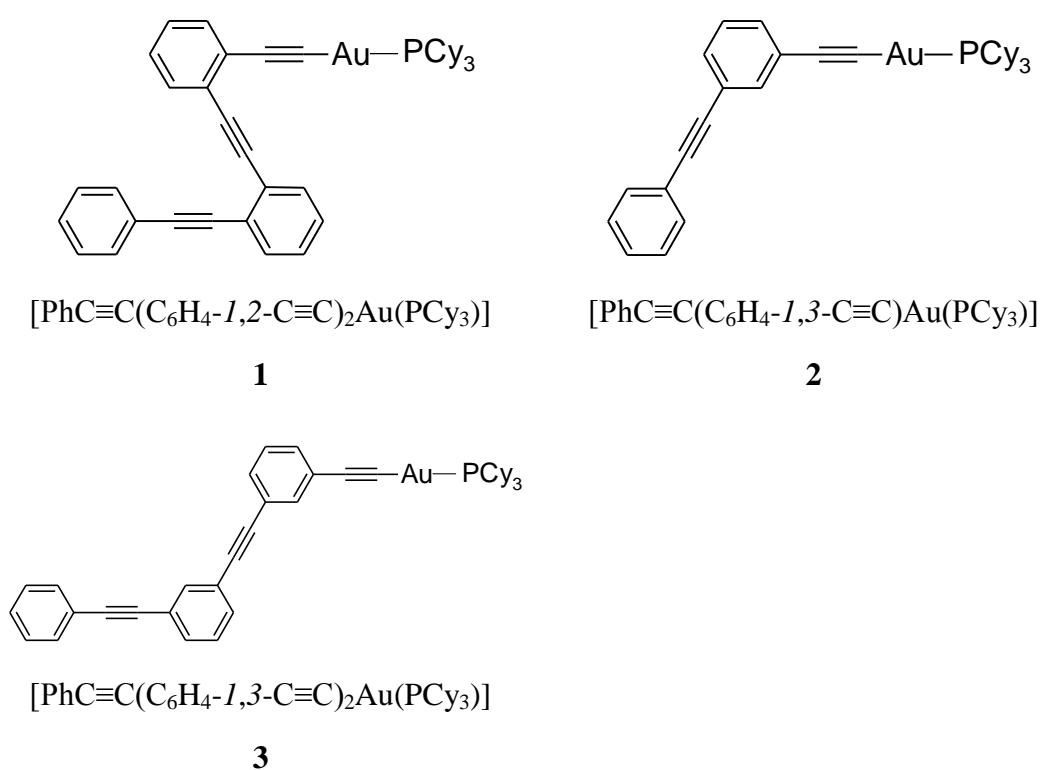
Immense efforts have been devoted towards searching for highly efficient organic phosphorescent light emitters. Among the various protocols, one

effective mean is to harness the heavy-atom effect on triplet excited states to “switch on” phosphorescence from varied polymer-based materials. For instance, doping the poly-(fluorene) polymer with residual palladium catalyst generated during synthesis was found to allow substantial enhancement in the phosphorescence quantum yield under ambient conditions.⁷⁴ Solid-state room-temperature phosphorescence was also detected from co-crystal of some polycyclic aromatic hydrocarbons and multinuclear planar mercury(II) complexes.⁷⁵ Besides, two research groups independently showed recently that intense phosphorescence can be observed from pure organic crystals consisting of the triplet-producing $^3(n-\pi^*)$ chromophores and the triplet-promoting heavy atom such as bromine.⁷⁶

In addition, incorporation of the bis(phosphine) platinum(II) moieties into the oligo- and poly-(*p*-PE) chains has been found to facilitate photo- and electro-luminescence from the triplet excited states of these platinum-containing polymers and oligomers in solution at the room temperature.⁷⁷ It is noted however that the low-energy d-d excited states of platinum(II) ion have an unfilled d orbital, which may disturb delocalization of the singlet and triplet excitons along the π conjugated *p*-PE systems. This may in turn introduce unwanted competing nonradiative deactivation channel and hence prohibit effective phosphorescence from platinum(II)-containing polymers in solutions.

An effective approach to eliminate the influence of d-d state is to employ gold and indeed complexes that have $[\text{Au}(\text{PCy}_3)]^+$ moiety attached to the termini of oligo(*p*-PE) compounds through Au-C \equiv C ligation have been synthesized in this regard.^{64-66,78} The $[\text{Au}(\text{PCy}_3)]^+$ moiety can, on one hand, facilitate the singlet

to triplet ISC through enhancing the SOC between the two states, and on the other hand, due to the closed-shell d^{10} configuration of gold(I) ion, the gold(I) complexes have no low lying d-d state to affect negatively the emission property of the complexes. In fact, emission due to phosphorescence and in some cases dual emission composed of phosphorescence and DF have been observed for a series of gold(I) oligo(*p*-PE) complexes in both solution or in the solid state at room temperature.^{66,78c}



Scheme 1.3 Chemical structures of selected oligo(*o*-PE) and oligo(*m*-PE) gold(I) complexes.

The property of showing dual emission from both the triplet and long-lived singlet excited state of some gold(I) oligo(*o*-PE) and oligo(*m*-PE) complexes is interesting since both the emissive singlet and triplet are harnessed in giving emission, which could present a mean for improving the efficiency as

well as the wavelength coverage of the emission. On the basis of this, three oligo(*o*-PE) and oligo(*m*-PE) gold(I) complexes (Scheme 1.3) were selected for time-resolved spectroscopic investigation in Chapter 6. A prominent feature exhibited by these complexes is that they display unit length and PE conjugation dependent emission properties. Both the intensities and the emission bands maxima, together with the emission quantum yield vary substantially depending on the length and substitution pattern of the PE ligand. Dual emission comprising a high-energy fluorescence and a low-energy phosphorescence implies a closeness in energy between the emissive singlet and triplet excited states. Such a feature is not seen in most of reported transition metal complexes, such as the diimine complexes containing Ru(II),⁵⁷ Re(I),⁵⁸ Pt(II),⁵⁹ and Fe(II)⁶⁰ and some cyclometalated Ir(III) complexes.⁶¹

As reported in the literature, all of these complexes show emissions mainly from their long-lived triplet excited states due to presence of ultrafast ISC (rate $\approx 10^{12}$ s⁻¹) leading to ultra-short singlet excited state lifetimes (about tens of femtoseconds to several picoseconds) and thus a minute involvement of fluorescence in their steady state emission spectra. In addition, the gold(I) complexes selected here are also different from the previously reported Rh(I)⁶³ and Au(I)⁶⁴ complexes bearing ethynylethene ligands; these complexes emit only fluorescence (~0.2-0.7 quantum yield) implying present of relatively long-lived singlet excited states (~1-3 ns lifetime), challenging the traditional picture of heavy atom effect in promoting the ISC.

The distinct dual emission behavior of the oligo(*o*-PE) and oligo(*m*-PE) complexes in Scheme 1.3 makes them good model systems for exploring a

number of basic but so far unclear issues about the excited states of light-emitting organometallic complexes, this includes the spectral and dynamics character of the related singlet and triplet excited states, the time scale and controlling factor affecting the ISC, and more important, the interaction between the singlet and triplet excited states in leading to the dual emission exhibited by the complexes.

To help address these issues and to elucidate the structure-emission relationship, a combination of time-resolved spectroscopic methods including fs-TRF, fs-TA, and ns-TRE are employed to directly monitoring the temporal evolution of excited state spectra over a wide range of time scale. The result obtained is able to not only unravel the excited state deactivation cascade but also to determine time constants for the ISC and lifetime for both the singlet and triplet excited states. The data thus provide explicit evidence for the origin of DF and how the dual emission is affected by the substitution pattern as well as the unit length of the PE ligand.

1.7 References

1. Turro, N. J.; Ramamurthy, V.; Scaniano, J. C. *Modern Molecular Photochemistry of Organic Molecules*; University Science Books, Sausalito, California, **2010**.
2. Turro, N. J. *Modern Molecular Photochemistry*; University Science Book, Mill Valley, CA, **1991**.
3. Barltrop, J. A.; Coyle, J. D. *Principles of Photochemistry*; John Wiley & Sons, Chichester, New York, **1978**.
4. Montalti, M.; Credi, A.; Prodi, L.; Gandolfi, M. T. *Handbook of Photochemistry*; 3rd ed., Boca Raton: CRC/Taylor & Francis, **2006**.
5. Lu, W.; Kwok, W. M.; Ma, C.; Chan, C. T. L.; Zhu, M. X.; Che, C. M. *J. Am. Chem. Soc.* **2011**, *133*, 14120-14135.
6. Ma, C.; Chan, C. T. L.; Kwok, W. M.; Che, C. M. *Chem. Sci.* **2012**, *3*, 1883-1892.
7. (a) Swenberg, C. E. *J. Chem. Phys.* **1969**, *51*, 1753-1764. (b) Azumi, T.; McGlynn, S. P. *J. Chem. Phys.* **1963**, *39*, 1186-1194.
8. Turek, A. M.; Krishnamoorthy, G.; Phipps, K.; Salteil, J. *J. Phys. Chem. A* **2002**, *106*, 6044-6052.
9. (a) Gerhard, A.; Bässler, H. *J. Chem. Phys.* **2002**, *117*, 7350-7356. (b) Hertel, D.; Bässler, H.; Guentner, R.; Scherf, U. *J. Chem. Phys.* **2001**, *115*, 10007-10013. (c) Hertel, D.; Setayesh, S.; Nothofer, H.-G.; Scherf, U.; Müllen, K.;

- Bässler, H. *Adv. Mater.* **2001**, *13*, 65-69. (d) Romanovskii, Y. V.; Bässler, H. *Chem. Phys. Lett.* **2000**, *326*, 51-57.
10. Bodunov, E. N.; Berberan-Santos, M. N.; Martinho, J. M. G. *Chem. Phys.* **2005**, *316*, 217-224.
11. Grabowski, Z. R.; Rotkiewicz, K.; Rettig, W. *Chem. Rev.* **2003**, *103*, 3899-4031.
12. Lippert, E.; Rettig, W.; Bonacic-Koutechy, V.; Heisel, F.; Mee, J. A. *Adv. Chem. Phys.* **1987**, *68*, 1-173.
13. Roscher, N. M.; Lindemann, M. K. O.; Kong, S. B.; Cho, C. G.; Jiang, P. *J. Photochem. Photobiol., A* **1994**, *80*, 417-421.
14. Vanquerp, V.; Rodriguez, C.; Coiffard, C.; Coiffard, L. J. M.; De Roeck-Holtzhauer, Y. *J. Chromatogr. A* **1999**, *832*, 273-277.
15. Gasparro, F. P.; Mitchnick, M.; Nash, J. F. *Photochem. Photobiol.* **1998**, *68*, 243-256.
16. Rettig, W. *Angew. Chem., Int. Ed. Engl.* **1986**, *25*, 971-988.
17. (a) Hrnjez, B. J.; Yazdi, P. T.; Fox, M. A.; Johnston, K. P. *J. Am. Chem. Soc.* **1989**, *111*, 1915-1916. (b) Sun, Y. P.; Fox, M. A.; Johnston, K. P. *J. Am. Chem. Soc.* **1992**, *114*, 1187-1192.
18. Grégoire, G.; Dimicoli, I.; Mons, M.; Dedonder-Lardeux, C.; Jouvet, C.; Martrenchard, S.; Solgadi, D. *J. Phys. Chem. A* **1998**, *102*, 7896-7902.

19. Zachariasse, K. A.; Druzhinin, S. I.; Kovalenko, S. A.; Senyushkina, T. J. *Chem. Phys.* **2009**, *131*, 224313.
20. Pigliucci, A.; Vauthey, E.; Rettig, W. *Chem. Phys. Lett.* **2009**, *469*, 115-120.
21. Zachariasse, K. A.; Druzhinin, S. I.; Mayer, P.; Kovalenko, S. A.; Senyushkina, T. *Chem. Phys. Lett.* **2009**, *484*, 28-32.
22. Changenet, P.; Plaza, P.; Martin, M. M.; Meyer, Y. H. *J. Phys. Chem. A* **1997**, *101*, 8186-8194.
23. Kwok, W. M.; George, M. W.; Grills, D. C.; Ma, C.; Matousek, P.; Parker, A. W.; Phillips, D.; Toner, W. T.; Towrie, M. *Angew. Chem., Int. Ed.* **2003**, *42*, 1826-1830.
24. Druzhinin, S. I.; Ernsting, N. P.; Kovalenko, S. A.; Lustres, L. P., Senyushkina, T.; Zachariasse, K. A. *J. Phys. Chem. A* **2006**, *110*, 2955-2969.
25. Gustavsson, T.; Coto, P. B.; Serrano-Andrés, L.; Fujiwara, T.; Lim, E. C. *J. Chem. Phys.* **2009**, *131*, 031101.
26. Rettig, W.; Lutze, S. *Chem. Phys. Lett.* **2001**, *341*, 263-271.
27. (a) Platt, J. R. *Chem. Phys.* **1949**, *17*, 484-495. (b) Murrell, J. N. *The Theory of the Electronic Spectra of Organic Molecules*; Chapman and Hall, London, **1971**.
28. Fisz, J. J.; van Hoek, A. *Chem. Phys.* **1997**, *270*, 432-442.
29. Fuß, W.; Pushpa, K. K.; Rettig, W.; Schmid, W. E.; Trushin, S. A. *Photochem. Photobiol. Sci.* **2002**, *1*, 255-262.

30. Gómez, I.; Reguero, M.; Boggio-Pasqua, M.; Robb, M. A. *J. Am. Chem. Soc.* **2005**, *127*, 7119-7129.
31. (a) Józefowicz, M.; Aleksiejew, M.; Heldt, J. R.; Heldt, J. *J. Mol. Liq.* **2010**, *157*, 61-66. (b) Aleksiejew, M.; Heldt, J.; Heldt, J. R. *J. Lumin.* **2009**, *129*, 208-220.
32. Parusel, A. B. J.; Köhler, G.; Grimme, S. *J. Phys. Chem. A* **1998**, *102*, 6297-6306.
33. (a) Ma, C.; Kwok, W. M.; Chan, W. S.; Zuo, P.; Kan, J. T. W.; Toy, P. H.; Phillips, D. L. *J. Am. Chem. Soc.* **2005**, *127*, 1463-1472. (b) Ma, C.; Kwok, W. M.; Chan, W. S.; Du, Y.; Kan, J. T. W.; Toy, P. H.; Phillips, D. L. *J. Am. Chem. Soc.* **2006**, *128*, 2558-2570.
34. (a) Singh, A. K.; Palit, D. K.; Mukherjee, T. *J. Phys. Chem. A* **2002**, *106*, 6084-6093. (b) Palit, D. K. *Res. Chem. Intermed.* **2005**, *31*, 205-225. (c) Singh, A. K.; Bhasikuttan, A. C.; Palit, D. K.; Mittal, J. P. *J. Phys. Chem. A* **2000**, *104*, 7002-7009. (d) Singh, A. K.; Ramakrishna, G.; Ghosh, N.; Palit, D. K. *J. Phys. Chem. A* **2004**, *108*, 2583-2597.
35. (a) Aloïse, S.; Ruckebusch, C.; Blanchet, L.; Réhault, J.; Buntinx, G.; Huvenne, J. P. *J. Phys. Chem. A* **2008**, *112*, 224-331. (b) Kwok, W. M.; Guan, X.; Chu, L. M.; Tang, W. J.; Phillips, D. L. *J. Phys. Chem. B* **2008**, *112*, 11794-11797.
36. Fujiwara, W.; Lee, J. K.; Zgierski, M. Z.; Lim, E. C. *Chem. Phys. Lett.* **2009**, *481*, 78-82.

37. (a) Cadet, J.; Vigny, P. *The Photochemistry of Nucleic Acids*; ed. H. Morrison, Wiley, New York, **1990**. (b) Moysan, A.; Viari, A.; Vigney, P.; Voituriez, L.; Cadet, J.; Moustacchi, E.; Sage, E. *Biochemistry* **1991**, *30*, 7080-7088.
38. Lamola, A. A.; Yamane, T. *Proc. Natl. Acad. Sci. U. S. A.* **1967**, *58*, 443-446.
39. Gut, I. G.; Wood, P. D.; Redmond, R. W. *J. Am. Chem. Soc.* **1996**, *118*, 2366-2373.
40. Kwok, W. M.; Ma, C.; Matousek, P.; Parker, A. W.; Phillips, D.; Toner, W. T.; Towrie, M.; Umaphy, S. *J. Phys. Chem. A* **2001**, *105*, 984-990.
41. Chan, C. T. L.; Cheng, C. C. W.; Ho, K. Y. F.; Kwok, W. M. *Phys. Chem. Chem. Phys.* **2011**, *13*, 16306-16313.
42. Rettig, W.; Bliss, B.; Dirnberger, K. *Chem. Phys. Lett.* **1999**, *305*, 8-14.
43. Chattopadhyay, N.; Rommens, J.; Van der Auweraer, M.; De Schryver, F. C. *Chem. Phys. Lett.* **1997**, *264*, 265-272.
44. Samanta, A.; Paul, B. K.; Guchhait, N. *J. Lumin.* **2012**, *132*, 517-525.
45. Ito, A.; Ishizaka, S.; Kitamura, N. *Phys. Chem. Chem. Phys.* **2010**, *12*, 6641-6649.
46. Kobihiro, K.; Inoue, Y. *J. Am. Chem. Soc.* **2003**, *125*, 421-427.
47. Papper, V.; Kharlanov, V.; Rettig, W. *Phys. Chem. Chem. Phys.* **2002**, *4*, 1752-1759.
48. Józefowicz, M. *Chem. Phys.* **2011**, *383*, 19-26.

49. Józefowicz, M.; Aleksiejew, A.; Abramov, A. V.; Ling, S.; Gutowski, M.; Heldt, J.; Heldt, J. R. *J. Fluoresc.* **2011**, *21*, 1749-1762.
50. Okada, T.; Uesugi, M.; Köhler, G.; Rechthaler, K.; Rotkiewicz, K.; Rettig, W.; Grabner, G. *Chem. Phys.* **1999**, *241*, 327-337.
51. Kwok, W. M.; George, M. W.; Grills, D. C.; Ma, C.; Matousek, P.; Parker, A. W.; Phillips, D.; Toner, W. T.; Towrie, M. *Photochem. Photobiol. Sci.* **2007**, *6*, 987-994.
52. Han, K. L.; Zhao, G. J. *Hydrogen Bonding and Transfer in the Excited State*; Hoboken, NJ, Wiley: USA, **2010**.
53. Zhao, G. J.; Han, K. L. *J. Comput. Chem.* **2008**, *29*, 2010-2017.
54. Bakova, R.; Chergui, M.; Daniel, C.; Vlček, A.; Zálaiš, S. *Coord. Chem. Rev.* **2011**, *255*, 975-989.
55. (a) Yersin, H.; Finkenzeller, W. J. in *Highly Efficient OLEDs with phosphorescent Materials*, ed. H. Yersin, Wiley-VCH, Weinheim, **2008**. (b) Rausch, A. F.; Homeier, H. H. H.; Yersin, H. *Top. Organomet. Chem.* **2010**, *29*, 193-235.
56. Rurack, K. *Spectrochim. Acta, Part A*, **2001**, *57*, 2161-2195.
57. (a) Damrauer, N. H.; Cerullo, G.; Yeh, A.; Boussie, T. R.; Shank, C. V.; McCusker, J. K. *Science* **1997**, *275*, 54-57. (b) Yeh, A.; Shank, C. V.; McCusker, J. K. *Science* **2000**, *289*, 935-938. (c) Bhasikuttan, A. C.; Suzuki, M.; Nakashima, S.; Okada, T. *J. Am. Chem. Soc.* **2002**, *124*, 8398-8405. (d)

- Cannizzo, A.; Mourik, F.; Gawelda, W.; Zgrablic, G.; Bressler, C.; Chergui, M. *Angew. Chem., Int. Ed.* **2006**, *45*, 3174-3176.
58. (a) Cannizzo, A.; Blanco-Rodriguez, A. M.; Nahhas, A. E.; Šebera, J.; Záliš, S.; Vlček, A.; Chergui, M. *J. Am. Chem. Soc.* **2008**, *130*, 8967-8974. (b) Nahhas, A. E.; Cannizzo, A.; Mourik, F.; Blanco-Rodríguez, A. M.; Záliš, S.; Vlček, A.; Chergui, M. *J. Phys. Chem. A* **2010**, *114*, 6361-6369. (c) Busby, M.; Matousek, P.; Towrie, M.; Vlček, A. *J. Phys. Chem. A* **2005**, *109*, 3000-3008.
59. (a) Ramakrishna, G.; Goodson, T., III; Rogers-Haley, J. E.; Cooper, T. M.; McLean, D. G.; Urbas, A. *J. Phys. Chem. C* **2009**, *113*, 1060-1066. (b) Whittle, C.; Weinstein, J. A.; George, M. W.; Schanze, K. S. *Inorg. Chem.* **2001**, *40*, 4053-4062. (c) Hissler, M.; Connick, W. B.; Geiger, D. K.; McGarrah, J. E.; Lipa, D.; Lachicotte, R. J.; Eisenberg, R. *Inorg. Chem.* **2000**, *39*, 447-457.
60. Gawelda, W.; Cannizzo, A.; Pham, V.-T.; Mourik, F.; Bressler, C.; Chergui, M. *J. Am. Chem. Soc.* **2007**, *129*, 8199-8206.
61. (a) Quochi, F.; Saba, M.; Artizzu, F.; Mercuri, M. L.; Deplano, P.; Mura, A.; Bongiovanni, G. *J. Phys. Chem. Lett.* **2010**, *1*, 2733-2737. (b) Ramachandra, S.; Polo, F.; Edafe, F.; Schuermann, K. C.; Nijhuis, C. A.; Belser, P.; Reus, W. F.; Whitesides, G. M.; De Cola, L. *Pure Appl. Chem.* **2011**, *83*, 779-799.
62. (a) Abedin-Siddique, Z.; Ohno, T.; Nozaki, K.; Tsubomura, T. *Inorg. Chem.* **2004**, *43*, 663-673. (b) Abedin-Siddique, Z.; Yamamoto, Y.; Ohno, T.; Nozaki, K. *Inorg. Chem.* **2003**, *42*, 6366-6378.

63. Steffen, A.; Tay, M. G.; Batsanov, A. S.; Howard, J. A. K.; Beeby, A.; Vuong, K. Q.; Sun, X.-Z.; George, M. W.; Marder, T. B. *Angew. Chem., Int. Ed.* **2010**, *49*, 2349-2353.
64. Lu, W.; Zhu, N.; Che, C. M. *J. Organomet. Chem.* **2003**, *670*, 11-16.
65. Tong, G. S. M.; Chow, P. K.; Che, C. M. *Angew. Chem., Int. Ed.* **2010**, *49*, 9206-9209.
66. Chao, H. Y.; Lu, W.; Li, Y.; Chan, M. C. W.; Che, C. M.; Cheung, K. K.; Zhu, N. *J. Am. Chem. Soc.* **2002**, *124*, 14696-14706.
67. (a) Tour, J. M. *Chem. Rev.* **1996**, *96*, 537-554. (b) Schwab, P. F. H.; Levin, M. D.; Michl, J. *Chem. Rev.* **1999**, *99*, 1863-1934. (c) Bunz, U. H. F. *Chem. Rev.* **2000**, *100*, 1605-1644. (d) McQuade, D. T.; Pullen, A. E.; Swager, T. M. *Chem. Rev.* **2000**, *100*, 2537-2574. (e) Hill, D. J.; Mio, M. J.; Prince, R. B.; Hughes, T. S.; Moore, J. S. *Chem. Rev.* **2001**, *101*, 3893-4011.
68. (a) Grubbs, R. H.; Kratz, D. *Chem. Ber.* **1993**, *126*, 149-157. (b) Baldwin, K. P.; Simons, R. S.; Rose, J.; Zimmerman, P.; Hercules, D. M.; Tessier, C. A.; Youngs, W. J. *J. Chem. Soc., Chem. Commun.* **1994**, 1257-1258. (c) Wong, M. S.; Nicoud, J. F. *Tetrahedron Lett.* **1994**, *35*, 6113-6116. (d) Orita, A.; Yoshioka, N.; Struwe, P.; Braier, A.; Beckmann, A.; Otera, J. *Chem. Eur. J.* **1999**, *5*, 1355-1363. (e) Youngs, W. J.; Tessier, C. A.; Bradshaw, J. D. *Chem. Rev.* **1999**, *99*, 3153-3180. (f) Jones, T. V.; Blatchly, R. A.; Tew, G. N. *Org. Lett.* **2003**, *5*, 3297-3299. (g) Jones, T. V.; Slutsky, M. M.; Laos, R.; de Greef, T. F. A.; Tew, G. N. *J. Am. Chem. Soc.* **2005**, *127*, 17235-17240. (h) Khan, A.; Hecht, S. J. *Polym. Sci., Part A: Polym. Chem.* **2006**, *44*, 1619-1627. (i)

- Slutsky, M. M.; Phillip, J. S.; Tew, G. N. *New J. Chem.* **2008**, *32*, 670-675. (j)
- Jones, T. V.; Slutsky, M. M.; Tew, G. N. *New J. Chem.* **2008**, *32*, 676-679.
69. (a) Devadoss, C.; Bharathi, P.; Moore, J. S. *J. Am. Chem. Soc.* **1996**, *118*, 9635-9644. (b) Tretiak, S.; Chernyak, V.; Mukamel, S. *J. Phys. Chem. B* **1998**, *102*, 3310-3315.
70. (a) Onitsuka, K.; Yamamoto, S.; Takahashi, S. *Angew. Chem., Int. Ed.* **1999**, *38*, 174-176. (b) MacDonald, M. A.; Puddephatt, R. J. *Organometallics* **2000**, *19*, 2194-2199. (c) Vicente, J.; Chicote, M. T.; Abrisqueta, M. D.; Alvarez-Falcon, M. M. *J. Organomet. Chem.* **2002**, *663*, 40-45. (d) Vicente, J.; Chicote, M. T.; Alvarez-Falcon, M. M.; Abrisqueta, M. D.; Hernandez, F. J.; Jones, P. G. *Inorg. Chim. Acta* **2003**, *347*, 67-74. (e) Zhu, M. X.; Lu, W.; Zhu, N.; Che, C. M. *Chem. Eur. J.* **2008**, *14*, 9736-9746.
71. (a) Bruce, M. I. *Coord. Chem. Rev.* **1997**, *166*, 91-119. (b) Manna, J.; John, K. D.; Hopkins, M. D. *Adv. Organomet. Chem.* **1995**, *38*, 79-154.
72. (a) Wohlgenannt, M.; Tandon, K.; Mazumdar, S.; Ramasesha, S.; Vardeny, Z. V. *Nature* **2001**, *409*, 494-497. (b) Wilson, J. S.; Dhoot, A. S.; Seeley, A. J. A. B.; Khan, M. S.; Köhler, A.; Friend, R. H. *Nature* **2001**, *413*, 828-831. (c) Lin, L. C.; Meng, H. F.; Shy, J. T.; Horng, S. F.; Yu, L. S.; Chen, C. H.; Liaw, H. H.; Huang, C. C.; Peng, K. Y.; Chen, S. A. *Phys. Rev. Lett.* **2003**, *90*, 036601. (d) Segal, M.; Baldo, M. A.; Holmes, R. J.; Forrest, S. R.; Soos, Z. G. *Phys. Rev. B* **2003**, *68*, 075211.

73. (a) Baldo, M. A.; O'Brien, D. F.; You, Y.; Shoustikov, A.; Sibley, S.; Thompson, M. E.; Forrest, S. R. *Nature* **1998**, *395*, 151-154. (b) Köhler, A.; Wilson, J. S.; Friend, R. H. *Adv. Mater.* **2002**, *14*, 701-707.
74. Lupton, J. M.; Pogantsch, A.; Piok, T.; List, E. J. W.; Patil, S.; Scherf, U. *Phys. Rev. Lett.* **2002**, *89*, 167401.
75. (a) Omary, M. A.; Kassab, R. M.; Haneline, M. R.; Elbjeirami, O.; Gabbai, F. *P. Inorg. Chem.* **2003**, *42*, 2176-2178. (b) Burrell, C.; Elbjeirami, O.; Omary, M. A.; Gabbai, F. P. *J. Am. Chem. Soc.* **2005**, *127*, 12616-12617.
76. (a) Yuan, W. Z.; Shen, X. Y.; Zhao, H.; Lam, J. W. Y.; Tang, L.; Lu, P.; Wang, C. L.; Liu, Y.; Wang, Z. M.; Zheng, Q.; Sun, J. Z.; Ma, Y. G.; Tang, B. *Z. J. Phys. Chem. C* **2010**, *114*, 6090-6099. (b) Bolton, O.; Lee, K. W.; Kim, H.-J.; Lin, K. Y.; Kim, J. S. *Nature Chem.* **2011**, *3*, 205-210.
77. (a) Wilson, J. S.; Chawdhury, N.; Köhler, A.; Friend, R. H.; Al-Mandhary, M. R. A.; Khan, M. S.; Younus, M.; Raithby, P. R. *J. Am. Chem. Soc.* **2001**, *123*, 9412-9417. (b) Liu, Y.; Jiang, S.; Glusac, K.; Powell, D. H.; Anderson, D. F.; Schanze, K. S. *J. Am. Chem. Soc.* **2002**, *124*, 12412-12413. (c) Wilson, J. S.; Wilson, R. J.; Friend, R. H.; Köhler, A.; Al-Suti, M. K.; Al-Mandhary, M. R. A.; Khan, M. S. *Phys. Rev. B* **2003**, *67*, 125206.
78. (a) Che, C. M.; Chao, H. Y.; Miskowski, V. M.; Li, Y.; Cheung, K. K. *J. Am. Chem. Soc.* **2001**, *123*, 4985-4991. (b) Lu, W.; Xiang, H. F.; Zhu, N.; Che, C. M. *Organometallics* **2002**, *21*, 2343-2346. (c) Lu, W.; Zhu, N.; Che, C. M. *J. Am. Chem. Soc.* **2003**, *125*, 16081-16088.

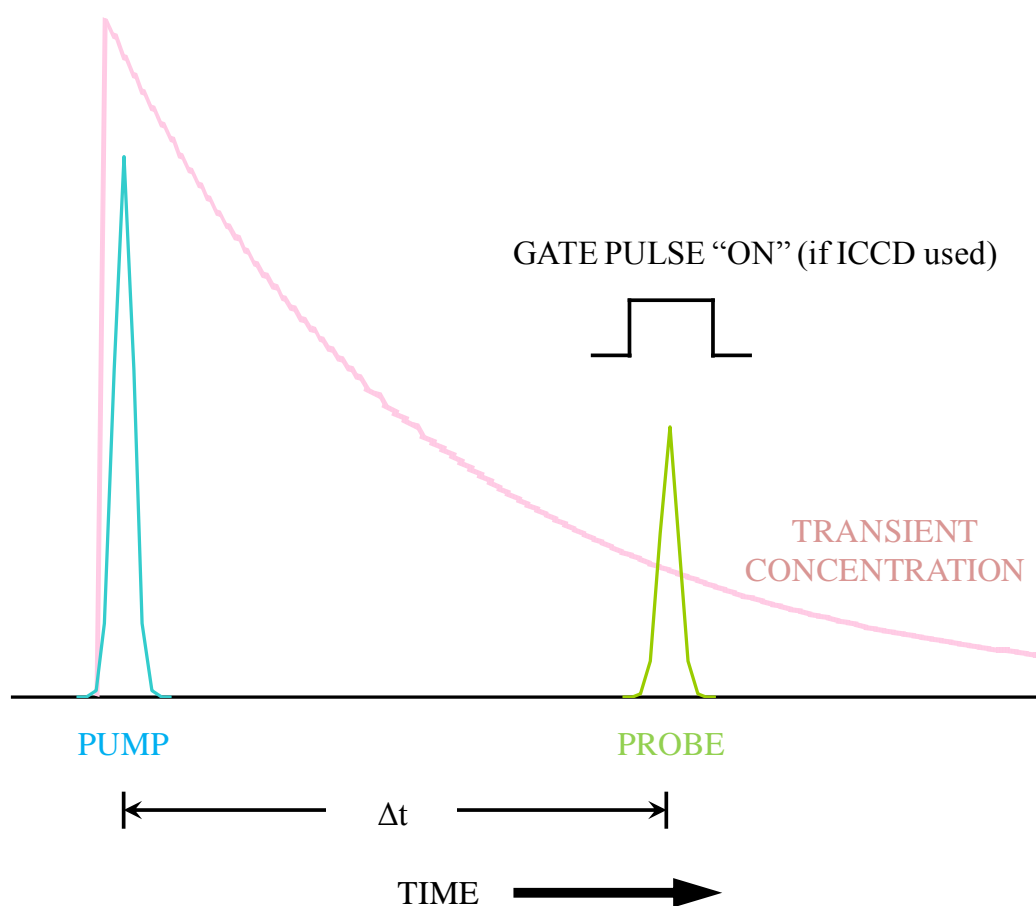
Chapter 2 Experimental Methodologies

2.1 Introduction to Pump-Probe Spectroscopy

To be able to directly probe processes taking place after the photo-excitation is important in understanding the photophysics or photochemistry of the excited state molecules.¹ Time-resolved spectroscopy based on the pump-probe technique is one of the most frequently used methods to monitor the involved transient species and their dynamics.^{1,2}

In the pump-probe time-resolved spectroscopic measurement, the molecular system under investigation is first excited by a short pulse of radiation, which is called “pump”. This generates a high concentration of transient species which can be detected using various spectroscopic methods (Scheme 2.1). After the excitation, the system is allowed to evolve for a period of time during which the transient species decays. At a designated time after the excitation (Δt in Scheme 2.1), a second pulse, called the “probe” pulse, is used to induce and collect spectral information about the identity and/or the concentration of the transient species. Different time-resolved spectroscopic methods make use of the different spectral character for the probe of the transient species. For example, time-resolved resonance Raman and time-resolved infra-red (IR) spectroscopy monitor the temporal change in the Raman scattering and the IR absorption of the transient species; transient absorption (TA) spectroscopy measures the change in the electronic absorption spectra of the system caused by the photo-excitation. Besides, Kerr-gated time-resolved fluorescence (TRF) and time-resolved emission (TRE) techniques probe the temporal change in the emission

spectra of the emissive species involved upon and after the photo-excitation. Nevertheless, with all the spectroscopic methods, by changing systematically the time between the pump and the probe (Δt), the kinetic behavior and temporal evolution of the transient species can be determined.



Scheme 2.1 Schematic presentation for pump-probe spectroscopic technique. (Δt = the time between the pump and the probe; ICCD = intensified charge-coupled device)

2.2 Time-Resolved Spectroscopic Techniques

2.2.1 Background of time-resolved spectroscopy

To probe the excited state processes mentioned in Chapter 1 which proceed from the sub-picoseconds to microseconds timescale, it is necessary to use time-resolved spectroscopic method that has fast enough time resolution and can, at the same time, be able to cover the broad time window from sub-picosecond (ps) to microseconds. It is noted that the time resolution of a time-resolved method is governed mainly by the temporal width of the light source. The time duration of the pump and probe pulses needs to be significantly shorter than the lifetime of the transient species in which we are interested.

For instance, light pulse with ten nanoseconds time duration, as used in the so-called nanosecond (ns) time-resolved spectroscopy, would be suitable for detecting transient species that has lifetime of tens ns and longer; while femtosecond (fs) laser pulse, as used in the fs time-resolved spectroscopy, would be appropriate for monitoring transient species having lifetimes of picoseconds or longer. It is noted that spectroscopic methods with different time resolution usually have different time window for the detection. The fs time-resolved spectroscopy can normally detect transient species and associated dynamics processes within several nanoseconds after the photo-excitation; while the ns time-resolved methods may probe species and dynamics that are involved from tens ns to microsecond (μ s) and even millisecond after the excitation.

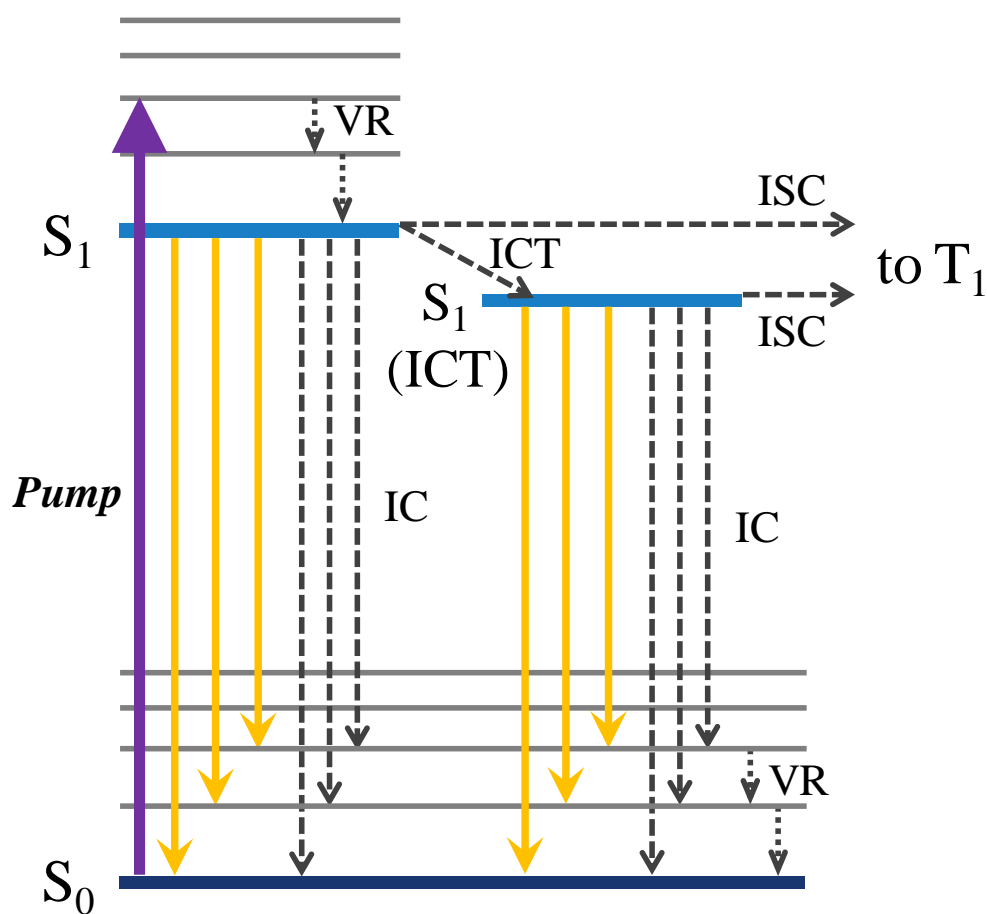
In this thesis, time-resolved techniques based on electronic transient absorption and emission spectroscopy covering time window from fs to μ s have

been employed to probe the overall excited state processes of the examined molecular system. In contrast to other time-resolved spectroscopic techniques, like fluorescence up-conversion and time-correlated single photon counting which can only monitor excited state kinetics at a single selected wavelength at a time, our time-resolved methods both the detection of absorption or emission have the broadband feature, can probe not only the temporal change of spectral intensity, but also the broadband spectral signature of the involved transient species. In addition, by combining the fs time-resolved method with the corresponding ns time-resolved methods, our measurements allow seamless detection of species occurring in timescale from fs to μ s.

2.2.1.1 Background of fs-TRF spectroscopy

In the fs-TRF spectroscopy, the dynamics of species giving fluorescence emission can be detected at time intervals from tens fs to ~ 6 ns after the photo-excitation (Scheme 2.2). Upon photo-excitation (the purple upward arrow), the molecule is promoted from its ground state (S_0) to the lowest singlet excited state (*i.e.* the S_1 here). To dissipate the absorbed photo-energy, the S_1 molecule may then undergo various relaxation processes radiatively or non-radiatively. Our broadband fs-TRF spectroscopy is capable of capturing the fluorescence signature of the emissive state (S_1). An optical gating unit, called Kerr-gate device, is used to work as an ultrafast shutter to enable detection of fluorescence at any selected time delay after the photo-excitation; by changing the time delay between the pump and the opening time of the Kerr-gate device, the temporal evolution of fluorescence (the orange downward arrows in Scheme 2.2) and

therefore the dynamics of S_1 state can be monitored as a function of time after the photo-excitation. From the emission wavelengths of the acquired transient fluorescence spectrum, the energy difference between the emissive S_1 and the S_0 can be estimated. On the other hand, the temporal decay of transient fluorescence signal provide information for the timescale and rate at which the S_1 is deactivated through various pathway available to the system under investigation.



Scheme 2.2 Schematic diagram for the principle of fs-TRF measurement. The solid and dashed arrow represents the radiative and non-radiative process respectively. (S = singlet state; T = triplet state; ICT = intramolecular charge transfer; VR = vibrational relaxation; IC = internal conversion; orange arrows: fluorescence)

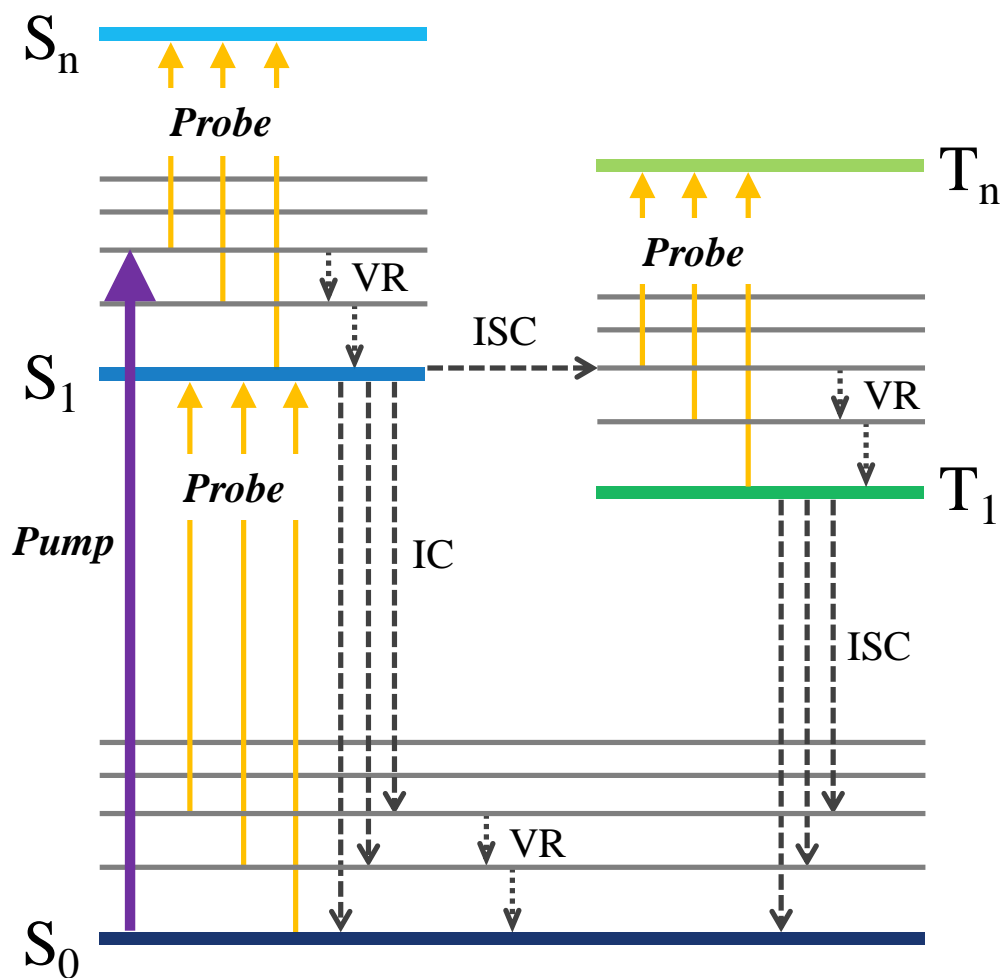
2.2.1.2 Background of fs-TA spectroscopy

It is known that fs-TRF can detect only the fluorescence from highly emissive singlet natured excited state. For system that possesses high efficiency of intersystem crossing (ISC), such as the transition metal complexes investigated in Chapter 5 and 6 of the thesis, to detect solely the singlet natured excited state is not sufficient; spectroscopic method that is capable of probing relatively weakly emissive state or non-emissive state, such as the triplet natured excited state and the S_0 , is needed for revealing the overall picture of the excited state deactivation. For this purpose, broadband fs-TA spectroscopy has been used in conjunction with the fs-TRF to allow monitoring temporal change of the excited singlet and in addition the triplet natured state. The principle for broadband fs-TA measurement is depicted in Scheme 2.3.

After excitation of the molecule to its singlet excited state (the purple upward arrow in Scheme 2.3), the excited state molecule may lose the energy it gained through various deactivation pathways, such as the vibrational relaxation (VR), internal conversion (IC) to the S_0 and ISC to the T_1 , *etc.* To probe the transient species involved in these relaxation processes, a broadband probe pulse which is in our measurement a pulse of white light continuum (WLC; orange upward arrows in Scheme 2.3) covering wavelength from ~290 nm to 750 nm is used to detect change in the absorption spectra at designated delay time after the photo-excitation. The TA measurement can probe excited state absorption (ESA) spectra due to both the singlet (the S_1 in Scheme 2.3) and the triplet (the T_1 in Scheme 2.3) state. The former arises due to the transition from the S_1 and higher singlet excited states ($S_1 \rightarrow S_n$); and the latter the T_1 to higher triplet excited

states ($T_1 \rightarrow T_n$). In addition, by measuring the S_0 to S_1 absorption in the S_0 absorption region of the molecule, the TA measurement also allows probing directly temporal change of the S_0 bleach; and thus provides a mean to monitor the dynamics of S_0 recovery arising due to the decay of the excited state system.

In this way, the TA measurement can probe temporal change of not only the strongly emissive state (the S_1 here in Scheme 2.3) but also the weakly emissive T_1 and the non-emissive S_0 . Therefore, combined application of the TRF and the TA on one hand affords complementary information on the electronic properties of the transient states and on the other hand generates direct formation on the dynamics of conversions between the various transient species in the photophysical processes.



Scheme 2.3 Schematic diagram for the principle of fs- and ns-TA measurement. The solid and dashed arrows represent radiative and non-radiative transition, respectively. (S = singlet state; T = triplet state; VR = vibrational relaxation; IC = internal conversion; ISC = intersystem crossing)

2.2.1.3 Background of ns-TA and ns-TRE spectroscopy

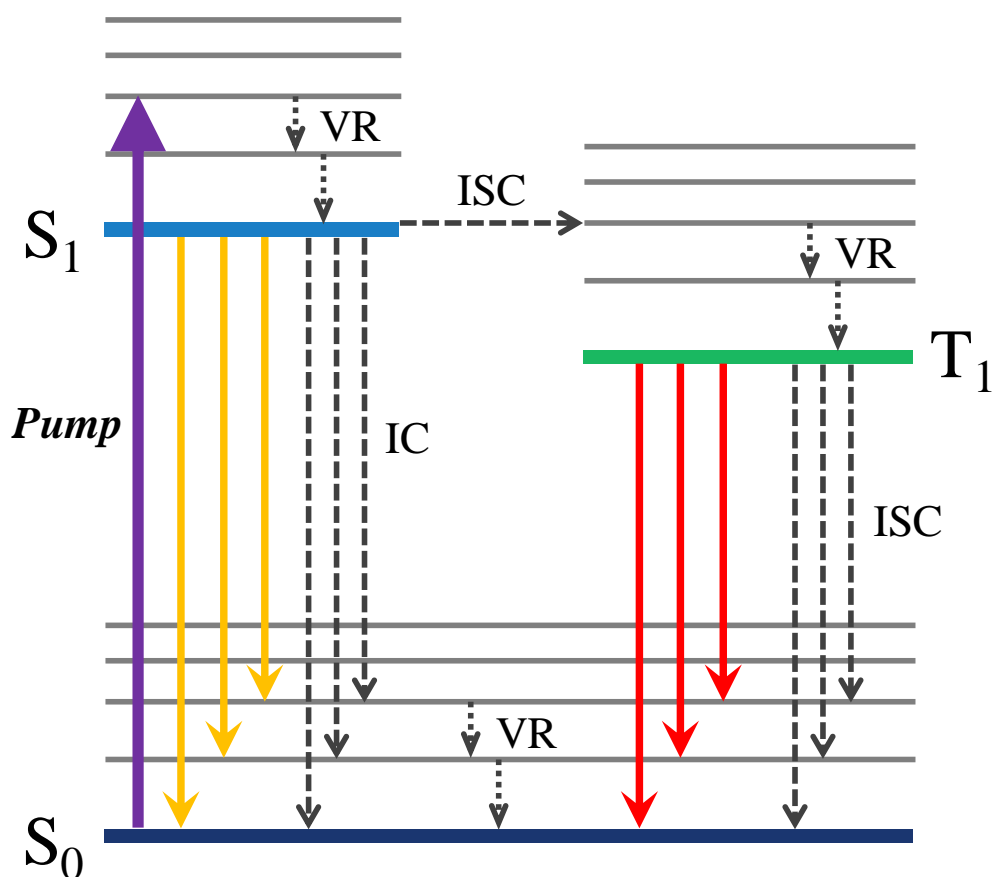
Given the limitation in detection time window (tens fs to 6 ns) of our fs broadband time-resolved spectroscopy, to detect dynamic processes related to the long-lived triplet state and those to the delayed fluorescence (DF) showed by the

gold(I) oligo-phenyleneethynylene (PE) complexes, time-resolved methods with ns time resolution covering detection time window from ns to μ s have been employed.

The principle of the ns-TA is in principle the same as that of the fs-TA measurement (Scheme 2.3) except the difference in the detection time window and the time resolution (mentioned above). The ns-TA is also capable of monitoring the ESA and therefore the temporal evolution of transient excited state species and at the same time repopulation of the S_0 for recovery dynamics of S_0 resulted due to decay of the excited state species.

On the other hand, ns-TRE technique has been used to complement the fs-TRF to allow measurement of transient emission in long timescale from several ns to μ s. This for the systems studied in this thesis includes mainly the phosphorescence (the red downward arrow in Scheme 2.4) from the T_1 formed by ISC from the singlet manifold (Scheme 2.4) and the DF in the gold(I) oligo-PE complexes. The capacity of ns-TRE to measure emission from weakly emissive state, such as the triplet natured state, comes due to the relatively long “gating” duration of the measurement. Unlike fs-TRF which has the “gating” duration of tens fs, the gating duration in our ns-TRE measurement is no shorter than 2 ns. The long “gating” duration allows the ns-TRE to be particularly sensitive to weakly emissive state. To achieve the broadband measurement of ns-TRE, we use an intensified charge-coupled device (ICCD) as detector; the operation of ICCD is synchronized with the pump laser by using an electronic delay device (Scheme 2.1). The “gating” duration of ICCD and the time delay

between the “gating” and pump laser pulse can be controlled according to the nature of emission of the studied molecular system.



Scheme 2.4 Schematic diagram for the principle of ns-TRE measurement. The solid and dashed arrows represent the radiative and non-radiative processes respectively. (S = singlet state; T = triplet state; VR = vibrational relaxation; IC = internal conversion; ISC = intersystem crossing; orange arrows: fluorescence; red arrows: phosphorescence)

Details of the instrumental configuration for each of the methods mentioned (i.e., the fs-TRF, fs-TA, ns-TRE and ns-TA) together with fs time-resolved fluorescence anisotropy (fs-TRFA) will be given in sections 2.2.3 to

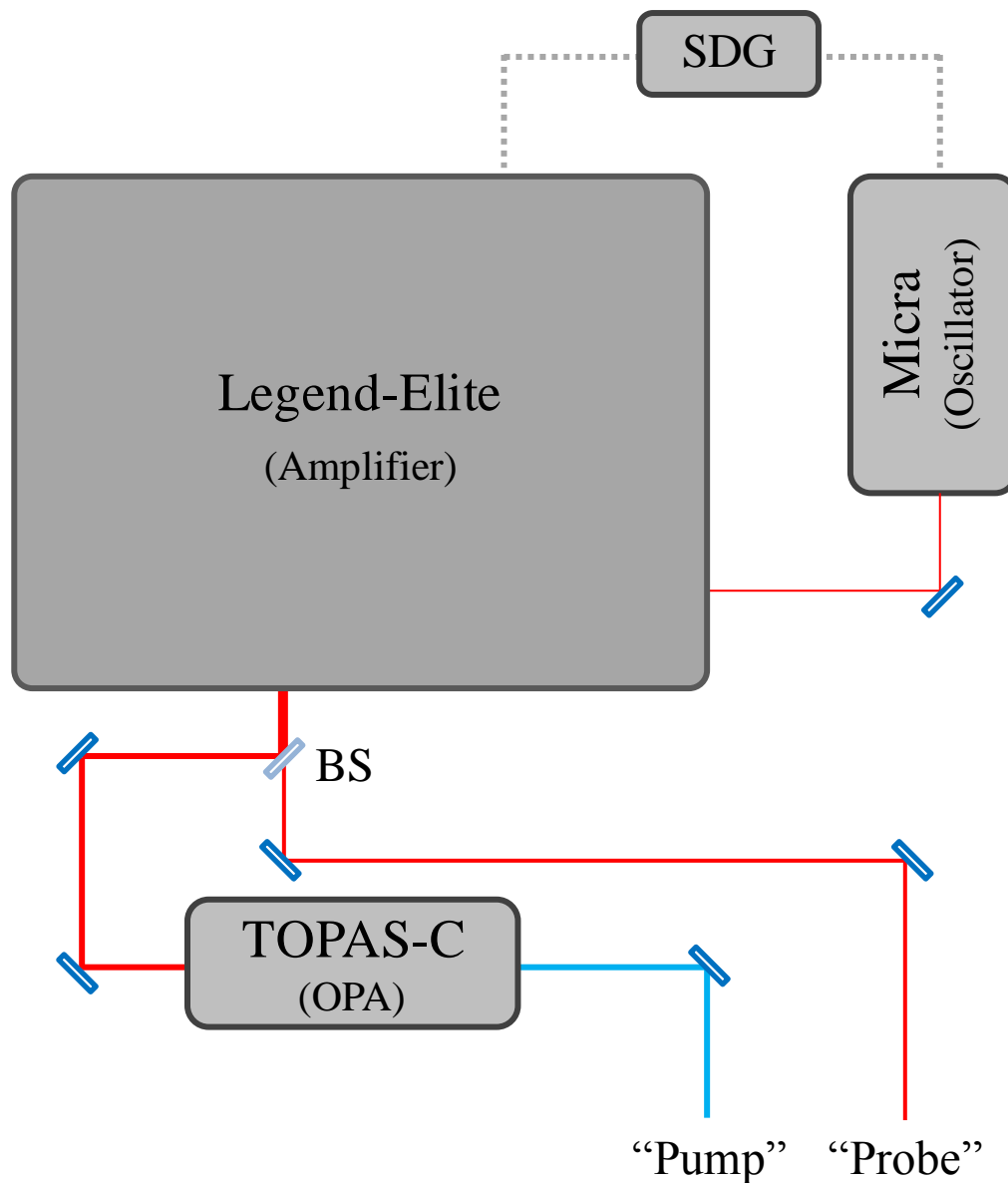
2.2.7. The fs broadband time-resolved spectroscopy which has been used for monitoring transient species in time regime from sub-ps to ns time region will first be introduced. After that, ns time-resolved spectroscopic techniques covering extensive time regime, from ns to μ s will be presented.

2.2.2 Femtosecond laser source

In general, our fs broadband time-resolved spectroscopic setup can be divided into three major parts: (i) the laser system which serves as the light source for producing the pump and probe pulses, (ii) a home-built TRF and TA spectrometer composed of a time delay controlling unit and a sample compartment for generation and probe of the transient species, and (iii) the detection system for signal recording and data processing.

First, to achieve the fs time-resolution, a fs laser system is needed for providing light source in the ultrafast time-resolved experiments. Our fs laser system is consisted of three main sections as depicted in Scheme 2.5: (i) the mode-locked Titanium:sapphire (Ti:sapphire) oscillator (Oscillator; Coherent, Micra), (ii) the regenerative Ti:sapphire amplifier (Amplifier; Coherent, Legend-Elite), and (iii) the wavelength tunable optical parametric amplifier (OPA; Light Conversion, TOPAS-C).

In brief, a 800 nm laser pulse (~ 0.4 W, ~ 80 MHz repetition rate of the pulse), called seeding pulse, is generated by the oscillator. This seeding pulse then enters the regenerative amplifier for amplification. Synchronization between the oscillator and the amplifier is achieved by using a synchronization and delay generator (SDG). The amplified 800 nm output, which now has a power of ~ 3.6 W and 1 kHz repetition rate, leaves the amplifier and is split into two portions by a beam splitter (BS in Scheme 2.5) which on one hand gives the desirable wavelength of pump laser pulse by pass through the OPA and on the other hand serves as the source for probe pulse to allow monitoring the broadband spectral feature of the transient species.



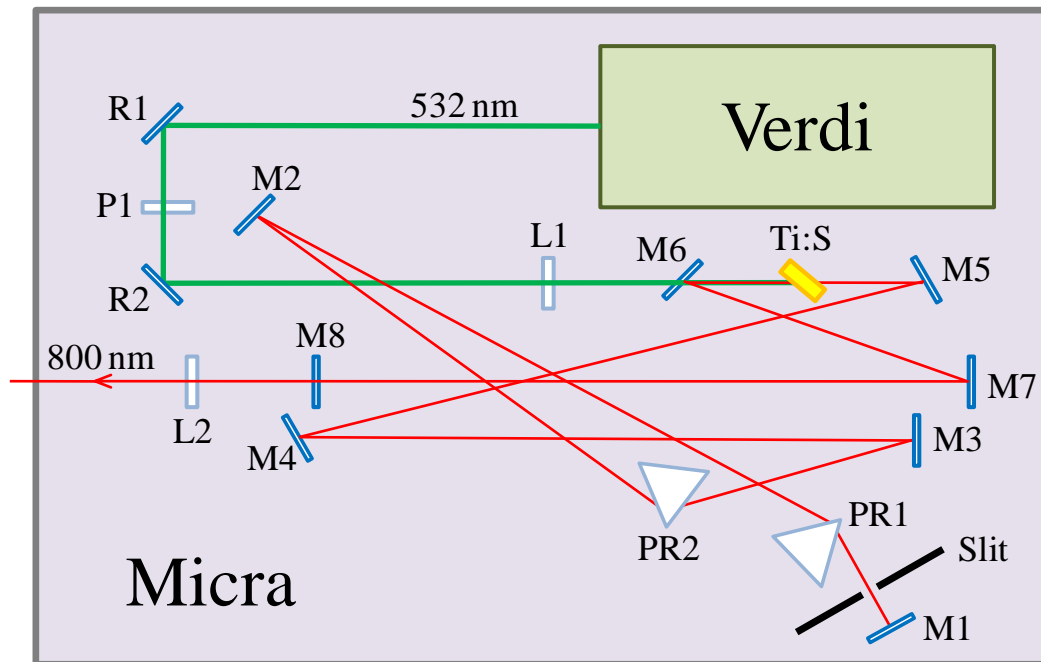
Scheme 2.5 Schematic layout of the ultrafast laser system. (SDG = synchronization and delay generator; OPA = optical parametric amplifier)

2.2.2.1 Oscillator

As displayed in Scheme 2.6, the 800 nm seeding pulse for the time-resolved experiment is generated in a fs Kerr lens mode-locked Ti:sapphire oscillator (Coherent, Micra) which is pumped by a continuous-wave, intracavity-doubled diode-pumped VerdiTM laser. Inside the Verdi cavity, a 1064 nm fundamental laser pulse is first generated by a semiconductor diode laser using Neodymium Yttrium orthovanadate (Nd:YVO₄) as the gain medium. Frequency-doubling of the 1064 nm laser pulse is achieved using a Lithium triborate nonlinear crystal. This produces a continuous 532 nm laser (typical energy of ~4.5 W) as the output which is used to pump the Ti:sapphire rod (Ti:S in Scheme 2.6) inside the Micra oscillator cavity.

The oscillator itself employs the Kerr lens mode-locking technique accompanied with an intra-cavity prism pair to generate the ultrafast pulses. The Micra laser system is incorporated of the Verdi pump laser within the oscillator cavity (Scheme 2.6). As illustrated in the diagram, the oscillator cavity is constituted of a set of mirrors (M1 to M8), a pair of prism (PR1 and PR2), lenses (L1 and L2), polarizer (P1) and other optical components (R1 and R2). The 532 nm output from the Verdi travels through the collimating mirrors (R1 and R2) and is focused onto the Ti:sapphire rod (Ti:S) by the pump beam focusing lens (L1). Automated initiation of mode-locking is achieved through the action of an instantaneous nonlinear Kerr lens in the laser rod by the solenoid-driven movable mirror mount (M1). The temporal dispersion (the so-called “chirp”) introduced in the laser rod can be compensated by a pair of Brewster-cut fused-silica prisms (PR1 and PR2). After adjusting the two prisms (PR1 and PR2) and the slit (Slit)

in the oscillator cavity which control the central wavelength and the bandwidth of output laser, the final output laser pulse features a ~50 fs time duration, a ~65 nm bandwidth with the centre wavelength at 800 nm and a repetition rate of ~80 MHz.



R1, R2	Pump beam routing optics	M1-M8	Oscillator cavity mirrors
P1	Polarizer	Ti:S	Ti:sapphire laser crystal
L1	Pump beam focusing lens	PR1, PR2	Prism pair
L2	Collimating lens		

Scheme 2.6 Schematic diagram of the Micra oscillator cavity.

2.2.2.2 Ultrafast Ti:sapphire amplifier

The 800 nm seeding pulse generated from the oscillator is then directed to the ultrafast Ti:sapphire amplifier (Legend-Elite) for amplification (Scheme 2.5). The amplification process is achieved by passing the input seeding pulse through the Ti:sapphire crystal which is optically excited by a second harmonic (527 nm; Scheme 2.7) of a 1054 nm Q-switched Neodymium Yttrium Lithium Fluoride (Nd:YLF) laser (Coherent, Evolution) inside the Kilohertz Legend Laser System.

The Ti:sapphire amplifier is composed of three essential parts: (i) an optical pulse stretcher, (ii) a Ti:sapphire regenerative amplifier (RGA), and (iii) an optical pulse compressor. The amplifier employs the technique called chirped-pulse amplification through which the input seeding pulse is first stretched, amplified and then recompressed. Using this technique, the possibility of damaging the optical materials can be avoided because in the first step the incoming 800 nm laser pulse is temporally stretched and this lowers the peak fluence of the laser pulse before it enters into the RGA cavity.²

In practice, the seeding pulse entering the amplifier is first stretched in the stretcher (Stretcher, Scheme 2.7). The stretching is achieved using a gold-coated diffraction grating (Grating, Scheme 2.7), through which the higher frequency (bluer) component of the seeding pulse is sent over a longer path than the lower frequency (redder) component and thus stretching temporally the seeding pulse. After that, the stretched laser pulse enters the RGA cavity in which there is a Ti:sapphire crystal rod (Ti:S in Scheme 2.7) locating at the centre of the resonator. The resonator is composed of the amplifier cavity mirrors (M9-M13), two Pockels cells (PC1 and PC2), a quarter-wave plate (WP1) and an

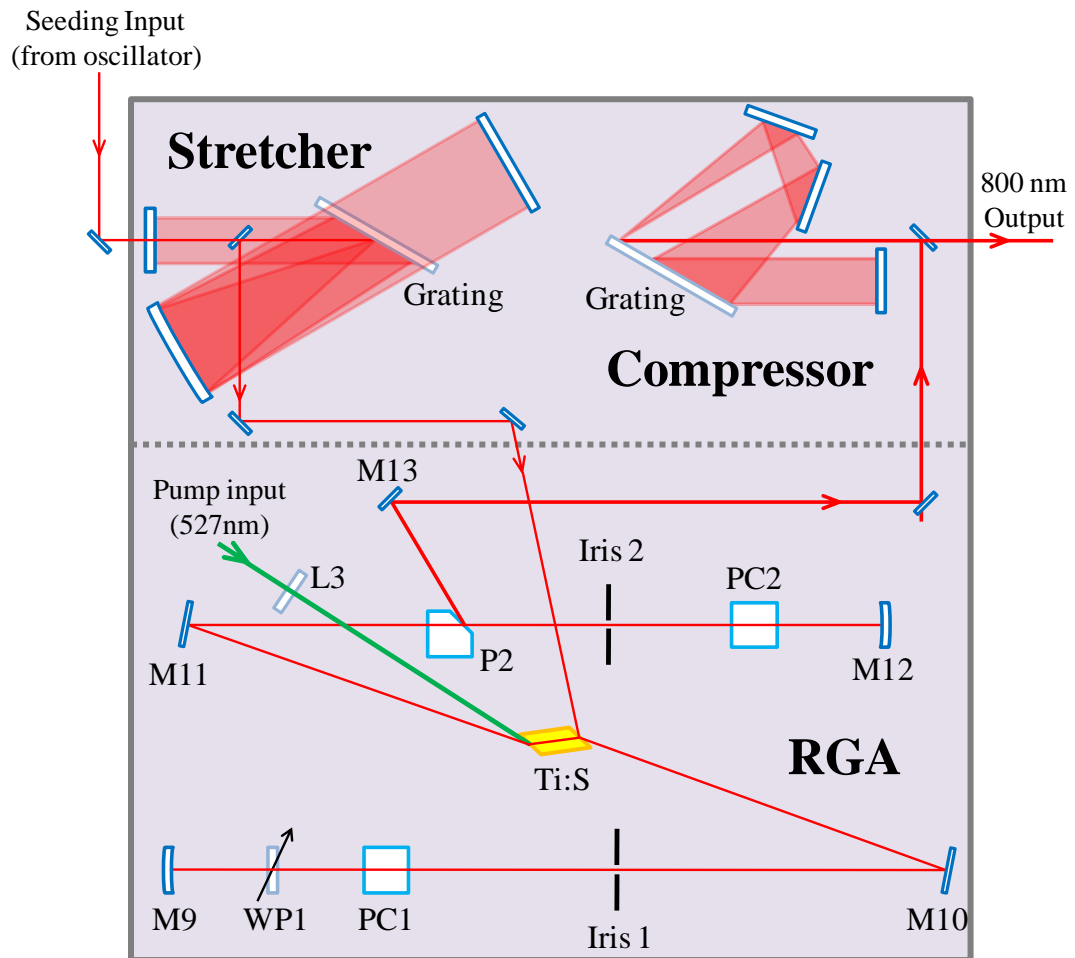
output polarizer (P2). The Ti:sapphire crystal is used as the gain medium and is being pumped by the 527 nm laser from a 1 kHz Q-switched Nd:YLF Evolution laser (the Pump input in Scheme 2.7).

After the gain of Ti:sapphire rod (pumped by the 527 nm laser) reaches its maximum, a vertical polarized seeding pulse is allowed to enter the resonator to start the amplification process. This is achieved by applying a voltage to the input Pockels cell (PC1, Scheme 2.7). By using WP1 (Scheme 2.7), the polarization direction of the input seeding pulse can be changed from vertical to horizontal. In this mean, the seeding pulse can be trapped inside the resonator (from M9 to M12 laser path) and allowed to multi-pass the Ti:S rod within the resonator cavity for amplification.

The amplification can lead an input pulse of only a few nanojoules of energy to experience a gain of over $\sim 10^6$ times and to have energy of over 1 millijoule (mJ). During the amplification process, other seeding pulses coming to the RGA which has vertical polarization are rejected out of the resonator. After a controlled number of round trips, the laser pulse trapped in the resonator is allowed to leave through the output Pockels cell (PC2 in Scheme 2.7). By rotating the polarization of the trapped pulse from horizontal back to vertical, the polarizer (P2 in Scheme 2.7) working with PC2 allows the amplified laser pulse to leave the resonator.

The timing for switch on of the two Pockels cells (PC1 and PC2, Scheme 2.7) to select the seeding pulse for amplification is controlled by the SDG (Scheme 2.5). After the amplification, the laser pulse exiting the RGA is temporally compressed in the compressor (Compressor, Scheme 2.7). The

compressor operates reversely compared to the stretcher. The compression is achieved by allowing the bluer frequency component to “catch up” the redder frequency component and thus compresses the temporally stretched pulse into its original duration (~35 fs) and featuring the centre wavelength at 800 nm but now with a 3.6 W power and a repetition rate of 1 kHz.



WP1	Quarter-wave plate	M9-M13	Amplifier cavity mirrors
PC1	Switching-in Pockels cell	Ti:S	Ti:sapphire laser crystal
P2	Output polarizer	Iris 1, Iris 2	Apertures
L3	Pump beam focusing lens	PC2	Switching-out Pockels cell

Scheme 2.7 Schematic diagram of stretcher, compressor and regenerative amplifier (RGA) in the Ti:sapphire amplifier.

2.2.2.3 *Wavelength conversion*

The amplified laser output from the RGA is wavelength tunable, but only in a very limited range wavelength by about ~ 100 nm from the centre wavelength (800 nm as mentioned above).² In this regard, the amplified 800 nm laser pulse needs to be converted into the wavelength at UV region to allow photo-excitation of the systems under study and investigation of the subsequent excited state processes after the photo-excitation. The wavelength conversion is achieved based on the optical parametric amplification and nonlinear optical technique by using the OPA (TOPAS-C, Scheme 2.5).

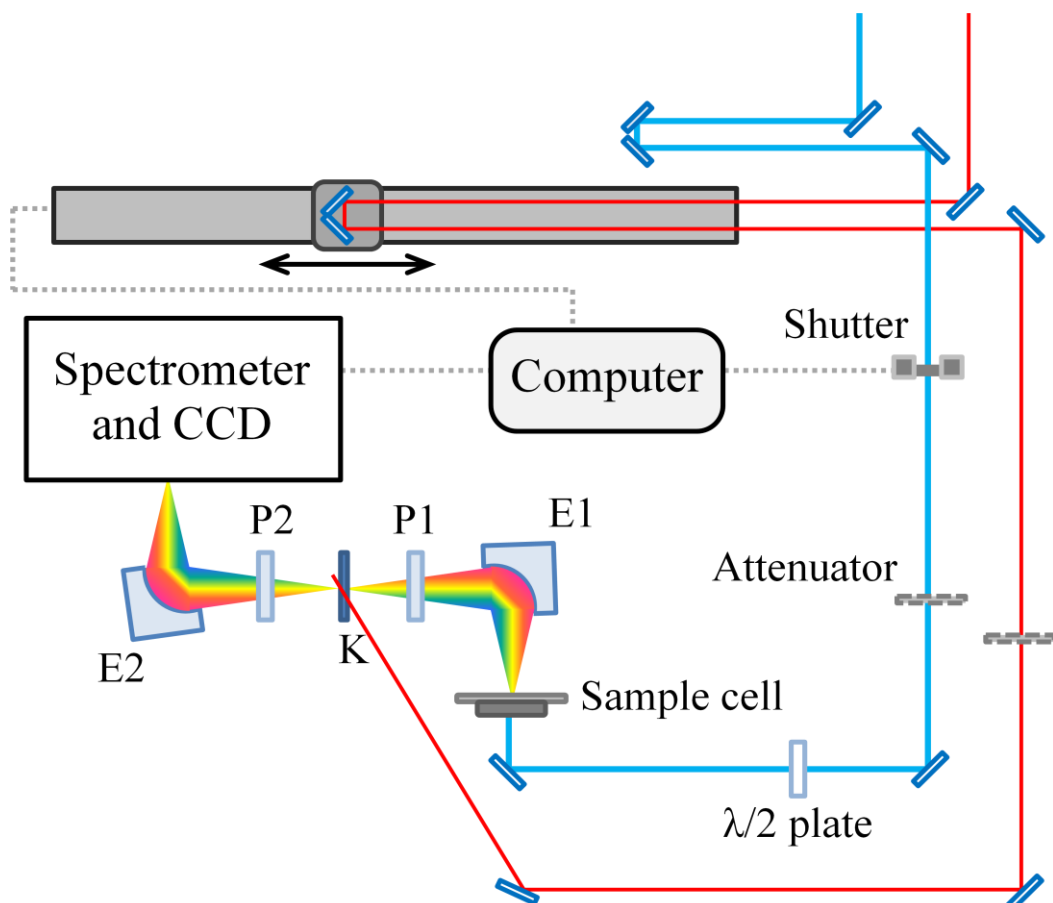
Taking the 280 nm excitation wavelength in Chapters 3 to 6 as an example, a portion of the amplified 800 nm laser led to the OPA is first converted into two lower frequency counterparts called signal (1400 nm) and idler (1867 nm) respectively. The desired 280 nm excitation is then generated by frequency mixing of the adequately wavelength tuned idler laser with the 800 nm fundamental ($1867 \text{ nm} + 800 \text{ nm} \rightarrow 560 \text{ nm}$) followed by second harmonic generation of the frequency mixing laser output ($560 \text{ nm} \rightarrow 280 \text{ nm}$). Before leaving the OPA, laser line with unwanted wavelengths are filtered off by a wavelength separator. The wavelength separator is composed of a set of dichroic mirrors which allows selective reflection of radiation in the desired wavelength range and with specified polarization direction.

2.2.3 Femtosecond broadband time-resolved fluorescence spectroscopy

The broadband fs-TRF experimental setup was constructed according to the method described in the literature.³⁻⁵ Briefly, the amplified 800 nm laser pulse from the amplifier was split into two parts to allow production of the pump and probe pulse respectively (Scheme 2.5). The pump pulse was generated from one portion of the 800 nm laser pulse which is directed to the OPA for wavelength conversion; the residue part of the 800 nm laser was used as the probe beam to drive the Kerr-gate device.^{6,7}

The Kerr-gate device is composed of a 1 mm thick Kerr medium (benzene contained in 1 mm quartz cell) equipped within a cross polarizer pair. It was driven by the 800 nm probe pulse (also called the gating pulse) and functioned as an ultrafast optical shutter to allow transient fluorescence spectrum from the sample to pass through at designated time delay between the pump and probe pulses.

The instrument response function (IRF) of the fs-TRF measurement is wavelength dependent. It changes from ~0.5 ps to ~2 ps as the detection wavelength varies from 600 nm to 280 nm. In order to avoid unwanted multi-photon effect, the power of excitation laser was kept as low as possible with a typical peak power of laser pulse being ~2 GW / cm².



Scheme 2.8 Schematic diagram for Kerr-gated fs-TRF and fs-TRFA spectrometer. The pump and probe pulses are indicated in blue and red line respectively. ($\lambda/2$ plate = half-wave plate; E1 & E2 = ellipsoidal mirror; P1 = entrance polarizer; P2 = exit polarizer; K = Kerr medium)

Scheme 2.8 shows the general diagram of the fs-TRF experimental setup. The excitation pump pulse (the blue line in Scheme 2.8) travels a fixed optical path, and the power of the pump pulse can be adjusted through the attenuator. To measure the full intensity TRF spectra and to eliminate unwanted effect caused by rotation diffusion of the excited molecules, by using a half-wave ($\lambda/2$) plate (Scheme 2.8), the polarization direction of the excitation laser was adjusted to be

at the magic angle (54.7°) with respect to that of the entrance polarizer (P1) in the Kerr-gate device. The excitation laser was then focused into the sample solution which was being circulated within a 0.5 mm thickness flow cell compartment.

On the other hand, the 800 nm probe pulse (red line in Scheme 2.8) was first directed into the optical delay line. The optical delay line is made of a pair of retro-reflective mirrors installed on a motor-controlled movable stage (Scheme 2.8). The two retro-reflective mirrors are perfectly perpendicular to each other and are properly oriented in order to direct the probe laser beam to and away from the translation stage in a parallel manner. The motor-driven optical delay line was used to vary the difference in optical path travelled by the probe laser pulse in relative to the pump pulse (ΔL) and therefore to control the temporal delay (Δt) of the probe with respect to the pump pulse. The relationship between the time delay (Δt) and relative distance (ΔL) is:

$$\Delta t = \frac{2\Delta L}{c}, \quad \text{where } c = 3 \times 10^{11} \text{ mm/s, is the speed of light.}$$

After photo-excitation, the transient fluorescence from the sample solution was first collected by an ellipsoidal mirror (E1 in Scheme 2.8) and directed to the entrance polarizer of the Kerr-gate device (P1 in Scheme 2.8). Transient fluorescence signal passing through the P1 was vertically polarized. The vertically polarized fluorescence signal was focused into the Kerr medium (K in Scheme 2.8) and was spatially overlapped with the 800 nm gating pulse. It is noted that, without the gating pulse, the transient fluorescence signal would not be able to pass through the Kerr-gate device, for the second polarizer (P2 in Scheme 2.8) which has polarization direction perpendicular to that of the P1,

would block the fluorescence signal. However, when the vertically polarized transient fluorescence and the gating pulse are temporally and spatially overlapped at K, the Kerr medium driven by the ultra-short gating pulse can act temporally as a wave-plate (the Kerr effect) which is capable of rotating the polarization of the incident transient fluorescence from vertical to horizontal and thus allows the transient fluorescence to transmit through the exit polarizer, the P2 in the Kerr-gate device. The transient fluorescence signal at designated time delay after passing the Kerr-gate device was collected by a second ellipsoidal mirror (E2 in Scheme 2.8) and was reflected into the spectrometer.

In the spectrometer, the fluorescence signal at different wavelength was focused into the monochromator and detected by a liquid nitrogen-cooled charge-coupled device (CCD) detector (Princeton Instrument). The digitized signal from the CCD was then transferred to a desktop computer for further analysis.

2.2.4 Femtosecond broadband time-resolved fluorescence anisotropy

The setup for measuring the broadband fs-TRFA is very similar to that of the fs-TRF measurement (Scheme 2.8).³ The key difference between the TRFA and TRF setup is that the sample in fs-TRFA measurement is excited with a polarized light with the polarization direction being either parallel or perpendicular with respect to the direction for detection. In practice, this is done by using a $\lambda/2$ plate to set the polarization direction of the excitation pump laser to be either parallel or perpendicular with respect to the polarization direction of the P1 in the Kerr-gate device. The intensity of the transient fluorescence acquired at a designated delay time (t) with the polarization of pump laser parallel and perpendicular to the P1 is denoted as $I_{para}(t)$ and $I_{perp}(t)$ respectively. The time-resolved anisotropy value at that time delay, $r(t)$, is then calculated according to the following equation:⁸

$$r(t) = \frac{(I_{para}(t) - I_{perp}(t))}{(I_{para}(t) + 2I_{perp}(t))}$$

It is worth noting that the anisotropy ($r(t)$) is a dimensionless quantity which is independent of the total fluorescence intensity of the sample. The measurement of TRFA can be classified as an intensity ratiometric measurement which reveals the average angular displacement of the fluorophore that occurs between the absorption and the subsequent emission process.

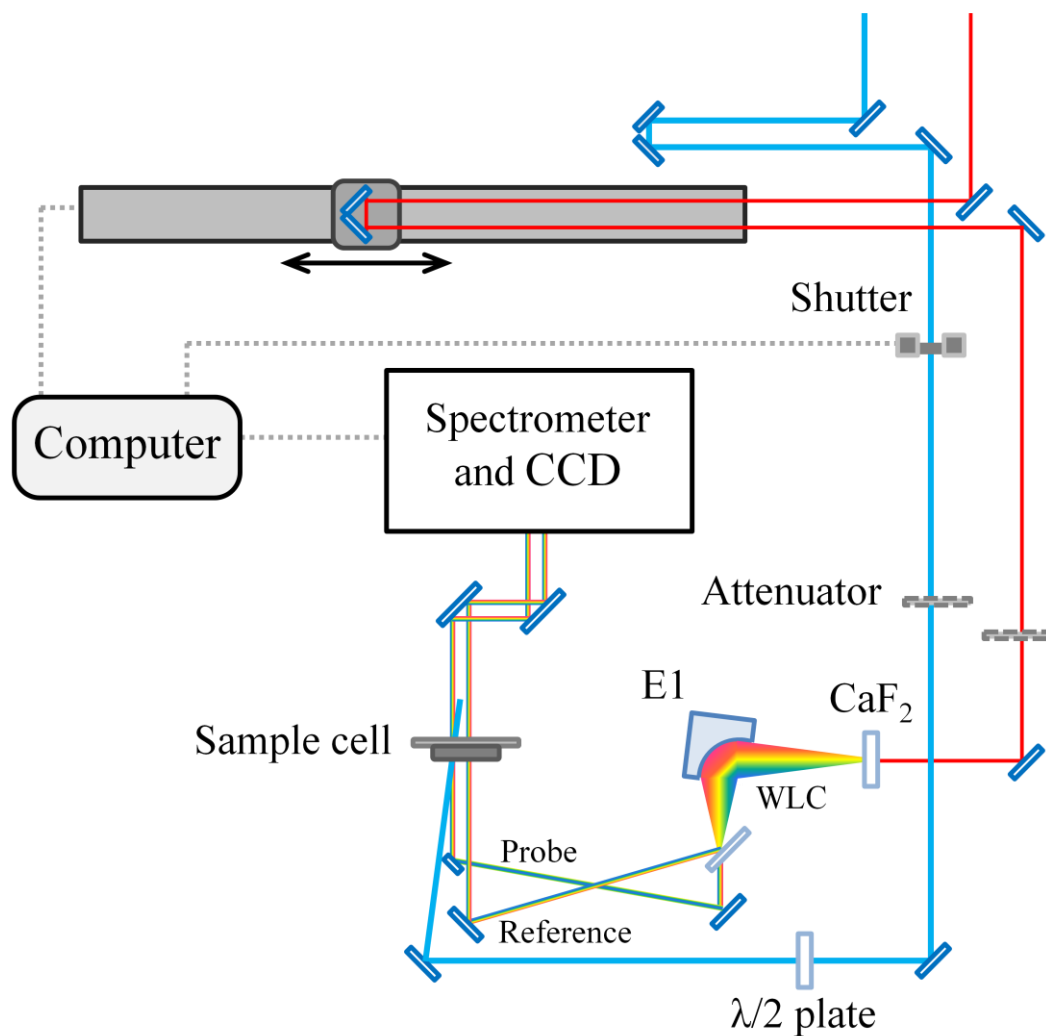
Ideally, the $r(t)$ would be equal to 1 according to the above equation if the absorption and emission polarization are parallel to each other, *i.e.* $I_{para}(t) = 1$ and $I_{perp}(t) = 0$. However, for sample molecules which are distributed randomly in homogeneous solution, the theoretical maximum value of the anisotropy is 0.4,

even for the case where the absorption and emission transition moments are collinear and there are no involvements of other depolarization processes.⁸ It is well accepted that an observation of r value lower than 0.4 is indicative for a loss in the anisotropy due to an angular displacement between the absorption and the emission transition or caused by other depolarization processes, such as the rotational diffusion of the excited state molecule or energy transfer between states of different polarization directions.

2.2.5 Femtosecond broadband transient absorption spectroscopy

The broadband fs-TA experimental setup was constructed with reference to the literature.³⁻⁵ Like in fs-TRF measurement; the sample in fs-TA measurement was also excited by the 280 nm excitation pump pulse. In the TA measurement, the probe pulse was an ultra-short WLC pulse which was generated by focusing the residual part of the amplified 800 nm laser pulse into a rotating calcium fluoride (CaF₂) plate. In our measurement, the WLC pulse has wavelengths covering a range from ~290 nm to 750 nm.

Similar to that in the TRF measurement, the excitation power in the fs-TA measurement was also kept as low as possible with a typical laser pulse peak power of ~2 GW / cm². This was done to avoid unwanted multi-photon effect to interfere with the measurement. Also, the IRF of fs-TA measurement is wavelength-dependent; it varies from ~100 fs to ~300 fs when the detection wavelength changes from 750 nm to 290 nm.



Scheme 2.9 Schematic diagram for the fs-TA experimental setup. The pump and the probe pulse are indicated in blue and red line respectively. ($\lambda/2$ = half-wave plate; CaF_2 = calcium fluoride plate; E1 = ellipsoidal mirror)

Scheme 2.9 shows the schematic diagram of the fs-TA system. After generation, the 280 nm excitation pump pulse (blue line in Scheme 2.9) travels a fixed optical path with its power adjusted by using an attenuator (Scheme 2.9). The excitation laser was then focused into a 0.5 mm thickness of sample solution. By using a $\lambda/2$ plate (Scheme 2.9), the polarization of excitation laser was set to

be at the magic angle (54.7°) with respect to that of the WLC probe pulse to remove unwanted effect due to such as the rotational diffusion.

On the other hand, a portion of the 800 nm laser pulse (red line in Scheme 2.9) first passed through the movable optical delay line for varying the time delay between the pump and probe pulse. Then, the 800 nm laser pulse was focused into a 1 mm thick CaF_2 plate which generates the ultra-short WLC pulse (WLC in Scheme 2.9). In order to avoid damage to the CaF_2 plate, the plate was attached on a motor and was set to rotate with a frequency of a few Hertz. The wavelength range of the WLC is from ~ 290 to 750 nm. The WLC after generation was, by using an ellipsoidal mirror (E1 in Scheme 2.9), collected and focused on the sample cell.

In order to improve the signal-to-noise (S/N) ratio of the fs-TA measurement, the WLC probe pulse was split into two beams of similar intensity, called the probe beam and the reference beam (Scheme 2.9). The two beams were then focused into two different positions of the sample solution. The probe beam when focused to the sample was aligned to overlap with the pump beam; while the reference beam was focused on the portion of sample which was not excited by the excitation pulse. The two-beam method (the probe and reference beam) was used to help minimizing the unwanted effect caused by power fluctuation of the laser pulses and thus enhanced the sensitivity and the S/N ratio of the fs-TA measurement.

After passing through the sample solution, the probe and reference beams were directed into the spectrometer. The two beams were recorded separately by

the liquid nitrogen-cooled CCD detector to produce digitized signal which was readout to a desktop computer.

To obtain fs-TA spectrum, a shutter (Scheme 2.9) was placed at the optical path of excitation pulse to control the timing for photo-excitation of the sample solution. The excitation induced change in absorbance, $\Delta OD(\lambda, t)$, at a certain wavelength (λ) and a particular delay time (t) can be derived from the signal, $I(\lambda, t)$, recorded from the pump and the reference beam. Let the intensity of signal from the probe and reference beam be $I_{pr}^0(\lambda, t)$ and $I_{ref}^0(\lambda, t)$ respectively in the absence of the excitation pump pulse (denoted by “0” index); and the corresponding signal intensity in the presence of excitation (denoted by “p” index) be $I_{pr}^p(\lambda, t)$ and $I_{ref}^p(\lambda, t)$, respectively. The $\Delta OD(\lambda, t)$ can then be calculated according to the following formula:

$$\Delta OD(\lambda, t) = -\log_{10} \frac{\left(\frac{I_{pr}^p(\lambda, t)}{I_{ref}^p(\lambda, t)} \right)}{\left(\frac{I_{pr}^0(\lambda, t)}{I_{ref}^0(\lambda, t)} \right)}$$

2.2.6 Nanosecond time-resolved emission spectroscopy

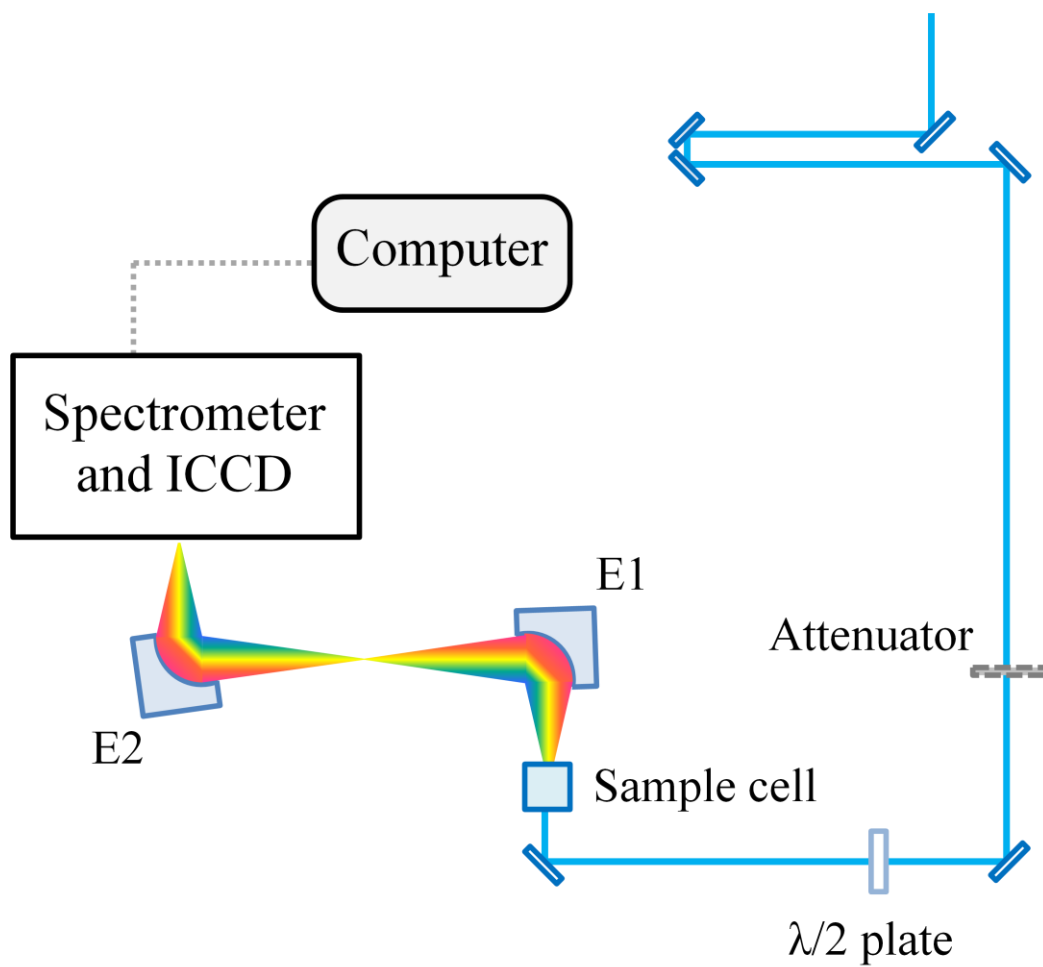
The overview of ns-TRE measurement is depicted in Scheme 2.10. The setup of ns-TRE is similar to that of the fs-TRF (Scheme 2.8).⁴⁻⁵ Like in the fs-TRF, ns-TRE also used the 280 nm excitation pulse which was generated from the OPA and was focused into sample solution which is contained in a sample cell of 1 cm thickness. Prior to excitation of the sample solution, the pump laser pulse travelled through a fixed optical path and was attenuated to a suitable power to avoid the unwanted effects such as the multi-photon excitation and photo-degradation. Similar to that in the TRF, during the measurement of ns-TRE, the sample solution was being circulated in a flow cell compartment but under deaerated condition.

In the ns-TRE measurement, transient emission from photo-excited sample was collected via a pair of ellipsoidal mirrors (E1 and E2, Scheme 2.10) and was directed into the spectrometer for detection. Instead of using the 800 nm laser pulse to drive Kerr-gate to work as an optical shutter and the use of mechanical optical delay line to vary the time delay between the pump and the probe pulse as in the fs-TRF measurement (Scheme 2.8), the ns-TRE measurement used the ICCD detector based on the so-called time gating technique (Scheme 2.10).

The ICCD detector is mainly consisted of a microchannel plate (MCP) and a CCD detector. The MCP is placed in front of the CCD detector. In principle, the ICCD detector is an “intensified” CCD detector where the signal is amplified by the MCP before translated to the CCD detector. The magnitude (or the gain) of the amplification can be adjusted by changing the voltage across the

MCP. The signal detected by the CCD is read out to a desktop computer for storage and further analysis.

To enable detection of ns-TRE at varied delay time after the photo-excitation, the operation of ICCD was synchronized with the fs laser system. The synchronization was achieved by sending an electronic gating pulse to the MCP of ICCD to allow incoming emission signal to pass through and strike the CCD detector. In this way, the time delay between the excitation and the ICCD detection can be controlled manually. In addition, the time duration for the ICCD to collect the incoming emission signal (called the gate width) can also be manually adjusted. Limited by the electronic response time, the fastest possible time resolution of the TRE measurement is ~ 2 ns.



Scheme 2.10 Schematic diagram for the ns-TRE experimental setup. The pump pulse is indicated in blue line. ($\lambda/2$ plate = half-wave plate; E1 & E2 = ellipsoidal mirror)

2.2.7 Nanosecond broadband transient absorption measurement

The setup for ns-TA measurement was constructed similarly to that of the fs-TA experiment (Scheme 2.9) and was described in the previous studies.³ However, unlike in the fs-TA measurement which used the 280 nm excitation pulse, excitation in ns-TA was achieved using a 266 nm pulse with ~1 ns pulse duration produced by a Q-switched Nd:YVO₄ laser. The 266 nm excitation pulse was the fourth harmonic of the 1064 nm fundamental from the Nd:YVO₄ laser. The excitation pulse was synchronized to the fs-TA laser system and the fs-TA spectrometer to enable detection of the broadband TA spectra at timescale from several ns to microseconds.

In the ns-TA experiment, the power of 266 nm excitation laser was attenuated to a suitable power and, by using the $\lambda/2$ plate, polarization direction of 266 nm laser was adjusted to be at magic angle (54.7°) with respect to the WLC probe pulse. The 266 nm laser was then focused into the sample solution and was aligned to overlap with the probe beam at the sample solution. Like that in the fs-TA measurement, the sample compartment in the ns-TA measurement was 0.5 mm thickness but under deaerated condition. Instead of the optical delay line in the fs-TA, the digital delay and pulse generator (DG535, Stanford Research Systems) was used to synchronize and to control the time delay between the 266 nm excitation pump pulse and the WLC probe pulse.

Like in the fs-TA, the transient signals from the WLC probe and reference beams were recorded separately by the liquid nitrogen-cooled CCD detector and were readout to a computer for storage and analysis.

2.3 Steady State Measurements

All the steady state measurements were performed at room temperature and atmospheric pressure.

2.3.1 Steady state absorption measurement

For steady state measurement, the UV-visible absorption was measured by Hitachi U-3900H spectrometer in wavelength range from 200 nm to 400 nm with a 2 nm spectral band-pass. The UV-Visible absorption measurement of the sample in each of the solvent was performed in a 1cm path-length quartz cell; and the absorption spectrum was obtained by subtraction of the corresponding solvent spectrum from the spectrum of sample solution.

2.3.2 Steady state fluorescence measurement

The steady state fluorescence spectrum was acquired by a Jobin Yvon Fluoromax-4 spectrofluorometer. The spectra were recorded in wavelength range from 290 nm to 700 nm. The spectral band-pass for the excitation and the emission was both set at 3 nm and the integration time for collection of the spectrum was 0.1 s. The fluorescence from sample solution and solvent were measured separately using a 2 mm path-length quartz cell. For the measurement of sample solution, the concentration of the sample is $\sim 10^{-4} - 10^{-5}$ M. The fluorescence spectrum from the sample was obtained by subtracting the corresponding solvent spectrum from the spectrum of sample solution.

For fluorescence spectra that cover wavelengths from near-UV (290-400 nm) to visible region (400-700 nm), two separate measurement was made in the absence and presence of a 400 nm long-pass filter at the emission side of the sample solution. The overall emission spectrum was reconstructed by jointing the two corresponding spectra manually. To do this, the two spectra were first intensity normalized and then combined at the wavelengths which were covered in both the spectra. Also, the unwanted signal such as the second order of excitation light source and the solvent Raman band were removed to avoid interfering with the fluorescence spectrum.

To avoid photo-degradation of the sample in the irradiation, the sample was stirred continuously in the course of the measurement.

2.3.3 Fluorescence quantum yield measurement

Fluorescence quantum yield (Φ_f) was measured based on the comparative method which used a compound with known Φ_f as the standard. Parallel fluorescence measurement under the same experimental condition was performed for the standard and the sample solution with known concentration. In the current measurement, 5-methyl-2'-deoxycytidine in pH7 buffered water was used as the standard ($\Phi_f = 5.6 \times 10^{-4}$).⁹ The Φ_f of the sample solution was then derived according to the following equation:

$$\Phi_{f(X)} = \frac{F_X}{F_S} \times \frac{A_S}{A_X} \times \left(\frac{n_X}{n_S} \right)^2 \times \Phi_{f(S)}$$

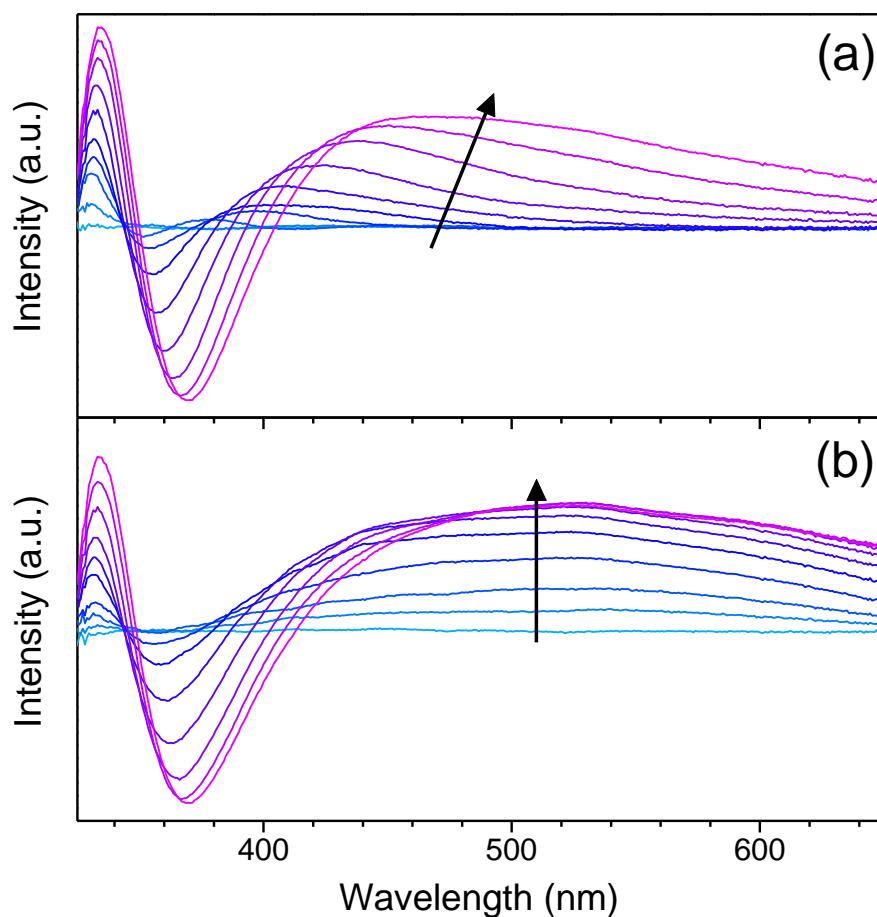
where F_X and F_S is the integrated intensity of the acquired fluorescence spectrum for the sample and the standard, respectively; A_X and A_S is respectively the absorbance at the excitation wavelength of the sample and the standard, n_x and n_s is the refractive index of the solvent used for the measurement of the sample and the standard, respectively, and the $\Phi_{f(X)}$ and $\Phi_{f(S)}$ is the fluorescence quantum yield of the sample and the standard respectively.

To minimize the uncertainty caused by the re-absorption effect, the absorbance for the sample solution and the standard solution at the excitation wavelength were controlled to be equal or slightly less than 0.1.

2.4 Spectra Calibration and Data Analysis

For all the time-resolved spectra presented in the subsequent chapters, the transient spectra at different pump-probe time delay were obtained by appropriate subtraction of the signal from the probe-before-pump time delay. In the fs time-resolved measurements, the fs-TRF spectra were calibrated in regarding the sensitivity variation at varied emission wavelengths covered by the measurement. For both the fs-TA and fs-TRF spectra, calibrations were done to eliminate the wavelength dependent time shift caused by the group velocity dispersion (GVD). GVD arises due to light of different wavelength travels at different speed through the same medium; light of shorter wavelength which has a higher index of refraction travels slower than light of longer wavelength.^{2,10} This leads to the so-called "chirp effect".

Practically in the fs-TA, the WLC probe beam, after generation, shows GVD when it passes through the CaF₂ plate and the several optical elements through which it travelled (e.g. the cell window). As a result, the different spectral components of the WLC spread in time and interact with the sample molecules at different time. On the other hand, in the fs-TRF measurement, both the sample cell window and the several optical components used for collecting the fluorescence emanated from the sample may contribute in causing the GVD, i.e., the transient fluorescence of different wavelength reaches the detector at different time. As a consequence, the raw time-resolved data of both the fs-TA and the fs-TRF shows a strong wavelength-dependent "time-zero" in the sub-ps time scale (Scheme 2.11). In order to minimize the GVD, the thickness of the cell window and the involved optical components were kept as thin as possible.



Scheme 2.11 Schematic diagram showing the fs-TA data at sub-ps delay time before (a) and after (b) the GVD correction. The arrows indicate the temporal evolution.

For fs-TRF as well as fs-TA, the spectra recorded were corrected for the wavelength dependent time shift caused by GVD before data analysis. It was done by conducting a parallel time-resolved measurement for a reference compound (e.g. trans-stilbene) under the same experimental condition. Regarding the wavelengths covered by our time-resolved measurements (from ~290 nm to 750 nm), the relation between the value of the temporal shift (δt) and

wavelength (λ) can be linked up by using a quadratic equation, $\delta t = a\lambda^2 + b\lambda + c$; where a, b and c are three different scaling factors related to the optical arrangement and solvent used in the experiment.¹¹ By adjusting these three factors (a, b and c), a “calibration curve” for the wavelength dependent time shift covering the range of detection wavelengths can be constructed. It was then acted as a paradigm to provide a proper time shift correction for the samples and hence restored the spectral and temporal evolution of the transient spectra at the sub-ps decay time (Scheme 2.11 (b)).

Kinetic analysis of the intensity decay profile ($S_\lambda(t)$) obtained from the recorded transient spectra at a certain wavelength (λ) was done by convolution of the IRF, represented by $g(\tau)$, with an exponential function, represented by $F_\lambda(t)$, as showed in equation 2.1:

$$S_\lambda(t) = \int_{-\infty}^t g(\tau)F_\lambda(t-\tau) d\tau \quad \text{eq. 2.1}$$

where the $g(\tau)$ is assumed to follow the Gaussian function:

$$g(\tau) = \frac{1}{\pi^{1/2}\sigma} \exp\left[-\left\{\frac{(\tau - \tau_0)}{\sigma}\right\}^2\right] \quad F_\lambda(t) \text{ is multi-exponential function}$$

$F_\lambda(t-\tau) = \sum_i a_i e^{-(t-\tau)/\tau_i}$ with the τ_i being the time constant and a_i the relative amplitude associated with the component τ_i .

With the $g(\tau)$ being the Gaussian function and $F_\lambda(t-\tau)$ being the multi-exponential function, eq. 2.1 can be derived analytically to the following form which is in fact corresponding to the so-called error function (erf, eq. 2.2).¹²

$$S_{\lambda}(t) = \sum_i a_i \frac{1}{2} \exp\left[-\frac{1}{\tau_i} \left(t - \tau_0 - \frac{\sigma^2}{4\tau_i}\right)\right] \times \left\{1 - \operatorname{erf}\left[\left(t - \tau_0 - \frac{\sigma^2}{2\tau_i}\right) \frac{1}{\sigma}\right]\right\}$$

eq. 2.2

where the τ_0 is the time-shift which can be used to determine the absolute time-zero. The full width half maximum of the experimental response (τ_M) can be related to the σ in eq. 2.2 by $\sigma = \frac{\tau_M}{1.6651}$. Besides, the parameters τ_i , τ_M and τ_0

can subsequently be evaluated using the least-squares fitting procedure of eq. 2.2.

2.5 Sample Information and Materials

The sample DMABME and DMABEE was purchased from Lanchester and Aldrich respectively. The gold(I) oligo-PE complexes were provided by Professor Chi-Ming Che's research group in the Department of Chemistry of the University of Hong Kong. Spectroscopic grade solvents, acetonitrile and methanol, were purchased from Tedia. The isotopic-modified derivatives of methanol (CH_3OD and CD_3OD) were purchased from Cambridge Isotope Laboratories. All the chemicals were used without further purification.

All the time-resolved spectroscopic measurements were done in solution phase and performed at room temperature under atmospheric pressure. For the fs-TRF and fs-TA experiments, ~ 0.5 - 1.5 mM sample solution was circulated in a ~ 0.5 mm path-length flow cell throughout the experiment to furnish fresh sample for every laser exposure. The flow cell compartment is ~ 0.5 mm thickness sandwiched between two 0.5 mm thick CaF_2 windows. To avoid photo-degradation, ~ 20 ml sample solution was circulated through the sampling cell which was connected through Teflon hoses to a stainless steel pump. The flow rate of the sample solution was controlled to be sufficiently high to ensure a fresh proportion of sample being exposed to each of the excitation laser pulse.

In the ns-TA and ns-TRE measurements, ~ 40 ml sample with concentration of ~ 10 - 50 μM was circulated in a 0.5 mm path-length and 1 cm path-length flow cell respectively. To avoid the oxygen quenching effect, the sample solution was purged by nitrogen gas for at least 20 minutes prior to and throughout the time-resolved measurements.

In all time-resolved measurements, the sample solutions were monitored by UV-visible absorption before and after the experiments to ensure no photo-degradation of sample during the time-resolved experiments.

2.6 References

1. Andrews, D. L.; Deidov, A. A. *An Introduction to Laser Spectroscopy*, 2nd Ed., Kluwer Academic/Plenum Publisher, New York, **2002**.
2. Reid, G. D.; Wynne, K. *Encyclopedia of Analytical Chemistry* **2000**, 13644-13670.
3. Chan, C. T. L.; Cheng, C. C. W.; Ho, K. Y. F.; Kwok, W. M. *Phys. Chem. Chem. Phys.* **2011**, *13*, 16306-16313.
4. Lu, W.; Kwok, W. M.; Ma, C.; Chan, C. T. L.; Zhu, M. X.; Che, C. M. *J. Am. Chem. Soc.* **2011**, *133*, 14120-14135.
5. Ma, C.; Chan, C. T. L.; Kwok, W. M.; Che, C. M. *Chem. Sci.* **2012**, *3*, 1883-1892.
6. Schmidt, B.; Laimgruber, S.; Zinth, W.; Gilch, P. *Appl. Phys. B* **2003**, *00*, 1-6.
7. Arzhantsev, S.; Maroncelli, M. *Applied Spectroscopy* **2005**, *59*, 206-220.
8. Lakowicz, J. R. *Principles of Fluorescence Spectroscopy*, 3rd Ed. Springer, **2006**.
9. Sharonov, A.; Gustavsson, T.; Marguet, S.; Markovitsi, D. *Photochem. Photobiol. Sci.* **2003**, *2*, 362-364.
10. Maciejewski, A.; Nashrecki, R.; Lorenc, M.; Ziolk, M.; Karolczak, J.; Kubicki, J.; Matysiak, M.; Szymanski, M. *J. Mol. Struct.* **2000**, *555*, 1-13.

11. Ruckebusch, C.; Silwa, M.; Pernot, P.; de Juan, A.; Tauler, R. *J. Photochem. Photobiol. C: photochem. rev.* **2012**, *13*, 1-27.
12. Raytchev, R.; Pandurski, E.; Buchvarov, I.; Modrakowski, C.; Fiebig, T. *J. Phys. Chem. A* **2003**, *107*, 4592-4600.

Chapter 3 Ultrafast Broadband Time-Resolved Study on the Excited States of Methyl-4-dimethylaminobenzoate in Acetonitrile

3.1 Results

3.1.1 Steady state absorption and fluorescence spectroscopy

Figure 3.1 depicts the steady state UV-visible absorption and fluorescence spectra recorded for methyl-4-dimethylaminobenzoate (DMABME) in acetonitrile; also shown in the figure are the molecular structure of DMABME and the transition polarization direction for the L_a and L_b $\pi\pi^*$ state, respectively. It is clear from the figure that the UV-visible absorption profile features two absorption bands peaking at wavelength maximum (λ_{\max}) ~ 225 nm and $\lambda_{\max} \sim 310$ nm respectively. Among the two bands, the $\lambda_{\max} \sim 310$ nm band ranging from ~ 270 - 330 nm is much stronger with the molar absorptivity maximum (ϵ_{\max}) of $\sim 2.3 \times 10^4 \text{ M}^{-1} \text{ cm}^{-1}$. According to the literature, the band is attributable to a combined contribution due to two strong and closely overlapping transition the $S_0 \rightarrow L_a$ and $S_0 \rightarrow L_b$.¹⁻³

The steady state fluorescence spectrum (Figure 3.1) shows two partially overlapped emissions bands, one is the so-called normal “blue” peaking at ~ 350 nm and the other the anomalous “red” fluorescence peaking at ~ 500 nm. The spectrum acquired here is closely resemble to that reported in the literature for closely related dual emission molecule in solvent of similar property.¹⁻⁵ The

“blue” and “red” fluorescence band can therefore be attributed to the locally excited (^1LE) and intramolecular charge transfer (^1ICT) state, respectively. The spectral data obtained for DMABME and the closely related ethyl-4-dimethylaminobenzoate (DMABEE) are summarized in Table 3.1.

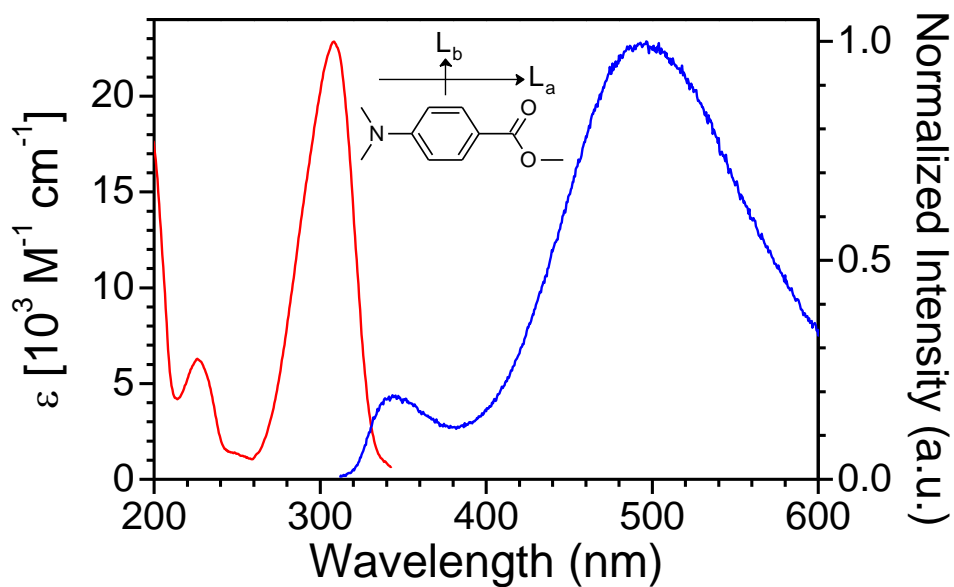


Figure 3.1 Steady state UV-visible absorption (red) and 280 nm excited fluorescence (blue) spectra of DMABME in acetonitrile. The inset shows the molecular structure and the polarization directions for the $S_0 \rightarrow L_a$ and $S_0 \rightarrow L_b$ transitions.

Table 3.1 Photophysical parameters obtained for DMABME and DMABEE in acetonitrile. ^a Ref. 5. ^b Ref. 14. ^c Ref. 15.

	ϵ_{\max} /M ⁻¹ cm ⁻¹	λ_{abs} /nm	$\lambda_{\text{f}}^{\text{LE}}$ /nm	$\lambda_{\text{f}}^{\text{ICT}}$ /nm	τ_{LE} /ps	τ_{ICT} /ps	τ_{T} /μs	Φ_{f}
DMABME	~22800	~308	~350	~500	~0.8	~1900	~4	2.6×10 ⁻² ^b 2.9×10 ⁻²
DMABEE	~23200	~307	~350	~500	~1.1 ^a 0.92	~1600		2.8×10 ⁻² ^b 1.7×10 ⁻² ^c 2.3×10 ⁻²

3.1.2 Femtosecond time-resolved fluorescence spectroscopy

In order to characterize temporal evolution of the ¹LE and ¹ICT states and to determine the spectral character and the conversion dynamics between these two excited states, fs-TRF experiment was first performed; the result obtained is delineated in Figure 3.2. Considering the large difference in the relative intensity of fluorescence signal, the time-resolved spectra are shown separately in two different time regimes, 0-5 ps (Figure 3.2(a)) and 5-5000 ps (Figure 3.2(b)). From Figure 3.2(a), it is clear that, instantly after excitation, a single emission band with λ_{max} at ~350 nm dominates the spectral window. This transient fluorescence signal then decays rapidly and evolves within 5 ps into a much weaker and red-shifted emission band with λ_{max} at ~500 nm (Figure 3.2(b)). After this, the λ_{max} ~500 nm signal decays in a slower time scale and vanishes at ~5000 ps after the excitation. Based on the spectral profile and the maximum emission

wavelength, it is straightforward to assign respectively the $\lambda_{\text{max}} \sim 350$ nm and $\lambda_{\text{max}} \sim 500$ nm emission band to the ^1LE and ^1ICT state observed in the steady state fluorescence measurement (Figure 3.1). Of note, the drastic drop of the “blue” ^1LE emission and the rapid growth of the “red” ^1ICT emission is accompanied by an isoemissive point at ~ 520 nm (inset in Figure 3.2(a)), manifesting a precursor-successor relationship between the two excited states. This direct spectral observation provides an explicit evidence for the rapid conversion from the ^1LE to the ^1ICT state through ICT reaction.

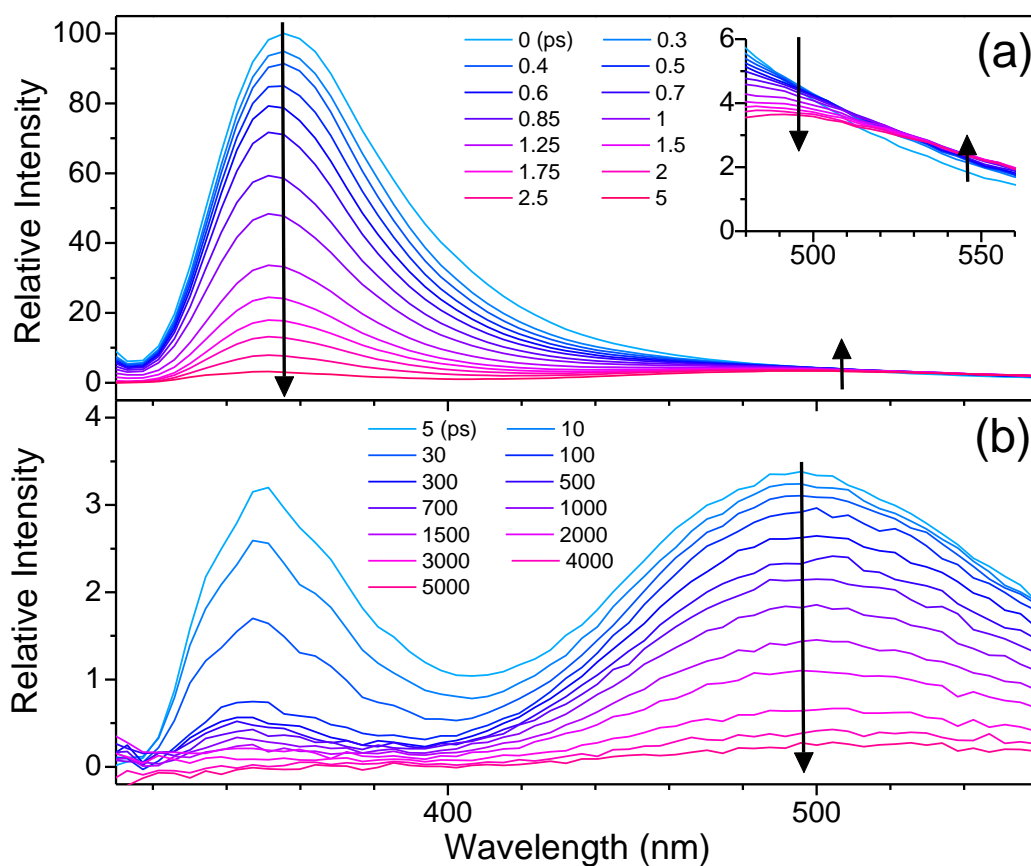


Figure 3.2 Broadband time-resolve fluorescence spectra of DMABME in acetonitrile recorded at 0-5 ps (a) and 5-5000 ps (b) after 280 nm excitation. Note the difference in the relative intensity scale between the spectra in (a) and (b).

The inset in (a) shows the isosbestic point observed as temporal evolution of the spectra. The arrows indicate temporal evolution of the spectra.

The time constant for the ICT reaction from the ^1LE and ^1ICT state and the ensuing decay dynamics of the ^1ICT state can be derived by analysis of kinetic decay profiles of the ^1LE and ^1ICT state fluorescence at representative wavelengths. Figure 3.3(a) shows the kinetic decay profiles obtained from the TRF spectra (Figure 3.2) at ~ 360 and ~ 560 nm, representing the ^1LE and ^1ICT state respectively. Global analysis of the experimental data reveals a common ~ 0.8 ps time constant for the decay of the ^1LE and the growth of the ^1ICT emission signal and a time constant of ~ 1.9 ns for the subsequent decay of the ^1ICT state. The ~ 0.8 ps time constant obtained is close to the ~ 1 ps time constant reported in the literature for DMABEE in the same solvent,^{5,6} implying that the ICT rate is little affected by the alkoxy carbonyl group of the molecule.

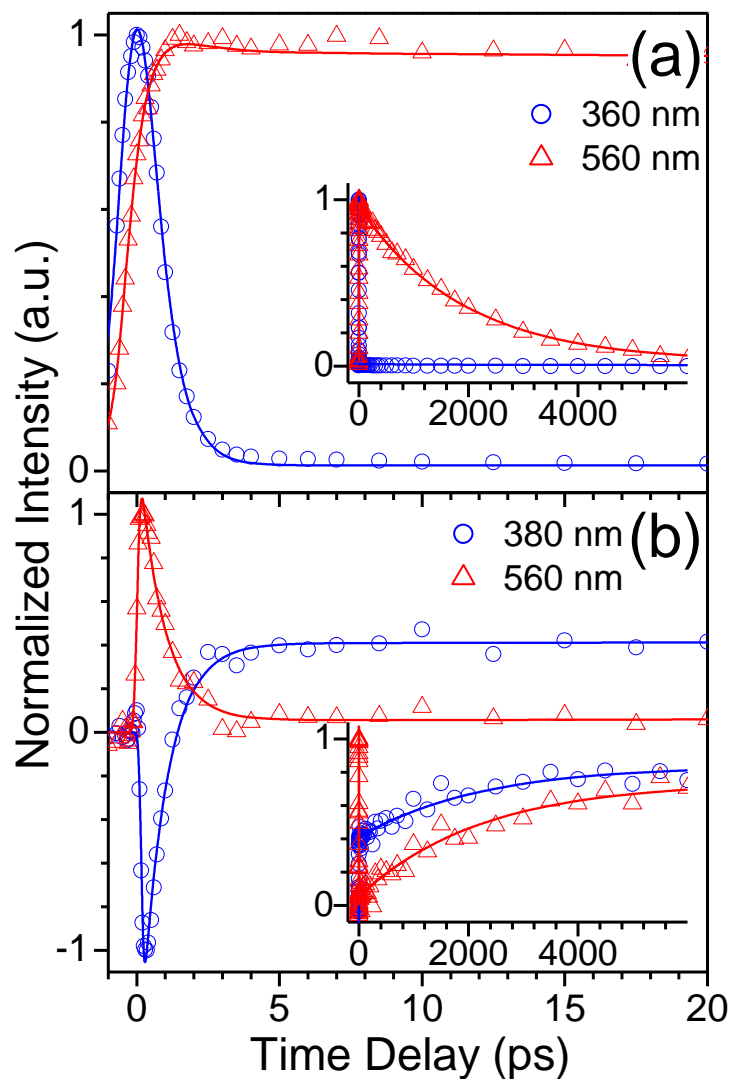


Figure 3.3 Experimental (\circ , Δ) and fitted (—) kinetic decay profiles of TRF (a) and TA (b) at indicated wavelengths for 280 nm excited DMABME in acetonitrile. The insets show the decay profiles at longer decay time up to ~ 6 ns.

3.1.3 Femtosecond time-resolved fluorescence anisotropy spectroscopy

Fs-TRFA experiments were performed to investigate the electronic origin for both the ^1LE and ^1ICT state. Figure 3.4 displays the anisotropy spectra $r(t)$

obtained in wavelength range from ~330 nm to ~550 nm and at three representative delay times, 0.5, 5, 50 ps, after the photo-excitation. The TRFA spectra present two important features. First, the r value is independent of the emission wavelength at each of the measured time delay. Second, the $r(t)$ spectrum at 0.5 ps after excitation, i.e. $r(0.5 \text{ ps})$, display a r value of ~0.3. The value of $r(t)$ decreases as increase of time delay, being ~0.20 at 5 ps and ~0 at 50 ps after the excitation.

The first observation provides direct evidence that, at each of the three delay times, the transient fluorescence signal is originated due to state of the same electronic polarization character.^{1,2,7,8} Given the ~0.8 ps ICT time constant, the result of $r(0.5 \text{ ps})$ indicates compellingly for a common electronic origin of the ^1LE and ^1ICT state. At 0.5 ps after excitation, the ICT reaction proceeds and transfers the excited state population from the precursor ^1LE state to the successor ^1ICT state in nearly halfway through. The ^1LE and ^1ICT states should both have a sufficient excited state population and respectively shows significantly contribute to the “blue” and “red” region of the acquired transient fluorescence anisotropy spectrum. If the ^1LE and ^1ICT states were different in the electronic polarization, the ICT reaction would be considered as a fluorescence depolarization process and as a result would lead to a significant decrease in the r value in the “red” compared to the “blue” region of the fluorescence anisotropy. This is, however, not observed in our experimental data. The wavelength independence of the $r(0.5 \text{ ps})$ spectrum across wavelength from 330 to 550 nm requires a common electronic origin for the ^1LE and ^1ICT state.

Given the fact that the ^1ICT state is inherently of the L_a character,^{1,2,7} the ^1LE and ^1ICT states now found to have the same polarization direction is indicative of the ^1LE state being also of the L_a in electronic nature. In other words, both the ^1ICT and the ^1LE state are of the L_a in the electronic parentage. Within this context, it can be inferred from the high r value (~ 0.3) at ~ 0.5 ps that the absorption at 280 nm excitation is accounted for mostly by the L_a associated transition along the long molecular axis (Figure 3.1). The deviation from the theoretical value (0.4) of the $r(0.5\text{ps})$ can then be attributed to originate from subtle contribution of the L_b state for absorption at 280 nm and an well-expected ultrafast (in fs timescale) internal conversion (IC) from L_b to L_a occurring due to the energy proximity between the two states.^{1,3-6,9,10}

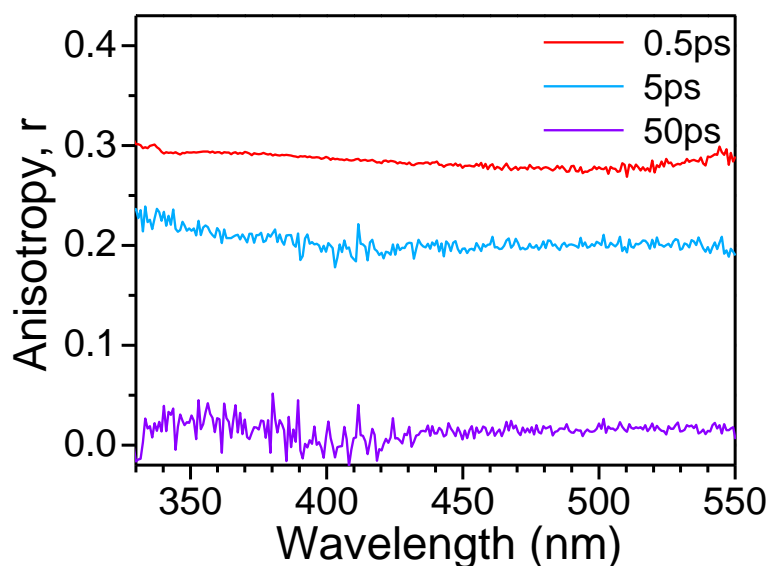


Figure 3.4 Broadband time-resolved fluorescence anisotropy spectra of DMABME in acetone recorded at 0.5, 5, 50 ps after 280 nm excitation.

Regarding that, irrespective of the delay times, the fluorescence emission is due to the state of L_a parentage, the progressive drop in anisotropy value from ~ 0.3 at 0.5 ps to ~ 0.2 at 5 ps and then ~ 0 at 50 ps can be ascribed to originate from the overall rotational diffusion of the excited molecule.^{2,7,8} The timescale for the loss of anisotropy observed here is close to the tens ps rotational diffusion time reported for the molecule of comparable size.¹¹

3.1.4 Femtosecond to microsecond transient absorption spectroscopy

In order to provide complementary information on the ICT dynamics and to probe directly the decay channel of the ^1ICT state as well as the nonradiative processes related to the intersystem crossing (ISC) and subsequently formed triplet ($^3\text{T}_1$) state, transient absorption (TA) measurement covering timescale from fs to μs were performed. The data acquired are depicted in Figure 3.5.

Promptly after the excitation, the initial TA profile (Figure 3.5(a)) features a sharp positive absorption at ~ 330 nm accompanied by a negative signal at ~ 360 nm and a broad positive absorption at wavelength from ~ 410 nm to 700 nm. The spectrum then evolves into a new profile which features also the positive ~ 330 nm absorption and the negative signal ~ 360 nm but with a clear added new positive absorption band at ~ 450 nm from ~ 0 to 100 ps time delay (Figure 3.5(a)). This spectral evolution takes place with an isosbestic point at ~ 495 nm.

TA time profile obtained at ~ 560 nm and ~ 380 nm for the decay of early spectrum and rise of later spectrum is displayed in Figure 3.3(b). Global analysis

of the ~560 nm and ~380 nm TA time profiles gives a time constant of ~0.8 ps, which coincides with the time constant for the ICT reaction obtained from the TRF measurement (Figures 3.2 and 3.3(a)). On the basis of this, it is clear that the above described temporal evolution of the TA spectrum is brought about by the ICT reaction; and as a result, the initial (~0 ps) TA spectrum can be ascribed to the ¹LE state and the late (~100 ps) TA spectrum the ¹ICT state. Recalling that the ¹LE state featuring fluorescence with $\lambda_{\text{max}} \sim 360$ nm (Figures 3.1 and 3.2(a)), the ~360 nm negative signal in the early time (<1 ps) TA spectra can be attributed to arise due to the contribution of stimulated emission from the ¹LE state.

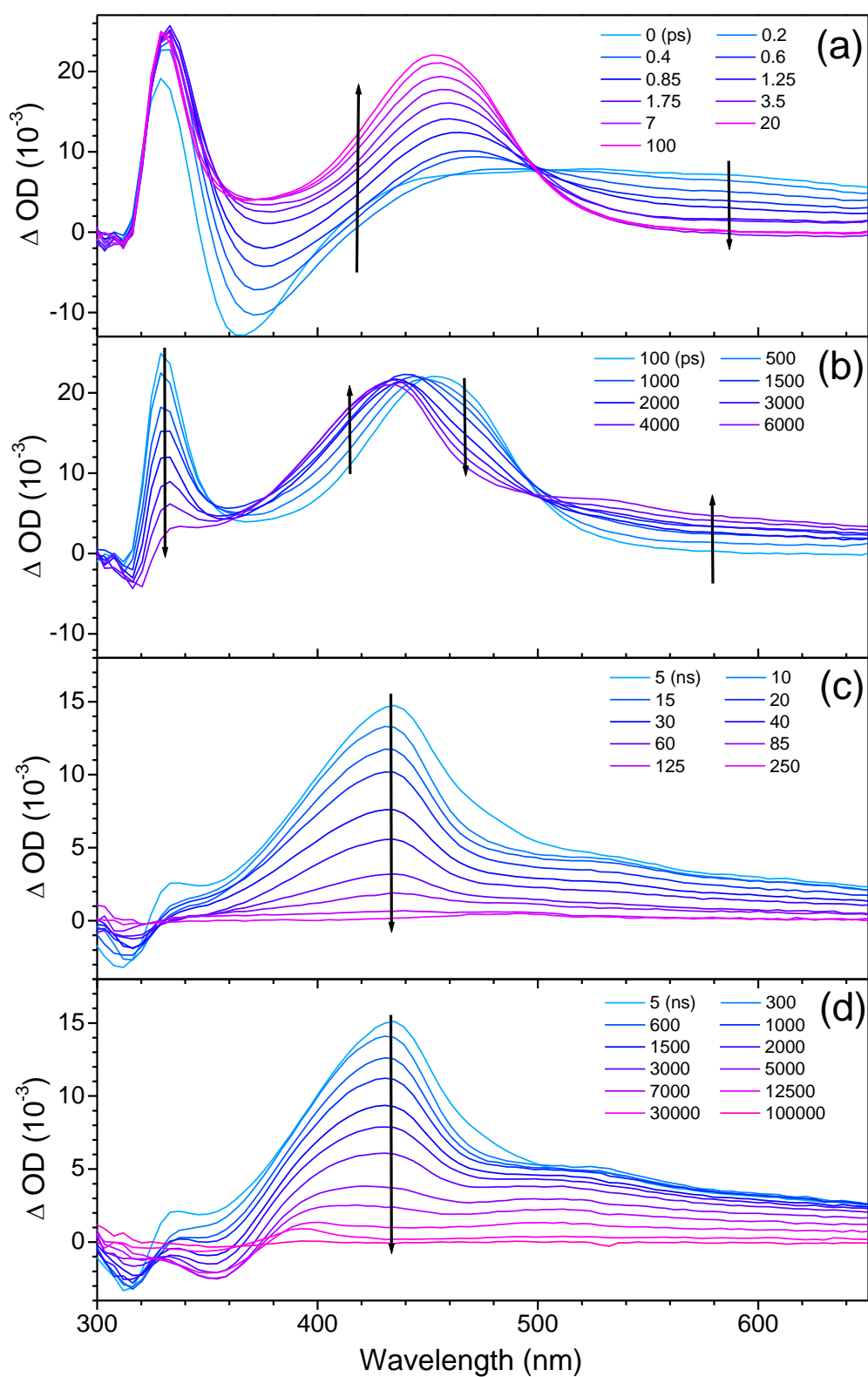


Figure 3.5 Broadband transient absorption of DMABME in acetonitrile recorded at 0-100 ps (a), 100-6000 ps (b), 5-250 ns (c) and 5-100000 ns (d) after

280 nm ((a) and (b)) or 266 nm ((c) and (d)) excitation. The arrows indicate temporal evolution of the spectra.

Figure 3.5(b) displays temporal evolution of TA after the formation of ^1ICT state. It can be seen that the ^1ICT state spectrum which features the ~ 330 and ~ 450 nm positive absorptions decays in hundreds to thousand ns into a profile that shows positive absorption with λ_{max} at ~ 430 nm and an extended absorption tail across long wavelength region from ~ 500 nm to 700 nm (the ~ 6000 ps TA spectrum in Figure 3.5(b)). This spectral transformation proceeds with two isosbestic points at ~ 360 and ~ 500 nm. The $\lambda_{\text{max}} \sim 430$ nm TA spectrum persists with little change in intensity up to ~ 6 ns, indicating a long-lived character of the corresponding species. Analysis of the TA time profiles at 380 nm and 560 nm resulted in a time constant of ~ 1.9 ns for the spectral transformation (inset in Figure 3.3(b)). This time constant matches exactly with the decay time of ^1ICT state derived from the fs-TRF measurement (inset in Figure 3.3(a)).

Figure 3.5(c) depicts TA spectra obtained at ns to μs in acetonitrile under open air environment. It is noteworthy that the ~ 430 nm species shows little absorption at wavelengths < 330 nm where the S_0 absorbs. Therefore, temporal evolution of the negative signal at wavelength < 330 nm, which is due to the S_0 bleach, can be used to acquire dynamics for recovery of the S_0 . The result of TA time profile at ~ 430 and ~ 310 nm for the decay of ~ 430 nm absorption and recovery of S_0 bleach is shown in Figure 3.6(a). Obviously, the dynamics of

transient species decay correlates well with the recovery of S_0 bleach, they can be described by a common time constant of ~ 50 ns.

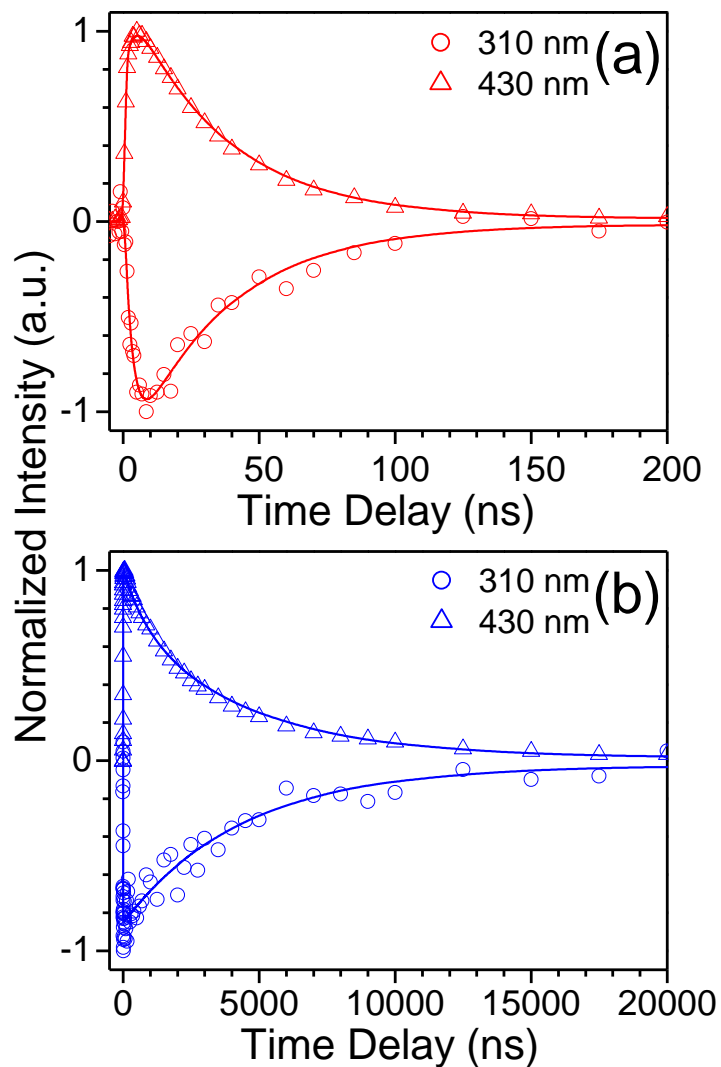
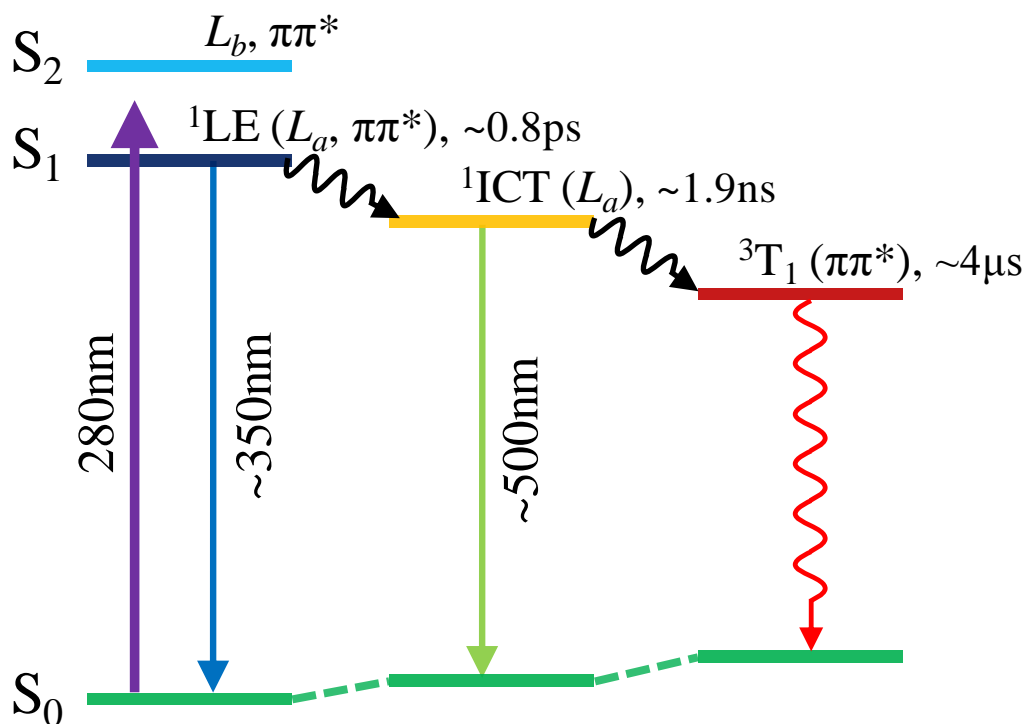


Figure 3.6 Experimental (\circ , Δ) and fitted ($—$) kinetic of ns-TA at 310 nm and 430 nm with 266 nm excitation of DMABME in acetonitrile under open air condition (a) and purged with nitrogen gas (b).

Parallel TA experiment was performed for the same sample system but with the sample solution being purged with nitrogen gas to reduce the effect of oxygen quenching. The TA spectra obtained are displayed in Figure 3.5(d). It can be seen that the TA spectra are nearly identical to those in Figure 3.5(c) except that the spectra decay in much slower timescale under nitrogen purge condition. Kinetic analysis of TA time profiles at ~310 nm for the S_0 recovery and ~430 nm for the transient species decay leads to a time constant of ~4 μ s (Figure 3.6(b)), about 80 times slower than that under the open air condition.

The much faster decay rate of the ~430 nm transient spectrum in oxygen richer condition (the open air environment) suggests a 3T_1 nature for the related species. Considering a typical $\sim 10^{-3}$ M oxygen concentration under the normal air condition,¹² the decay rates observed at the open air and nitrogen purged condition suggests a diffusion-controlled process with the oxygen quenching rate of $\sim 10^9$ s⁻¹ M⁻¹ under the open air condition.¹²

3.1.5 Deactivation cascade for photo-excited DMABME in acetonitrile



Scheme 3.1 Proposed deactivation pathways for photo-excited DMABME in acetonitrile.

Integrating the results of the steady state and time-resolved (TA and TRF) measurements, the deactivation cascade for photo-excited DMABME in acetonitrile can be constructed and is summarized in Scheme 3.1. After absorbing the 280 nm excitation, the molecule is promoted to the strongly allowed ${}^1L_a \pi\pi^*$ state, i.e. the ${}^1\text{LE}$ observed in the fluorescence spectra. The ${}^1\text{LE}$ state undergoes ICT reaction with ~ 0.8 ps time constant giving a charge separated ${}^1\text{ICT}$ state. The ${}^1\text{ICT}$ state then converts through ISC to the ${}^3\text{T}_1$ with ~ 1.9 ns time constant. The ${}^3\text{T}_1$ state decays into the S_0 with time constant of ~ 50 ns under open air condition or ~ 4 μs in nitrogen purged environment.

3.2 Discussion

3.2.1 The ICT reaction and electronic origination of ¹LE and ¹ICT states of DMABME in acetonitrile

The successive ¹LE(*L_a*) → ¹ICT(*L_a*) → ³T₁ deactivation pathway and the spectral and dynamic characterization of the excited states presented in the result section provides direct evidence for describing the hitherto unclear ICT reaction of DMABME in polar aprotic acetonitrile solution in one hand; and the ISC process of this *para*-substituted aromatic carbonyl compound on the other hand.

The fs-TRFA data in Figure 3.4 provides unequivocal evidence that the ¹LE and ¹ICT state feature a common electronic origin, the *L_a* in nature. This result leads strong support to the twisted ICT (TICT) model in predicting the ICT pathway for *para*-alkyl-dimethylaminobenzoates in acetonitrile.^{1,2,4} The minute involvement of *L_b* state in the ICT reaction casts doubt on the state coupling model.^{2,13}

According to the steady state absorption and the extinction coefficient (ϵ) in Figure 3.1 and Table 3.1, the radiative rate (k_f) of photo-populated ¹LE(*L_a*) state can be estimated to be $\sim 10^7 \text{ s}^{-1}$ ($k_f \approx \epsilon_{\text{max}} \times \Delta\nu_{1/2}$; $\epsilon_{\text{max}} = \sim 10^4 \text{ cm}^{-1} \text{ M}^{-1}$; $\Delta\nu_{1/2} = \sim 10^3 \text{ cm}^{-1}$, is the half-width of the absorption band),¹² consistent with the reported value of similar donor-acceptor (D-A) systems.¹ On the basis of the energy gap law and with reference to closely related systems,¹² it is reasonable that the ¹LE state, which is $\sim 3.5 \text{ eV}$ ($E \approx \frac{1240}{\lambda}$; $\lambda = \sim 350 \text{ nm}$) above the S₀, may have little possibility to deactivate in rapid time scale through IC back to the S₀. This plus the rapid rate ($\sim 0.8 \text{ ps}$) of the ICT reaction is indicative for a close to

unity population transfer from the ^1LE to ^1ICT state. Within this context, the large decrease in TRF intensity (100 *cf.* 4) as system evolving from the ^1LE to ^1ICT state (Figure 3.2) reflects that the k_f of ^1ICT is ~ 25 times smaller than that of the ^1LE state. This implies a substantial forbidden nature of optical transition associated with the ^1ICT state, which is in agreement with the full charge separation character of the zwitterionic form proposed for ^1ICT state of related D-A systems.^{1,2,4} In this regard, the ~ 0.8 ps ICT reaction can be considered an efficient nonradiative process that quenches effectively the radiative decay of the ^1LE state. The presence of this effective decay channel offers an explanation for the rather small fluorescence quantum yield (Φ_f) (on the order of 10^{-2}) displayed by this molecule and its related ester analogues (Table 3.1).^{1,14,15} Furthermore, the ~ 0.8 ps ICT reaction also explains the spectral profile of steady state fluorescence in Figure 3.1. The much larger contribution of the ^1ICT than ^1LE emission in the steady state fluorescence is accounted for by the much longer lifetime of the ^1ICT (~ 1.9 ns) than ^1LE state (~ 0.8 ps) which overcompensates inherently low radiative rate of the former than latter state.

It is essential to note two aspects of the ICT reaction, which are under extensive discussion for DMABME and related D-A molecules in the literature. One is about the reaction coordinate, in particular the role of solvent in the ICT reaction; and the other the structural conformation of the ^1ICT state.^{1,16}

As for the reaction coordinate, considerable attention had been paid on the interplay between the intramolecular structural motion and the dynamic solvent relaxation in promoting the ICT.^{1,3,9,17-23} The ~ 0.8 ps ICT reaction time is longer than the ~ 0.26 ps solvent reorientation time reported for acetonitrile.²⁴ It is

therefore plausible that the inner-sphere structural variation makes the major driving force for the ICT reaction. In this regard, the massive Stokes' shift ($\sim 8500\text{ cm}^{-1}$) observed for the fluorescence from ^1ICT ($\sim 500\text{ nm}$; 20000 cm^{-1}) than ^1LE ($\sim 350\text{ nm}$; 28500 cm^{-1}) state (Figures 3.1 and 3.2 and Table 3.1) indicates a large scale of conformational change induced by the ICT reaction. This is in supportive for the entropy activation controlled process proposed by the TICT model for the ICT reaction of *para*-alkyl-dimethylaminobenzoates.⁵

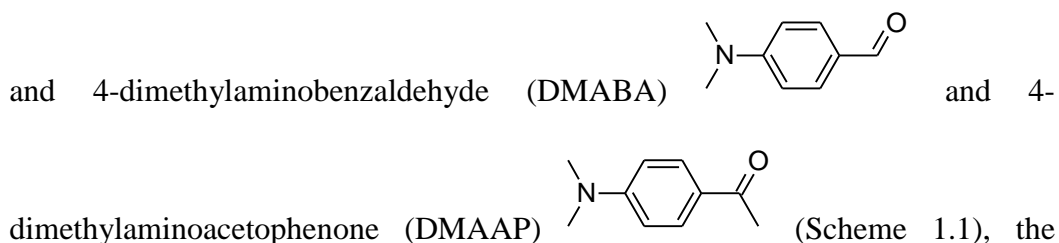
As for the conformation of ^1ICT state,^{1,16,25,26} it should be noted that, in recent years, a number of models have been proposed for conformation adopted by the ^1ICT state for explaining the anomalous “red” emission showed the D-A molecules. The twist conformation proposed by TICT model and the planar conformation by state coupling model (Planarized ICT (PICT) model) in describing relative orientation of the D *versus* A moiety are among the most discussed models in recent literature.^{1,27-33} Although most of the experimental and theoretical studies support the TICT model,^{1,16,28,31} the PICT model still remains possible.^{32,33} One of the key differences between these two models is that the PICT model requires a L_b parentage for the ^1LE state while the TICT model has no requirement for the nature of the ^1LE state.^{1,2,5,6} In this regard, our finding that the ^1LE state is actually of the L_a character affords a key piece of evidence supporting the TICT model. Given the planar structure of DMABME in S_0 ,^{1,3} it is likely that the photo-populated ^1LE state may also feature a planar conformation but with a certain degree of CT character promoted by the L_a associated absorption transition.¹ A full charge transfer as displayed by the ^1ICT state may requires breaking of the π conjugation between the amino lone pair and the π electron of the aromatic system which may impose a subtle but non-

negligible free energy barrier consist with the ~ 0.8 ps time constant observed for the ICT in DMABME.

In addition, it is interesting to note that, given the low k_f of the ^1ICT state, the ~ 1.9 ns lifetime for this state is much shorter than that expected by the natural radiative decay,¹² indicating presence of efficient nonradiative process for the decay of this state. Our data show that ISC is the major relaxation channel for decay of the ^1ICT state in acetonitrile. This closely resembles the deactivation of ^1ICT state of DMABN for which the dominant decay channel in polar aprotic like acetonitrile is also the ISC with a quantum efficiency of ~ 0.8 .^{1,34,35}

3.2.2 Comparison in excited state dynamics between DMABME and DMABA and DMAAP

Of note, despite the similar in molecular structure between DMABME



consecutive ${}^1\text{LE} \rightarrow {}^1\text{ICT} \rightarrow {}^3\text{T}_1$ relaxation pathway our data revealed for DMABME is in stark contrast to that reported for DMABA and DMAAP in the same solvent.³⁶ For DMABA and DMAAP, the ICT and ISC are kinetically competing process depleting at the same the photo-populated ${}^1\text{LE}$ state. The involvement of ISC at very early time proceeds with a time constant of ~ 3 ps for DMABA and DMAAP after the excitation can be attributed to presence of $n\pi^*$ state close lying to the photo-prepared $\pi\pi^*$, which is known to mediate effectively the ISC leading to formation of the $\pi\pi^*$ natured ${}^3\text{T}_1$ state (${}^3\pi\pi^*$).^{1,12,36-38} The absence of prompt ISC in DMABME suggests that the $n\pi^*$ state may lie at energy substantially higher than the ${}^1\text{LE}$ state,^{4,17} and be less accessible for promoting the ISC. As a result, the ICT reaction turns to be the major channel in the early stage deactivation of the ${}^1\text{LE}$ state. The dramatic difference in the rate of ISC *versus* ICT between DMABME and DMABA and DMAAP indicates a crucial role of carboxylate group in DMABME in varying the relative energy level of the $n\pi^*$ *versus* $\pi\pi^*$ state and to change the overall cascade of the excited state deactivation.

On the other hand, it is noted that the TA spectral feature we observed with the ${}^3\text{T}_1$ state of DMABME is very similar to that reported for DMABA and

DMAAP.³⁶ It is therefore plausible that, in spite of the different pathway and dynamics of the ISC, the triplet state in the three molecules (DMABME, DMABA and DMAAP) may in fact share a common electronic character. Indeed, according to the substitution effect reported in the literature, *para*-substituted aromatic carbonyl (AC) compounds^{12,37-39} like DMABME as well as DMABA and DMAAP are expected to have the $^3\pi\pi^*$. The $^3\pi\pi^*$ is consistent with the lack of hydrogen abstraction reactivity reported for several *para*-substituted AC compounds bearing DMA as one of the substituent.³⁸

3.2.3 Implication for practical application

The 3T_1 state of closely related AC compound has been reported to be able to sensitize through energy transfer the 3T_1 reaction of pyrimidine bases to produce harmful cyclobutane pyrimidine type of DNA photolesions.⁴⁰⁻⁴² The high efficiency of 3T_1 formation we observed for UV-excited DMABME appears to give an explanation to some trail photochemical studies⁴³⁻⁴⁵ which show potential danger in DNA damage when this type of compounds are being employed in sunscreen lotions.

3.3 References

1. Grabowski, Z. R.; Rotkiewicz, K.; Rettig, W. *Chem. Rev.* **2003**, *103*, 3899-4031.
2. Rettig, W.; Lutze, S. *Chem. Phys. Lett.* **2001**, *341*, 263-271.
3. (a) Józefowicz, M.; Aleksiejew, M.; Heldt, J. R.; Heldt, J. *J. Mol. Liq.* **2010**, *157*, 61-66. (b) Aleksiejew, M.; Heldt, J.; Heldt, J. R. *J. Lumin.* **2009**, *129*, 208-220.
4. Rettig, W. *Angew. Chem., Int. Ed. Engl.* **1986**, *25*, 971-988.
5. Pigliucci, A.; Vauthey, E.; Rettig, W. *Chem. Phys. Lett.* **2009**, *469*, 115-120.
6. Zachariasse, K. A.; Druzhinin, S. I.; Mayer, P.; Kovalenko, S. A.; Senyushkina, T. *Chem. Phys. Lett.* **2009**, *484*, 28-32.
7. Fisz, J. J.; van Hoek, A. *Chem. Phys.* **1997**, *270*, 432-442.
8. Onidas, D.; Markovitsi, D.; Marguet, S.; Sharonov, A.; Gustavsson, T. *J. Phys. Chem. B* **2002**, *106*, 11367-11374.
9. Grégoire, G.; Dimicoli, I.; Mons, M.; Dedonder-Lardeux, C.; Jouvét, C.; Martrenchard, S.; Solgadi, D. *J. Phys. Chem. A* **1998**, *102*, 7896-7902.
10. Zachariasse, K. A.; Druzhinin, S. I.; Kovalenko, S. A.; Senyushkina, T. *J. Chem. Phys.* **2009**, *131*, 224313.
11. Pereira, M. A.; Share, P. E.; Sarisky, M. J.; Hochstrasser, R. M. *J. Chem. Phys.* **1991**, *94*, 2513-2522.

12. Turro, N. J. *Modern Molecular Photochemistry*; University Science Book, Mill Valley, CA, **1991**.
13. Rettig, W.; Bliss, B.; Dirnberger, K. *Chem. Phys. Lett.* **1999**, *305*, 8-14.
14. Zhang, C. H.; Chen, Z. B.; Jiang, Y. B. *Spectrochim. Acta. A.* **2004**, *60*, 2729-2732.
15. Allen, N. S.; Edge, M.; Sethi, S.; Catalina, F.; Corrales, T.; Green, A. *J. Photochem. Photobiol. A* **2000**, *137*, 169-176.
16. Lippert, E.; Rettig, W.; Bonacic-Koutechy, V.; Heisel, F.; Mice, J. A. *Adv. Chem. Phys.* **1987**, *68*, 1-173.
17. (a) Hrnjez, B. J.; Yazdi, P. T.; Fox, M. A.; Johnston, K. P. *J. Am. Chem. Soc.* **1989**, *111*, 1915-1916. (b) Sun, Y. P.; Fox, M. A.; Johnston, K. P. *J. Am. Chem. Soc.* **1992**, *114*, 1187-1192.
18. Changenet, P.; Plaza, P.; Martin, M. M.; Meyer, Y. H. *J. Phys. Chem. A* **1997**, *101*, 8186-8194.
19. Kwok, W. M.; George, M. W.; Grills, D. C.; Ma, C.; Matousek, P.; Parker, A. W.; Phillips, D.; Toner, W. T.; Towrie, M. *Angew. Chem., Int. Ed.* **2003**, *42*, 1826-1830.
20. Dahl, K.; Biswas, R.; Ito, N.; Maroncelli, M. *J. Phys. Chem. B* **2005**, *109*, 1563-1585.
21. Minezawa, N.; Kato, S. *J. Phys. Chem. A* **2005**, *109*, 5445-5453.

22. (a) Fonseca, T.; Kim, H. J.; Hynes, J. T. *J. Mol. Liq.* **1994**, *60*, 161-200. (b) Fonseca, T.; Kim, H. J.; Hynes, J. T. *J. Photochem. Photobiol., A* **1994**, *82*, 67-79.
23. Kim, H. J.; Hynes, J. T. *J. Photochem. Photobiol., A* **1997**, *105*, 337-343.
24. Horng, M. L.; Gardecki, J. A.; Papazyan, A.; Maroncelli, M. *J. Phys. Chem.* **1995**, *99*, 17311-17337.
25. Rotkiewicz, K.; Grellmann, K. H.; Grabowski, Z. R. *Chem. Phys. Lett.* **1973**, *19*, 315-318.
26. Lippert, E.; Luder, W.; Boos, H. in *Advances in Molecular Spectroscopy*; European Conference on Molecular Spectroscopy, Bologna 1959, ed. A. Mangini, Pergamon Press, Oxford, **1962**.
27. Gómez, I.; Reguero, M.; Boggio-Pasqua, M.; Robb, M. A. *J. Am. Chem. Soc.* **2005**, *127*, 7119-7129.
28. (a) Kwok, W. M.; Ma, C.; Matousek, P.; Parker, A. W.; Phillips, D.; Toner, W. T.; Towrie, M.; Umapathy, S. *J. Phys. Chem. A* **2001**, *105*, 984-990. (b) Kwok, W. M.; Ma, C.; Matousek, P.; Parker, A. W.; Phillips, D.; Toner, W. T.; Towie, M. *Chem. Phys. Lett.* **2000**, *322*, 395-400.
29. Okamoto, H. *J. Phys. Chem. A* **2000**, *104*, 4182-4187.
30. Chudoba, C.; Kummrow, K.; Dreyer, J.; Stenger, J.; Nibbering, E. T. J.; Elsaesser, T.; Zachariasse, K. A. *Chem. Phys. Lett.* **1999**, *309*, 357-363.

31. (a) Köhn, A.; Hättig, C. *J. Am. Chem. Soc.* **2004**, *126*, 7399-7410. (b) Jamorski, C. J.; Casida, M. E. *J. Phys. Chem. B* **2004**, *108*, 7132-7141. (c) Dreyer, J.; Kummrow, A. *J. Am. Chem. Soc.* **2000**, *122*, 2577-2585.
32. (a) Zachariasse, K. A.; Druzhinin, S. I.; Bosch, W.; Machinek, R. *J. Am. Chem. Soc.* **2004**, *126*, 1705-1715. (b) Techert, S.; Zachariasse, K. A. *J. Am. Chem. Soc.* **2004**, *126*, 5593-5600. (c) Druzhinin, S. I.; Dubbaka, S. R.; Knochel, P.; Kovalenko, S. A.; Mayer, P.; Senyushkina, T.; Zachariasse, K. A. *J. Phys. Chem. A* **2008**, *112*, 2749-2761.
33. Amatatsu, Y. *J. Phys. Chem. A* **2005**, *109*, 7225-7235.
34. Druzhinin, S. I.; Demeter, A.; Galievsky, V. A.; Yoshihara, T.; Zachariasse, K. A. *J. Phys. Chem. A* **2003**, *107*, 8075-8085.
35. Chattopadhyay, N.; Rommens, J.; Van der Auweraer, M.; De Schryver, F. C. *Chem. Phys. Lett.* **1997**, *264*, 265-272.
36. Fujiwara, W.; Lee, J. K.; Zgierski, M. Z.; Lim, E. C. *Chem. Phys. Lett.* **2009**, *481*, 78-82.
37. (a) Ma, C.; Kwok, W. M.; Chan, W. S.; Zuo, P.; Kan, J. T. W.; Toy, P. H.; Phillips, D. L. *J. Am. Chem. Soc.* **2005**, *127*, 1463-1472. (b) Ma, C.; Kwok, W. M.; Chan, W. S.; Du, Y.; Kan, J. T. W.; Toy, P. H.; Phillips, D. L. *J. Am. Chem. Soc.* **2006**, *128*, 2558-2570.
38. (a) Singh, A. K.; Palit, D. K.; Mukherjee, T. *J. Phys. Chem. A* **2002**, *106*, 6084-6093. (b) Palit, D. K. *Res. Chem. Intermed.* **2005**, *31*, 205-225. (c) Singh, A. K.; Bhasikuttan, A. C.; Palit, D. K.; Mittal, J. P. *J. Phys. Chem. A*

- 2000**, *104*, 7002-7009. (d) Singh, A. K.; Ramakrishna, G.; Ghosh, N.; Palit, D. K. *J. Phys. Chem. A* **2004**, *108*, 2583-2597.
39. Yabumoto, S.; Shigeto, S.; Lee, Y. P.; Hamaguchi, H. *Angew. Chem., Int. Ed.* **2010**, *49*, 9201-9205.
40. (a) Cadet, J.; Vigny, P. *The Photochemistry of Nucleic Acids*; ed. H. Morrison, Wiley, New York, **1990**. (b) Moysan, A.; Viari, A.; Vigney, P.; Voituriez, L.; Cadet, J.; Moustacchi, E.; Sage, E. *Biochemistry* **1991**, *30*, 7080-7088.
41. Lamola, A. A.; Yamane, T. *Proc. Natl. Acad. Sci. U. S. A.* **1967**, *58*, 443-446.
42. Gut, I. G.; Wood, P. D.; Redmond, R. W. *J. Am. Chem. Soc.* **1996**, *118*, 2366-2373.
43. Roscher, N. M.; Lindemann, M. K. O.; Kong, S. B.; Cho, C. G.; Jiang, P. *J. Photochem. Photobiol., A* **1994**, *80*, 417-421.
44. Vanquerp, V.; Rodriguez, C.; Coiffard, C.; Coiffard, L. J. M.; De Roeck-Holtzhauer, Y. *J. Chromatogr. A* **1999**, *832*, 273-277.
45. Gasparro, F. P.; Mitchnick, M.; Nash, J. F. *Photochem. Photobiol.* **1998**, *68*, 243-256.

Chapter 4 Ultrafast Broadband Time-Resolved

Spectroscopic Study on Solvent Hydrogen Bonding Effect in Excited State Dynamics of Methyl-4-dimethylaminobenzoate

4.1 Results

4.1.1 Steady state absorption and fluorescence spectroscopy

Figure 4.1 compares steady state absorption and fluorescence spectra recorded for methyl-4-dimethylaminobenzoate (DMABME) in methanol and acetonitrile. It can be seen from the figure that, apart from a subtle red-shift (by <2 nm) in the wavelength maximum (λ_{\max}) and small increase in the molar absorptivity (ϵ), the absorption spectrum in methanol is very similar to that in acetonitrile. According to this and the result obtained in acetonitrile (Chapter 3), the intense ~270-320 nm absorption band featuring λ_{\max} at ~310 nm and $\epsilon_{\max} \approx 2.6 \times 10^4 \text{ M}^{-1} \text{ cm}^{-1}$ can be attributed to originate from combined contribution of two close lying $\pi\pi^*$ state, the L_a and L_b in the Platt's nomenclature¹ with the former at energy lower than the latter.²

As for the steady state fluorescence, like that in acetonitrile, the spectrum in methanol also shows dual emission, the “blue” and “red” emission with λ_{\max} at ~350 and 530 nm respectively. With reference to the result in the previous chapter, the two emission band can be assigned to arise from the ¹LE and ¹ICT state respectively.²⁻⁶ Note that, despite the nearly identical emission λ_{\max} for the ¹LE emission (~350 nm), a clear bathochromic shift (by ~30 nm) is observed for

the ^1ICT fluorescence in methanol (~ 530 nm) compared to that in acetonitrile (~ 500 nm). Moreover, the intensity ratio of ^1LE to ^1ICT state emission ($I_{\text{LE}}/I_{\text{ICT}}$) varies dramatically from being 0.08 in acetonitrile to 0.21 in methanol. Measurement of fluorescence quantum yield (Φ_f) observed that the Φ_f decreases from being $\sim 2.6 \times 10^{-2}$ in acetonitrile to $\sim 1.7 \times 10^{-3}$ in methanol.

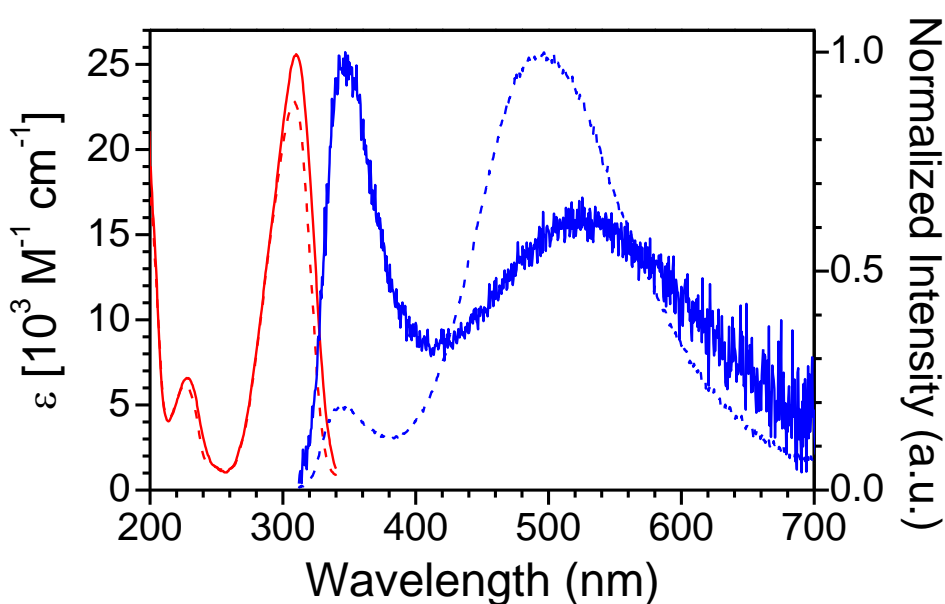


Figure 4.1 Steady state UV-visible absorption (red) and normalized 280 nm excited fluorescence (blue) spectra recorded for DMABME in methanol (solid line) and acetonitrile (dotted line).

The spectral parameters obtained from the absorption and fluorescence spectra are listed in Table 4.1. With the absorption being similar in the two solvents, the large difference in the fluorescence spectra implies that excited state

dynamics, especially those related to the ¹ICT state, varies significantly upon changing solvent from aprotic acetonitrile to protic methanol.

Besides, the spectroscopic data of ethyl-4-dimethylaminobenzoate (DMABEE) were also summarized in Table 4.1. It can be noted from the Table that not only the steady state absorption but also the steady state fluorescence data shows resemble spectral properties to DMABME in both acetonitrile and methanol. First, the steady state absorption displays a subtle red-shift in the λ_{max} , accompanied by a small increase in the ϵ_{max} in methanol ($2.5 \times 10^4 \text{ M}^{-1} \text{ cm}^{-1}$) compared to that in acetonitrile ($2.3 \times 10^4 \text{ M}^{-1} \text{ cm}^{-1}$). Besides, dual emission properties with nearly identical ¹LE state emission λ_{max} can be seen in the steady state fluorescence, despite a pronounced bathochromic shift of the ¹ICT state λ_{max} from ~500 nm in acetonitrile to ~540 nm in methanol. Moreover, a decrease in Φ_f is observed in acetonitrile (2.8×10^{-2}) compared to that in methanol (1.8×10^{-3}). Based on this, it can be stated that the steady state properties is little affected upon alkoxy carbonyl substitution of the molecule.

Table 4.1 Photophysical parameters obtained for DMABME and DMABEE in acetonitrile and methanol. ^a Ref. 7. ^b Ref. 9. ^c Ref. 29.

		ϵ_{max}	λ_{abs}	λ_f^{LE}	λ_f^{ICT}	τ_{LE}	τ_{ICT}	τ_{T}	Φ_f
		/M ⁻¹ cm ⁻¹	/nm	/nm	/nm	/ps	/ps	/μs	
DMABME	CH ₃ OH	~25600	~310	~350	~530	~0.9	~120		1.7×10^{-3}
	CH ₃ OD					~1	~170		
	CD ₃ OD					~1	~170		

	CH ₃ CN	~22800	~308	~350	~500	~0.8	~1900	~4	2.6×10 ⁻²
									^a 2.9×10 ⁻²
DMABEE	CH ₃ OH	~25000	~310	~350	~540	~1.1	~130		1.8×10 ⁻³
	CH ₃ CN	~23200	~307	~350	~500	~1.1	~1600		2.8×10 ⁻²
						^b 0.92			^a 1.7×10 ⁻²
									^c 2.3×10 ⁻²

4.1.2 Femtosecond time-resolved fluorescence in methanol

To determine the dynamics of ICT reaction as well as the decay time of the ¹ICT state, fs-TRF experiment was performed and the spectra obtained are depicted in Figure 4.2. Regarding the large difference in the transient signal intensity between the ¹LE and ¹ICT state emission, temporal evolution of TRF in time delay of 0-5 ps (Figure 4.2(a)) and 5-500 ps (Figure 4.2(b)) is shown separately in the figure. It can be seen that, prompt after the photo-excitation, the system features an intense fluorescence peaking at ~350 nm. The ~350 nm fluorescence decays rapidly and evolves by 5 ps into a much weaker and red-shifted emission centred at ~480 nm (Figure 4.2(b)). On the basis of the spectral profile and the wavelength locations of the two emission bands, it is plausible to assign the ~350 nm and ~480 nm fluorescence to originate from the ¹LE and ¹ICT state, respectively.^{6,7} It is noteworthy that the ¹LE state emission depletes concurrently with the growth of ¹ICT state emission. Such a temporal spectral variation is accompanied by an isoemissive point at ~520 nm (inset in Figure 4.2(a)), indicating a precursor-successor relationship between the two emitting states.

It is clear from Figure 4.2(b) that, after the full formation of ^1ICT state emission, the ^1ICT state emission decay along with a clear dynamic Stokes' shift (DSS) to longer wavelength, e.g. the λ_{max} shifts from ~ 480 nm at 5 ps to ~ 540 nm at 30 ps. In addition, unlike in acetonitrile where it decays in thousand ps timescale, the ^1ICT state emission in methanol decays much faster, vanishes by ~ 500 ps after the excitation.

The DSS of ^1ICT state emission can be described quantitatively by plotting the λ_{max} of transient ^1ICT state fluorescence as a function of delay time after the photo-excitation. The λ_{max} of transient fluorescence at varied delay time was obtained by using two log-normal functions to respectively simulate the ^1LE and ^1ICT state emission. The result obtained for the ^1ICT state emission is displayed in the inset of Figure 4.2(b). The corresponding data for the ^1LE state shows insignificant change in the emission λ_{max} with respect to the delay time. It indicates that the ^1LE state fluorescence is little affected by the solvent micro-environment along the relaxation cascade after photo-excitation. In contrast, kinetic analysis observed that the DSS of ^1ICT state emission can be described by two time constants, ~ 1.2 and ~ 13 ps, which are well correlated with the solvent orientation times reported for methanol.⁸

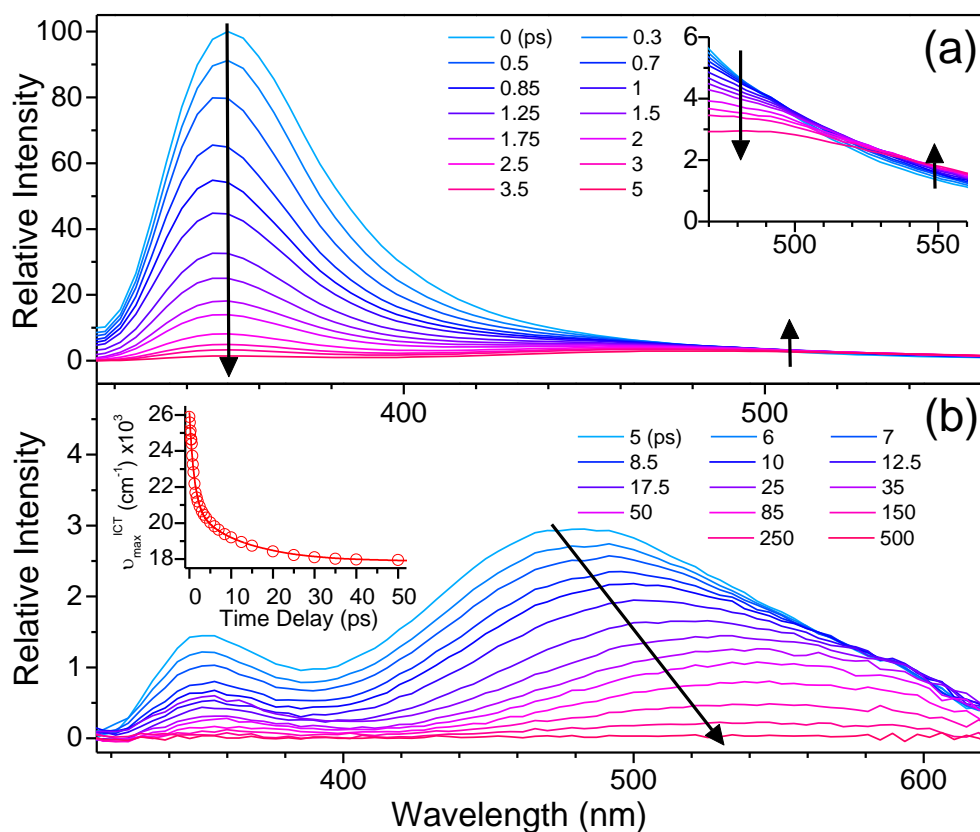


Figure 4.2 Temporal evolution of broadband time-resolved fluorescence spectra of DMABME recorded at 0-5 ps (a) and 5-500 ps (b) in methanol after 280 nm excitation. The inset in (a) shows magnified spectra revealing an isosbestic point at ~480 nm; The inset in (b) shows dynamic shift of ¹ICT emission maximum as a function of time. ν_{\max}^{ICT} corresponds to $\lambda_{\max}^{\text{ICT}}$ in unit of wavenumber. The arrows represent direction of temporal evolution of the spectra.

Dynamics of the ICT reaction and subsequent decay of the ¹ICT state were derived by following kinetic time profiles of TRF at representative wavelengths ~360 and 560 nm. The TRF time profiles at ~360 nm and 560 nm corresponding respectively to the dynamics of ¹LE and ¹ICT state were shown in

Figure 4.3(a). Global analysis of the TRF time profiles produced a common ~ 0.9 ps time constant to describe the rapid decay of the ^1LE state and the fast growth and ^1ICT state emission, indicating a precursor-successor relationship between the two excited states and a time constant of ~ 0.9 ps for the ICT reaction. The ensuing decay of ^1ICT state was found to feature a time constant of ~ 120 ps. The ~ 0.9 ps ICT time revealed for DMABME here is close to the ~ 1.1 ps ICT time obtained for DMABEE in the same solvent, suggesting a minute effect of alkoxy carbonyl group on the ICT reaction (Table 4.1). It is noticeable that, compared to that in acetonitrile (~ 1.9 ns, Chapter 3), the lifetime of ^1ICT state in methanol (~ 120 ps) is much shorter, shortening by ~ 16 times in the magnitude. This coincides with the decrease in fluorescence quantum yield when changing solvent from acetonitrile ($\Phi_f = 2.6 \times 10^{-2}$) to methanol ($\Phi_f = 1.7 \times 10^{-3}$) (Table 4.1), indicating the presence of additional nonradiative decay process in methanol which is not occurring in acetonitrile.

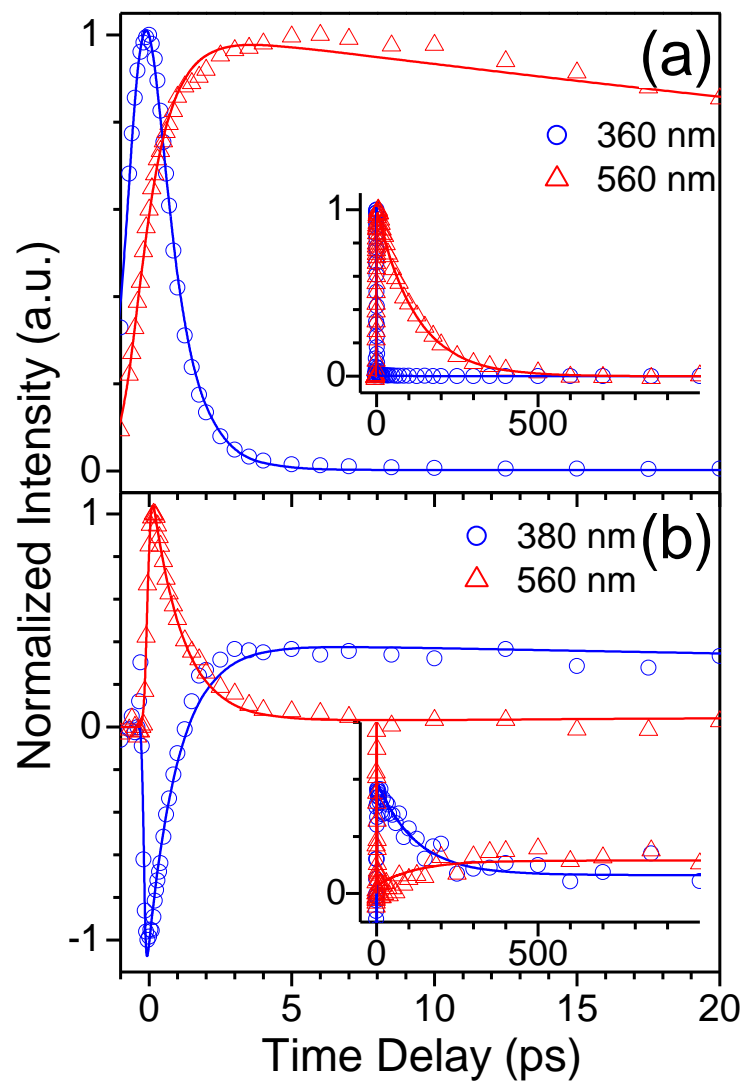


Figure 4.3 Experimental (\circ , Δ) and fitted (—) time profiles of TRF (a) and TA (b) at indicated wavelengths for 280 nm excited DMABME in methanol. The insets show the decay profiles at longer timescale up to ~ 1 ns.

4.1.3 Femtosecond time-resolved fluorescence anisotropy in methanol

To investigate further the influence of solvent on the electronic nature and dynamics of excited states, fs-TRFA measurement was performed at 0.5, 5

and 50 ps after the photo-excitation, and the spectra obtained are displayed in Figure 4.4. Like that in acetonitrile (Figure 3.4 in Chapter 3), the fs-TRFA in methanol at each of the examined time displays anisotropy (r) value which is nearly independence of the emission wavelength from ~330 nm to 550 nm. This testifies a common electronic origin of the ^1LE and ^1ICT states.⁶ Given the inherent L_a character of the ^1ICT state, it is straightforward that the ^1LE state is also of the L_a in electronic parentage. The value of r at 0.5 ps is ~0.3, lower than the theoretical value (0.4). This, as the case in acetonitrile, can be attributed to arise due to minute involvement of the L_b in the excitation process and the rapid internal conversion (IC) from L_b to L_a because of the energy proximity of the two states.^{3-5,9-13}

It can be seen from Figure 4.4 that, the r value drops from being ~0.3 at 0.5 ps to ~0.25 at 5 ps and then to ~0.05 at 50 ps. Such a loss of r value is indicative of depolarization process which can be ascribed to originate due to the rotational diffusion of the excited molecules. In support of this, it is noted that the timescale of depolarization we observed here is close to those reported in the same solvent for molecules of comparable size.^{14,15}

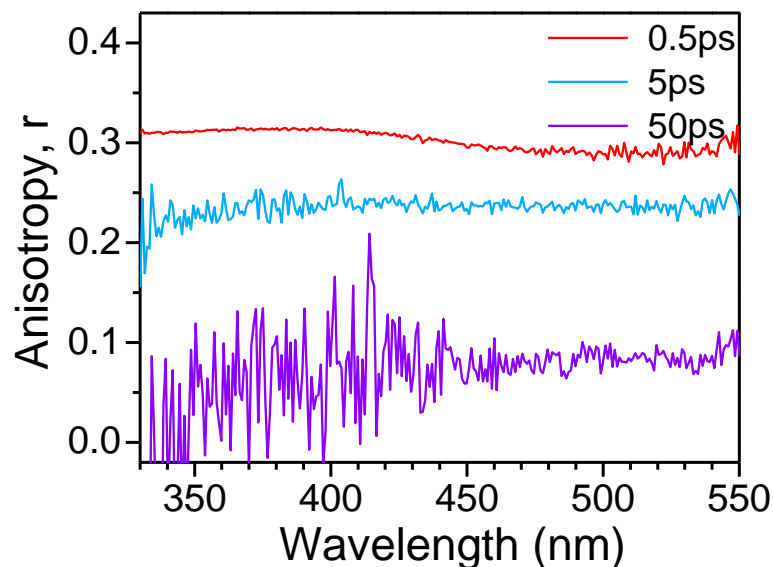


Figure 4.4 Femtosecond broadband time-resolved fluorescence anisotropy spectra of DMABME recorded in methanol at 0.5, 5, 50 ps after 280 nm excitation.

4.1.4 Femtosecond time-resolved fluorescence in deuterated methanol

To provide evidence for detailed nature of solvent effect in causing the different dynamics in methanol from acetonitrile, parallel TRF experiments were performed with the sample in solvent of deuterated methanols, CH_3OD and CD_3OD . The results obtained in the two deuterated methanol are depicted in Figure 4.5. It is clear from the figure that both the TRF spectral and the temporal evolution of TRF spectra are very similar in the two deuterated solvents, and the spectra are also close to those observed in normal methanol (CH_3OH , Figure 4.2). These observations imply that (i) the excited state dynamics is nearly identical in

the two deuterated solvents and (ii) the states involved in the deuterated solvents are the same (i.e. the ^1LE and ^1ICT state) as those in the normal CH_3OH .

Like the one in normal methanol (CH_3OH), prompt after the excitation, the system in the two deuterated solvents features an intense ~ 350 nm fluorescence. It decays rapidly accompanying by the formation of the ^1ICT state (Figure 4.5). The ^1ICT state emission decays with the emission λ_{max} shifts to longer wavelength with respect to time delay and vanishes at ~ 700 ps after the excitation. The extent of the ^1ICT state emission λ_{max} shift is similar to that in CH_3OH (Figure 4.2(b)), from ~ 480 nm at 5 ps to ~ 540 nm at 30 ps (insets in Figure 4.5). Kinetic analysis of the DSS of ^1ICT state emission in the two solvents can also be described by two time constants, ~ 1 ps and ~ 13 ps, which correlate well with that in CH_3OH .

In CH_3OD and CD_3OD , kinetic analysis of TRF time profiles at ~ 360 nm (for the decay of ^1LE state) and ~ 560 nm (for the growth and ensuing decay of the ^1ICT state) observed a time constant of ~ 1 ps for the ICT reaction and a decay time of ~ 170 ps for the ^1ICT state in both the solvents (Table 4.1). It is notable that the ICT time in CH_3OD and CD_3OD (insets in Figure 4.6) is nearly identical to that in CH_3OH (Figure 4.3(a)); but the decay time in the former solvent is substantially slower than that in the latter solvent (~ 120 ps). The TRF kinetic decay profiles obtained in the deuterated solvents and their comparison with the result in normal methanol are displayed in Figure 4.6.

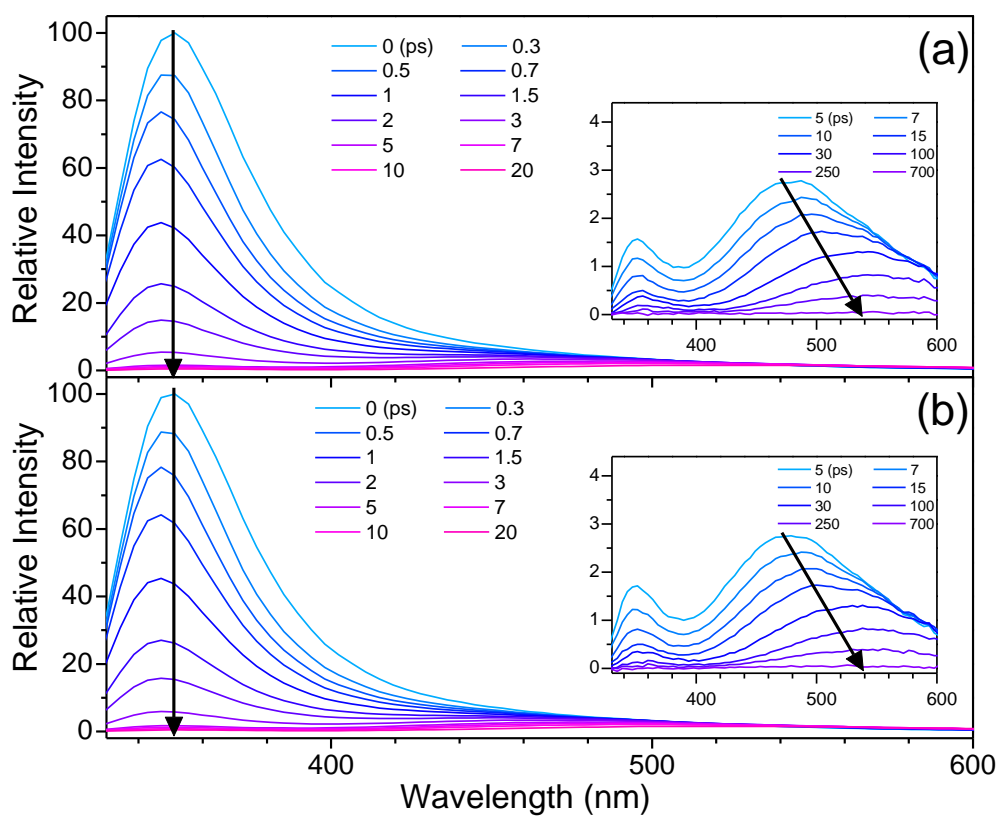


Figure 4.5 Femtosecond broadband time-resolved fluorescence spectra of DMABME recorded at 0-20 ps in CH₃OD (a) and CD₃OD (b) after 280 nm excitation. The insets show temporal evolution of TRF spectra at longer time delay from 5 ps to 700 ps after the photo-excitation. The arrows indicate direction of temporal evolution of the TRF spectra.

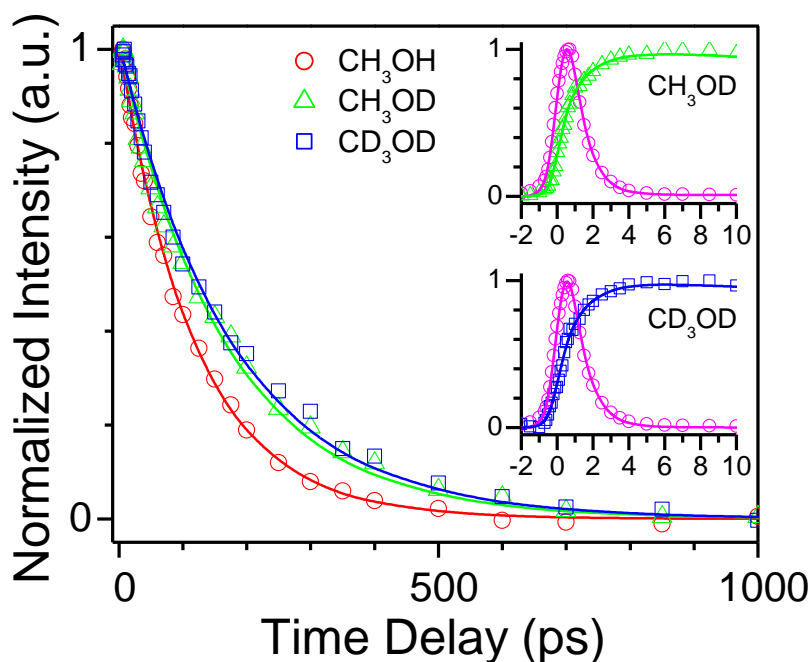


Figure 4.6 Comparison of normalized experimental (\circ , Δ , \square) and fitted (—) TRF time profile at ~ 560 nm of 280 nm excited DMABME in CH₃OH (red), CH₃OD (green) and CD₃OD (blue). The insets show the decay profiles at ~ 360 nm (\circ) and ~ 560 nm (Δ , \square) in CH₃OD and CD₃OD at the early delay times.

4.1.5 Femtosecond transient absorption spectroscopy

Figure 4.7 displays fs-TA spectra recorded with 280 nm excitation of DMABME in methanol. The result provides complementary information on the ICT reaction and the subsequent decay pathway of the ¹ICT state. It can be seen that, promptly after the excitation, the transient absorption (the 0 ps) spectrum feature a sharp positive absorption at ~ 330 nm and a negative signal at ~ 365 nm along with a broad positive absorption band across ~ 430 to 700 nm. This initial TA spectrum evolves rapidly into an alternative profile (e.g. 20 ps spectrum in

Figure 4.7(a) which shows also the ~ 330 nm absorption but with a new positive absorption band centred at ~ 460 nm. The spectral evolution produces an isosbestic point at ~ 490 nm (Figure 4.7(a)). It is noted that the initial (~ 0 ps) and relatively late (~ 20 ps) TA spectrum resembles closely the TA of ^1LE and ^1ICT state in acetonitrile (Figure 3.5(a) in Chapter 3). The spectra can therefore be assigned to the ^1LE and ^1ICT state respectively. With reference to the result of TRF (Figure 4.2) and the steady state fluorescence (Figure 4.1), the negative signal at ~ 365 nm in the early TA spectra can be ascribed to originate due to the simulated emission from the ^1LE state.

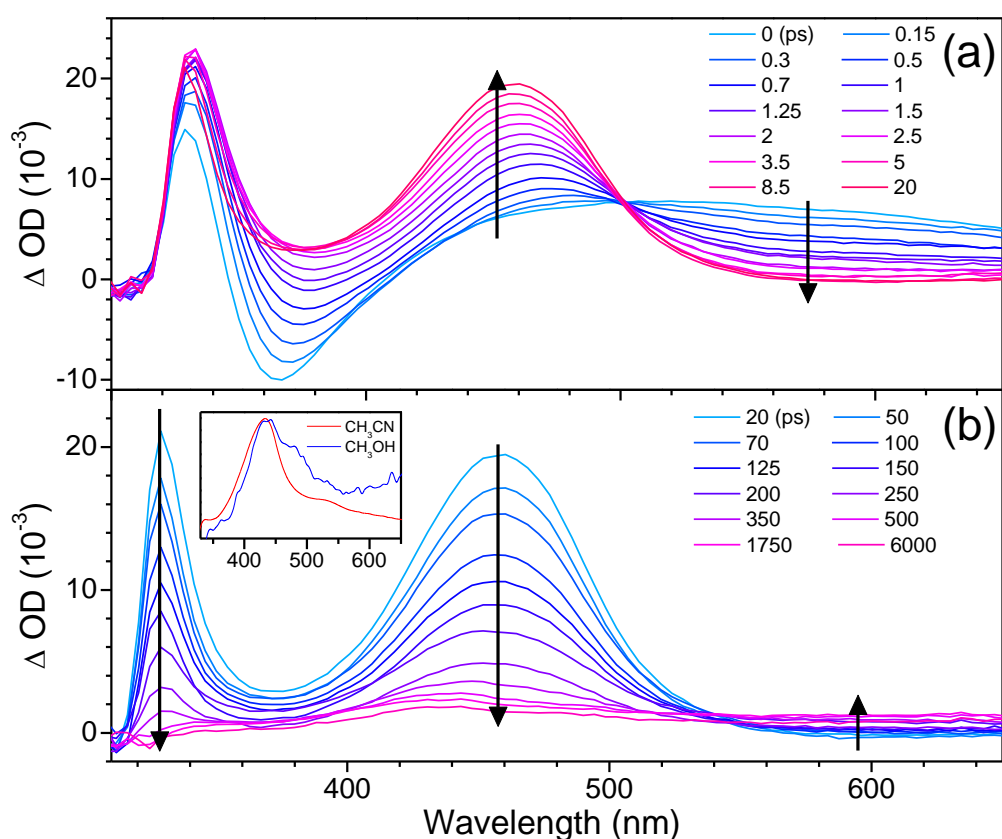


Figure 4.7 Femtosecond broadband transient absorption spectra of DMABME in methanol recorded at 0-20 ps (a) and 20-6000 ps (b) after

excitation at 280 nm. The inset in (b) compares TA spectra recorded at 6 ns after excitation in acetonitrile (red) and methanol (blue). The arrows indicate temporal evolutions of the spectra.

Figure 4.3(b) shows kinetic time profiles obtained from the TA spectra at ~380 nm and 560 nm to monitor respectively the rise of ^1ICT and decay of ^1LE state due to the ICT reaction. Global analysis of the TA time profiles gives a time constant of ~0.9 ps, coincide with the ICT time obtained from the TRF data (Figures 4.2 and 4.3(a)). This indicates that both the TA and TRF measurements are monitoring the same excited state process, *i.e.* the ICT reaction.

After its formation, the ^1ICT state decays in hundreds ps timescale into a very weak spectrum which features broad positive absorption over wavelength from ~340 nm to 630 nm and with the λ_{max} at ~430 nm (Figure 4.7(b)). This spectral change takes place with an isosbestic point at ~540 nm, indicating a precursor-successor relationship between the ^1ICT state and the λ_{max} ~430 nm related species. The λ_{max} ~430 nm TA was attributed to the $\pi\pi^*$ triplet ($^3\pi\pi^*$) state for the spectrum appears similar in profile to the TA spectrum of $^3\pi\pi^*$ state in acetonitrile (inset in Figure 4.7).⁶ Dynamic fitting of the late time decay of ^1ICT and the growth of $^3\text{T}_1$ state produced a time constant of ~120 ps (inset in Figure 4.3(b)), consistent well with the decay time of ^1ICT state determined in the fs-TRF (inset in Figure 4.3(a)).

4.2 Discussion

Making comparison of the corresponding steady state and time-resolved spectra and kinetic decays of time-resolved spectra in methanol (Figures 4.1 to 4.3 and 4.7) and in acetonitrile (Figures 3.2, 3.3 and 3.5) reveals important similarities and differences. The major similarities involve that: (i) apart from a subtle red-shift (by no more than 2 nm) in the spectral wavelength, the steady state absorption and the fluorescence (of both steady state and time-resolved spectra) of ^1LE state is respectively very close in methanol as that in acetonitrile (Figure 4.1); (ii) the ICT time constant is nearly identical; being ~ 0.9 ps in both the solvents (Table 4.1); (iii) like that in acetonitrile, the fluorescence from ^1LE and ^1ICT state in methanol share the same anisotropy (Figures 4.4 and 3.4), implying a common electronic parentage (of $\pi\pi^* L_a$ nature) for the two states in the latter solvent; and (iv) upon the decay of ^1ICT state, long-lived species featuring similar TA spectra (with $\lambda_{\text{max}} = \sim 430$ nm) attributable to $^3\pi\pi^*$ state is observed both in methanol and acetonitrile (inset in Figure 4.7). The above similarities show clearly that the same set of excited states, i.e., the $\pi\pi^* L_a$ natured ^1LE and ^1ICT state and the $^3\pi\pi^*$ state are involved in the excited state processes in acetonitrile and in methanol.

The differences in the two solvents include mainly the energy and the decay dynamics related to the ^1ICT state: (i) the ^1ICT steady state fluorescence red-shifts from $\lambda_{\text{max}} = \sim 500$ nm in acetonitrile to ~ 530 nm in methanol; (ii) unlike in acetonitrile where the TRF show no DSS (Figure 3.2), the TRF in methanol (Figure 4.2) displays pronounced DSS from ~ 480 nm at 5 ps to ~ 540 nm at 30 ps after the photo-excitation; (iii) the lifetime of ^1ICT state is remarkably shorter in

methanol (~120 ps) than in acetonitrile (~1.9 ns). The shorter lifetime provides direct evidence for presence of an additional non-radiative path to compete effectively with the ISC for the ^1ICT state deactivation in methanol compared to in acetonitrile. This correlates well with the smaller involvement of triplet state in methanol (Figure 4.7(b)) than in acetonitrile (Figure 3.5(b)). It also explains the smaller Φ_f and reduced I_{LE}/I_{ICT} of steady state fluorescence in methanol than in acetonitrile. Clearly, changing solvent from aprotic acetonitrile to protic methanol varies significantly the decay path and the excited state dynamics of DMABME.

4.2.1 Solvent effect on the dynamics of ICT reaction

The ~0.9 ps time constant of ICT reaction is much faster than the solvation time of CH_3OH (5 ps).¹⁶ This indicates that, like that in acetonitrile, the ICT reaction in methanol is also an inner-sphere event not controlled by solvent. This is substantiated further by the large DSS displayed by the TRF in methanol. Of note, the observed DSS time constants ($\tau_1 = \sim 1.2$ ps; $\tau_2 = \sim 13$ ps) coincide with the $\tau_1 = 1.4$ ps and $\tau_2 = 13$ ps solvation time corresponding respectively to the rotational diffusion of the free CH_3OH molecule and the rotation of hydroxyl group around the C-O bond in CH_3OH .⁸ This provides direct evidence for formation from a less solvated nascent ^1ICT state to a fully solvated state, denoted as $^1\text{HICT}$ state which bears enhanced hydrogen bonding (H-bonding) with surrounding solvent molecules.^{17,18}

Being respectively the electron donor and electron acceptor, the DMA nitrogen and benzoate carbonyl (C=O) oxygen are expected to form H-bonding

with protic solvent molecule in the ground state (S_0).⁵ Upon photo-excitation and formation of ^1ICT state, the electron density decreases in the donor (D) site while it increases in the acceptor (A) site,^{19,20} making the former more positively charged and the latter more negatively charged; this is manifested by a significant increase in the molecular dipole moment, from ~ 4.0 D in S_0 to ~ 6.2 D in ^1LE and ~ 12.4 D in ^1ICT state.⁴ As a result, the H-bonding at the D and the A site tends to become respectively weakened and strengthened in the ^1ICT state compared to in the S_0 .^{5,19,20} It is conceivable that after solvation, the H-bonding between $^1\text{HICT}$ state and the CH_3OH solvent molecules may primarily occur through the carbonyl oxygen at the benzoate carbonyl group.^{18,21-24}

The further fluorescence red-shift of solvated ^1ICT state in methanol compared to in acetonitrile indicates a more energy stabilization of this state in the former than in the latter solvent. Given that the dielectric constants of methanol (32.66) and acetonitrile (35.94) are similar,²⁵ it is reasonable that the extra stabilization of solvated ^1ICT state is brought about by the solute-solvent H-bonding occurring only in protic solvent methanol. In addition to this, the shorter lifetime of solvated ^1ICT state in methanol (i.e., the $^1\text{HICT}$ state) indicates that the H-bonding is also a key factor for the involvement of an extra non-radiative channel of the charge transfer state in methanol.

4.2.2 H-bonding effect on the decay dynamics of charge transfer state

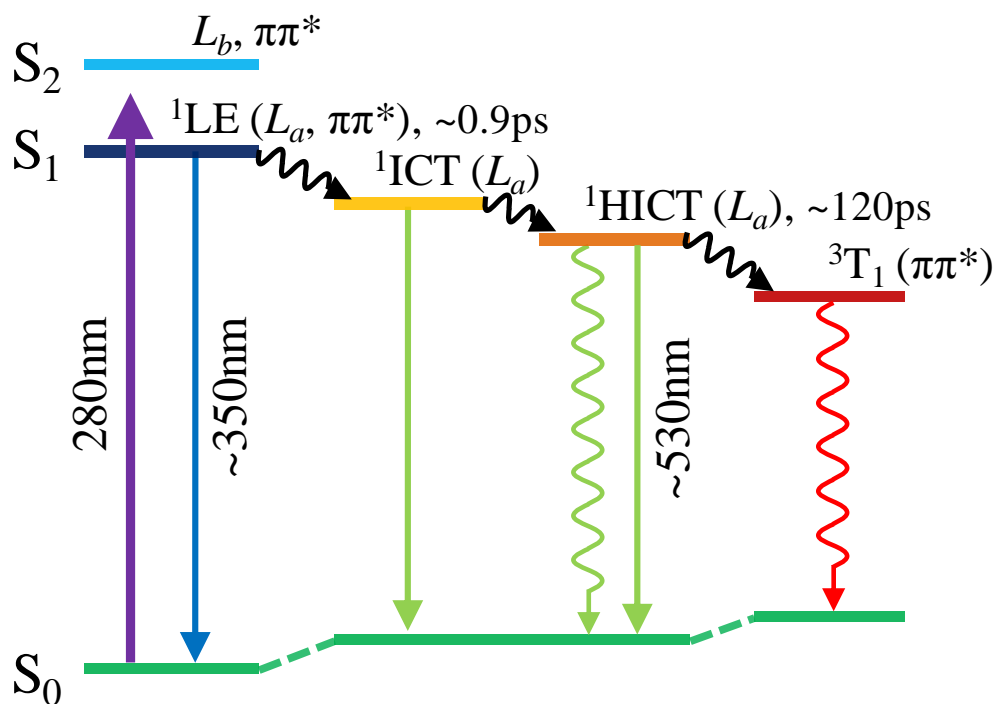
The extra nonradiative process in methanol can be attributed to IC of the $^1\text{HICT}$ state to the S_0 promoted by the H-bonding interaction of the $^1\text{HICT}$ state with solvent molecules.²⁶ This is reminiscent of the solvent H-bonding effect

reported for DMABN in methanol and other protic solvent, like butanol.^{17,18,27} Facilitated by the high vibrational frequency of the solvent hydroxyl (-OH) stretching vibration, the solute-solvent H-bonding occurring through the hydroxyl group may provide an effective accepting mode for transferring the excitation energy from ¹HICT state into the vibrational energy (i.e. heat energy) of the interacted solvent molecules which is then dissipated by vibration of other surrounding solvent molecules.¹⁸

The above assignment is supported strongly by the kinetic isotope effect observed for the decay time of ¹HICT state in normal methanol (CH₃OH) *versus* in deuterated methanol (CH₃OD and CD₃OD) (Figure 4.6). The decay time is ~120 ps in CH₃OH and it is ~170 ps in CH₃OD and CD₃OD. The fact that the decay time is identical in CH₃OD and CD₃OD indicates that the methyl (-CH₃) group of methanol has negligible contribution to the excited state relaxation process; the kinetic isotope effect is therefore originated mainly due to the hydroxyl hydrogen, the hydrogen that participates the H-bonding with carbonyl oxygen in the ¹HICT state. It is known that, upon deuteration, the vibration frequency of hydroxyl stretching decreases from ~3350 cm⁻¹ (for O-H stretching) to ~2500 cm⁻¹ (for O-D stretching);²⁸ this implies a reduced ability of CH₃OD (CD₃OD as well) than CH₃OH in promoting the nonradiative IC, leading to a longer lifetime of the ¹HICT state in the deuterated than normal methanol.

4.2.3 Overall deactivation pathway for photo-excited DMABME in methanol

Taking together the steady state and time-resolved data as well as the above analysis on the similarities and differences between the excited state dynamics in methanol and in acetonitrile, the following deactivation cascade (in Scheme 4.1) can be established for DMABME in methanol.



Scheme 4.1 Proposed deactivation pathways for photo-excited DMABME in methanol.

After the 280 nm excitation, the molecule is promoted to the $L_a \pi\pi^*$ 1LE state. This state then undergoes a rapid ICT with a ~ 0.9 ps time constant to give

the $L_a \pi\pi^*$ ^1ICT state. The rapid ICT time constant implies a minute energy barrier for the ICT reaction; the nearly identical time constant of ICT reaction in methanol and in acetonitrile implies that the reaction itself is little affected by the H-bonding property of solvent. In response to the significant increase in the molecular dipole moment, the ^1ICT state upon rapid formation is subject to large scale of solvent re-orientation on timescale corresponding to the dynamic solvation time of methanol. This leads to formation of the $^1\text{HICT}$ state which bears H-bonding with solvent molecules most likely at the carbonyl oxygen of DMABME. Through vibration of the solvent molecules, the solute-solvent H-bonding introduces the nonradiative IC to compete with ISC for deactivation of the charge transfer state. This accounts for the much smaller fluorescence quantum yield and the much faster charge transfer state decay in methanol than in acetonitrile.^{7,18,29,30}

4.2.4 Implication of solvent H-bonding effect on the practical application of DMABME type of molecules

The potential damaging effect of DMABME type of molecules in application like sunscreen ingredient is related mostly to the high yield of $^3\text{T}_1$ state which, through triplet-triplet energy transfer, may sensitize formation of DNA photolesion.^{31,32} In this regard, the involvement of an additional IC channel in protic solvent to compete with the ISC may reduce significantly the $^3\text{T}_1$ state population. Indeed, this is manifested by the much smaller $^3\text{T}_1$ state transient signal in methanol (the ~6 ns spectrum in Figure 4.7) than that in acetonitrile (the ~6 ns spectrum in Figure 3.5(b)).⁶ On the basis of this, it can be inferred that the

DMABME type of molecule may bear much alleviated potential for DNA photo-damage when being used as an ingredient in water-based sunscreen lotion.³³⁻³⁶

4.3 References

1. Platt, J. R. *Chem. Phys.* **1949**, *17*, 484-495.
2. (a) Józefowicz, M. *Chem. Phys.* **2011**, *383*, 19-26. (b) Józefowicz, M.; Aleksiejew, A.; Abramov, A. V.; Ling, S.; Gutowski, M.; Heldt, J.; Heldt, J. *R. J. Fluoresc.* **2011**, *21*, 1749-1762.
3. Józefowicz, M.; Aleksiejew, M.; Heldt, J. R.; Heldt, J. *J. Mol. Liq.* **2010**, *157*, 61-66.
4. Aleksiejew, M.; Heldt, J.; Heldt, J. R. *J. Lumin.* **2009**, *129*, 208-220.
5. Grabowski, Z. R.; Rotkiewicz, K.; Rettig, W. *Chem. Rev.* **2003**, *103*, 3899-4031.
6. Chan, C. T. L.; Cheng, C. C. W.; Ho, K. Y. F.; Kwok, W. M. *Phys. Chem. Chem. Phys.* **2011**, *13*, 16306-16313.
7. Zhang, C. H.; Chen, Z. B.; Jiang, Y. B. *Spectrochim. Acta Part A* **2004**, *60*, 2729-2732.
8. Lakowicz, J. R. *Principles of Fluorescence Spectroscopy*, 3rd Ed. Springer, **2006**.
9. Pigliucci, A.; Vauthey, E.; Rettig, W. *Chem. Phys. Lett.* **2009**, *469*, 115-120.
10. Rettig, W. *Angew. Chem., Int. Ed. Engl.* **1986**, *25*, 971-988.
11. Zachariasse, K. A.; Druzhinin, S. I.; Mayer, P.; Kovalenko, S. A.; Senyushkina, T. *Chem. Phys. Lett.* **2009**, *484*, 28-32.

12. Grégoire, G.; Dimicoli, I.; Mons, M.; Dedonder-Lardeux, C.; Jouvet, C.; Martrenchard, S.; Solgadi, D. *J. Phys. Chem. A* **1998**, *102*, 7896-7902.
13. Zachariasse, K. A.; Druzhinin, S. I.; Kovalenko, S. A.; Senyushkina, T. *J. Chem. Phys.* **2009**, *131*, 224313.
14. Pereira, M. A.; Share, P. E.; Sarisky, M. J.; Hochstrasser, R. M. *J. Chem. Phys.* **1991**, *94*, 2513-2522.
15. Gustavsson, T.; Cassara, L.; Marguet, S.; Gurzadyan, G.; van der Meulen, P.; Pommeret, S.; Mialocq, J.-C. *Photochem. Photobiol. Sci.* **2003**, *2*, 329-341.
16. Kwok, W. M.; George, M. W.; Grills, D. C.; Ma, C.; Matousek, P.; Parker, A. W.; Phillips, D.; Toner, W. T.; Towrie, M. *Angew. Chem., Int. Ed.* **2003**, *42*, 1826-1830.
17. Horng, M. L.; Gardecki, J. A.; Papazyan, A.; Maroncelli, M. *J. Phys. Chem.* **1995**, *99*, 17311-17337.
18. Han, K. L.; Zhao, G. J. *Hydrogen Bonding and Transfer in the Excited State*; Hoboken, NJ, Wiley: USA, **2010**.
19. Krauß, O.; Brutschy, B. *Chem. Phys. Lett.* **2001**, *350*, 427-433.
20. Zakharov, M.; Krauss, O.; Nosenko, Y.; Brutschy, B.; Dreuw, A. *J. Am. Chem. Soc.* **2009**, *131*, 461-469.
21. Mitambo, M. M.; Loppnow, G. R. *Chem. Phys. Lett.* **1996**, *261*, 691-697.

22. (a) Longarte, A.; Fernández, J. A.; Unamuno, I.; Castaño, F. *J. Chem. Phys.* **2000**, *112*, 3170-3180. (b) Fernández, J. A.; Longarte, A.; Unamuno, I.; Castaño, F. *J. Chem. Phys.* **2000**, *113*, 5804-5811.
23. Kim, Y. H.; Cho, D. W.; Yoon, M. *J. Phys. Chem.* **1996**, *100*, 15670-15676.
24. Kim, Y.; Cheon, H. W.; Yoon, M.; Song, N. W.; Kim, D. *Chem. Phys. Lett.* **1997**, *264*, 673-679.
25. Montalti, M.; Credi, A.; Prodi, L.; Gandolfi, M. T. *Handbook of Photochemistry*; 3rd ed., Boca Raton: CRC/Taylor & Francis, **2006**.
26. Zhao, G. J.; Han, K. L. *J. Comput. Chem.* **2008**, *29*, 2010-2017.
27. Kwok, W. M.; George, M. W.; Grills, D. C.; Ma, C.; Matousek, P.; Parker, A. W.; Phillips, D.; Toner, W. T.; Towrie, M. *Photochem. Photobiol. Sci.* **2007**, *6*, 987-994.
28. Bertie, J. E.; Zhang, S. L. *J. Mol. Struct.* **1997**, *413*, 333-363.
29. Rettig, W.; Lutze, S. *Chem. Phys. Lett.* **2001**, *341*, 263-271.
30. Allen, N. S.; Edge, M.; Sethi, S.; Catalina, F.; Corrales, T.; Green, A. *J. Photochem. Photobiol., A*, **2000**, *137*, 169-176.
31. Lamola, A. A.; Yamane, T. *Proc. Natl. Acad. Sci. U. S. A.* **1967**, *58*, 443-446.
32. Gut, I. G.; Wood, P. D.; Redmond, R. W. *J. Am. Chem. Soc.* **1996**, *118*, 2366-2373.
33. Roscher, N. M.; Lindemann, M. K. O.; Kong, S. B.; Cho, C. G.; Jiang, P. *J. Photochem. Photobiol., A* **1994**, *80*, 417-421.

34. Gasparro, F. P.; Mitchnick, M.; Nash, J. F. *Photochem. Photobiol.* **1998**, *68*, 243-256.
35. Vanquerp, V.; Rodriguez, C.; Coiffard, C.; Coiffard, L. J. M.; De Roeck-Holtzhauer, Y. *J. Chromatogr. A* **1999**, *832*, 273-277.
36. Krishnan, R.; Nordlund, T. M. *J. Fluoresc.* **2008**, *18*, 203-217.

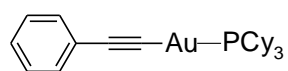
Chapter 5 Ultrafast Broadband Time-Resolved Study on the Excited States of Selected Phenyleneethynylene Gold (I) Complexes: Ligand π -Conjugation Controlled Intersystem Crossing

5.1 Results

5.1.1 Excited state dynamics of monomeric gold(I) PE complex

5.1.1.1 Femtosecond time-resolved fluorescence and transient absorption study

To characterize the excited state dynamics of monomeric gold(I)-phenyleneethynylene (PE) complexes, femtosecond time-resolved fluorescence (fs-TRF) measurement was first performed on [PhC≡CAu(PCy₃)]



(PCy₃ = tricyclohexylphosphine, **1a**; Scheme 1.2) in

acetonitrile (CH₃CN) with 280 nm excitation. In Figure 5.1(a), it can be seen that, instantly after the photo-excitation, an intense fluorescence band peaking at ~304 nm (~0.1 ps) dominates in the detection spectral window. This transient emission decays rapidly and the signal vanishes by ~10 ps after the excitation.

In order to provide complementary information on the excited state dynamics, fs transient absorption (fs-TA) experiment was then performed. The TA spectra obtained from the measurement are depicted in Figure 5.1(b). Immediate after the photo-excitation, the TA at very early time (~0.1 ps) features

two overlapping bands with the absorption maximum (λ_{max}) at ~360 nm and 415 nm, respectively. Within time interval of ~10 ps, this initial TA evolves into an alternative profile, which contains a minor absorption at ~350 nm and a major sharp absorption with the λ_{max} at ~430 nm. This temporal evolution of the TA is accompanied by two isosbestic points at ~390 and 470 nm. The ~430 nm late time spectrum then keeps constant in intensity from ~10 ps to ~6000 ps after the photo-excitation (Figure 5.1(b) inset).

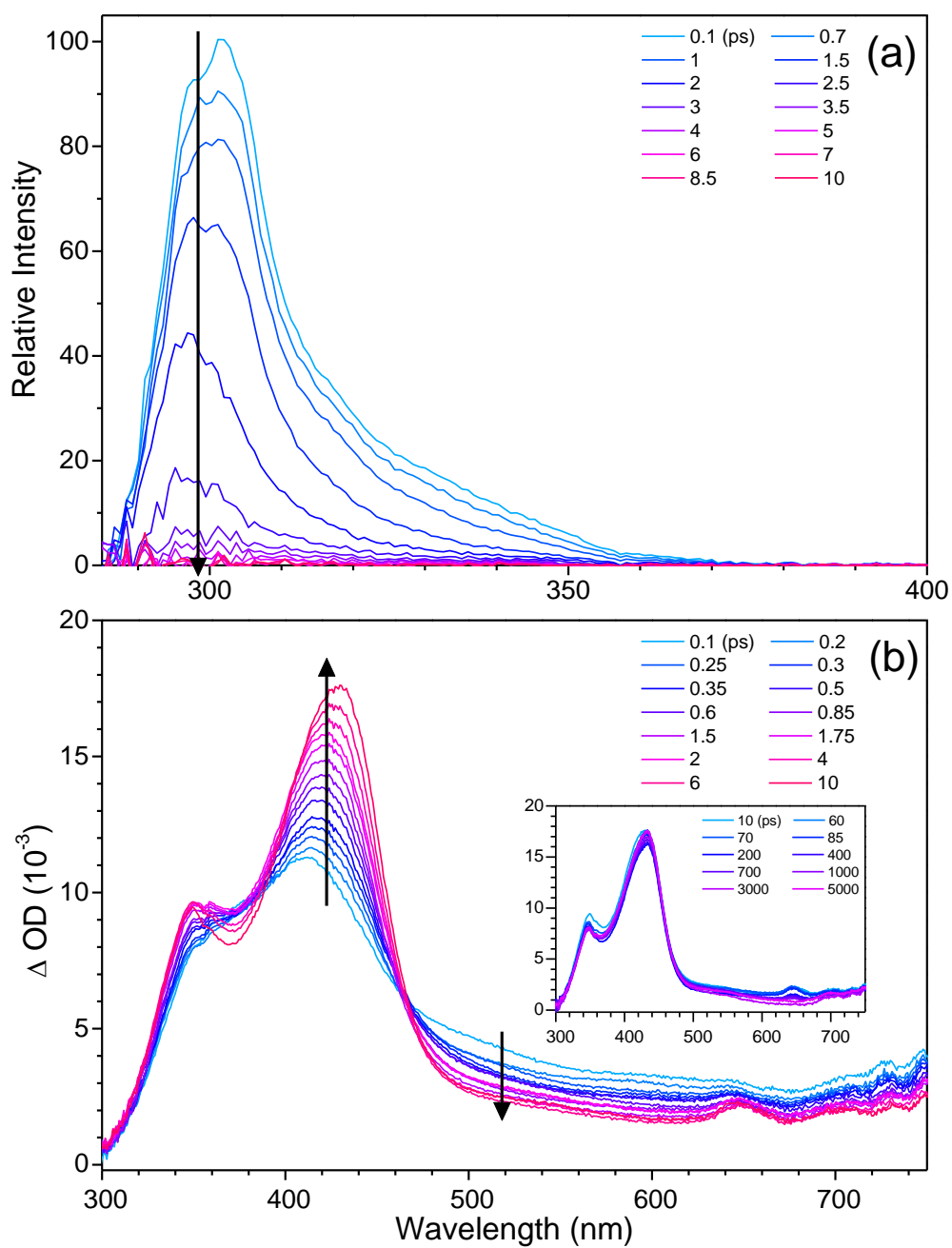
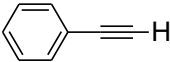


Figure 5.1 Broadband time-resolve fluorescence (a) and transient absorption (b) spectra of **1a** in acetonitrile recorded at indicated time delays after excitation at 280 nm. The inset shows the spectra recorded at late times after the excitation. The arrows indicate temporal evolutions of the spectra.

Figure 5.2 displays experimental and fitted temporal decay profiles of TRF and TA obtained at selected wavelengths of the TRF and TA spectra. Kinetic analysis of these decay profiles reveals a common time constant of ~0.8 ps for both the TRF and TA, suggesting that the two measurements are probing the same process of the excited state evolution. In other words, the spectral evolutions observed from the two types of time-resolved measurements are originated from the same process, which accounts for the complete quenching of the ~304 nm transient fluorescence signal in the TRF (Figure 5.1(a)) and the formation of the ensuing long-lived species featuring the ~430 nm absorption in TA (Figure 5.1(b)). On the basis of this, the initially observed ~304 nm transient fluorescence and the ~415 nm TA can be attributed to the photo-prepared ligand centred (LC) S_1 $^1\pi\pi^*$ state (Figure 5.1). This assignment is supported further by the immediate formation of these spectra after the photo-excitation, the narrow Stokes' shift of the ~304 nm TRF from the ~280 nm absorption due to the $S_0 \rightarrow S_1$ $^1\pi\pi^*$ transition (Figure S7(a)) and the similarity of the ~304 nm TRF to the steady state fluorescence of the free ligand [PhC≡C-H]  (**1b**; Scheme 1.2) (Figure S8(a)).¹ Of note, the ~0.8 ps short lifetime of fluorescence from the S_1 $^1\pi\pi^*$ state of **1a** explains the absence of prompt fluorescence (PF) in the steady state fluorescence (Figure S7(a)).¹

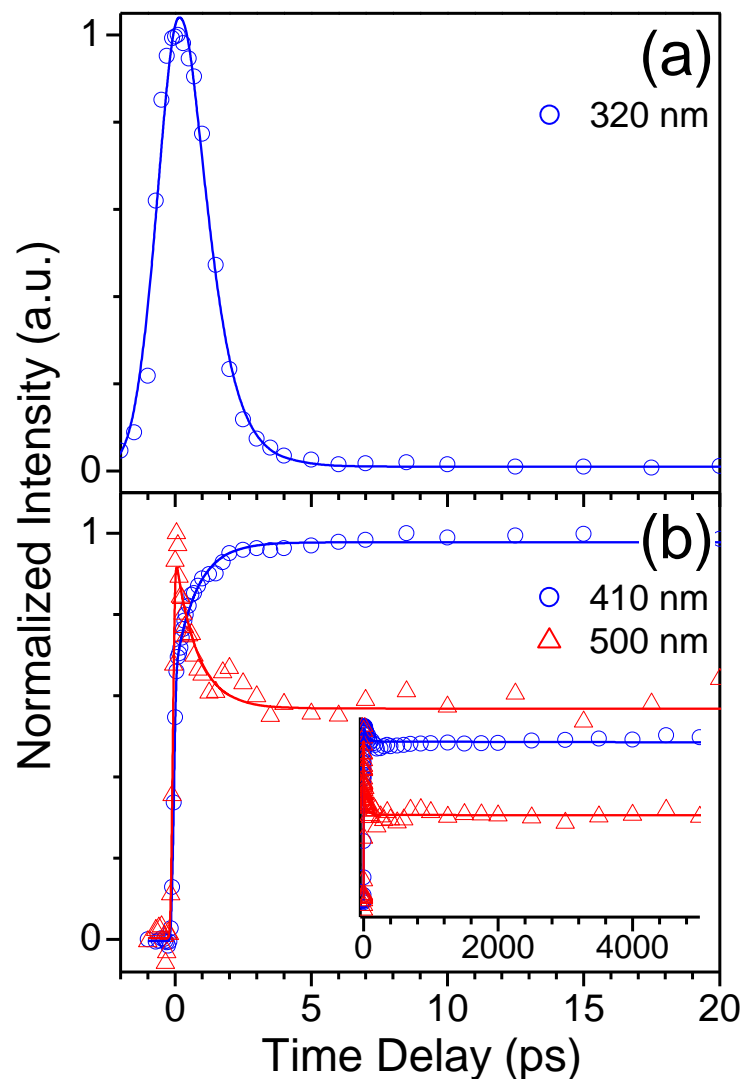


Figure 5.2 Experimental (\circ , Δ) and fitted (—) decay profiles of fs-TRF (a) and fs-TA (b) at indicated wavelengths obtained with 280 nm excitation of **1a** in acetonitrile. The inset shows the decay profiles at longer delay time after the excitation.

The relatively long-lived ~ 430 nm transient species observed at late time in the TA measurement ($> \sim 10$ ps; Figure 5.1(b) inset) can be attributed to the LC $T_1^3 \pi\pi^*$ state. This assignment is made based on (i) the weakly emissive nature of

the corresponding species which is indicated by the lack of the corresponding dynamics component in the fs-TRF, (ii) the slow decay dynamics of this species, and (iii) the similarity of the ~430 nm absorption to the absorption of $^3\pi\pi^*$ state of some closely related phenylacetylene derivatives.² The absence of the emission due to T_1 $^3\pi\pi^*$ state in TRF, (Figure 5.1(a)) is owing to the inherent low radiative rate constant³ (k_r) which is usually $\sim 10^4$ -folded lower than that of the S_1 $^1\pi\pi^*$ state (Table 5.1), making the triplet state virtually invisible in the TRF measurement.⁴

Table 5.1 Spectral parameters of **1a – 3a** and **1b – 3b**.

$\lambda_{\text{abs}}/\text{nm}$ ($10^{-4}\epsilon/\text{M}^{-1}\text{cm}^{-1}$)	λ_{F}^a /nm	λ_{Ph}^b /nm	$\lambda(\text{S}_1)^c$ /nm	$\lambda(\text{T}_1)^c$ /nm	τ_{PF}^d /ps	τ_{DF}^e / μs	τ_{Ph}^f / μs	$10^{-8}k_{\text{r}}^g$ /s ⁻¹	k_{ISC} /s ⁻¹	Φ_{e}^h
1a 280 (2.7)	304	420	415	430	0.8		10	1	1.2×10^{12}	0.08^i
1b 270 (0.03)	296									
2a 338 (7.9)	390	550	690	560	450	25.8	52.3	5.8	1.6×10^8	0.66^i
2b 321 (4.7)	360		650	530	600			3.5		
3a 283 (7.3)	345	470	490	440	38	32.8	63.4	3.6	2.6×10^{10}	0.12^j
3b 281 (3.5)	338		490, 650	430	5200			1.6		

^a Maximum wavelength of fluorescence. ^b Maximum wavelength of phosphorescence emission.

^c Maximum wavelength of excited state absorption. ^d Prompt fluorescence lifetime.

^e Delayed fluorescence lifetime. ^f Phosphorescence lifetime.

^g Radiative rate constant of fluorescence. (estimated based on Strickler-Berg equation¹⁵)

^h Overall emission yield. ⁱ Ref. 7. ^j Ref. 4.

5.1.1.2 Nanosecond time-resolved emission study

By using a much prolonged time ($> \sim 2$ ns) for detection, nanosecond time-resolved emission (ns-TRE) measurement has been conducted to probe the emission and the decay dynamics of the T_1 $^3\pi\pi^*$ state of **1a**. Figure 5.3 displays the TRE spectra obtained for **1a** in deoxygenated CH_3CN at time intervals from 1 μs and afterwards after the photo-excitation. The TRE at wavelengths from ~ 400 to 650 nm and with vibronic features decays completely by ~ 50 μs after the photo-excitation. Noted that the wavelength location and the spectral profile of the TRE spectra match exactly with the steady state emission, indicating the TRE is due to the phosphorescence of **1a**, reinforce the assignment of T_1 $^3\pi\pi^*$ state to the TRE.¹

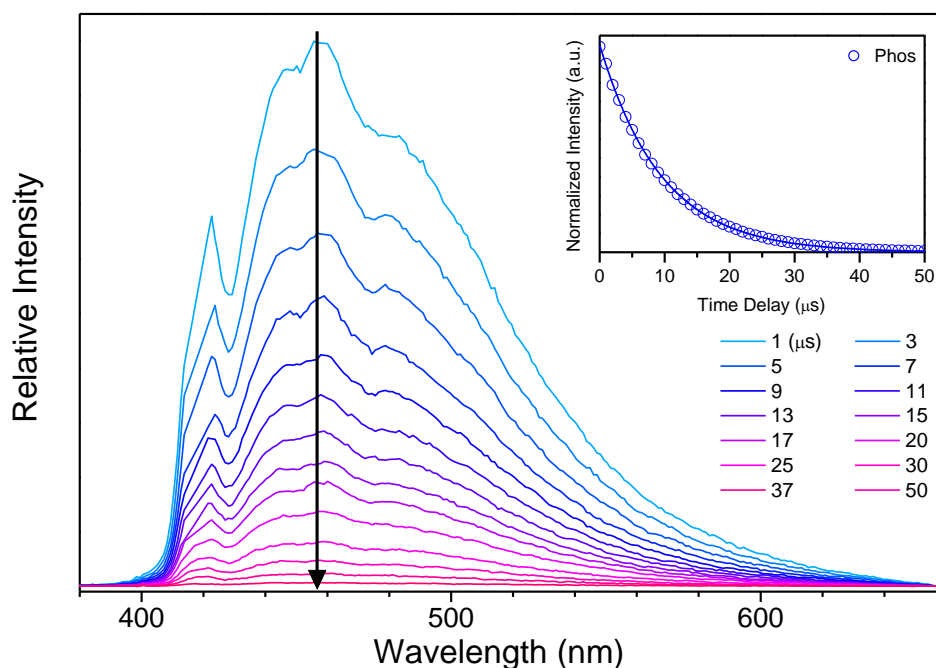
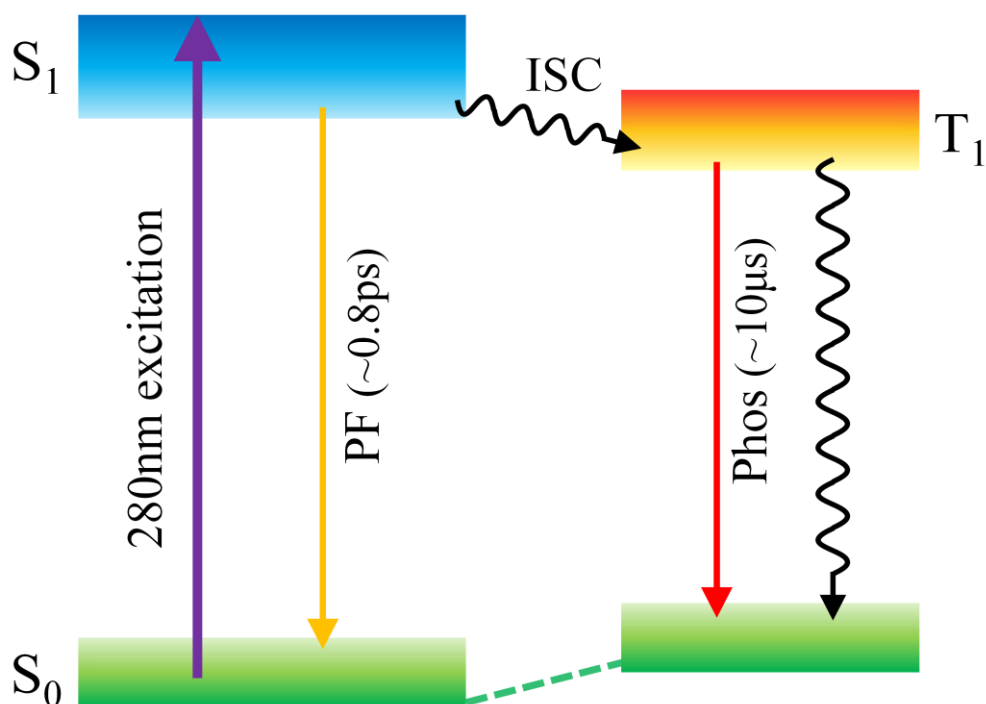


Figure 5.3 ns-TRE spectra recorded after 280 nm excitation of **1a** in deoxygenated acetonitrile recorded at indicated time delays. The inset shows the

experimental (○) and fitted (—) phosphorescence (Phos) kinetic trace obtained for **1a** in deoxygenated acetonitrile. The arrow indicates temporal evolution of the spectra.

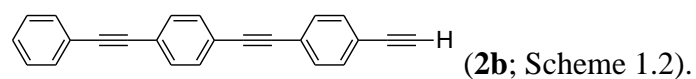
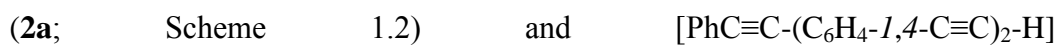
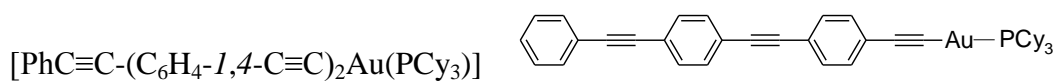
Dynamic fitting of the kinetic decay of TRE intensity (Figure 5.3 inset) observed a lifetime of ~ 10 μs . Taking together the assignment of $S_1^1\pi\pi^*$ state to the initial TRF (Figure 5.1(a)) and ~ 415 nm TA (Figure 5.1(b)) and the $T_1^3\pi\pi^*$ state to the late time ~ 430 nm TA and the ~ 400 to 650 nm TRE, we conclude that the ~ 0.8 ps time constant we observed from the fs-TRF decay and initial fs-TA conversion is originated due to intersystem crossing (ISC) which converts the excited state population from the LC $S_1^1\pi\pi^*$ to $T_1^3\pi\pi^*$ state. In view of a minute involvement of other non-radiative decay in this rapid timescale,⁵ the ultrafast ISC we attributed to the LC $S_1^1\pi\pi^*$ state suggests a nearly unit efficiency of the ISC ($\Phi_{\text{ISC}} = 1$), according to which the rate of ISC (k_{ISC}) can be estimated to be $\sim 1.2 \times 10^{12} \text{ s}^{-1}$ ($k_{\text{ISC}} \approx 1/\tau_{\text{PF}}$, $\tau_{\text{PF}} = \sim 0.8$ ps; Table 5.1). Putting together the time-resolved data (Figures 5.1, 5.2 and 5.3) and the above analysis, a deactivation cascade as showed in Scheme 5.1 is constructed for **1a**.



Scheme 5.1 Dynamics and major deactivation pathways proposed for **1a** in acetonitrile after 280 nm excitation. Radiative and non-radiative transitions are indicated by straight and wavy arrows respectively. (PF = prompt fluorescence; Phos = phosphorescence; ISC = intersystem crossing)

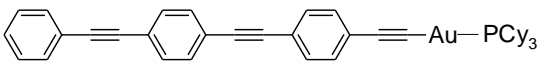
After formation of the photo-prepared S_1 $^1\pi\pi^*$ state, the ISC acts as a major process to quenching the PF and leads to a nearly unitary excited state population transfer from the S_1 $^1\pi\pi^*$ to the T_1 $^3\pi\pi^*$ state. Upon the formation of T_1 $^3\pi\pi^*$ state, the molecule emits phosphorescence over timescale up to tens microseconds. It is worth noting that, the S_1 $^1\pi\pi^*$ to T_1 $^3\pi\pi^*$ state ISC in aromatic hydrocarbons like **1b** (Scheme 1.2) is prohibited according to the El-Sayed's rule,^{3,6} and is thus usually accompanied by a modest k_{ISC} no greater than the order of 10^7 s⁻¹.³ With this as a reference, the value of k_{ISC} in **1a** is enhanced by

~5 order of magnitude. Such a massive enhancement can be correlated to the heavy-atom effect (the gold(I) in the current case), a convention that has been used to account for the very rapid ISC in many transition metal complexes. However, as displayed below, a different situation is encountered in the case of



5.1.2 Excited state dynamics of oligo(*p*-PE) and gold(I) oligo(*p*-PE) complex

5.1.2.1 Femtosecond time-resolved fluorescence and transient absorption study

In parallel to the study on **1a**, fs-TRF and fs-TA measurements have been conducted on **2a**  in CH₃CN. The fs-TRF and fs-TA spectra obtained from these measurements are depicted in Figure 5.4(a) and Figure 5.4(b), respectively. It can be seen from the figure that a single emission band peaking at ~390 nm is observed promptly after the photo-excitation. This initial fluorescence due to the S₁ ¹ππ* state displays a small degree of growth in the emission intensity with accompanying of a subtle decay in the blue edge (~360-520 nm) in the time interval from ~0.3 to 6 ps after the photo-excitation (Figure 5.4(a) inset). The 6 ps TRF spectrum then decays in hundreds ps timescale, achieving a remnant signal with ~3% of the original intensity by ~3000 ps after the excitation (Figure 5.4(a)).

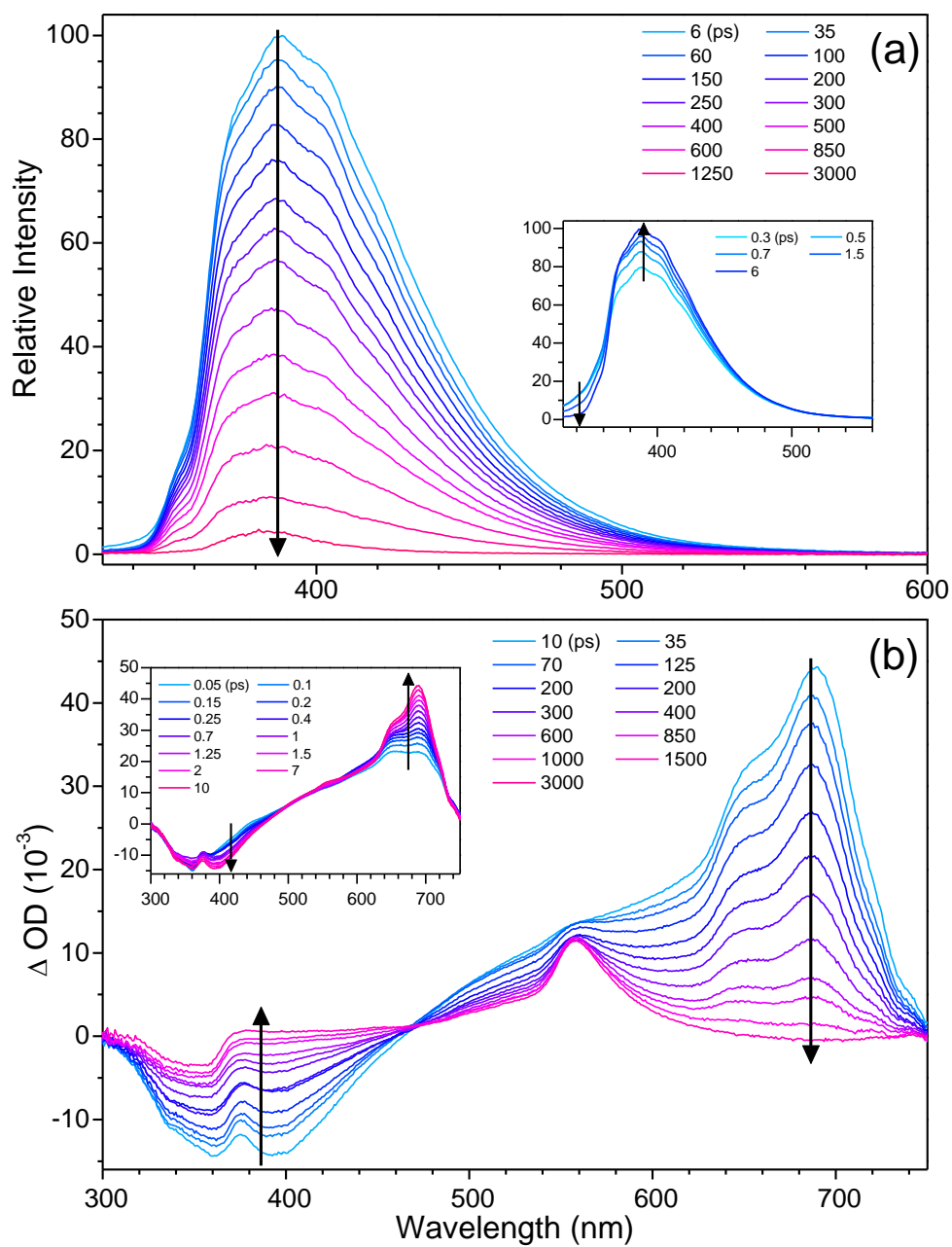


Figure 5.4 Broadband time-resolve fluorescence (a) and transient absorption (b) spectra of **2a** in acetonitrile recorded at indicated time delays after excitation at 280 nm. The insets show the early time delay of the spectra. The arrows indicate temporal evolution of the spectra.

As to the spectra obtained in the fs-TA measurement (Figure 5.4(b)), immediately after the photo-excitation, an initial TA (~ 0.05 ps) is observed which contains a broad positive band across ~ 480 - 740 nm due to the excited state absorption (ESA) and two partially overlapped negative bands with the λ_{max} at ~ 360 nm and ~ 395 nm, respectively. On the basis of that (i) the ~ 360 nm and ~ 395 nm negative band resembles respectively to the ground state (S_0) absorption and the S_1 fluorescence (Figure S7(b)),¹ and (ii) there is correlation between the dynamics of these components with the decay of the TRF and ESA (Figure 5.5), the negative bands at ~ 370 - 460 nm and $< \sim 370$ nm can be respectively assigned with certain to the stimulated emission (SE) from the S_1 $^1\pi\pi^*$ state and the S_0 bleach (GB) arising due to the photo-excitation of the S_0 molecules.

For **2a**, the initial TA spectra (Figure 5.4(b) inset) evolve within time intervals of ~ 10 ps into a profile featuring a sharp band due to ESA at ~ 690 nm, this is accompanied with a subtle rise in the SE signal but with no significant change in the GB. This spectral evolution of the fs-TA takes place at the same timescale as the early-stage spectral evolution displayed by the TRF (Figure 5.4(a) inset). After this early time spectral evolution, a more massive change in the fs-TA is observed to occur in the hundred ps timescale, parallel to the decay of TRF as displayed in Figure 5.4(a). It can be seen from Figure 5.4(b) that, the ~ 690 nm ESA decays together with diminishing of the SE, leading to formation of TA with an alternative profile featuring a relatively weak and long-lasting absorption with the $\lambda_{\text{max}} \sim 560$ nm. Such a spectral evolution, which produces an isosbestic point observed at ~ 485 nm, is accompanied by recovery of the GB by $\sim 72\%$ at ~ 3000 ps after the excitation (Figure 5.4(b)).

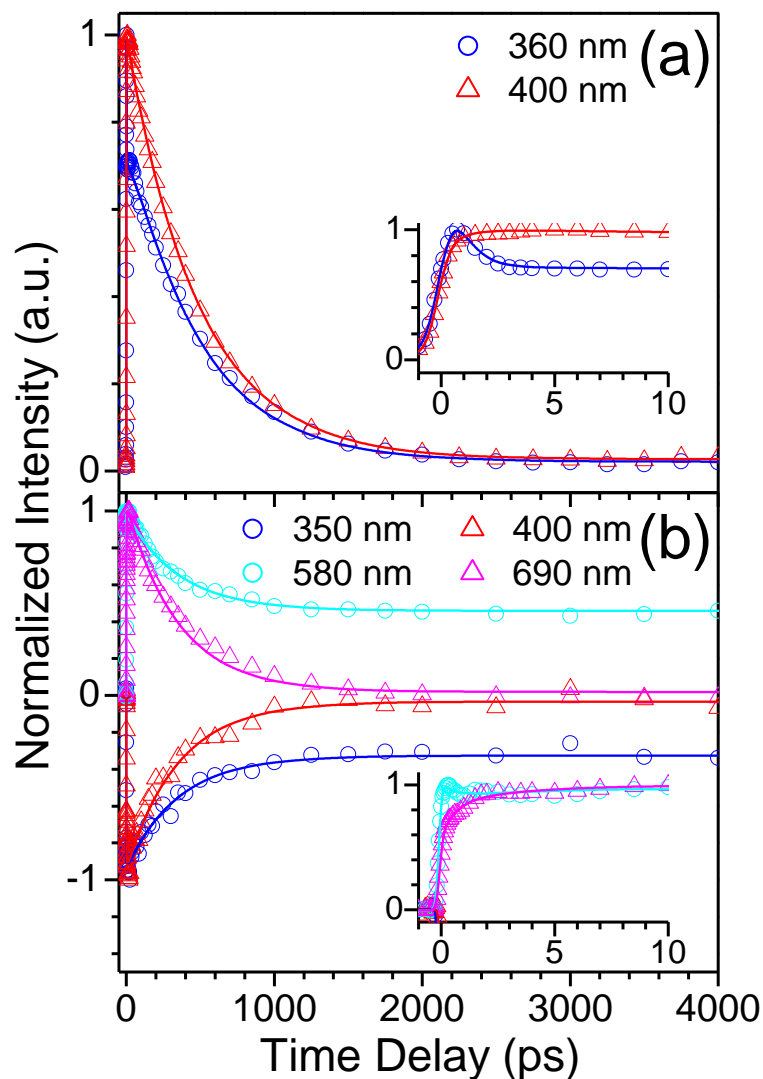


Figure 5.5 Experimental (\circ , Δ) and fitted (—) decay profiles of fs-TRF (a) and TA (b) at indicated wavelengths obtained with 280 nm excitation of **2a** in acetonitrile. The insets show the decay profiles at the early delay times.

Analysis of the kinetics changes of the fs-TRF and fs-TA intensity show that the changes occurring at the early (before ~ 10 ps) and late (after ~ 10 ps) times of the spectral evolution (TRF, Figure 5.5(a) and TA, Figure 5.5(b)) can be described well by time constant of ~ 0.8 ps (τ_1) and ~ 450 ps (τ_2) respectively

(Table 5.1). The mutual correlation in the dynamics between TRF and TA allows to attribute with certain both the ~480-740 nm (~0.05 ps) and ~690 nm (~10 ps) ESA to originate from the brightly emissive $^1\pi\pi^*$ S₁ as revealed in the fs-TRF experiment (Figure 5.4(a)).

According to its long-lived nature and the lack of time-resolved counterpart in the TRF, the ~560 nm TA observed at late time after excitation (at ~3000 ps) is ascribed to come from the T₁ $^3\pi\pi^*$ state of **2a**. As a result, the major spectral changes displayed by both the fs-TRF and fs-TA in the hundreds ps timescale is considered to occur due to the ISC from the $^1\pi\pi^*$ S₁ to $^3\pi\pi^*$ T₁ of **2a**.

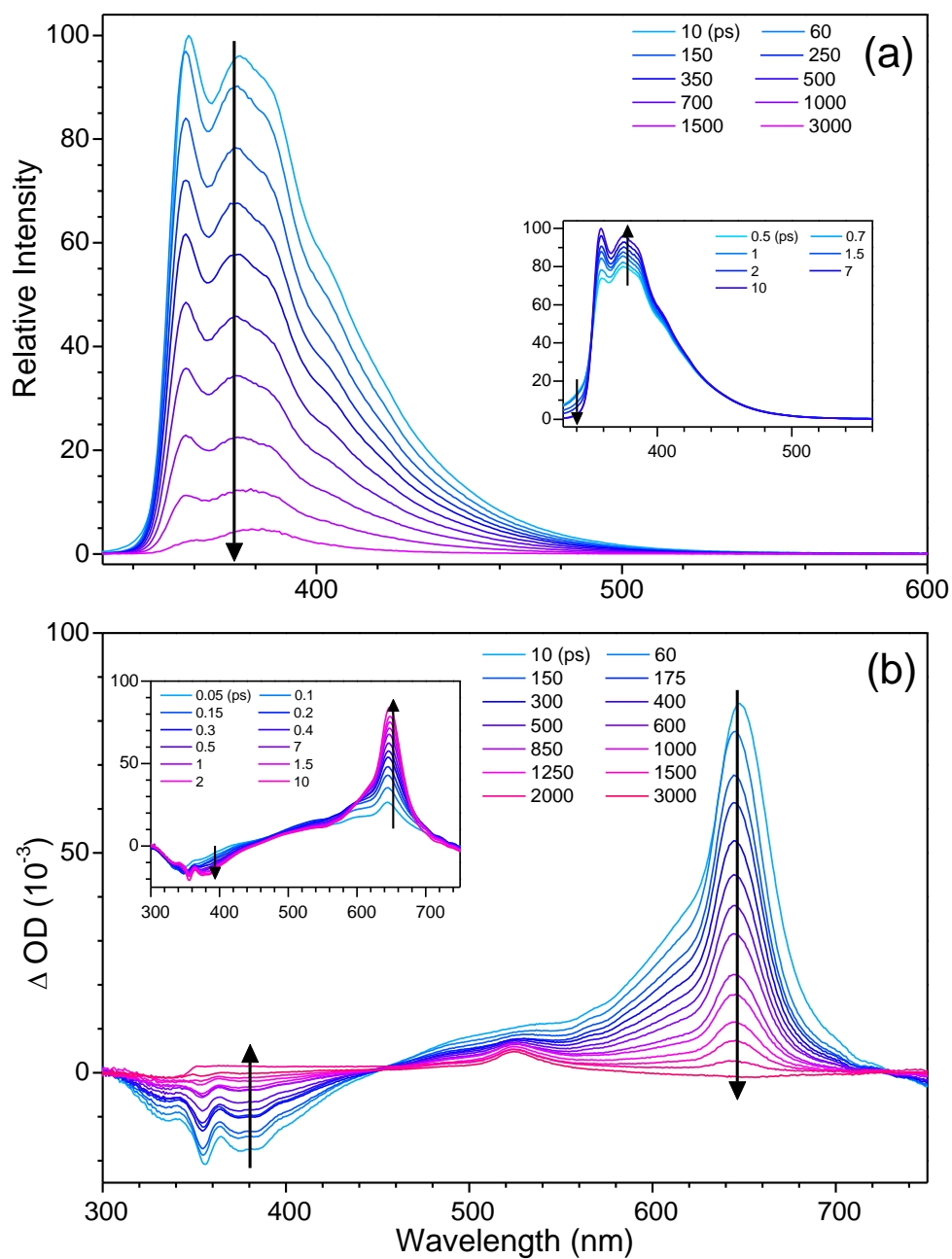
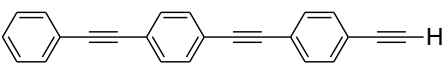


Figure 5.6 Broadband time-resolve fluorescence (a) and transient absorption (b) spectra of **2b** in acetonitrile recorded at indicated time delays after excitation at 280 nm. The insets show the early time delay of the spectra. The arrows indicate temporal evolutions of the spectra.

Figure 5.6 displays the TRF and TA spectra obtained for the corresponding free ligand (**2b**; ) of **2a** in CH₃CN. It is noteworthy that the TA and TRF spectra of **2b**, in terms of the spectral profile and the time-dependent evolution, are nearly identical to the counterpart spectra of **2a**. The similarity in the TRF between the two compounds lends strong support to the assignment of the LC ¹ππ* transition to the fluorescence component of the dual emission (Figure S7(b)) of **2a**.⁷ Besides, based on the similarity in the fs-TA between **2a** and **2b**, it is clear that the involved transient species (e.g. the S₁ ¹ππ* and T₁ ³ππ* states) in the two systems share a common set of oligo(*p*-PE) based electronic transitions (e.g. the S₁ → S_n and T₁ → T_n in the ESA and the S₀ → S₁ in SE), which is barely affected by the presence of the extra Au(PCy)₃⁺ moiety in **2a** relative to **2b**.

Analysis of the kinetic changes of the fs-TRF and fs-TA shows that the spectral and temporal evolutions of the transient spectra of **2b** can also be fitted by a bi-exponential function with time constants of τ₁ = ~0.9 ps and τ₂ of ~600 ps (Figure 5.7; Table 5.1).

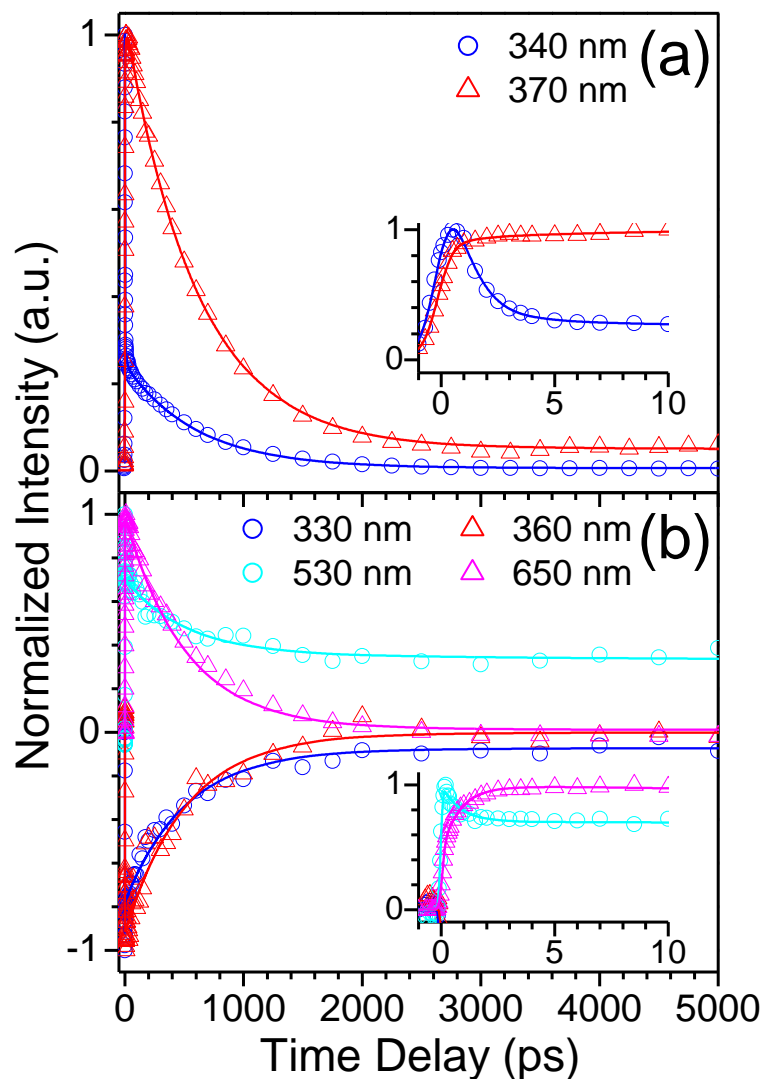


Figure 5.7 Experimental (\circ , Δ) and fitted (—) decay profiles of fs-TRF (a) and TA (b) at the indicated wavelengths obtained with 280 nm excitation of **2b** in acetonitrile. The insets show the decay profiles at early delay times.

5.1.2.2 Nanosecond time-resolved emission study

Ns-TRE experiments were performed on **2a** in deoxygenated CH_3CN solution to assess the origin and the precise composition of the dual emission

observed in the steady state measurement (Figure S7(b)).⁷ The ns-TRE measurements were done with varied detection time windows so as to enable the transient emission spectra to be measured over a large time span covering up to hundreds μs after the photo-excitation (Figure 5.8). The time ranges that are probed in the ns-TRE are referred to the third stage of the excited state decay for the system under investigation.

From Figure 5.8, it can be seen clearly two emission components, a high energy emission at $\lambda_{\text{max}} \sim 400$ nm and a low energy emission at $\lambda_{\text{max}} \sim 545$ nm, which according to their wavelength locations and their emission profiles can be attributed to the delayed fluorescence (DF) from the S_1 $^1\pi\pi^*$ state and the phosphorescence from the T_1 $^3\pi\pi^*$ state, respectively. Although the high-energy $\lambda_{\text{max}} \sim 400$ nm emission in ns-TRE occurs in timescale very different from the $\lambda_{\text{max}} \sim 390$ nm transient fluorescence (PF) in the fs-TRF (Figure 5.4(a)), their nearly identical wavelength locations and the spectral profiles (Figure 5.8 inset) indicates strongly that they are having the same electronic origin, *i.e.* the S_1 $^1\pi\pi^*$ state. We therefore exclude any other assignment to the $\lambda_{\text{max}} \sim 400$ nm long-lived high-energy emission in TRE and considered that it is due to DF⁷ from the S_1 $^1\pi\pi^*$ state that also emits the PF in the first ($< \sim 10$ ps) and the second stage (~ 10 ps to thousand ps) of time regimes.

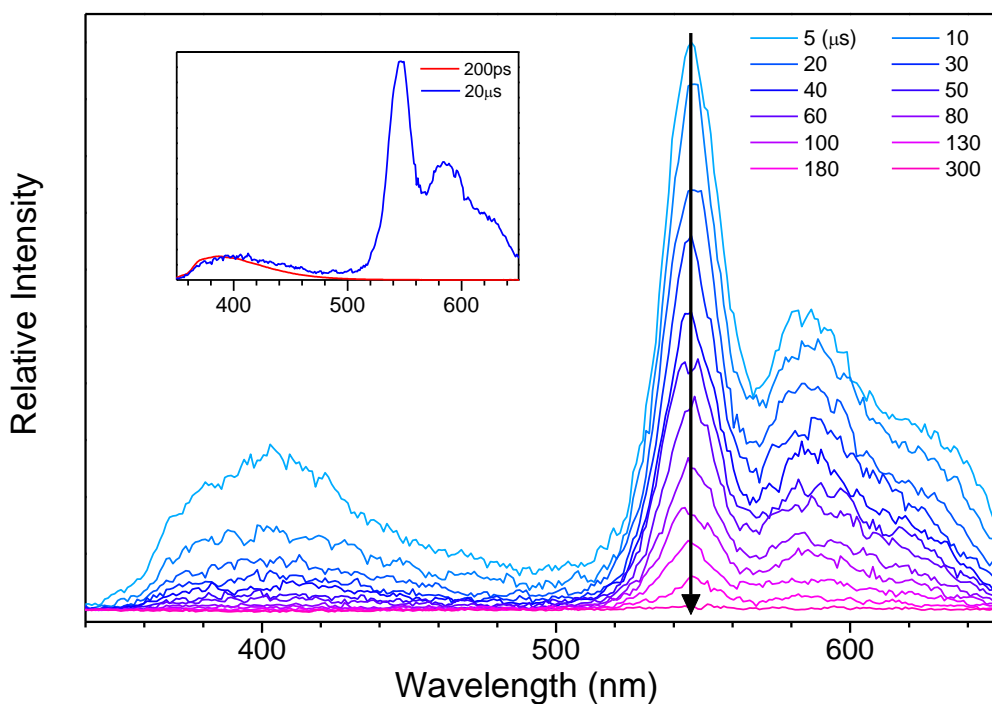


Figure 5.8 ns-TRE spectra recorded after 280 nm excitation of **2a** in deoxygenated acetonitrile recorded at indicated time delays. The inset shows the comparison of spectra obtained at the indicated delay times from fs-TRF (red line) and ns-TRE (blue line) measurement of **2a** in deoxygenated acetonitrile after 280 nm excitation. The arrow indicates temporal evolution of the spectra.

Dynamic analysis of the ns-TRE time profile (Figure 5.9) produced lifetime of $\sim 25.8 \mu\text{s}$ for the DF (τ_{DF}) and $\sim 52.3 \mu\text{s}$ for the phosphorescence (τ_{Ph}) under the deoxygenated condition as in the measurement. It is important to note that the τ_{DF} is about half of the τ_{Ph} . Such an observation is a signature indicating that the DF is formed through a mechanism known as triplet-triplet annihilation (TTA) ($T_1 + T_1 \rightarrow S_1 + S_0$) DF.⁷⁻¹⁰ Of note, the alternative mechanism, namely

the thermal activation induced triplet-to-singlet up-conversion ($T_1 \rightarrow S_1$)^{3,8} can be excluded for this mechanism requires an identical lifetime between the DF and phosphorescence.^{8,11}

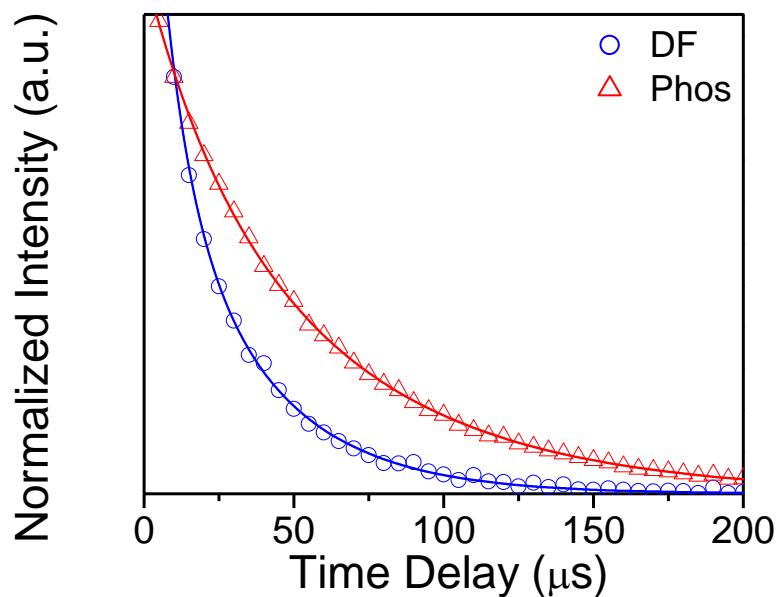


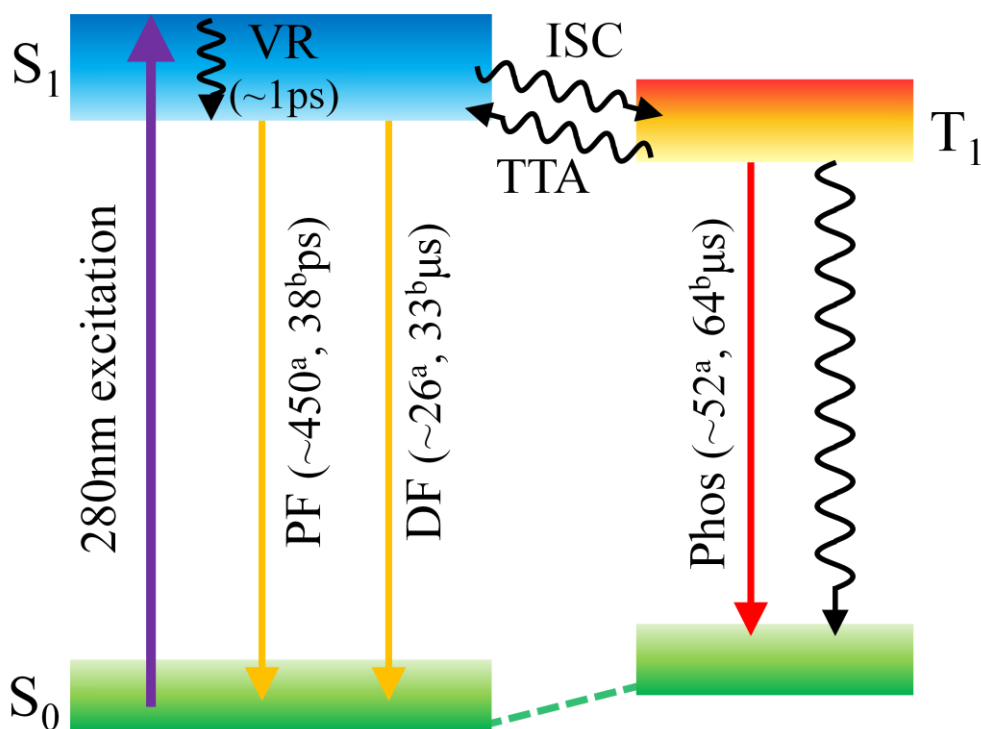
Figure 5.9 Experimental (\circ , Δ) and fitted ($—$) phosphorescence (Phos) and delayed fluorescence (DF) kinetic traces of **2a** obtained from ns-TRE with 280 nm excitation in deoxygenated acetonitrile.

It is worth noting the obviously low intensity of the transient DF when comparing to that of the phosphorescence in Figure 5.8. Regarding the much larger k_r (by $\sim 10^4$ times) of the S_1 $^1\pi\pi^*$ than the T_1 $^3\pi\pi^*$ state, it can be inferred that in the third stage of excited state relaxation, the majority of excited state population is at the T_1 $^3\pi\pi^*$ state with only a minute percentage ($< \sim 0.01\%$)

converted back to the S_1 $^1\pi\pi^*$ state by TTA. Therefore, the DF, despite of its long lifetime, contributes only modestly to the overall emission observed in the steady state measurement (Figure S7(b)).

Putting together the decay dynamics observed for the PF in the fs-TRF and the DF in the ns-TRE, it can be derived that the PF in hundreds ps timescale contributes ~90% to the total fluorescence emission in the steady state spectrum (Figure S7(b)) with only ~10% is accounted for by the DF in the ns to microsecond (μ s) timescale. Taking into consideration of the weakly emissive nature of the T_1 $^3\pi\pi^*$ state, the abnormally large emission yield (Φ_e) $(0.66)^7$ of **2a** can be attributed to the effective production of PF with a fairly long lifetime (~450 ps) which is only modestly quenched by the ISC.

The major deactivation pathways constructed according to the above analysis are summarized in Scheme 5.2 for **2a**.



Scheme 5.2 Dynamics and major deactivation pathways proposed for **2a^a** and **3a^b** in acetonitrile after 280 nm excitation. Radiative and non-radiative transitions are indicated in straight and wavy arrows respectively. (VR = vibrational relaxation; PF = prompt fluorescence; DF = delayed fluorescence; Phos = phosphorescence; ISC = intersystem crossing; TTA = triplet-triplet annihilation)

Upon photo-excitation from S_0 to the S_1 $^1\pi\pi^*$ state, the S_1 $^1\pi\pi^*$ state molecule first undergoes vibrational or structural relaxation. After that, it decays as a result of radiatively transition giving the PF and ISC to transfer the excited state population to the T_1 $^3\pi\pi^*$ state. Upon the formation of T_1 $^3\pi\pi^*$ state through ISC, the molecule at T_1 $^3\pi\pi^*$ state emit phosphorescence and at the same time undergoes intermolecular TTA to transfer partially its population back to the S_1

$^1\pi\pi^*$ state which decays with lifetime half of the triplet emitting DF at the ns to μs timescale.

5.1.3 Excited state dynamics of oligo(*m*-PE) and gold(I) oligo(*m*-PE) complex

5.1.3.1 Femtosecond time-resolved fluorescence and transient absorption study

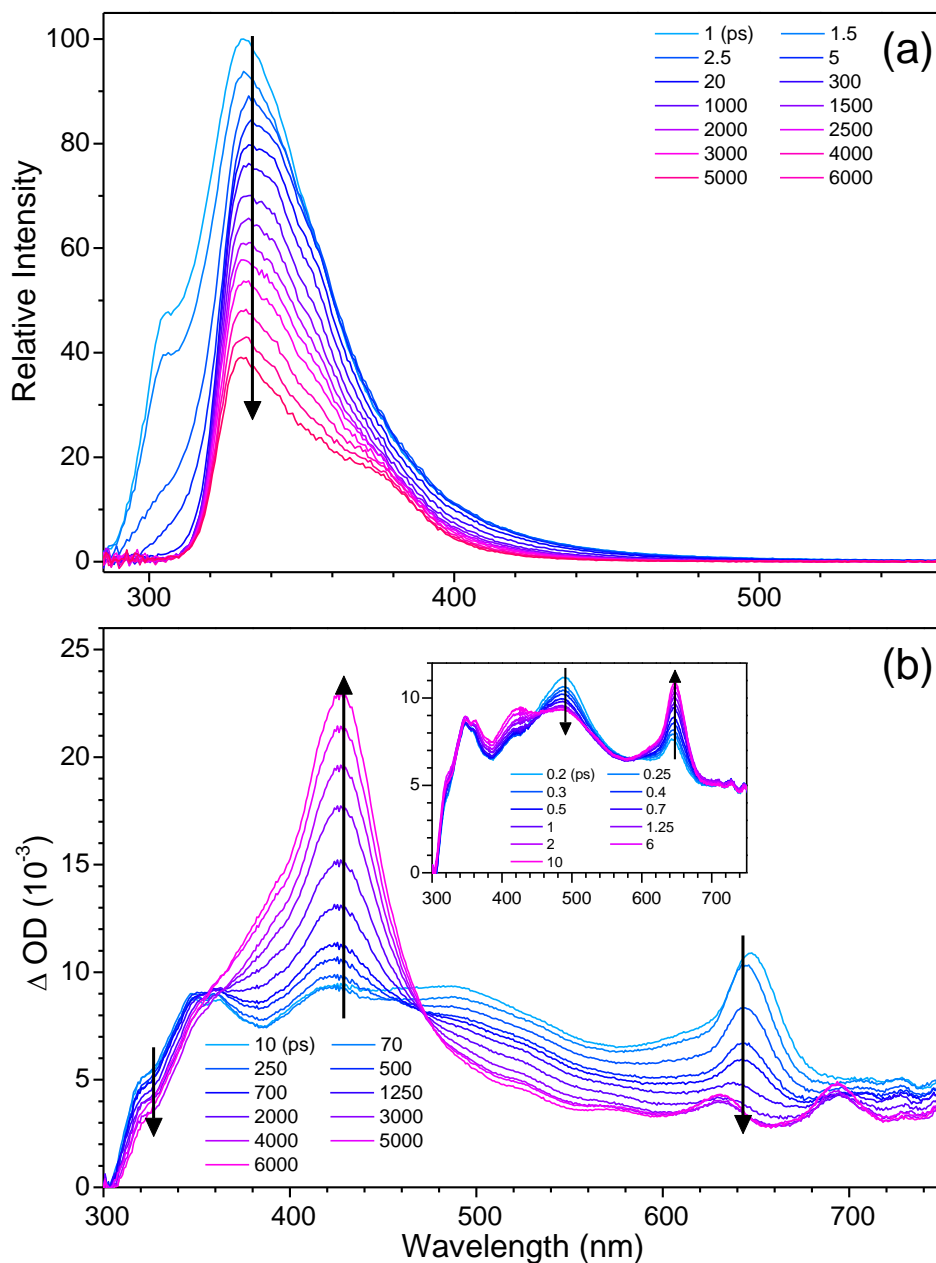
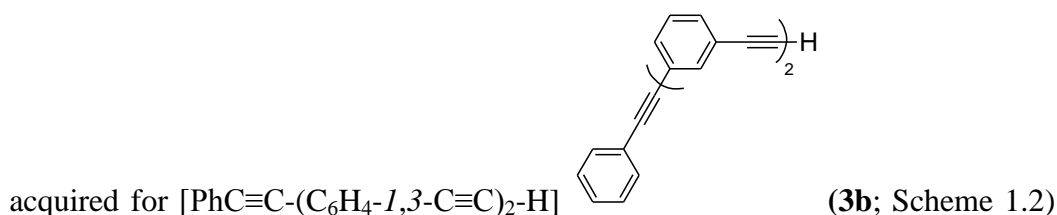


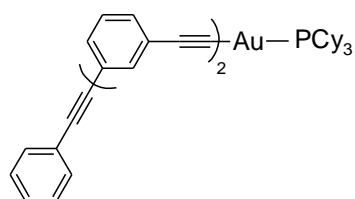
Figure 5.10 Broadband time-resolve fluorescence (a) and transient absorption (b) spectra of **3b** in acetonitrile recorded at indicated time delays after excitation

at 280 nm. The inset shows the early time delay of the spectra. The arrows indicate temporal evolutions of the spectra.

Figure 5.10 displays the temporal evolution of fs-TRF and fs-TA



in CH_3CN . These spectra were measured to probe directly the excited state dynamics of the oligo(*m*-PE) which is corresponding to the free ligand of the gold(I) complex **3a** $[(\text{PhC}\equiv\text{C}-(\text{C}_6\text{H}_4-1,3-\text{C}\equiv\text{C})_2\text{Au}(\text{PCy}_3)]$



(Scheme 1.2) and the measurements were done to

provide reference data for accessing the role of metal (the gold(I) in the current case) on one hand and the ligand structure on the other hand in affecting the excited state dynamics, in particular that of the ISC.

The fs-TRF and fs-TA data we observed with **3b** are very similar to those obtained for **3a** (Figures 6.1(c) and 6.3(d) in the next chapter).⁴ It can be seen from Figure 5.10 that, the TRF (Figure 5.10(a)) feature a single emission band with $\lambda_{\text{max}} \sim 338$ nm that decays in thousand ps timescale with no significant change in the spectral profile. On the other hand, the TA featuring a broad positive absorption at $\sim 350\text{-}700$ nm after a subtle grows in the ESA intensity at ~ 650 nm in <10 ps (Figure 5.10(b) inset) decays in the similar thousand ps

timescale as in the fs-TRF and, as a result, transforms into a different spectra having the $\lambda_{\text{max}} \sim 430$ nm (~ 10 ps, Figure 5.10(b)). The $\lambda_{\text{max}} \sim 338$ nm fluorescence in the fs-TRF and ~ 350 - 700 nm ESA in the fs-TA are attributed to the fluorescence ($S_1 \rightarrow S_0$) and the ESA ($S_1 \rightarrow S_n$) of the S_1 $^1\pi\pi^*$ state, respectively. While the $\lambda_{\text{max}} \sim 430$ nm absorption in the late time fs-TA is ascribed to the ESA from the T_1 $^3\pi\pi^*$ state ($T_1 \rightarrow T_n$) of **3b**. Note that the excited state spectra (of both the fs-TRF and fs-TA) are very similar between **3a** and **3b**. This implies that the addition of $\text{Au}(\text{PCy})_3^+$ in **3a** has insignificant effect on the electronic properties and the energy of the oligo(*m*-PE) ligand system.

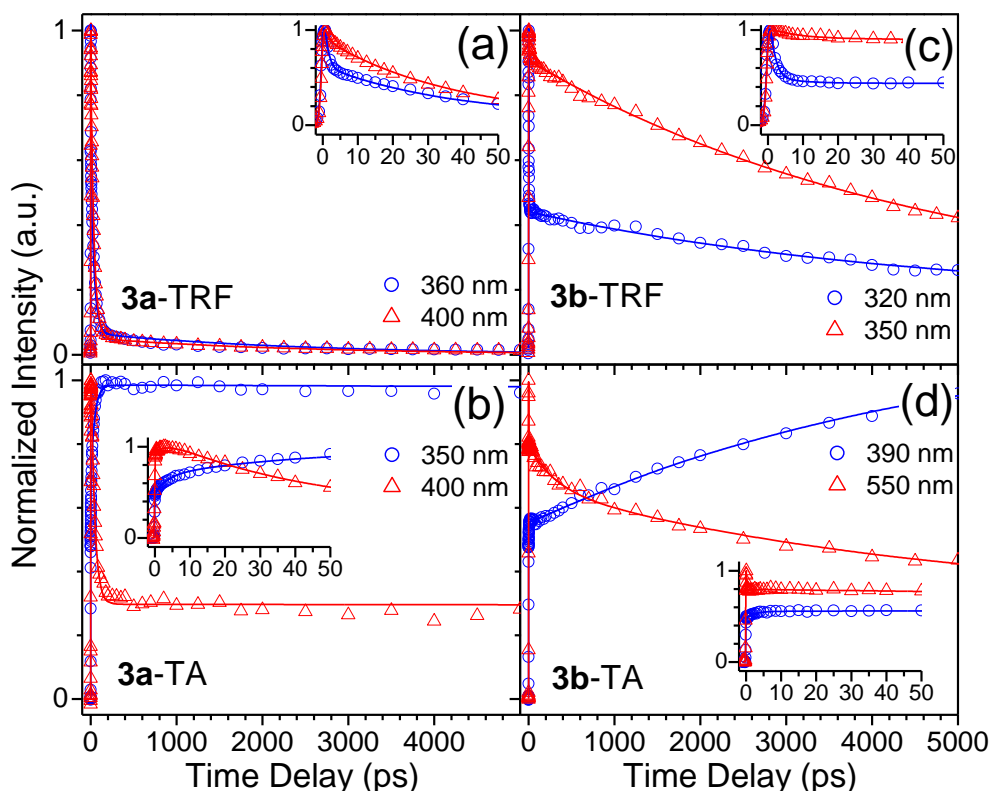


Figure 5.11 Experimental (\circ , Δ) and fitted (—) kinetic time profiles of fs-TRF ((a), (c)) and TA ((b), (d)) at indicated wavelengths obtained with 280 nm

excitation of **3a** ((a), (b)) and **3b** ((c), (d)) in acetonitrile. The insets show the decay profiles at early delay times.

A comparison between the kinetic decay traces obtained from the fs-TRF and fs-TA of **3b** and **3a** is depicted in Figure 5.11. Dynamic fitting of the TRF and TA time profiles observed bi-exponential dynamics with mutually related time constants (τ_1 and τ_2) between fs-TRF and fs-TA for both **3a** and **3b**. The time constant of τ_1 was found to be nearly identical, being ~ 1 ps in both **3a** and **3b**. The time constant of τ_2 was however observed to be very different, being ~ 38 ps for **3a** and ~ 5.2 ns for **3b**. The τ_1 (~ 1 ps) component accounts for the initial (first stage) relaxation of the photo-populated S_1 $^1\pi\pi^*$ state ($< \sim 6$ ps, Figure 5.10(b) inset); while τ_2 (~ 38 ps/ 5.2 ns for **3a/3b**) is corresponding to the decay of the relaxed S_1 $^1\pi\pi^*$ state leading to formation of the T_1 $^3\pi\pi^*$ state as indicated by the long-lived $\lambda_{\text{max}} \sim 430$ nm ESA seen in the fs-TA (Figure 5.10(b)). The ISC from the S_1 $^1\pi\pi^*$ to T_1 $^3\pi\pi^*$ state is corroborated by the observation of a pair of well defined isosbestic points at ~ 360 and 470 nm (Figure 5.10(b)) produced from the spectral transfer at the timescale corresponding to the τ_2 (Figures 5.11(c) and 5.11(d); Table 5.1).

The major deactivation pathways proposed for **3a** also summarized in Scheme 5.2 together with those of **2a**.

5.2 Discussion

5.2.1 Comparison of the spectral and temporal evolution character of oligo(*p*-PE) and gold(I) oligo(*p*-PE) complex

Despite the general similarity in terms of the spectral profiles and the spectral transformation showed by **2a** and **2b** (Figures 5.4 and 5.6), distinct differences in the precise wavelength maxima and the decay dynamics are noted between the two compounds. According to the results obtained from the time-resolved measurements, the TRF and ESA spectra of **2b** (Figure 5.6) all occur at energy modestly higher than those of **2a** (Figure 5.4 and Table 5.1); in addition, although the two compounds feature a nearly identical τ_1 (~0.9 ps), their time constant of τ_2 is clearly different: the τ_2 of **2b** is ~600 ps, slower than the τ_2 ~450 ps of **2a** (Figures 5.5 and 5.7; Table 5.1).

Moreover, **2b** shows a much greater extent of GB recovery (~94%) and a noticeably lesser involvement of the T_1 $^3\pi\pi^*$ ESA in the late time TA (~3000 ps). It is noticed that, in addition to the energy red-shifts in the S_1 $^1\pi\pi^*$ fluorescence and the T_1 $^3\pi\pi^*$ absorption, the S_0 absorption also shows substantial energy red-shift (by ~1600 cm^{-1}) from **2b** (321 nm) to **2a** (338 nm) (Table 5.1). These observations imply that the Au-C bonding interaction between the oligo(*p*-PE) ligand and $\text{Au}(\text{PCy})_3^+$ moiety as that occurs in complex **2a** decreases the transition energies associated with all three states, i.e., the S_0 , S_1 $^1\pi\pi^*$ and T_1 $^3\pi\pi^*$ states.⁷

The similarity and differences in the decay dynamics between **2a** and **2b** are instructive for elucidating the impact of $\text{Au}(\text{PCy})_3^+$ moiety on the emission

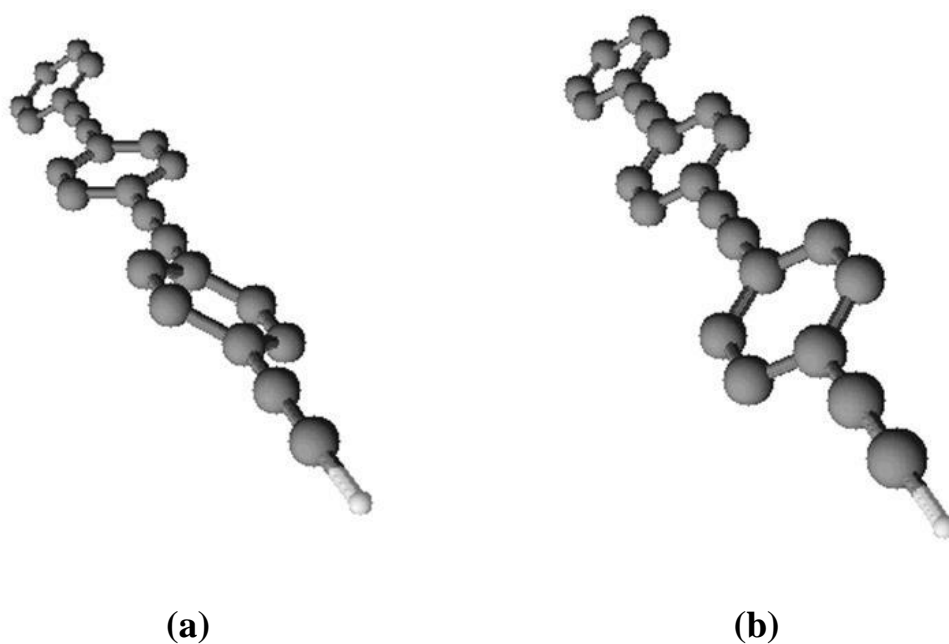
pathways and the deactivation mechanism of the two systems. In the first stage of spectral evolution at time interval up to ~6 ps after the excitation, **2a** and **2b** exhibit very similar spectral evolutions both in the fs-TRF (insets of Figures 5.4(a) and 5.6(a)) and the fs-TA (insets of Figures 5.4(b) and 5.6(b)). These temporal changes of fs-TRF and fs-TA spectra are most likely a result of structural re-arrangement of the common initial S_1 $^1\pi\pi^*$ state which is localized in the oligo(*p*-PE) system both in **2a** and **2b**.

It is known that the oligo-aryleneethnylenes, like the case in **2b**, exist in the S_0 as a continuous distribution of rotational isomers upon free rotation of the phenyl rings along the sp^2 - sp^3 bonds.¹²⁻¹⁴ The collapse at the blue edge (~310-360 nm) of the early-time TRF (Figure 5.6(a) inset) is an indication for the structural rearrangement of the S_1 $^1\pi\pi^*$ state from the initial orientation disordered structure (Scheme 5.3(a)) into a fully planarized conformation (Scheme 5.3(b)). This structural rearrangement is driven by the enhancement of π -conjugation in the S_1 $^1\pi\pi^*$ state compared to the S_0 after photo-excitation.¹²⁻¹⁴ The growth as the structural change of the TRF intensity at other wavelengths suggests that the relaxed S_1 $^1\pi\pi^*$ state with planar structure may feature a larger k_f than the initial S_1 $^1\pi\pi^*$ state at the Frank-Condon (FC) region. Such an inference is in line with those reported in literature for *p*-PE oligomers with different lengths and different substitution pattern.¹⁴

In analogy, the large growth in the initial ESA at the first stage of spectral evolution (Figure 5.6(b) inset) can also be considered as a result of the structural change of the initial S_1 $^1\pi\pi^*$ state. According to this, the relaxed S_1 $^1\pi\pi^*$ state feature an enhanced absorption cross section in relative to that of the S_1 $^1\pi\pi^*$

state at the FC. To the best of our knowledge, such an effect has not been reported in the literature before this work. Taking together the initial magnitude of GB (Figures 5.4(b) and 5.6(b)) and the known molar absorptivity (ϵ) of the S_0 absorption,¹ the ϵ of the relaxed S_1 $^1\pi\pi^*$ state can be estimated to be in the order of $\sim 10^5$ mol⁻¹ cm⁻¹ for **2a** and **2b**. This implies that, upon photo-excitation, the compounds may act as effective visible light absorbers, especially at the wavelength region from ~ 600 nm to 700 nm.

Nevertheless, the key aspect presented here is that the nearly identical first stage dynamics displayed by **2a** and **2b** indicates that the additional Au(PCy)₃⁺ moiety has only little effect in **2a** compared to **2b** at the very early stage of the excited state relaxation.



Scheme 5.3 Schematic representation of the torsional disordered (a) and the planar (b) structure of the oligo(*p*-PE) chromophore in **2a** and **2b**.

At the second stage of deactivation, the decay dynamics displayed by **2a** and **2b** are clearly different: **2a** features a time constant of ~450 ps and **2b** features a time constant of ~600 ps (Table 5.1). During this stage of excited state relaxation, the temporal evolutions of the TRF and TA arise due to the decay of the structurally relaxed S_1 $^1\pi\pi^*$ state which can be caused by three possible processes including the radiative transition to S_0 in giving PF, the nonradiative processes due to ISC from S_1 $^1\pi\pi^*$ to T_1 $^3\pi\pi^*$ state and a direct internal conversion (IC) from the S_1 $^1\pi\pi^*$ state to S_0 .³

According to the late time percentage recovery of the GB and the inclusion of no photochemical reaction of these compounds,⁷ the fraction of the S_1 decay through the radiative transition ($S_1 \rightarrow S_0$, radiative yield; Φ_R) and the nonradiative ISC ($S_1 \rightarrow T_1$, Φ_{ISC}) can be estimated to be ~0.72/0.94 and ~0.28/0.06 for **2a/2b** respectively ($\Phi_{ISC} = 1 - \Phi_R$). Clearly, the ISC yield (Φ_{ISC}) is significantly larger in **2a** (~0.28) compared to **2b** (~0.06).

In order to extract the value of k_{ISC} , the relative contribution of the radiative vs. nonradiative decay channel in the $S_1 \rightarrow S_0$ conversion has to be examined. In this regard, it is noted that high value of Φ_R (0.94) and the ~600 ps S_1 $^1\pi\pi^*$ lifetime we determined for **2b** are respectively in good agreement with the fluorescence quantum yield and the fluorescence lifetime reported for analogue *p*-PE oligomer, of which the S_1 $^1\pi\pi^*$ state decay is dominated by the radiative transition negligible involvement of the IC during the decay of the S_1 $^1\pi\pi^*$ state.^{13a,14} Therefore, the second stage dynamic recovery of S_0 in **2b**, and also presumably for **2a**, can be attributed to arise primarily due to the radiative transition of the S_1 $^1\pi\pi^*$ state with only a minute contribution of the IC.

On the basis of this and the estimated values for Φ_{ISC} and k_f (Table 5.1), the k_{ISC} of **2a** can then be derived to be $\sim 1.6 \times 10^8 \text{ s}^{-1}$ ($k_{\text{ISC}} \approx \Phi_{\text{ISC}} \times k_f$), corresponding to a ~ 7 times faster than that of **2b** (Table 5.1). Even so, it is noted that the value of k_{ISC} we observed with **2a** appears to be the slowest in those reported in the literature for the transition metal complexes. Such a rate of k_{ISC} corresponds to an ISC time constant of $\sim 6 \text{ ns}$ ($\tau_{\text{ISC}} = 1/k_{\text{ISC}}$). Such an ISC time constant is ~ 4 orders lower than the ISC time we derived for **1a**, which is indicative for a remarkable role of ligand π -conjugation in affecting the rate of ISC.

5.2.2 Comparison of the spectral and temporal evolution character of oligo(*m*-PE) and gold(I) oligo(*m*-PE) complex

According to the TRF and TA results obtained for **3a** (Figures 6.1(c) and 6.3(d) in the next chapter) and **3b** (Figures 5.10(a) and 5.10(b)), prompt after the photo-excitation, **3a** and **3b** exhibit similar changes in fs-TRF and fs-TA profiles described by nearly identical time constant of $\sim 1 \text{ ps}$. In analogous to the early time processes observed with **2a** and **2b**, it is plausible that the $\sim 1 \text{ ps}$ spectral changes are due to structural and vibrational relaxation of the initial $S_1 \ ^1\pi\pi^*$ state produced by the photo-excitation.¹²⁻¹⁴

As for the spectral evolution in the second-stage from ~ 10 to 6000 ps after the photo-excitation, the decay of $S_1 \ ^1\pi\pi^*$ state proceeds with a much faster rate in **3a** ($\sim 38 \text{ ps}$) than **3b** ($\sim 5.2 \text{ ns}$). Notably, the decay time obtained for **3b** is close to the radiative lifetime (τ_r) that can be derived from steady state absorption spectrum (Figure S8(c)) using the Strickler-Berg equation (eq. 5.1).^{1,15}

$$k_f = \frac{1}{\tau_r} = \frac{1}{N_A} 8\pi c n^2 \left(2303 \langle \tilde{\nu}_f^{-3} \rangle^{-1} \right) \cdot \int \frac{\varepsilon(\tilde{\nu}_{abs})}{\tilde{\nu}_{abs}} d\tilde{\nu}_{abs} \quad \text{eq. 5.1}$$

where N_A is the Avogadro's constant; c is the speed of light; n is the refractive index of the solvent; $\tilde{\nu}_f$ is the emission frequency in wavenumbers; $\int \frac{\varepsilon(\tilde{\nu}_{abs})}{\tilde{\nu}_{abs}} d\tilde{\nu}_{abs}$ is the integral of the $S_0 \rightarrow S_1$ absorption band plotted in molar extension coefficient *vs.* energy in wavenumbers. The factor $\tilde{\nu}_f$ in eq. 5.1 was approximated by the wavenumber of the emission maximum ($\tilde{\nu}_{max}$).

The similarity between the experimental and the lifetime calculated from the Strickler-Berg equation implies that the decay of the S_1 $^1\pi\pi^*$ state in **3b** is mainly caused by the radiative transition with limited participation of the non-radiative processes such as the IC and ISC.³

On the basis of this, the much faster decay of the S_1 $^1\pi\pi^*$ state and the corresponding growth of the T_1 $^3\pi\pi^*$ state observed for **3a** is indicative for the presence of an effective ISC not seen in **3b** (Table 5.1). Or in other words, there is a great enhancement in the rate of ISC caused by the presence of $\text{Au}(\text{PCy})_3^+$ moiety in **3a** compared to **3b**. With the lifetime of S_1 $^1\pi\pi^*$ state and regarding that the S_1 $^1\pi\pi^*$ state decay rate is about $\sim 10^2$ times faster than the rate of radiative decay rate (k_f , Table 5.1), it is sensible to ascribe the decay of the S_1 $^1\pi\pi^*$ state in **3a** to the ISC; accordingly, the Φ_{ISC} can be estimated to be close to unity and the k_{ISC} be deduced to be $\sim 2.6 \times 10^{10} \text{ s}^{-1}$ ($k_{ISC} \approx 1/\tau_{PF}$, Table 5.1). Of note, the close to unitary Φ_{ISC} displayed by **3a** is the same as that of **1a** but is in a stark contrast to that of **2a** ($\Phi_{ISC} = \sim 0.28$).

In order to characterize the dynamics and the composition of the emission at long time scale after the formation of the $T_1^3\pi\pi^*$ state, ns-TRE measurement had been performed on **3a** in deoxygenated solution of CH_3CN . The data (Figure 6.5(c)) reveals two emission components, a high energy component at $\lambda_{max} \sim 330$ nm and a lifetime of ~ 32.8 μs and a low energy component at $\lambda_{max} \sim 470$ nm and a lifetime of ~ 63.7 μs . The two emission components are respectively attributed to the DF from the $S_1^1\pi\pi^*$ state and the phosphorescence from the $T_1^3\pi\pi^*$ state.⁴ The DF features lifetime half of the phosphorescence indicates the DF is produced from the mechanism of TTA, similar to the case of **2a**.

Joint analysis of fs-TRF (Figure 6.1(c)) and ns-TRE (Figure 6.5(c)) showed that the TTA induced DF is the major component ($\sim 90\%$) in the time-integrated fluorescence, the PF contributes only $\sim 10\%$ to the fluorescence intensity mainly due to the very short lifetime (~ 38 ps) of the PF. Such a relative contribution of DF and PF to the overall fluorescence deviates strongly to the result discovered for the fluorescence in **2a** ($\sim 90\%$ PF/ $\sim 10\%$ DF). The low quantum yield of the PF ($\Phi_{PF} = k_f \times \tau_{PF}$; ~ 0.01) of **3a** is the main reason for its low Φ_e (~ 0.12).⁷ On the other hand, the high $\Phi_e \sim 0.66$ displayed by **2a** is accounted for mainly by the large Φ_{PF} which is due to the extended lifetime of PF (~ 450 ps). In view of the limited absolute contribution of DF to the overall fluorescence in both **2a** and **3a**,⁴ the much lower Φ_{PF} in **3a** compared to **2a** is also a major factor for the much lower fluorescence to phosphorescence intensity ratio in the dual emission displayed by the former (**3a**) than the later (**2a**) complex.¹ The overall deactivation pathway of **3a** is depicted in Scheme 5.2 to compare with those of **1a** and **2a**. It is obviously that the general deactivation pattern of **3a** is identical to that of **2a**. However, the two complexes are in stark

differences in terms of the dynamics of PF, ISC and the makeup of the fluorescence emission.

5.2.3 General remarks on the photophysics of the gold(I) PE complexes

In general, the data presented above provides direct evidences for a number of striking features of the excited states of the examined systems. First of all, the rate of the theoretical forbidden LC $^1\pi\pi^* \rightarrow ^3\pi\pi^*$ ISC is remarkably different between the three complexes despite that they have a common $[\text{Au}(\text{PCy})_3]^+$ moiety attached to the PE ligand systems. The value of k_{ISC} decreases consecutively by ~ 2 orders of magnitude from $\sim 1.2 \times 10^{12} \text{ s}^{-1}$ in **1a**, to $\sim 2.6 \times 10^{10} \text{ s}^{-1}$ and then to $\sim 1.6 \times 10^8 \text{ s}^{-1}$ in **3a** and **2a**, respectively. As a result, the PF from the photo-prepared $S_1 ^1\pi\pi^*$ is quenched to vastly different extent between the three complexes. This is indicated clearly by the lifetime of ~ 0.8 , 38 and 450 ps for **1a**, **3a** and **2a** respectively (Table 5.1). The ISC then proceeds from the electronically and vibrationally relaxed $S_1 ^1\pi\pi^*$ state with the different rates in **2a** and **3a**; the Φ_{ISC} is close to unity in **1a** and **3a** but is noticeable small (~ 0.28) in **2a**. The long PF lifetime of **2a** thus accounts for the unusually high Φ_e and the much larger fluorescence to phosphorescence intensity ratio than that of **3a**.

Second, for **2a** and **3a**, upon formation, $T_1 ^3\pi\pi^*$ state undergoes intermolecular TTA which converts part of its population back to the $S_1 ^1\pi\pi^*$ state, giving the DF with lifetime halved to that of the $T_1 ^3\pi\pi^*$ state. The PF and DF from the $S_1 ^1\pi\pi^*$ state and the phosphorescence from $T_1 ^3\pi\pi^*$ state altogether give the dual emission observed for **2a** and **3a** in the steady state emission

spectrum. With reference to the previously reported Au(PCy₃)⁺ complexes with oligo(*o*-PE) analogues,⁴ it can be concluded that, irrespective of the substitution pattern of the oligo-PE ligand, the dual emission composed of PF, TTA induced DF, and phosphorescence could be a general phenomenon and spectroscopic features of the gold(I) oligo-PE complexes.

The absence of the fluorescence component in the steady state emission of **1a** is due to the minor PF yield and the negligible efficiency of TTA in its T₁ ³ππ* state. The negligible efficiency of TTA is consistent with the finding that the efficiency of TTA increases with the increase of the oligo-PE ligand length.^{4,7} Such a tendency is useful for enhancing the efficiency of TTA from the T₁ ³ππ* state in the family of the gold(I)-PE complexes.

Third, making comparison between systems with and without incorporation of the Au(PCy₃)⁺ moiety through Au-C≡C- bond indicates that the presence of Au(PCy₃)⁺ moiety facilitates π-conjugation in the case of *para*-substituted oligomeric PE (**2a** vs. **2b**; Figures 5.4 and 5.6; Table 5.1). This is manifested by the obvious energy red-shift in the absorption and emission spectra of **2a** (Figure S7(b)) compared to **2b** (Figure S8(b)). However, the bonding to Au(PCy₃)⁺ appears to have little impact on the electronic properties and energy for the monomeric and *meta*-substituted PEs (**1a** vs. **1b** and **3a** vs. **3b**; Table 5.1). On the other hand, it is noted that, according to the spectral data of both the absorption and emission, the S₁ ¹ππ* state of the gold(I)-PE complexes shows increasing red shift in energy from **1a** to **3a** to **2a** (Table 5.1). This suggests an increasing degree of π-conjugation in the S₁ ¹ππ* state following the

order of **1a** < **3a** < **2a**, which is in accordance with the result reported for the corresponding metal-free *meta*- and *para*-PE oligomers.^{4,7,12-14,16}

For the three complexes **1a**, **3a** and **2a**, the degree of π electron conjugation in the S_1 $^1\pi\pi^*$ (i.e., **1a** < **3a** < **2a**) turns to correlate well with the decreasing order of the S_1 k_{ISC} ($k_{ISC}(\mathbf{1a}) > k_{ISC}(\mathbf{3a}) > k_{ISC}(\mathbf{2a})$). This observation is significant for it indicates that the ISC in these gold(I) containing complexes is not merely determined by the metal, but is controlled largely by the extent of the ligand conjugation.

5.2.4 Implication of the excited state dynamics of gold(I) oligo(PE) complexes

The results presented above have important impact on both the fundamental and application aspects of the PE-based compounds and materials. The discovery of the ligand-dependent ISC rate is unprecedented in the literature, as it demonstrates that the tendency of ISC is neither merely controlled by the metal ion nor the LC electronic excitation. It is however dictated by the extent of π -conjugation of the ligand system. The result challenges the conventional proposition of the heavy-atom prompted ISC, and provides an important complement to the so far reported ultrafast k_{ISC} for various transition metal complexes,¹⁷⁻²² In this regard, it is noted that recent time-resolved studies reported ISC with time constants of ~70 fs and 2 ps for Pt(II)-containing PE complexes analogues to **1a** and **2a**.^{19a} Also, the k_{ISC} we observed with **2a** is even smaller than that reported for Ir(III)-doped polyfluorenes where the ISC is induced by external heavy-atom effect.²³

It appears that, rather than depending solely on the atomic number of the metal ion, the rate of ISC in a metal complex is affected by an ensemble of factors, in particular those related to the electronic and structural properties of the ligand. This may include, for instance, the spatial separation between the metal centre and the electron involved in the $S_0 \rightarrow S_1$ electronic transition,³ the details of the symmetry and structural configuration of the ligand,^{22,24,25} and the presence or not of close lying d-d states²⁶, *etc.* In addition, the second-order term of the spin-orbit coupling (SOC) interaction and the mechanism of vibration-induced ISC could also contribute.³ For the complexes (**1a** - **3a**) studied in this case, the major factor accounting for the ample decline in the k_{ISC} from **1a** to **3a** to **2a** could be the increase in the spatial separation between the metal centre and the excited electron in the $S_1 \pi\pi^*$ state which is induced by the increasing π -conjugation in the PE ligand system. The larger ligand PE-centred electron delocalization in the $S_1 \pi\pi^*$ state of **2a** (to a lesser extent in **3a**) may lead to the excited π electron to be further away from the end-attached gold(I) atom, which may weaken the effect of SOC in the S_1 and therefore the reduced k_{ISC} when compared to **1a**, where the PE ligand is the less conjugated.

It is interesting to note that the large variation in the k_{ISC} values from **1a** to **3a** to **2a** demonstrates that the ISC of a metal complex can proceed in a wide range of time regime, ranging from <1 ps to at least several ns. The presence of sluggish ISC has been mentioned sparsely in the literature. As a consequence, not only the mostly considered T_1 , but also the precursor S_1 in its thermally relaxed form, can play a significant role in the excited state processes of transition metal complexes. In this regard, complex **2a** presents a compelling case in showing that the radiative decay of the initial S_1 surmounts the ISC and T_1 emission to the

extent that it predominantly contributes most of the photoluminescence of the system. As a result of this, other excited state processes, such as the excited state charge transfer, energy transfer and other environment related relaxation processes may also participate in the deactivation cascade not through the T_1 , but the photo-populated S_1 . Such a scenario may occur in various organometallic complexes. The conventional notion of the ultrafast ISC may be applicable only to a limited number of systems, such as those with excitation having character of metal-to-ligand charge transfer (MLCT) or ligand-to-metal charge transfer (LMCT) transition(s),¹⁷⁻²² or those having LC excitation but with the excited electron being sufficiently close to the metal ion centre, like the case in **1a**.

Last but not least, considering the potential applications of *p*-PE oligomers and polymers in the organic optoelectronics²⁷⁻²⁹ and the growing interest of exploiting *m*-PE scaffolds for the purpose of energy transfer in the light harvesting systems,³⁰ the effects presented in this chapter about the gold(I) on the dynamics, energy and efficiency of the oligo-(*p/m*-PE) centred fluorescence and phosphorescence emissions are useful in rational design of *p/m*-PE based molecules for improved application in the related areas.

5.3 References

1. Ma, C.; Chan, C. T. L.; Kwok, W. M.; Che, C. M. *Chem. Sci.* **2012**, *3*, 1883-1892.
2. (a) Hirata, Y.; Okada, T.; Mataga, N.; Nomoto, T. *J. Phys. Chem.* **1992**, *96*, 6559-6563. (b) Hirata, Y.; Okada, T.; Nomoto, T. *Chem. Phys. Lett.* **1996**, *257*, 513-518.
3. Turro, N. J. *Modern Molecular Photochemistry*; University Science Book, Mill Valley, CA, **1991**.
4. Lu, W.; Kwok, W. M.; Ma, C.; Chan, C. T. L.; Zhu, M. X.; Che, C. M. *J. Am. Chem. Soc.* **2011**, *133*, 14120-14135.
5. (a) Hui, M. H.; Rice, S. A. *J. Chem. Phys.* **1974**, *61*, 833-842. (b) Ribblett, J. W.; Borst, D. R.; Pratt, D. W. *J. Chem. Phys.* **1999**, *111*, 8454-8461. (c) Serrano-Andres, L.; Merchan, M.; Jablonski, M. *J. Chem. Phys.* **2003**, *119*, 4294-4304.
6. (a) El-Sayed, M. A. *J. Chem. Phys.* **1963**, *38*, 2834-2838. (b) El-Sayed, M. A. *J. Chem. Phys.* **1962**, *36*, 573-574.
7. Chao, H. Y.; Lu, W.; Li, Y.; Chan, M. C. W.; Che, C. M.; Cheung, K. K.; Zhu, N. *J. Am. Chem. Soc.* **2002**, *124*, 14696-14706.
8. (a) Swenberg, C. E. *J. Chem. Phys.* **1969**, *51*, 1753-1764. (b) Azumi, T.; McGlynn, S. P. *J. Chem. Phys.* **1963**, *39*, 1186-1194.

9. (a) Gerhard, A.; Bässler, H. *J. Chem. Phys.* **2002**, *117*, 7350-7356. (b) Hertel, D.; Bässler, H.; Guentner, R.; Scherf, U. *J. Chem. Phys.* **2001**, *115*, 10007-10013. (c) Hertel, D.; Setayesh, S.; Nothofer, H.-G.; Scherf, U.; Müllen, K.; Bässler, H. *Adv. Mater.* **2001**, *13*, 65-69. (d) Romanovskii, Y. V.; Bässler, H. *Chem. Phys. Lett.* **2000**, *326*, 51-57.
10. Bodunov, E. N.; Berberan-Santos, M. N.; Martinho, J. M. G. *Chem. Phys.* **2005**, *316*, 217-224.
11. Turek, A. M.; Krishnamoorthy, G.; Phipps, K.; Salteil, J. *J. Phys. Chem. A* **2002**, *106*, 6044-6052.
12. (a) Liu, L. T.; Yaron, D. J.; Sluch, M. I.; Berg, M. A. *J. Phys. Chem. B* **2006**, *110*, 18844-18852. (b) Sluch, M. I.; Godt, A.; Bunz, U. H. F.; Berg, M. A. *J. Am. Chem. Soc.* **2001**, *123*, 6447-6448.
13. (a) Beeby, A.; Findlay, K. S.; Low, P. J.; Marder, T. B. *J. Am. Chem. Soc.* **2002**, *124*, 8280-8284. (b) Beeby, A.; Findlay, K. S.; Low, P. J.; Marder, T. B.; Matousek, P.; Parker, A. W.; Rutter, S. R.; Towie, M. *Chem. Commun.* **2003**, 2406-2407.
14. Duvanel, G.; Grilj, J.; Schuwey, A.; Gossauer, A.; Vauthey, E. *Photochem. Photobiol. Sci.* **2007**, *6*, 956-963.
15. Strickler, S. J.; Berg, R. A. *J. Chem. Phys.* **1962**, *37*, 814-822.
16. (a) Gaab, K. M.; Thompson, A. L.; Xu, J. J.; Martínez, T. J.; Bardeen, C. J. *J. Am. Chem. Soc.* **2003**, *125*, 9288-9299. (b) Thompson, A. L.; Gaab, K. M.; Xu, J.; Bardeen, C. J.; Martínez, T. J. *J. Phys. Chem. A* **2004**, *108*, 671-682.

17. (a) Damrauer, N. H.; Cerullo, G.; Yeh, A.; Boussie, T. R.; Shank, C. V.; McCusker, J. K. *Science* **1997**, *275*, 54-57. (b) Yeh, A.; Shank, C. V.; McCusker, J. K. *Science* **2000**, *289*, 935-938. (c) Bhasikuttan, A. C.; Suzuki, M.; Nakashima, S.; Okada, T. *J. Am. Chem. Soc.* **2002**, *124*, 8398-8405. (d) Cannizzo, A.; Mourik, F.; Gawelda, W.; Zgrablic, G.; Bressler, C.; Chergui, M. *Angew. Chem., Int. Ed.* **2006**, *45*, 3174-3176.
18. (a) Cannizzo, A.; Blanco-Rodriguez, A. M.; Nahhas, A. E.; Šebera, J.; Záliš, S.; Vlček, A.; Chergui, M. *J. Am. Chem. Soc.* **2008**, *130*, 8967-8974. (b) Nahhas, A. E.; Cannizzo, A.; Mourik, F.; Blanco-Rodríguez, A. M.; Záliš, S.; Vlček, A.; Chergui, M. *J. Phys. Chem. A* **2010**, *114*, 6361-6369. (c) Busby, M.; Matousek, P.; Towrie, M.; Vlček, A. *J. Phys. Chem. A* **2005**, *109*, 3000-3008.
19. (a) Ramakrishna, G.; Goodson, T., III; Rogers-Haley, J. E.; Cooper, T. M.; McLean, D. G.; Urbas, A. *J. Phys. Chem. C* **2009**, *113*, 1060-1066. (b) Whittle, C.; Weinstein, J. A.; George, M. W.; Schanze, K. S. *Inorg. Chem.* **2001**, *40*, 4053-4062. (c) Hissler, M.; Connick, W. B.; Geiger, D. K.; McGarrah, J. E.; Lipa, D.; Lachicotte, R. J.; Eisenberg, R. *Inorg. Chem.* **2000**, *39*, 447-457.
20. Gawelda, W.; Cannizzo, A.; Pham, V.-T.; Mourik, F.; Bressler, C.; Chergui, M. *J. Am. Chem. Soc.* **2007**, *129*, 8199-8206.
21. (a) Quochi, F.; Saba, M.; Artizzu, F.; Mercuri, M. L.; Deplano, P.; Mura, A.; Bongiovanni, G. *J. Phys. Chem. Lett.* **2010**, *1*, 2733-2737. (b) Ramachandra, S.; Polo, F.; Edafe, F.; Schuermann, K. C.; Nijhuis, C. A.; Belser, P.; Reus, W. F.; Whitesides, G. M.; De Cola, L. *Pure Appl. Chem.* **2011**, *83*, 779-799.

22. (a) Abedin-Siddique, Z.; Ohno, T.; Nozaki, K.; Tsubomura, T. *Inorg. Chem.* **2004**, *43*, 663-673. (b) Abedin-Siddique, Z.; Yamamoto, Y.; Ohno, T.; Nozaki, K. *Inorg. Chem.* **2003**, *42*, 6366-6378.
23. Liao, H. H.; Yang, C. M.; Wu, C. H.; Horng, S. F.; Lee, W. S.; Meng, H. S.; Shy, J. T.; Hsu, C. S. *Appl. Phys. Lett.* **2007**, *90*, 013504.
24. Tong, G. S. M.; Chow, P. K.; Che, C. M. *Angew. Chem., Int. Ed.* **2010**, *49*, 9206-9209.
25. Tong, G. S. M.; Che, C. M. *Chem. Eur. J.* **2009**, *15*, 7225-7237.
26. Williams, J. A. G. *Top. Curr. Chem.* **2007**, *281*, 205.
27. (a) Bruce, M. I. *Coord. Chem. Rev.* **1997**, *166*, 91-119. (b) Manna, J.; John, K. D.; Hopkins, M. D. *Adv. Organomet. Chem.* **1995**, *38*, 79-154. (c) John, K. D.; Hopkins, M. D. *Chem. Commun.* **1999**, 589-590.
28. (a) Ma, Y. G.; Chan, W. H.; Zhou, X. M.; Che, C. M. *New J. Chem.* **1999**, *23*, 263-265. (b) Chan, S. C.; Chan, M. C. W.; Che, C. M.; Wang, Y.; Cheung, K. K.; Zhu, N. *Chem. Eur. J.* **2001**, *7*, 4180-4190. (c) Lu, W.; Mi, B. X.; Chan, M. C. W.; Hui, Z.; Zhu, N.; Lee, S. T. Che, C. M. *Chem. Commun.* **2002**, 206-207.
29. (a) Walters, K. A.; Dattelbaum, D. M.; Ley, K. D.; Schoonover, J. R.; Meyer, T. J.; Schanze, K. S. *Chem Comm.* **2001**, 1834-1835. (b) Liao, C.; Yarnell, J. E.; Glusac, K. D.; Schanze, K. S. *J. Phys. Chem. B* **2010**, *144*, 14763-14771. (c) Walters, K. A.; Ley, K. D.; Cavalaheiro, C. S. P.; Miller, S. E.; Gosztola,

D.; Wasielewski, M. R.; Bussandri, A. P.; Willogen, H.; Schanze, K. S. *J. Am. Chem. Soc.* **2001**, *123*, 8329-8342.

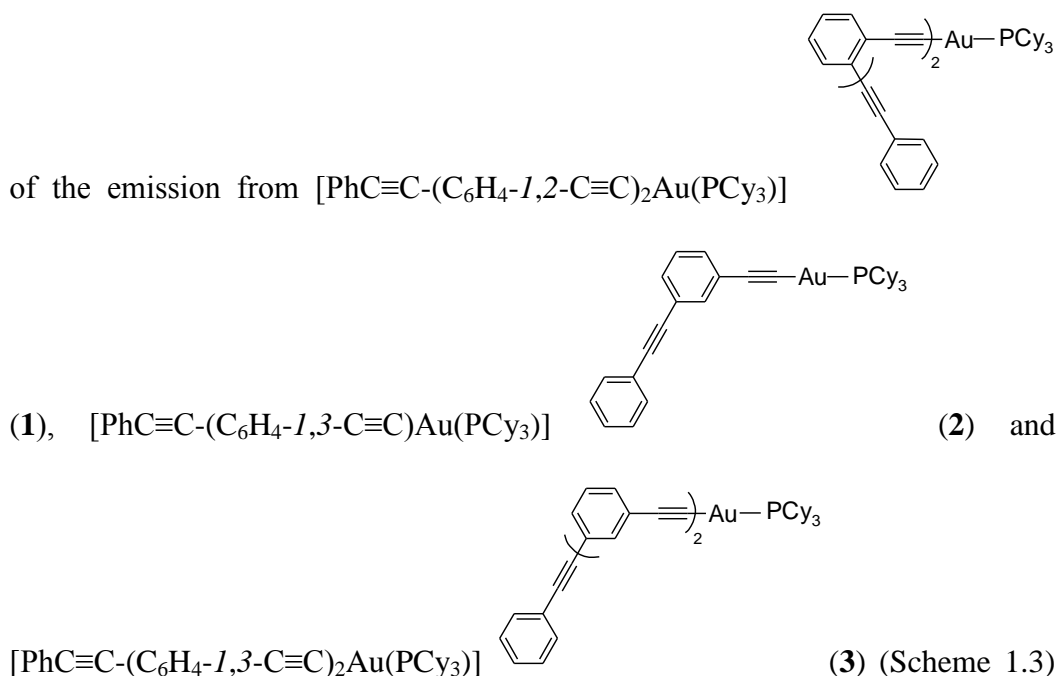
30. (a) Devadoss, C.; Bharathi, P.; Moore, J. S. *J. Am. Chem. Soc.* **1996**, *118*, 9635-9644. (b) Tretiak, S.; Chernyak, V.; Mukamel, S. *J. Phys. Chem. B* **1998**, *102*, 3310-3315.

Chapter 6 Ultrafast Broadband Time-Resolved Study on Selected Gold (I) oligo(*o*- or *m*-phenyleneethynylene) Complexes: Substitution Dependent Luminescence Dynamics and Pathway

6.1 Results

6.1.1 Time-resolved fluorescence study of gold(I) oligo(*o*- or *m*-PE) complexes

To understand the dynamics and factors in particular role of substitution in affecting the spectral and dynamics of the dual emission (Figure S9) from the gold(I) oligo-phenyleneethynylene (PE) complexes, fs-TRF measurement was first performed to probe directly the emission spectra and the temporal evolutions



in acetonitrile. The TRF spectra produced from these measurements are depicted

in Figure 6.1. The spectra from the three complexes are displayed together to facilitate direct comparison.

It can be seen from Figure 6.1 that, instantly after the excitation, complex **1**, **2** and **3** exhibit intense fluorescence band with λ_{max} at ~380, ~340 and ~345 nm respectively. These spectra are respectively very similar to the fluorescence component in the corresponding steady state spectra (Figure S9).¹ On the basis of this, the ~380, ~340 and ~345 nm TRF can be attributed with certain to originate from the S_1 state of each of the complexes; and thus they are corresponding to the prompt fluorescence (PF) in each of the complex. Within several ps after the photo-excitation, the TRF spectra of all three complexes narrow at the blue edge of the spectra, followed by a minute red shift in the emission wavelength (Figure 6.1). The TRF spectra decay rapidly in tens ps timescale, leaving a small fluorescence signal of only several percentage of the original intensity at ~2000 ps after the photo-excitation. The signal persists with no change in intensity up to 6000 ps in each of the complexes.

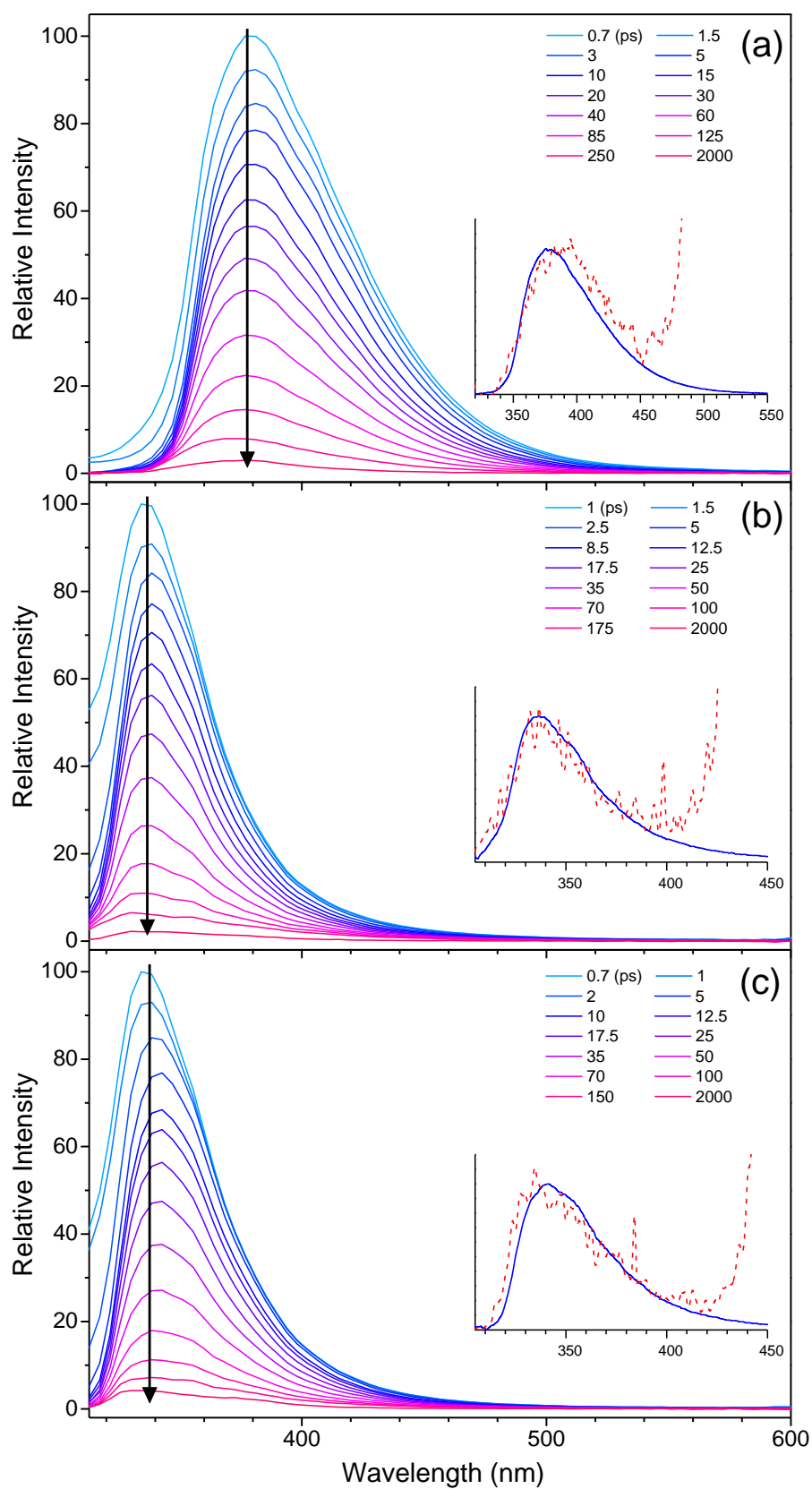


Figure 6.1 Broadband time-resolve fluorescence spectra of **1** (a), **2** (b) and **3** (c) recorded at indicated time delays in acetonitrile after excitation at 280 nm.

The insets show comparisons between fs-TRF recorded at ~50 ps (solid line) and ns-TRE recorded at ~3 μ s (dotted line) after the excitation. The arrows indicate temporal evolution of the spectra.

The kinetic decays of the TRF can be obtained by following the change as time of the fluorescence intensity at selected wavelength. For all the three complexes, such obtained fluorescence time profile is nearly independence of the fluorescence wavelength except at the very blue edge where the fluorescence was found to decay slightly faster. Figure 6.2 shows the fluorescence decay profiles at two representative wavelengths, ~360 and 380 nm for **1** (Figure 6.2(a)), ~330 and 350 nm for **2** (Figure 6.2(b)), and ~330 and 360 nm for **3** (Figure 6.2(c)). The fluorescence decay profiles at ~380 nm for **1**, 350 nm for **2** and 360 nm for **3** can all be fitted by bi-exponential function, containing a predominant component with time constant of ~49 (**1**), 35 (**2**) and 38 ps (**3**) and a common >200 ns time constant describing the small residual signal observed at >2000 ps after the photo-excitation (Figure 6.1). As for the fluorescence decay at the blue edge (~360 nm for **1**, 330 nm for **2** and **3**), in addition to the above mentioned two time constants, a third component with modest contribution and a time constant of ~1-2 ps is observed with all the three complexes. The time component, according to the change in the spectral profile at the corresponding time scale can be attributed to arise due to vibrational and/or structural relaxation of the initial S_1 upon photo-excitation to evolve into the energy minimum of this state.

It is straightforward that the TRF with decay of ~49/35/38 ps is the prompt fluorescence from the S_1 state for complexes **1/2/3** (Table 6.1), while the

residual signal with decay time $> \sim 200$ ns is the delayed fluorescence (DF) exhibited in these complexes (which is confirmed further by the ns-TRE data showed later in this chapter). Clearly, owing to its long lifetime and the limit to 6 ns detection time window of our fs measurement, the decay dynamics of the DF cannot be assessed fully by the fs-TRF experiment.

Table 6.1 Spectral parameters of **1 – 3**.

	λ_F^a/nm	$\lambda_{\text{Ph}}^b/\text{nm}$	$\lambda(\text{S}_1)^c/\text{nm}$	$\lambda(\text{T}_1)^c/\text{nm}$	$\tau_{\text{PF}}^d/\text{ps}$	$\tau_{\text{DF}}^e/\mu\text{s}$	$\tau_{\text{Ph}}^f/\mu\text{s}$
1	380	510	440, 620	400, 685	49	1.9	4.3
2	340	465	420	425	35	30.5	61.5
3	345	470	430	440	38	32.8	63.4

^a Maximum wavelength of fluorescence.

^b Maximum wavelength of phosphorescence.

^c Maximum wavelength of excited state absorption.

^d Prompt fluorescence lifetime. ^e Delayed fluorescence lifetime.

^f Phosphorescence lifetime.

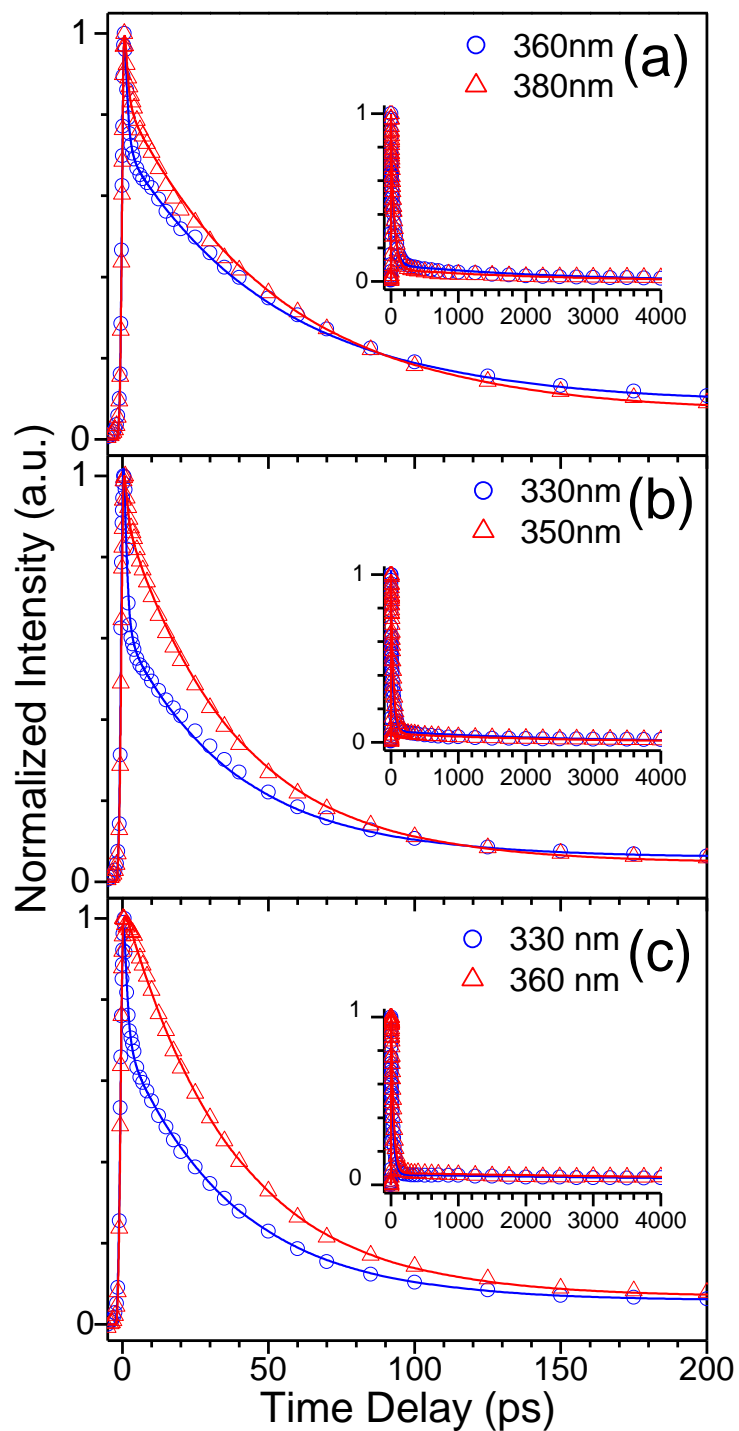


Figure 6.2 Experimental (\circ , Δ) and fitted ($—$) decay profiles of TRF at indicated wavelengths obtained after 280 nm excitation of **1** (a), **2** (b) and **3** (c) in acetonitrile. The insets show the decay profiles at long decay times after the excitation.

6.1.2 Femtosecond transient absorption study of gold(I) oligo(*o*- or *m*-PE) complexes

To provide complementary information on the excited state dynamics of **1**, **2** and **3**, fs-TA measurements were also performed for the three complexes in acetonitrile. The spectra recorded are depicted in Figure 6.3. The TA spectra obtained for the three complexes are plotted together to facilitate direct comparison. From Figure 6.3, it can be seen that, for all the three complexes, the major variations in the TA profiles occur in tens to hundred of ps after the excitation, and after that, the spectra remained nearly unchanged both in the spectral profile and the intensity of the spectra (insets in Figure 6.3).

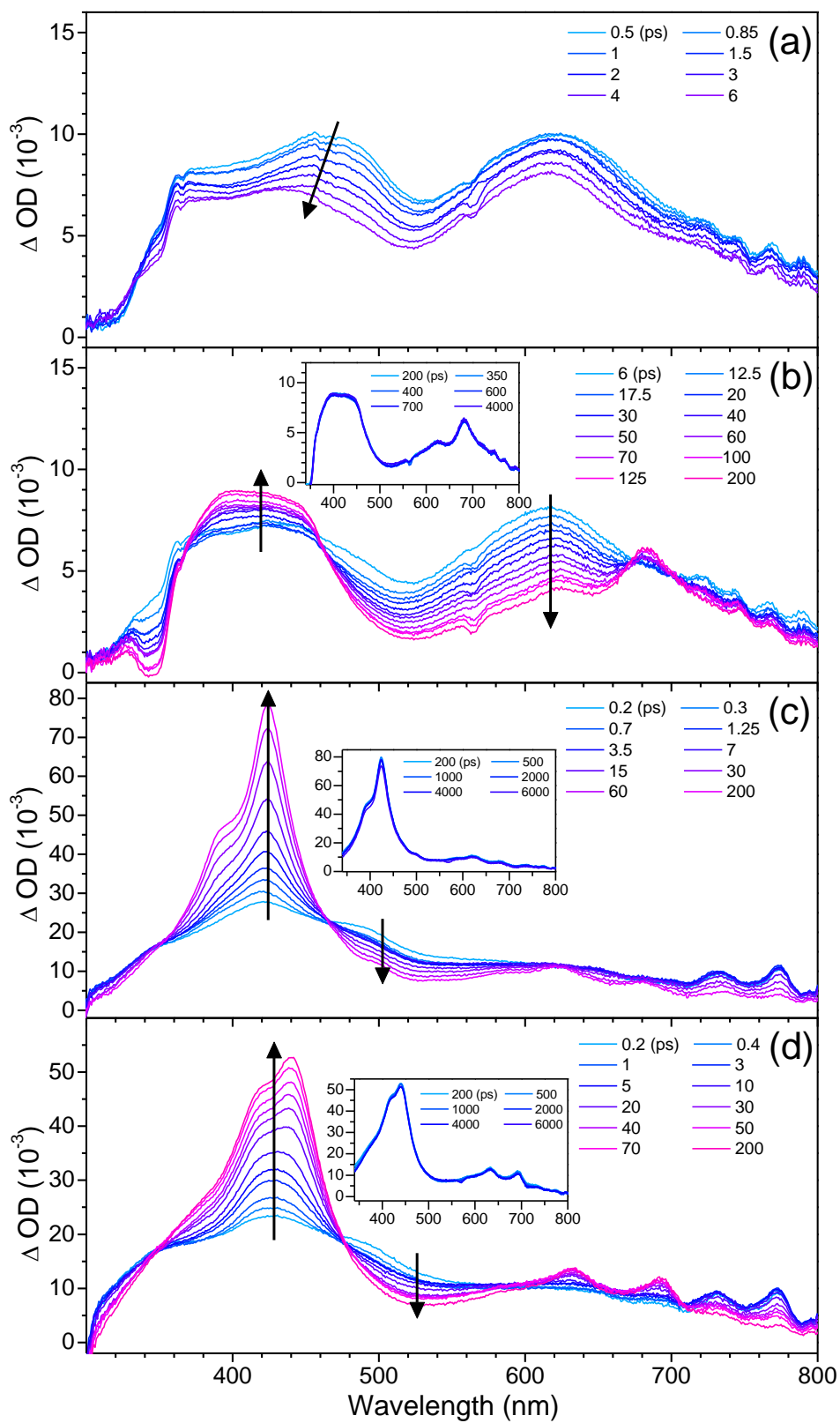


Figure 6.3 Broadband transient absorption of **1** ((a) and (b)), **2** (c) and **3** (d) in acetonitrile recorded at indicated delay times after excitation at 280 nm. The

insets show the spectral evolution at long delay times after the photoexcitation. The arrows indicate directions of spectral evolutions.

For complex **1**, immediate after excitation, the complex exhibits broad positive absorption band (~ 0.5 ps) at wavelength ranging from ~ 300 to 800 nm with λ_{max} at ~ 370 , 460 and 675 nm. After this and within ~ 6 ps after the excitation, this initial absorption displays a subtle decay and a minute blue shift while maintaining its spectral profile largely unchanged (Figure 6.3(a)). Within tens to hundreds ps after the excitation, the newly developed absorption (at ~ 6 ps) features two λ_{max} at ~ 440 and 620 nm then evolves into a different profile showing a broad absorption at ~ 400 nm along with a series of structured features peaking at, e.g. ~ 685 nm and 750 nm, at the late delay time (~ 200 ps) (Figure 6.3(b)). This temporal evolution of the spectrum is accompanied by isosbesitic points at ~ 370 , 460 , 675 and 700 nm. After this by ~ 6000 ps after the excitation, the TA spectrum (~ 200 ps) displays little change in the profile and intensity (inset of Figure 6.3(b)).

From Figures 6.3(c) and (d), it can be seen that the transient absorption of complexes **2** and **3** are very similar, suggesting that the two complexes with the *m*-PE ligands share similar natures of the electronic states involved in the fs-TA. There is however modest difference in the precise wavelength location and the decay dynamics of the fs-TA between **2** and **3**, which is obvious arising due the presence of an extra PE unit in **3** compared to **2**.

For both **2** and **3**, promptly after the excitation, they display TA spectra (~ 0.2 ps) featuring broad absorption at wavelength ranging from ~ 300 to 800 nm

peaking at ~420 nm and ~430 nm for **2** and **3** respectively. The initial TA then evolve into alternative profile, having a relatively sharp and intense absorption band peaking at ~425 and ~440 nm for **2** and **3** respectively by ~200 ps after the excitation. Such a TA spectral evolution proceeds with isosbestic points at ~350 and 470 nm. At late delay times, such as from ~200 to 6000 ps, the fs-TA show little change in profile and intensity (insets of Figure 6.3(c) and Figure 6.3(d)). It is noted that the spectra of **2** and **3** are completely different from those of the **1**, indicating entirely different electronic configurations for states involved in the fs-TA between the gold(I) *o*-PE (**1**) and the gold(I) *m*-PE complexes (**2** and **3**).

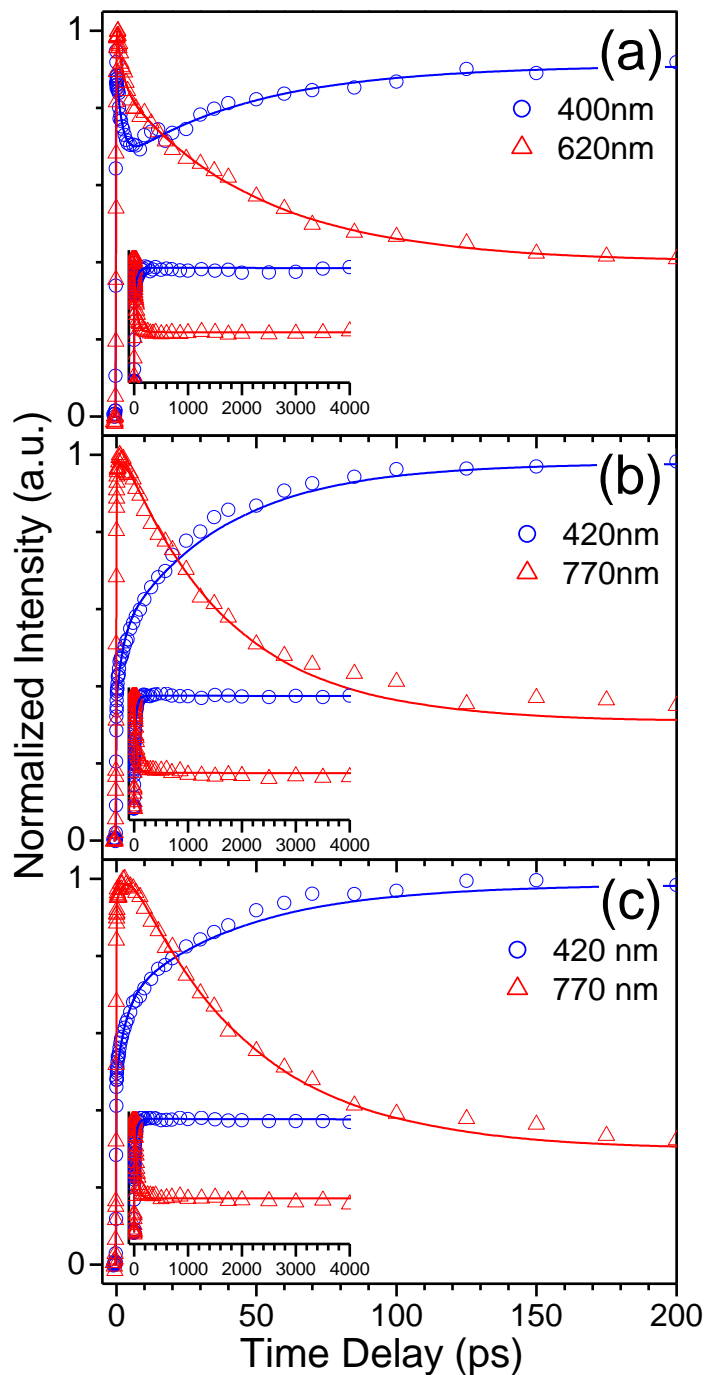


Figure 6.4 Normalized experimental (\circ , Δ) and fitted (—) kinetic time profiles obtained from TA (Figure 6.3) at selected wavelengths of **1** (a), **2** (b) and **3** (c) in acetonitrile after 280 nm excitation. The insets show the corresponding temporal evolution at late delay times after the photo-excitation.

Dynamic fitting of the TA time traces at selected wavelengths (Figure 6.4) revealed three time components for each of the three complexes. In each of the complex, depending on the selected wavelength, the TA decay profile can be described by two components with modest contributions respectively for the early time spectral relaxation (τ_1) and the persistence of the late time spectra (τ_3) and a major component (τ_2) representing the spectral transformation occurring at the tens to hundreds ps time scale.

The time constant τ_1 was found to be ~1-2 ps for complexes **1-3** describing the early time spectral relaxation which can be attributed to the vibrational and structural relaxation taking place in the $S_1 \pi\pi^*$ state upon photopopulation to relax into the energy minimum of the state. The τ_3 was found to be described by time constant >200 ns, indicating presence of very long-lived state featuring the spectra that was observed by ~200 ps after the excitation. The time constant of τ_2 was determined to be ~50, 35 and 40 ps for **1**, **2** and **3** respectively. This time constant described decay of the early relaxed spectra and at the same time the growth of the spectra that were observed at ~200 ps and afterwards.

Obviously, the time constants (τ_1 - τ_3) produced from the TA measurement coincide exactly with the time constants observed in the TRF, manifesting that the spectral transformations observed in the TRF (Figure 6.1) and TA (Figure 6.3) are originated from the same excited state processes. On the basis of this, the τ_2 time component in the fs-TA can be attributed to the intersystem crossing (ISC) from the $S_1 {}^1\pi\pi^*$ to $T_1 {}^3\pi\pi^*$ state. As a result, the spectra obtained before and after several ps provide signature absorption spectra for the $S_1 {}^1\pi\pi^*$ and $T_1 {}^3\pi\pi^*$ state in each of the complex.

According to the steady state absorption,¹ the radiative rate constant of the S_1 $^1\pi\pi^*$ state ($k_r(S_1)$) can be estimated to be on the order of 10^8 s⁻¹ ($k_r \approx \epsilon/10^{-4}$; $\epsilon \approx 10^4$) for the three complexes, equivalent to a radiative lifetime of several to 10 ns in each case.² Providing the minute involvement of other non-radiative process(es) during the deactivation of the excited state decay, it is plausible that the ISC acts as the primary channel in depopulating the photo-prepared brightly emissive S_1 $^1\pi\pi^*$ state. As a result, the decay time of the S_1 (~50/35/40 ps for **1/2/3**) can be considered as the time constant for the ISC in each of the system.

It is worth noting that the ISC time constants of the three complexes are not very different, indicating that the ISC rate of these gold(I) complexes is affected insignificantly by the substitution pattern (*ortho* vs. *meta*) and length (two vs. three repeating unit) of the PE ligand. Based on the ISC time constants and the lack of other channel in deactivating the S_1 $^1\pi\pi^*$ state, a close to unitary efficiency of the ISC (Φ_{ISC}) can be derived, which is consistent with those reported previously for many organometallic complexes.³⁻⁹

In addition, according to the measured lifetime (τ_T) (see below) and the quantum yield for the T_1 $^3\pi\pi^*$ state ($\Phi_T = \Phi_{ISC}$),¹ the radiative rate of the T_1 $^3\pi\pi^*$ state ($k_r(T_1)$) can be estimated to be no greater than 10^4 s⁻¹ ($k_r = \Phi_T/\tau_T$), corresponding to a decrease by ~4 order of magnitude from the value of the radiative decay rate of the S_1 $^1\pi\pi^*$ ($k_r(S_1)$). The low radiative rate of the T_1 $^3\pi\pi^*$ state indicates a very “dark” nature of the T_1 $^3\pi\pi^*$ state in relative to the S_1 $^1\pi\pi^*$ state, explaining the lack of the emission from the T_1 $^3\pi\pi^*$ state in the fs-TRF spectra (Figure 6.1) of all the three complexes.

It is interesting to note that the $\tau_1 \sim 1\text{-}2$ ps process is featured by the narrowing at the blue edge of the TRF spectra (Figure 6.1) and the subtle variation in the early TA spectra (Figure 6.3). We attributed this process to the vibrational cooling and conformational relaxation of the initial photo-populated S_1 $^1\pi\pi^*$ state. Indeed, according to the steady state absorption and the fluorescence spectra,¹ the 280 nm excitation may introduce an amount of $\sim 4000\text{-}7000$ cm^{-1} excess vibrational energy above the 0-0 level transition of the initial S_1 $^1\pi\pi^*$ state. It is known that vibrationally hot species tends to feature a broader absorption spectrum than its relaxed form and may relax within several picoseconds after excitation.¹⁰

As demonstrated in the previous chapter (Chapter 5), time-resolved measurements on related oligo(*p*-PE) systems without the coordinating metal ions observed similar changes in the early time TRF and TA, which was ascribed to the intramolecular structural variation of PE ligand to achieve a more constrained planar structure in the S_1 from the S_0 .^{11,12} On the basis of the similarity in the early time spectral evolution, it appears reasonable that the intramolecular structural relaxation like that occurs in the oligo(*p*-PE) systems may also take place in the gold(I) complexes especially with the *ortho*-PE ligand (complex **1**), which was found to show a greater extent of the TA relaxation than the *meta*-counterparts **2** and **3** (Figure 6.3).

In addition, it is relevant to note that the relaxation of the vibrationally “hot” S_1 $^1\pi\pi^*$ state ($\sim 1\text{-}2$ ps) occurs at timescale well separated from that of the ISC ($\sim 35\text{-}50$ ps). Therefore, for the gold(I) complexes investigated in this chapter, the ISC proceed from the fully relaxed S_1 $^1\pi\pi^*$ state. This is different from the

ultrafast (tens to hundreds of fs) ISC reported in the literature for a number of the organometallic complexes which have the ISC occurs from the vibrationally hot S_1 instantly after the photo-excitation.³⁻⁹

6.1.3 Nanosecond time-resolved emission study of gold(I) oligo(*o*- or *m*-PE) complexes

The fs time-resolved data (Figures 6.2 and 6.4) presented in the previous sections showed that after ~ 200 ps after the photo-excitation, the excited state population is dominated by the T_1 $^3\pi\pi^*$ state with only a small percentage in the S_1 $^1\pi\pi^*$ state. In order to characterize the subsequent spectral and temporal evolution of the T_1 $^3\pi\pi^*$ and S_1 $^1\pi\pi^*$ state in a long timescale from nanoseconds to milliseconds after the excitation, time-resolved emission (TRE) measurements have been performed for complexes **1-3** in deoxygenated acetonitrile. The result of these measurements provide direct evidence for elucidating the formation mechanism of the long-lived DF and the detailed composition of the dual emission revealed in the steady state measurement (Figure S9).

In the ns-TRE measurements, by using the time-gating technique and adjusting carefully the gating time duration for the detection of the transient emission, we were able to record the weak transient emission from both the weakly emissive T_1 $^3\pi\pi^*$ and the S_1 $^1\pi\pi^*$ state which carries only minute fraction of the excited state population.

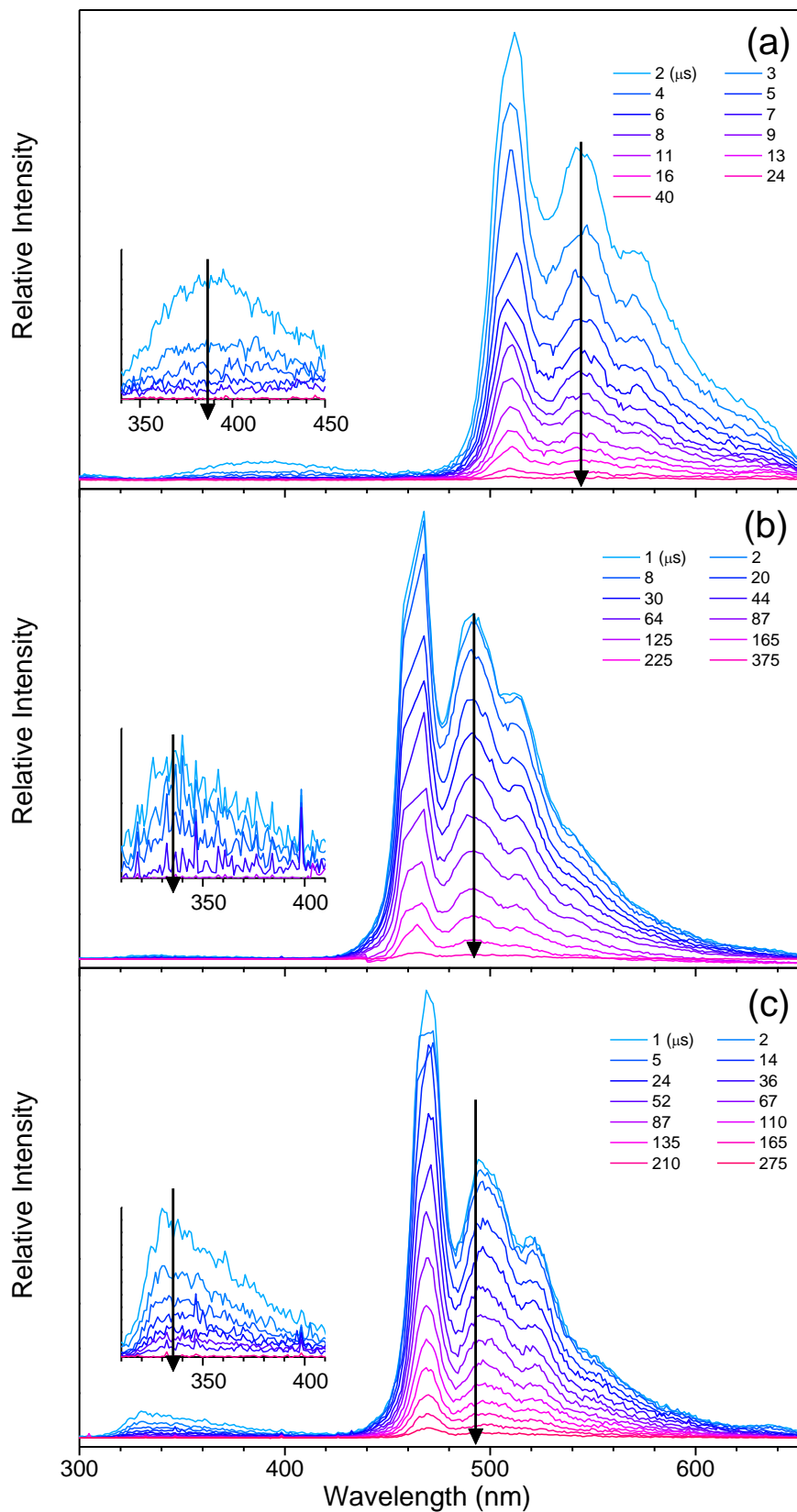


Figure 6.5 Broadband time-resolved emission spectra of **1** (a), **2** (b) and **3** (c) recorded at indicated decay times in deoxygenated acetonitrile with nitrogen purging after 280 nm excitation. The insets show the magnified spectra

corresponding to the delayed fluorescence of the respective system. The arrows indicate the directions of spectral evolutions.

Figure 6.5 displays ns-TRE spectra recorded for complexes **1**, **2** and **3** in deoxygenated acetonitrile at delay time $1\mu\text{s}$ after excitation. For all the three complexes, the ns-TRE reveals dual emission with their wavelength locations and the spectral profiles matching with those in the steady state emission of the respective complexes (Figure S9).¹ This indicates that the high and low energy component in the TRE of each complex is originated due to the DF and phosphorescence from the $S_1^1\pi\pi^*$ and the $T_1^3\pi\pi^*$ state, respectively. Moreover, a direct comparison between the time-resolved spectra obtained for DF in the ns-TRE and the PF from the fs-TRF (insets of Figure 6.1) shows identical feature manifesting that the two emissions, although occur at vastly different time regimes (10 ps for PF *versus* $10\mu\text{s}$ for DF), are having the same intrinsic origin *i.e.*, the ligand centred $\pi\pi^* S_1 \rightarrow S_0$ transition for each of the complex. As a consequence, other probable assignments, like excimer, can be excluded for the formation of long-lived fluorescence displayed by these complexes.

It can be seen from Figure 6.5 that the transient emission in the nanosecond to microsecond time regime is prevailed by the phosphorescence from $T_1^3\pi\pi^*$ state with only minute involvement of the DF from the $S_1^1\pi\pi^*$ state. On the basis of this and taking into consideration of the much faster radiative decay rate of the $S_1^1\pi\pi^*$ ($k_f(S_1)$) than $T_1^3\pi\pi^*$ state ($k_f(T_1)$), it can be derived a subtle involvement of the $S_1^1\pi\pi^*$ in relative to $T_1^3\pi\pi^*$ state with the

population ratio between the two state being no greater than 10^{-4} at delay time beyond tens nanoseconds after the photo-excitation.

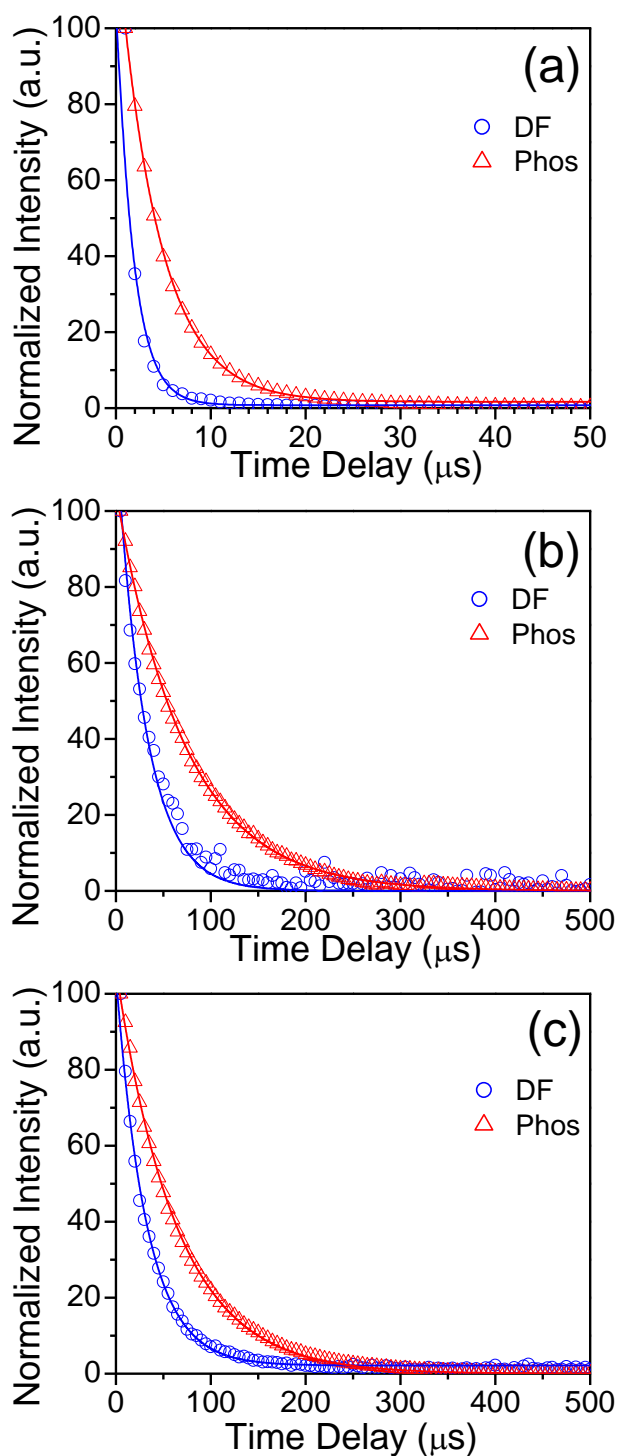


Figure 6.6 Normalized experimental (\circ , Δ) and fitted (—) phosphorescence (Phos) and delayed fluorescence (DF) kinetic traces obtained for **1** (a), **2** (b) and **3** (c) after 280 nm excitation in deoxygenated acetonitrile.

Figure 6.6 shows the kinetic traces of the DF and phosphorescence extracted from the TRE spectral data for complexes **1-3** (Figure 6.5). Analysis of the kinetic decay of the emission intensity observed a single exponential dynamics with the lifetime determined to be $\sim 1.9/4.3 \mu\text{s}$, $30.5/61.5 \mu\text{s}$, and $32.8/63.7 \mu\text{s}$ for the DF/phosphorescence ($\tau_{\text{DF}}/\tau_{\text{phos}}$) of **1**, **2**, and **3** respectively (Table 6.1). It is notable that the value τ_{DF} is about half of that for τ_{phos} in all the three complexes. In addition, it is noted that the $\tau_{\text{DF}}/\tau_{\text{phos}}$ for **2** is respectively similar to that of **3** but is significantly longer than the counterpart values in **1**.

Parallel experiment but under aerated condition was also performed for the three complexes, which revealed a simultaneous shortening of both the τ_{DF} and τ_{phos} . This implies that oxygen may lead to a simultaneous quenching of both the excited state emissions. Taking complex **2** as an example, the $\tau_{\text{DF}}/\tau_{\text{phos}}$ was determined to be $\sim 0.4/0.5 \mu\text{s}$ (τ_0) under the aerated conditions. Considering that the oxygen concentration ($[\text{O}_2]$) is $\sim 10^{-3} \text{ M}$ in the aerated solution and $< \sim 10^{-5} \text{ M}$ under nitrogen gas purging environment, the DF and phosphorescence quenching rate (k_q) can be estimated to be $\sim 2.3 \times 10^9$ and $2.0 \times 10^9 \text{ M}^{-1} \text{ s}^{-1}$ respectively ($1/\tau = 1/\tau_0 + k_q[\text{O}_2]$).² The nearly identical quenching rate between the two emission bands implies that both the emissions should have the same dynamic origin.

DF from long-lived S_1 state could be produced by two possible mechanisms: (i) triplet-triplet annihilation (TTA; $T_1 + T_1 \rightarrow S_1 + S_0$) and (ii) thermally activated triplet-to-singlet upconversion ($T_1 \rightarrow S_1$).^{2,13,14} The thermally activated process is in essence a unimolecular process where the lifetime of DF is expected to be identical to the phosphorescence decay.^{2,13,15} In the contrary, the TTA pathway is a bimolecular process which involves annihilation of two T_1

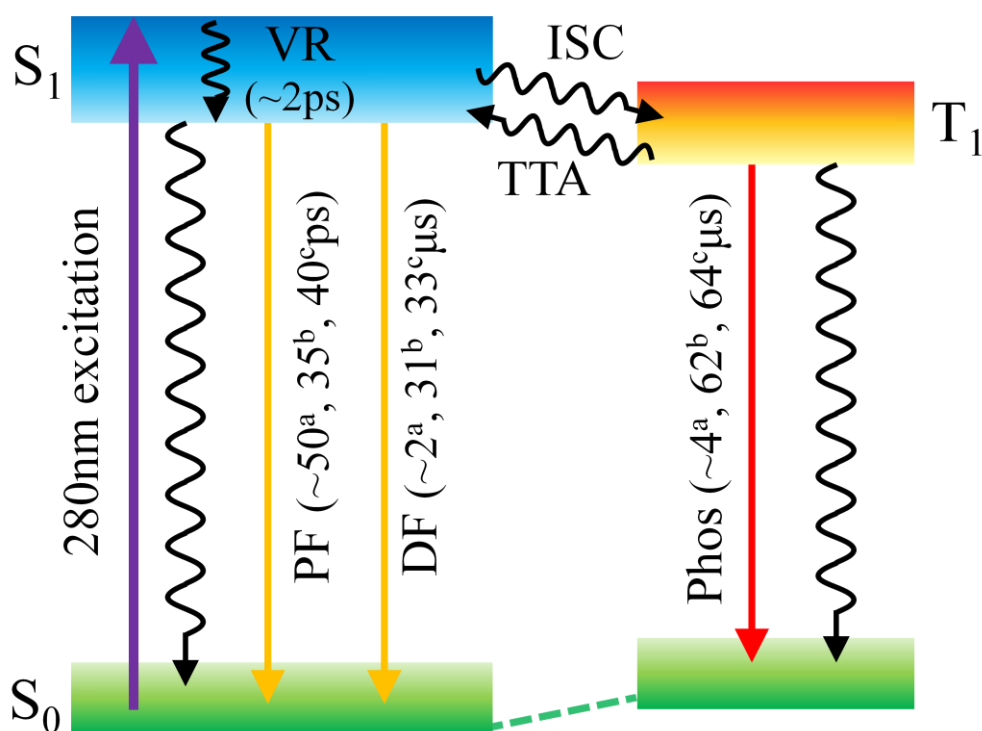
state molecules to form one singlet excited species (S_1).^{2,13} According to the rate law, a characteristic of TTA-induced DF is that the lifetime of DF (τ_{DF}) is half of the lifetime of the phosphorescence (τ_{Ph}).^{13,16,17}

On the basis of this and the result of the oxygen quenching experiment and more important the observation that for all the three complexes the τ_{DF} is about half of the τ_{Ph} , it is with certain that DF observed in complexes **1-3** is originated due to the TTA mechanism. It is noteworthy that although the TTA-induced DF has been known as a common phenomenon in various organic systems, especially in the area of conjugated polymer,^{13,16,18} such a phenomenon is rarely reported in transition metal complexes, to the best of our knowledge.¹⁹ In this regard, the gold(I) complexes selected in this study present rare cases for the involvement of this procedure in transition metal complexes.

6.2 Discussion

6.2.1 Emission pathways of gold(I) oligo(*o*- or *m*-PE) complexes

Putting together the fs to ns and the ns to μs time-resolved spectral and dynamic results obtained for **1**, **2** and **3** in acetonitrile (Figures 6.1 to 6.6) shows clearly that the low-energy component of the dual emission in the steady state spectrum is due solely to the phosphorescence, while both the PF and DF are involved to give the high-energy component in each of the complexes. The deactivation cascade and the emission pathway for these complexes can be constructed and is summarized in Scheme 6.1.



Scheme 6.1 Proposed deactivation and emission pathways for oligo(PE) gold(I) complexes **1**^a, **2**^b and **3**^c in acetonitrile after 280 nm excitation. Radiative and non-radiative transitions are indicated in straight and wavy arrows respectively.

(VR = vibrational relaxation; PF = prompt fluorescence; DF = delayed fluorescence; Phos = phosphorescence; ISC = intersystem crossing; TTA = triplet-triplet annihilation)

After photo-excitation, the photo-populated S_1 $^1\pi\pi^*$ state first undergoes vibrational or structural relaxation and then transfers its population to the T_1 $^3\pi\pi^*$ state through ISC. These relaxation processes proceed with time constants of ~ 2 ps and ~ 35 - 50 ps respectively. The rate of ISC appears to be affected by both the length and the substitution pattern of the PE ligand. The ISC leads to a rapid quench of the PF and the formation of the T_1 $^3\pi\pi^*$ state with a nearly unitary yield. Given the time constants (τ_{PF}) and the radiative rate constants ($k_f(S_1)$) of the PF, the PF quantum efficiency ($\Phi_{PF} = \tau_{PF} \times k_f(S_1)$) can be estimated to be on the order of $\sim 10^{-2}$ - 10^{-3} for the three complexes under investigation.

Upon the formation of the T_1 $^3\pi\pi^*$ state and in the timescale from nanoseconds to microseconds, the T_1 $^3\pi\pi^*$ state decays and at the same time undergoes intermolecular TTA to convert partially its population back to the S_1 $^1\pi\pi^*$ state, leading to the DF with lifetime being about half of that of the phosphorescence from the T_1 $^3\pi\pi^*$ state. Owing to its long lifetime, the S_1 $^1\pi\pi^*$ state derived DF, albeit arising due to only a minute fraction of the excited state population, may contribute significantly to the overall fluorescence as measured in the steady state emission spectrum.¹ In addition, given the much greater radiative rate constant of the S_1 $^1\pi\pi^*$ than the T_1 $^3\pi\pi^*$ state ($k_r(S_1) \gg k_r(T_1)$), the TTA-induced T_1 $^3\pi\pi^*$ to S_1 $^1\pi\pi^*$ excited state conversion, although occurs to a

limited extent, may cause a pronounced increase in the fluorescence in relative to the phosphorescence in the steady state emission spectrum.

6.2.2 Comparison of the emission property between gold(I) oligo(*o*-PE) and gold(I) oligo(*m*-PE) complexes

Taking together the fluorescence decay dynamics at the various time regime (Figures 6.2 and 6.6) allow for deriving the percentage contribution of the DF to the overall fluorescence observed in the steady state emission. The percent contribution made by the DF is ~90% for **3**, ~60% for **2** and ~52% for **1**. The much greater involvement of DF in **3** compared to that of **2** and **1** suggests a distinct feature in excited state of **3** in relative to **1** and **2**. However, the larger contribution of DF in **3** compared to **2** and **1** appears to arise from different causes.

For **2** and **3**, the varied ratio in the steady state emission of the fluorescence to the phosphorescence (Figure S9) is mainly due to the greater weighting factor of the DF in **3** than **2**; this is implied by the fs-TRF (Figure 6.1) which suggests the DF to contribute ~3.6% in **3** but ~0.5% in **2** to the overall fluorescence emission. According to the rate law,^{16,17} this may reflect a higher efficiency of the TTA in **3** than in **2**. Given the different PE ligand length between **2** and **3** (i.e., two repeating PE unit in **2** vs. three repeating PE unit in **3**), it is plausible that the TTA efficiency is enhanced upon elongating the PE ligand.

When making comparison between **1** and **3**, besides the slightly lower TTA efficiency as suggested by the fs-TRF (Figures 6.1 and 6.2), the much

smaller DF involvement in **1** (~1%) than **3** (~3.6%) could also be related to the much shorter DF lifetime (~1.9 μs) than that of **3** (~32.8 μs) (Table 6.1). Given the ligand-centred $\pi\pi^*$ excitation of the S_1 and T_1 states and the known photochemical instability of the *o*-PE systems (in performing the Bergman cyclization reaction),^{20,21} the shorter DF lifetime displayed by **1** might be accounted for by involvement of a photochemical decay path in the particular case of complex **1**. The photochemical reaction is most likely to proceed in the T_1 $^3\pi\pi^*$ state, providing a channel to compete with the TTA and therefore quenches the excited state population and shortens the lifetimes of both the T_1 $^3\pi\pi^*$ state and the DF from the TTA produced S_1 $^1\pi\pi^*$ state.

The presence of this additional relaxation channel in the *o*-PE but not the *m*-PE containing complex may constitute a major factor for the shorter $\tau_{\text{DF}}/\tau_{\text{Ph}}$ lifetime observed for **1** ($\tau_{\text{DF}}/\tau_{\text{Ph}} = 1.9/4.3$ μs) than **3** ($\tau_{\text{DF}}/\tau_{\text{Ph}} = 32.8/63.7$ μs) (Table 6.1). This may also provide an explanation for the different emission behaviors between the two complexes, including for instance, the low emission quantum yield of **1** compared to **3** and the less involvement of the phosphorescence in the steady state emission of **1** than **3** (Figure S9).¹ This observation underscores the role of substitution pattern in varying significantly the emission property between the gold(I) oligo(*o*-PE) and the gold(I) oligo(*m*-PE) complexes.

6.2.3 General features of the excited states of gold(I) oligo(*o*- or *m*-PE) complexes

To sum up, the results on the emission property of the *o*- and *m*-PE gold(I) complexes provide important insights as follows: first, as a common feature, all the three systems display nearly unitary ISC efficiency with the ISC time constant at tens of picoseconds timescale. Second, the efficiency of the T_1 $^3\pi\pi^*$ state to perform TTA in giving DF is favored by longer PE ligand length in the gold(I) oligo(*m*-PE) complexes. Third, the propensity toward photochemical reaction displayed by the gold(I) oligo(*o*-PE) complex accounts for the distinct emission property showed by the gold(I) oligo(*o*-PE) from the gold(I) oligo(*m*-PE) complexes.¹

It is worth noting that, although these gold(I) *o*-PE and *m*-PE complexes exhibit the nearly unitary ISC efficiency, their ISC time constant is indeed much slower than the ultrafast ISC times ($< \sim 1$ ps) reported for many other transition metal complexes.⁵⁻⁹ Regarding the increasing attention on the precise timescale and the factor(s) that may affect the rate of ISC in transition metal complexes,^{4e,5-9,22} the ISC time constants obtained here for the varied selected gold(I) PE complexes add new information that may help for more fully understanding the ISC in transition metal complexes.

6.3 References

1. Lu, W.; Kwok, W. M.; Ma, C.; Chan, C. T. L.; Zhu, M. X.; Che, C. M. *J. Am. Chem. Soc.* **2011**, *133*, 14120-14135.
2. Turro, N. J. *Modern Molecular Photochemistry*; University Science Book, Mill Valley, CA, **1991**.
3. (a) Wilson, J. S.; Chawdhury, N.; Köhler, A.; Friend, R. H.; Al-Mandhary, M. R. A.; Khan, M. S.; Younus, M.; Raithby, P. R. *J. Am. Chem. Soc.* **2001**, *123*, 9412-9417. (b) Liu, Y.; Jiang, S.; Glusac, K.; Powell, D. H.; Anderson, D. F.; Schanze, K. S. *J. Am. Chem. Soc.* **2002**, *124*, 12412-12413. (c) Wilson, J. S.; Wilson, R. J.; Friend, R. H.; Köhler, A.; Al-Suti, M. K.; Al-Mandhary, M. R. A.; Khan, M. S. *Phys. Rev. B* **2003**, *67*, 125206.
4. (a) Che, C. M.; Chao, H. Y.; Miskowski, V. M.; Li, Y.; Cheung, K. K. *J. Am. Chem. Soc.* **2001**, *123*, 4985-4991. (b) Lu, W.; Xiang, H. F.; Zhu, N.; Che, C. M. *Organometallics* **2002**, *21*, 2343-2346. (c) Chao, H. Y.; Lu, W.; Li, Y.; Chan, M. C. W.; Che, C. M.; Cheung, K. K.; Zhu, N. *J. Am. Chem. Soc.* **2002**, *124*, 14696-14706. (d) Lu, W.; Zhu, N.; Che, C. M. *J. Organomet. Chem.* **2003**, *670*, 11-16. (e) Lu, W.; Zhu, N.; Che, C. M. *J. Am. Chem. Soc.* **2003**, *125*, 16081-16088. (f) Tong, G. S. M.; Chow, P. K.; Che, C. M. *Angew. Chem., Int. Ed.* **2010**, *49*, 9206-9209.
5. (a) Damrauer, N. H.; Cerullo, G.; Yeh, A.; Boussie, T. R.; Shank, C. V.; McCusker, J. K. *Science* **1997**, *275*, 54-57. (b) Yeh, A.; Shank, C. V.; McCusker, J. K. *Science* **2000**, *289*, 935-938. (c) Bhasikuttan, A. C.; Suzuki, M.; Nakashima, S.; Okada, T. *J. Am. Chem. Soc.* **2002**, *124*, 8398-8405. (d)

- Browne, W. R.; Coates, C. G.; Brady, C.; Matousek, P.; Towrie, M.; Botchway, S. W.; Parker, A. W.; Vos, J. G.; McGarvey, J. J. *J. Am. Chem. Soc.* **2003**, *125*, 1706-1707. (e) Cannizzo, A.; Mourik, F.; Gawelda, W.; Zgrablic, G.; Bressler, C.; Chergui, M. *Angew. Chem., Int. Ed.* **2006**, *45*, 3174-3176.
6. (a) Cannizzo, A.; Blanco-Rodríguez, A. M.; Nahhas, A. E.; Šebera, J.; Záliš, S.; Vlček, A.; Chergui, M. *J. Am. Chem. Soc.* **2008**, *130*, 8967-8974. (b) Nahhas, A. E.; Cannizzo, A.; Mourik, F.; Blanco-Rodríguez, A. M.; Záliš, S.; Vlček, A.; Chergui, M. *J. Phys. Chem. A* **2010**, *114*, 6361-6369. (c) Busby, M.; Matousek, P.; Towrie, M.; Vlček, A. *J. Phys. Chem. A* **2005**, *109*, 3000-3008. (d) Liard, D. J.; Busby, M.; Farrell, I. R.; Matousek, P.; Towrie, M.; Vlček, A. *J. Phys. Chem. A* **2004**, *108*, 556-567.
7. (a) Ramakrishna, G.; Goodson, T., III; Rogers-Haley, J. E.; Cooper, T. M.; McLean, D. G.; Urbas, A. *J. Phys. Chem. C* **2009**, *113*, 1060-1066. (b) Abedin-Siddique, Z.; Ohno, T.; Nozaki, K.; Tsubomura, T. *Inorg. Chem.* **2004**, *43*, 663-673. (c) Whittle, C.; Weinstein, J. A.; George, M. W.; Schanze, K. S. *Inorg. Chem.* **2001**, *40*, 4053-4062. (d) Hissler, M.; Connick, W. B.; Geiger, D. K.; McGarrah, J. E.; Lipa, D.; Lachicotte, R. J.; Eisenberg, R. *Inorg. Chem.* **2000**, *39*, 447-457.
8. Gawelda, W.; Cannizzo, A.; Pham, V.-T.; Mourik, F.; Bressler, C.; Chergui, M. *J. Am. Chem. Soc.* **2007**, *129*, 8199-8206.
9. (a) Quochi, F.; Saba, M.; Artizzu, F.; Mercuri, M. L.; Deplano, P.; Mura, A.; Bongiovanni, G. *J. Phys. Chem. Lett.* **2010**, *1*, 2733-2737. (b) Ramachandra,

- S.; Polo, F.; Edafe, F.; Schuermann, K. C.; Nijhuis, C. A.; Belser, P.; Reus, W. F.; Whitesides, G. M.; De Cola, L. *Pure Appl. Chem.* **2011**, *83*, 779-799.
10. (a) Liard, D. J.; Busby, M.; Matousek, P.; Towrie, M.; Vlček, A. *J. Phys. Chem. A* **2004**, *108*, 2363-2369. (b) Hester, R. E.; Matousek, P.; Moore, J. N.; Parker, A. W.; Toner, W. T.; Towrie, M. *Chem. Phys. Lett.* **1993**, *208*, 471-478. (c) Matousek, P.; Parker, A. W.; Towrie, M.; Toner, W. T. *J. Chem. Phys.* **1997**, *107*, 9807-9817. (d) Weaver, W. L.; Huston, L. A.; Iwata, K.; Gustafson, T. L. *J. Phys. Chem.* **1992**, *96*, 8956-8961. (e) Iwata, K.; Hamaguchi, H. *J. Phys. Chem. A* **1997**, *101*, 632-637.
11. Duvanel, G.; Grilj, J.; Schuway, A.; Gossauer, A.; Vauthey, E. *Photochem. Photobiol. Sci.* **2007**, *6*, 956-963.
12. Sluch, M. I.; Godt, A.; Bunz, U. H. F.; Berg, M. A. *J. Am. Chem. Soc.* **2001**, *123*, 6447-6448.
13. (a) Swenberg, C. E. *J. Chem. Phys.* **1969**, *51*, 1753-1764. (b) Azumi, T.; McGlynn, S. P. *J. Chem. Phys.* **1963**, *39*, 1186-1194.
14. Bohne, C.; Abuin, E. B.; Scaiano, J. C. *J. Am. Chem. Soc.* **1990**, *112*, 4226-4231.
15. Turek, A. M.; Krishnamoorthy, G.; Phipps, K.; Saltiel, J. *J. Phys. Chem. A* **2002**, *106*, 6044-6052.
16. (a) Gerhard, A.; Bässler, H. *J. Chem. Phys.* **2002**, *117*, 7350-7356. (b) Hertel, D.; Bässler, H.; Guentner, R.; Scherf, U. *J. Chem. Phys.* **2001**, *115*, 10007-10013. (c) Hertel, D.; Setayesh, S.; Nothofer, H.-G.; Scherf, U.; Müllen, K.;

- Bässler, H. *Adv. Mater.* **2001**, *13*, 65-69. (d) Romanovskii, Y. V.; Bässler, H. *Chem. Phys. Lett.* **2000**, *326*, 51-57.
17. Bodunov, E. N.; Berberan-Santos, M. N.; Martinho, J. M. G. *Chem. Phys.* **2005**, *316*, 217-224.
18. (a) Partee, J.; Frankevich, E. L.; Uhlhorn, B.; Shinar, J.; Ding, Y.; Barton, T. *J. Phys. Rev. Lett.* **1999**, *82*, 3673-3676. (b) Baldo, M. A.; Adachi, C.; Forrest, S. R. *Phys. Rev. B* **2000**, *62*, 10967-10977. (c) Baldo, M. A.; Forrest, S. R. *Phys. Rev. B* **2000**, *62*, 10958-10966.
19. Abedin-Siddique, Z.; Yamamoto, Y.; Ohno, T.; Nozaki, K. *Inorg. Chem.* **2003**, *42*, 6366-6378.
20. Grubbs, R. H.; Kratz, D. *Chem. Ber.* **1993**, *126*, 149-157.
21. Jones, R. R.; Bergman, R. G. *J. Am. Chem. Soc.* **1972**, *94*, 660-661.
22. Steffen, A.; Tay, M. G.; Batsanov, A. S.; Howard, J. A. K.; Beeby, A.; Vuong, K. Q.; Sun, X.-Z.; George, M. W.; Marder, T. B. *Angew. Chem., Int. Ed.* **2010**, *49*, 2349-2353.

Chapter 7 Conclusions

In this thesis, the dynamics, electronic nature and deactivation pathway of photo-induced excited states have been examined for two main types of systems, (i) methyl-4-dimethylaminobenzoate (DMABME) and its derivatives and (ii) the gold(I) oligo-phenyleneethynylene (PE) complexes and derivatives, including free ligands of several gold(I) PE complexes.

The roles of aromatic carbonyl (AC) substitution, solvent, ligand conjugation, ligand substitution pattern as well as ligand length on the excited state dynamics, including the rate of intramolecular charge transfer (ICT) reaction, the rate of intersystem crossing (ISC) efficiency, as well as the emission pathway have been investigated by a combined application of femtosecond broadband time-resolved fluorescence (fs-TRF), fs-TRF anisotropy (fs-TRFA), fs transient absorption (fs-TA), nanosecond time-resolved emission (ns-TRE) and ns-TA. A joint application of these time-resolved spectroscopic methods allows complementary experimental data to be obtained for monitoring directly the excited state spectra and the temporal evolution of excited state spectra, so as to provide direct evidence for determining the dynamics and factors affecting the dynamics of the excited state systems.

The combined fs-TRF, fs-TRFA, fs-TA and ns-TA study on DMABME in acetonitrile observed directly the excited state ICT reaction from the photo-prepared locally excited (^1LE) state to the intramolecular charge transfer (^1ICT) state, followed by ISC from the ^1ICT to triplet ($^3\text{T}_1$) state ($^1\text{LE} \rightarrow ^1\text{ICT} \rightarrow ^3\text{T}_1$). The time constant for the ICT reaction was determined to be ~ 0.8 ps and that for the ISC was found to be ~ 1.9 ns. Broadband fs-TRFA measurement affords

explicit evidence for a common $L_a \pi\pi^*$ parentage for both the ^1LE and the ^1ICT states. This coupled with the large Stokes' shift displayed by the ^1ICT fluorescence from the $L_a \pi\pi^*$ absorption suggests the importance of large scale intramolecular structural rearrangement accompanied by the ICT reaction.

The result lends strong support to the widely known twisted ICT (TICT) model in describing the ICT reaction. The ~ 1.9 ns time constant of ISC is at variation with the typical ultrafast ISC known for AC compounds. This result highlights a crucial role of the *para*-DMA-carboxylate substitution in affecting the dynamics and deactivation pathway of the excited state decay. Given that the $^3\text{T}_1$ state of compound like DMABME may act to photo-sensitize reaction of DNA in producing harmful photoproduct (e.g. Cyclobutane Pyrimidine Dimer, CPD), the high efficiency of the $^3\text{T}_1$ formation in DMABME may explain the observation of some related DNA photolesions in trial experiment on the safety for using the DMABME type of compounds as ingredient in sunscreen products.

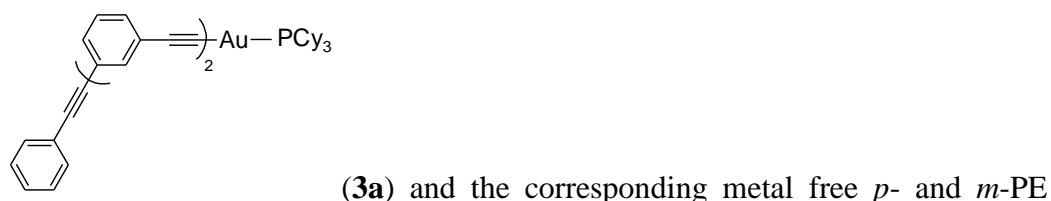
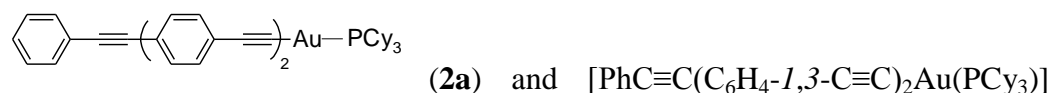
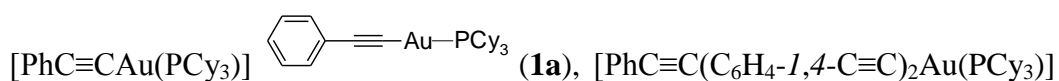
The effect of solvent hydrogen-bonding (H-bonding) on the excited state decay of DMABME was investigated by comparison of the spectra and dynamics results obtained in aprotic solvent acetonitrile and protic solvent methanol. The nearly identical ICT reaction time constant (~ 1 ps) in the two solvents indicates that the ^1LE state and ICT reaction is not affected significantly by the H-bonding interaction between solute and solvent molecules. In contrast, the drastic drop in the ^1ICT state lifetime, from ~ 1.9 ns in acetonitrile to ~ 120 ps in methanol, indicates a strong effect of H-bonding in affecting the dynamics of the ^1ICT state.

The dramatic shortening of the ^1ICT state lifetime in methanol from in acetonitrile is indicative of the presence of a solvent-assisted deactivation

channel which must compete effectively with the ISC for the depopulation of the ^1ICT state. The much greater degree of dynamic Stokes' shift exhibited by the fluorescence of ^1ICT state in methanol than in acetonitrile suggests formation of the fully solvated H-bonded ICT ($^1\text{HICT}$) state, which is energetically more stabilized by the solute-solvent H-bonding when comparing to the nascent ^1ICT state formed from the initial ^1LE state. The additional deactivation channel is assigned to the internal conversion (IC) from the $^1\text{HICT}$ state to the ground state (S_0).

This assignment is supported by the kinetic isotope effect on the $^1\text{HICT}$ state lifetime which found that the lifetime in CH_3OD is ~ 1.4 times longer than that in CH_3OH . This combined with the nearly identical $^1\text{HICT}$ state lifetime in CH_3OD and CD_3OD indicates compellingly that it is the hydroxyl hydrogen, not the hydrogen in the methyl group that is involved primarily in the H-bonding interaction and affecting the nonradiative decay of the $^1\text{HICT}$ state. The presence of this additional deactivation channel suppresses the $^3\text{T}_1$ state formation, which may, as a result, alleviate the potential harmful effect that may cause by the compound like DMABME in using as an ingredient of sunscreen products.

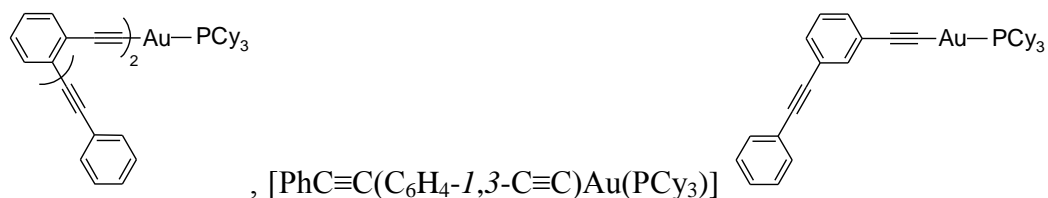
The excited state and the emission properties of the gold(I)-PE complexes

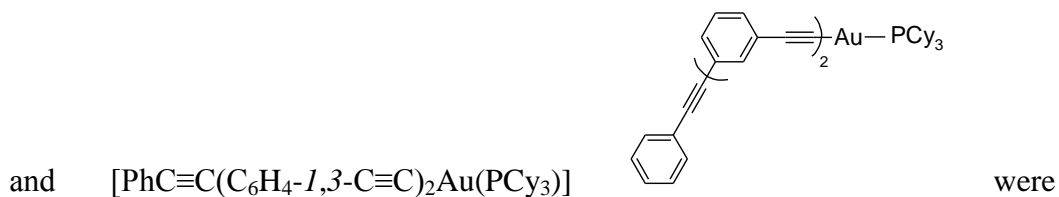


oligomers (**2b** and **3b**) were studied using fs-TRF, fs-TA and ns-TRE spectroscopy. The electronic origins of the excited states of the gold(I) complexes are assessed by the direct comparison of the spectral and dynamic data obtained for the counterpart system with and without the gold(I) metal centre. The experimental results indicate a ligand-centred (LC) $\pi\pi^*$ nature for the S_1 and T_1 states, and shows that the ligand π -conjugation plays an essential role in dictating the rate of ISC (k_{ISC}) for the gold(I) complexes **1a-3a**.

A significant decrease by ~ 4 orders of magnitude in the k_{ISC} from **1a** ($\sim 1.2 \times 10^{12} \text{ s}^{-1}$) to **3a** ($\sim 2.6 \times 10^{10} \text{ s}^{-1}$) to **2a** ($\sim 1.6 \times 10^8 \text{ s}^{-1}$) is arising mainly due to the increase in the π -conjugation of the PE ligand involved in these complexes. The variation in the k_{ISC} leads to varied rates of the ISC in quenching the prompt fluorescence (PF) in the three complexes. This, together with the ligand substitution pattern dependent triplet-triplet annihilation (TTA) for the formation of delayed fluorescence (DF), provide in-depth explanation for the largely different emission properties (such as the emission quantum yield and the ratio of the fluorescence to phosphorescence) displayed by the three gold(I) PE complexes.

Detailed investigation utilizing the broadband fs-TA, fs-TRF and ns-TRE on three gold(I) oligo-PE complexes, $[\text{PhC}\equiv\text{C}(\text{C}_6\text{H}_4\text{-}i,2\text{-C}\equiv\text{C})_2\text{Au}(\text{PCy}_3)]$





conducted to study effect of substitution pattern and the length of PE ligand on the excited states dynamics and the emission property of the gold(I)-PE complexes. The results show that, despite of the difference in the ligand substitution pattern and varied length of the PE ligand, the ISC from the S_1 $^1\pi\pi^*$ to T_1 $^3\pi\pi^*$ state takes place rapidly in very similar timescale with nearly unity efficiency for all the three complexes. The three complexes were found to feature LC dual emission comprising high energy emission due to the fluorescence from the lowest singlet S_1 $^1\pi\pi^*$ state and a low energy emission due to the phosphorescence from the lowest triplet T_1 $^3\pi\pi^*$ state.

The results obtained from the fs-TRF and ns-TRE show direct evidence that the fluorescence component of the dual emission is composed of PF and DF which are both from the S_1 $^1\pi\pi^*$ state but occurring in distinctively different timescales. The PF arises due to the tens picoseconds lifetime of the initial photo-populated S_1 $^1\pi\pi^*$ state, while the DF is produced from the T_1 $^3\pi\pi^*$ state through the process known as triplet-triplet annihilation (TTA).

The efficiency of TTA was found to vary with both the substitution pattern and the length of substitution of the PE ligand. It is facilitated by the increase of the PE ligand length for the *m*-PE containing complexes, and is decreased on going from the *m*-PE to *o*-PE containing complexes most likely due to the presence of additional photochemical reaction in the latter system. The nearly unitary T_1 $^3\pi\pi^*$ formation yield and the involvement of TTA in giving DF

are the salient feature of the gold(I) PE complexes under investigation. Such a feature allows the complexes to display dual emission with a wide range of wavelength coverage, which could have important implication for the development of PE-based optoelectronic materials for the future optical applications.

To conclude, broadband time-resolved spectroscopy based on the combined application of fs-TRF, fs-TRFA, fs-TA, ns-TRE and ns-TA has been demonstrated to be a powerful and versatile tool for revealing the excited state dynamics and varied factors affecting the dynamics of both the organic molecule DMABME and the transition metal complexes, the gold(I) PE systems. The results obtained provide comprehensive yet detailed characterization of the electronic nature, temporal evolution and the overall deactivation cascades for the excited states of the compounds under investigation. The spectral and dynamic information gathered in this work help to clarify uncertainties in the literature for some of the studied systems and are also useful for potential applications that might be made based on the compounds investigated in this thesis.

Appendix

Supplementary Figures

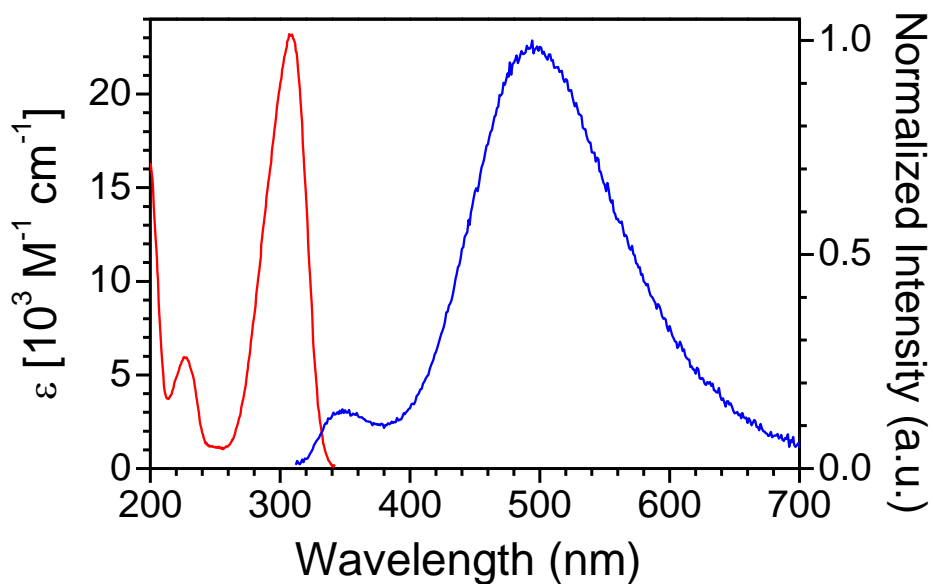


Figure S1 Steady state UV-visible absorption (red) and normalized 280 nm excited fluorescence (blue) spectra recorded for DMABEE in acetonitrile.

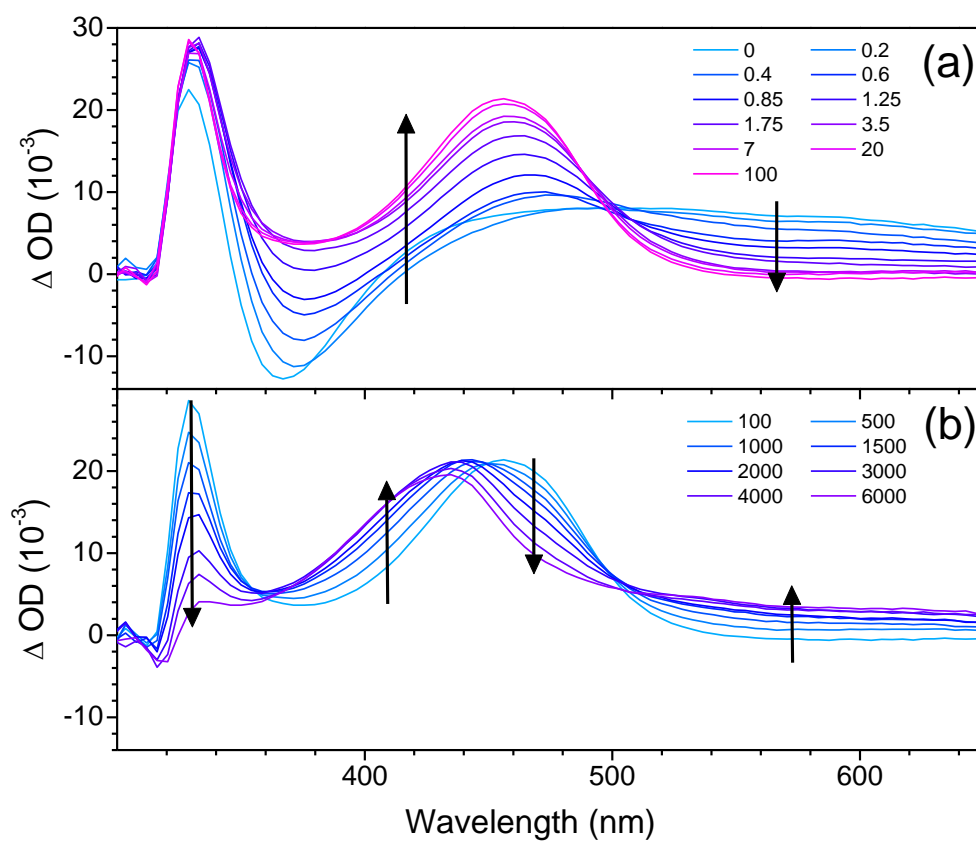


Figure S2 Broadband transient absorption of DMABEE in acetonitrile recorded at 0-100 ps (a) and 100-6000 ps (b) after 280 nm excitation. The arrows indicate temporal evolution of the spectra.

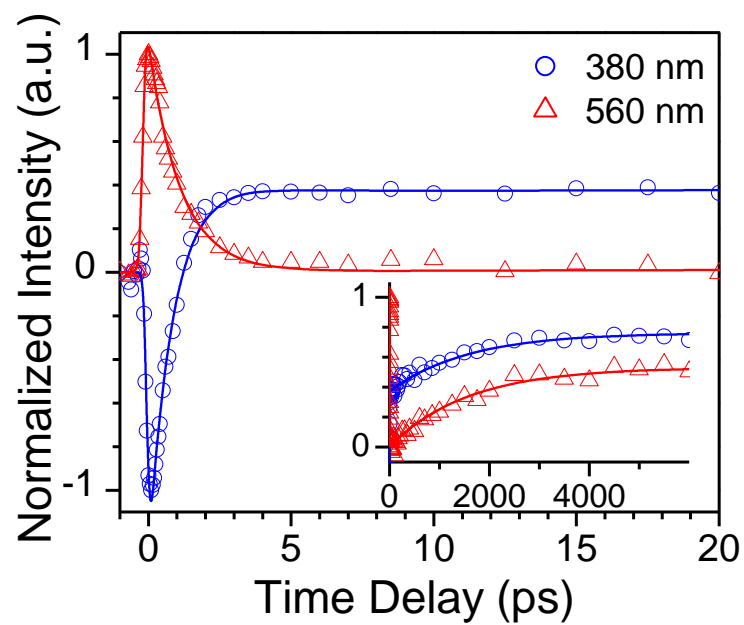


Figure S3 Experimental (\circ , Δ) and fitted (—) kinetic decay profiles of TA at indicated wavelengths for 280 nm excited DMABEE in acetonitrile. The inset shows the decay profiles at longer decay time up to ~6 ns.

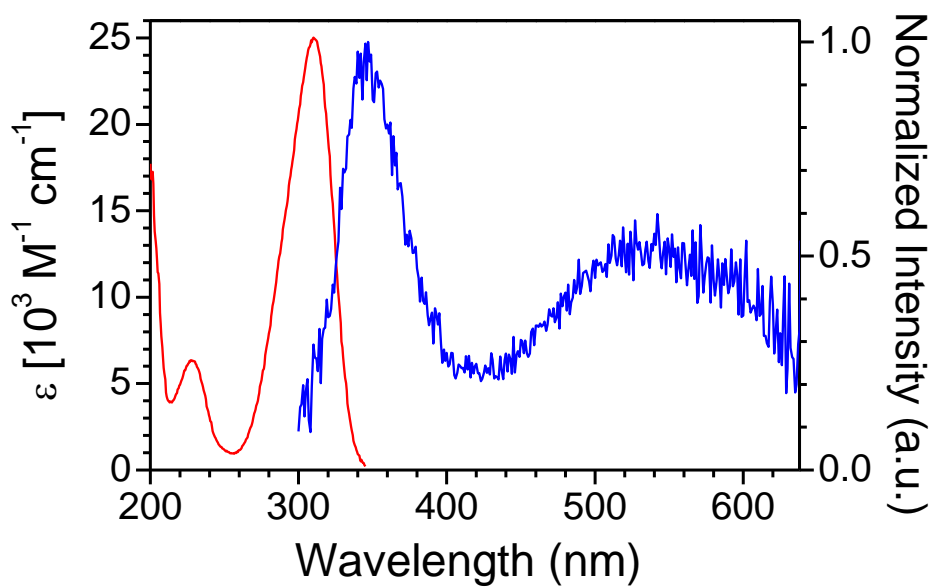


Figure S4 Steady state UV-visible absorption (red) and normalized 280 nm excited fluorescence (blue) spectra recorded for DMABEE in methanol.

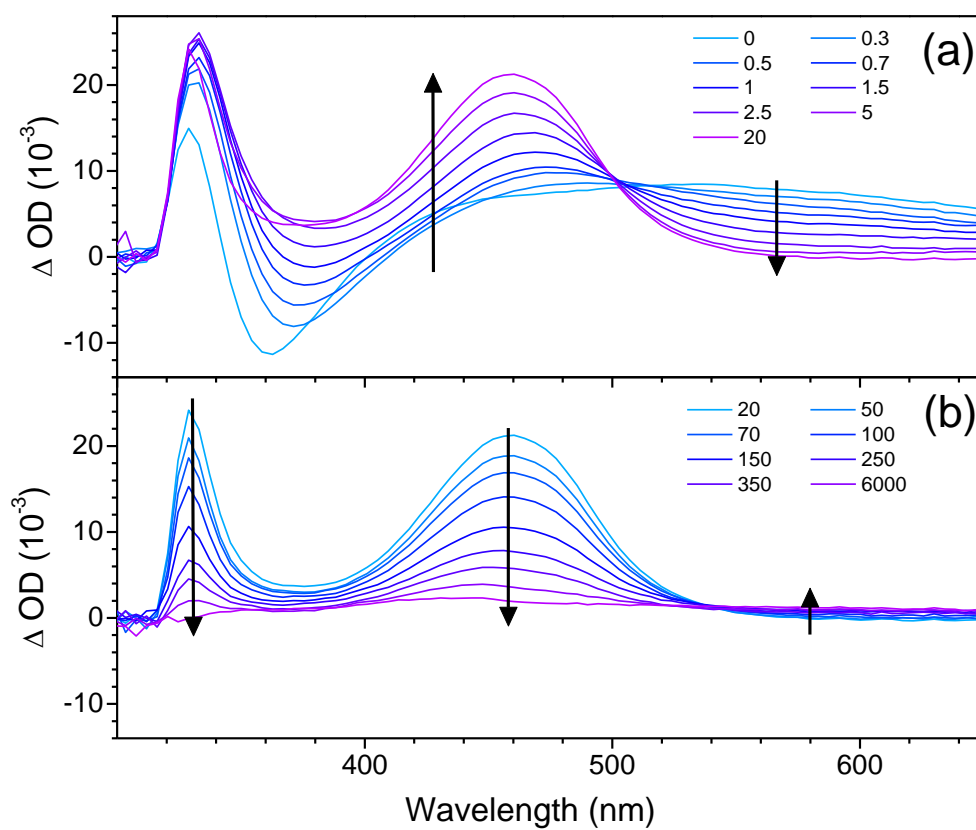


Figure S5 Broadband transient absorption of DMABEE in methanol recorded at 0-20 ps (a) and 20-6000 ps (b) after 280 nm excitation. The arrows indicate temporal evolution of the spectra.

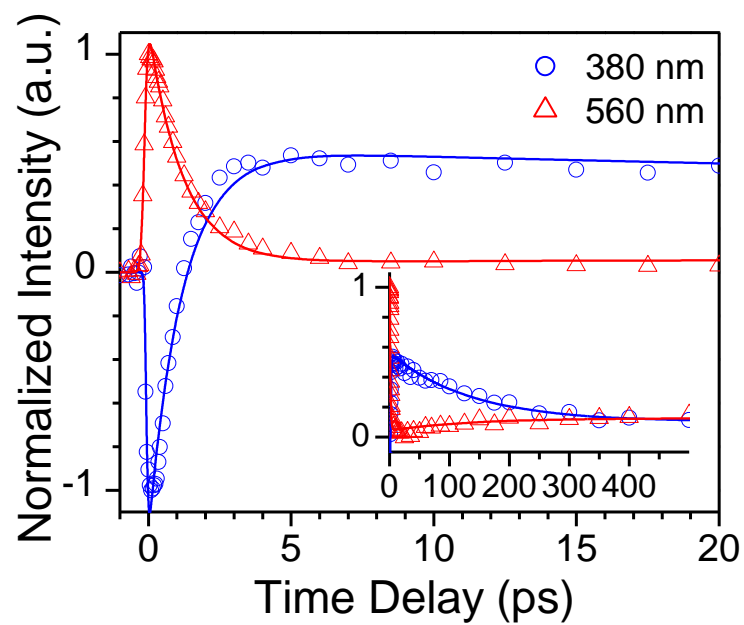


Figure S6 Experimental (\circ , Δ) and fitted (—) kinetic decay profiles of TA at indicated wavelengths for 280 nm excited DMABEE in methanol. The inset shows the decay profiles at longer decay time up to ~1 ns.

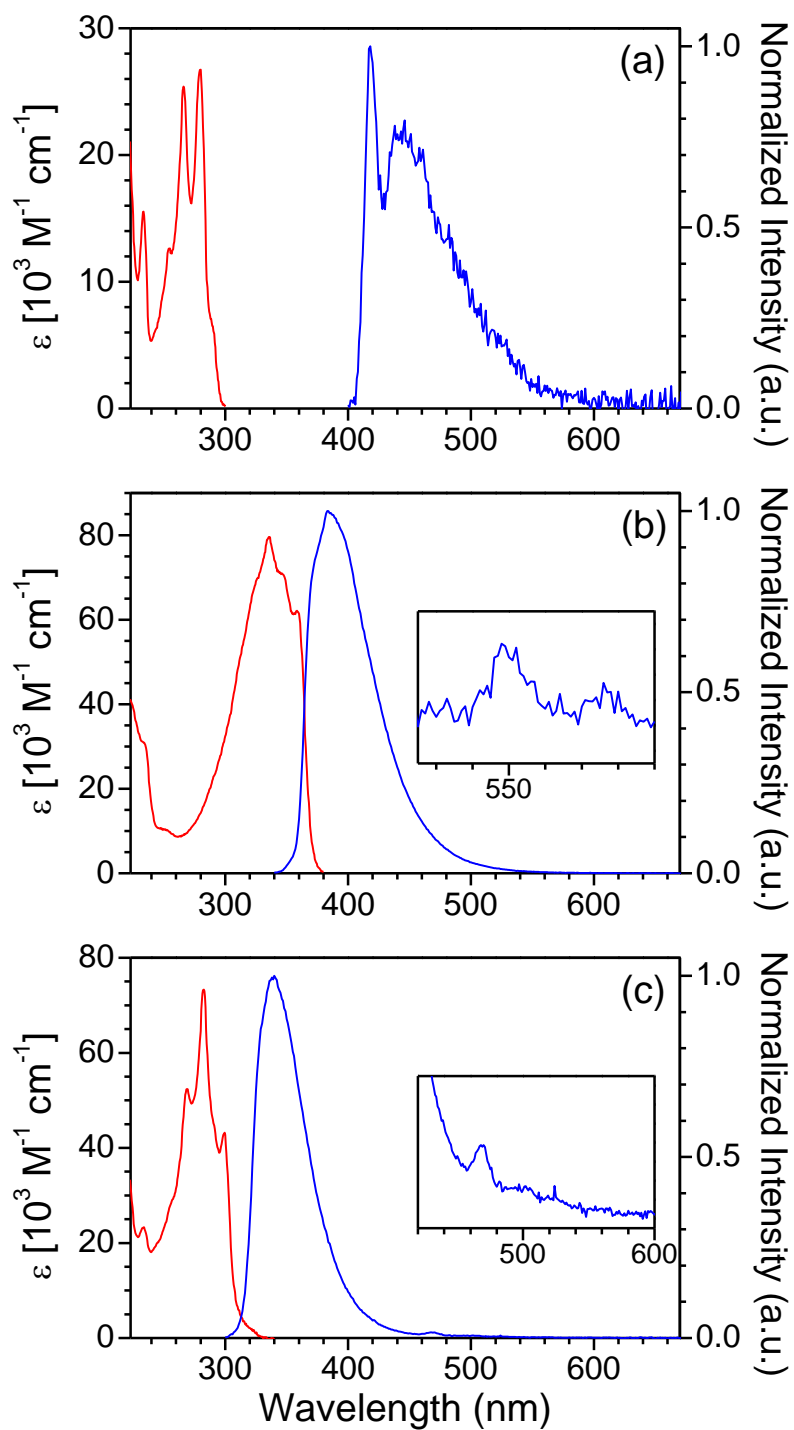


Figure S7 Steady state UV-visible absorption (red) and normalized 280 nm excited fluorescence (blue) spectra recorded for **1a** (a), **2a** (b) and **3a** (c) in acetonitrile. The insets show the magnified view of the fluorescence spectra.

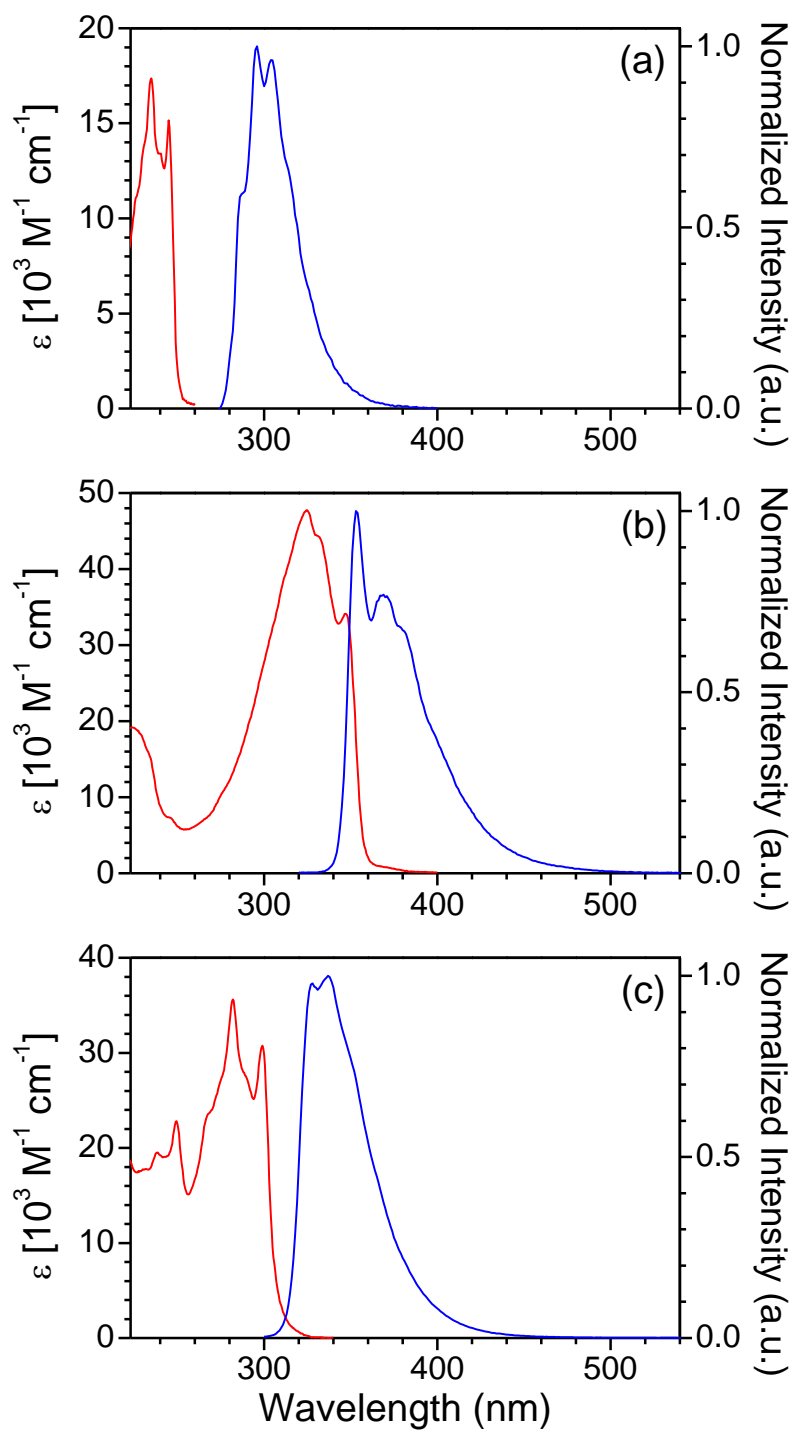


Figure S8 Steady state UV-visible absorption (red) and normalized 280 nm excited fluorescence (blue) spectra recorded for **1b** (a), **2b** (b) and **3b** (c) in acetonitrile.

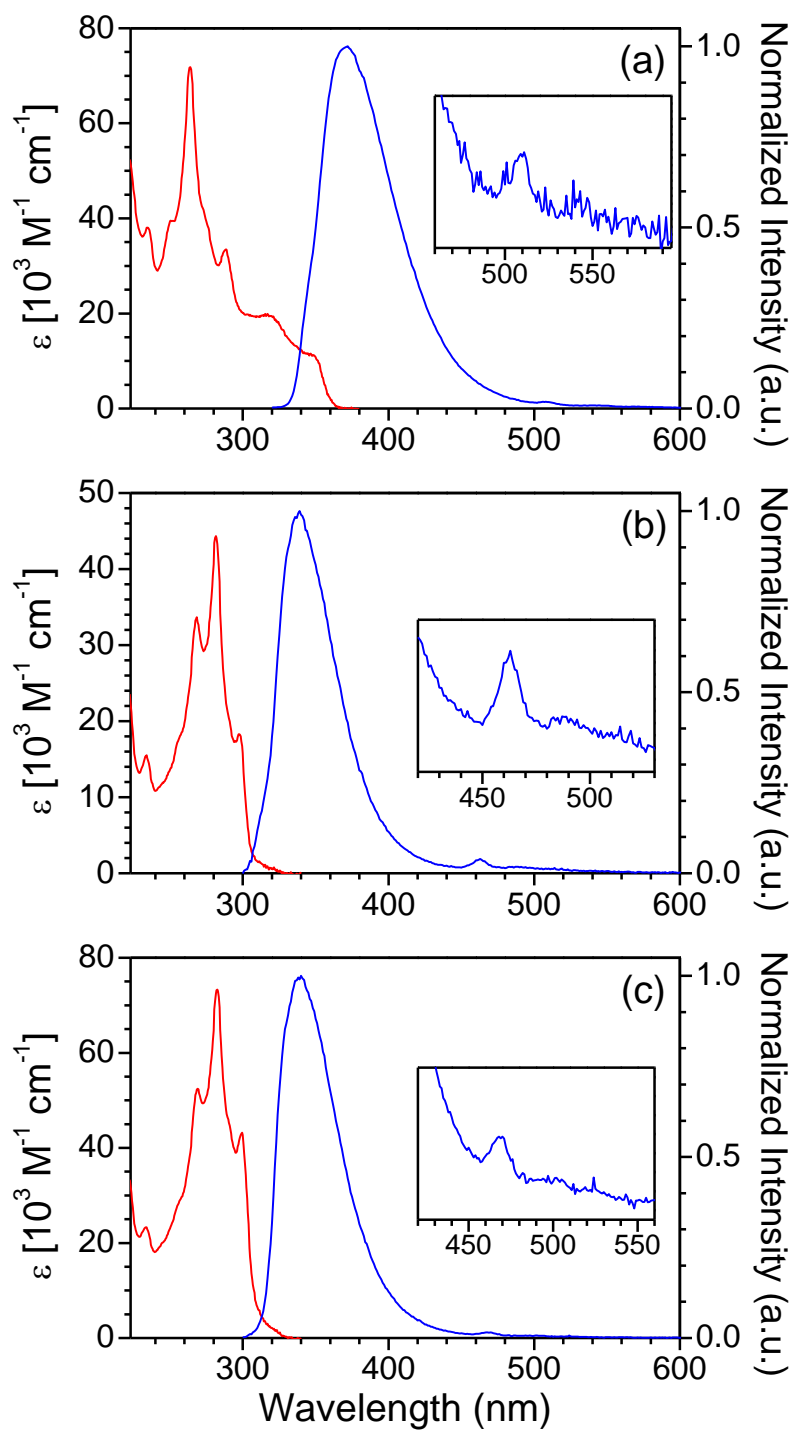


Figure S9 Steady state UV-visible absorption (red) and normalized 280 nm excited fluorescence (blue) spectra recorded for **1** (a), **2** (b) and **3** (c) in acetonitrile. The insets show the magnified view of the fluorescence spectra.

Supplementary Program Code for the Computer Control in ns-TA Measurement

In order to control the fs time-resolved spectroscopic systems, *i.e.* the CCD detector, the optical delay line, the shutter and the data acquisition procedure, a computer program written in Visual Basic 6.0 under Window 2000 has been run.

However, in the ns-TA measurement, the timing between the pump and probe is controlled using the digital delay and pulse generator (DG535, Stanford Research Systems), instead of the optical delay line. Therefore, supplementary program is needed to link up the generator with the data acquisition procedure. The respective coding of the supplementary program (*Move_ns*) is shown below:

```
Public Sub Move_ns (Delay As Single)
  Const GPIB0 = 0
  Dim instruments(2) As Integer
  Dim Start
  Call SendIFC(0) ' Call for Controller-In-Charge of the
                  board address 0
  instruments(0) = 15 ' Assign instrument GPIB address (15)
  instruments(1) = NOADDR
  Call EnableRemote (GPIB0, instruments()) ' Remote the instruments
  Call ibwrt(0, "dt 2, 3, " & Delay * -1 * 10 ^ -9) ' Set the time delay (ns)
  Call ibwrt(0, "dl 1,0,0") ' Display the delay time of the channel
  Start = Timer 'Get the starting time
  Do While Timer < Start + 50 'Loop and do nothing for 500ms
  Loop
End Sub
```

Other Publications

1. Ma, C.; Chan, C. T. L.; To, W. P.; Kwok, W. M.; Che, C. M. “*Deciphering photoluminescence dynamics and reactivity of the luminescent metal-metal-bonded excited state of a binuclear gold(I) phosphine complex containing open coordination sites*” *Chem. Eur. J.* **2015**, *21*, 13888-13893.
2. Ma, C.; Cheng, C. C. W.; Chan, C. T. L.; Chan, R. C. T.; Kwok, W. M. “*Remarkable effects of solvent and substitution on the photo-dynamics of cytosine: a femtosecond broadband time-resolved fluorescence and transient absorption study*” *Phys. Chem. Chem. Phys.* **2015**, *17*, 19045-19057.
3. Lee, S. H.; Chan, C. T. L.; Wong, K. M. C.; Lam, W. H.; Kwok, W. M.; Yam, V. W. W. “*Design and synthesis of bipyridine platinum(II) bisalkynyl fullerene donor-chromophore-acceptor triads with ultrafast charge separation*” *J. Am. Chem. Soc.* **2014**, *136*, 10041-10052.
4. Lee, S. H.; Chan, C. T. L.; Wong, K. M. C.; Lam, W. H.; Kwok, W. M.; Yam, V. W. W. “*Synthesis and photoinduced electron transfer in platinum(II) bis(N-(4-ethynylphenyl)carbazole)-bipyridine fullerene complexes*” *Dalton Trans.* **2014**, *43*, 17624-17634.
5. Ho, Y. M.; Au, N. P. B.; Wong, K. L.; Chan, C. T. L.; Kwok, W. M.; Law, G. L.; Tang, K. K.; Wong, W. Y.; Ma, C. H. E.; Lam, M. H. W. “*A lysosome specific two-photon phosphorescent binuclear cyclometalated platinum(II) probe for in vivo imaging of live neurons*” *Chem. Commun.* **2014**, *50*, 4161-4163.
6. Cheng, C. C. W.; Ma, C.; Chan, C. T. L.; Ho, K. Y. F.; Kwok, W. M. “*The solvent effect and identification of a weakly emissive state in nonradiative*

dynamics of guanine nucleosides and nucleotides – a combined femtosecond broadband time-resolved fluorescence and transient absorption study” *Photochem. Photobiol. Sci.* **2013**, *12*, 1351-1365.

7. Ho, C. L.; Wong, K. L.; Kong, H. K.; Ho, Y. M.; Chan, C. T. L.; Kwok, W. M.; Leung, K. S. Y.; Tam, H. L.; Lam, M. H. W.; Ren, X. F.; Feng, J. K.; Wong, W. Y. “*Strong two-photon induced phosphorescent golgi-specific in-vitro marker based on a heteroleptic iridium complex*” *Chem. Commun.* **2012**, *48*, 2525-2527.
8. Ho, Y. M.; Koo, C. K.; Wong, K. L.; Kong, H. K.; Chan, C. T. L.; Kwok, W. M.; Chow, C. F.; Lam, M. H. W.; Wong, W. Y. “*The synthesis and photophysical studies of cyclometalated Pt(II) complexes with C,N,N-ligands containing imidazolyl donors*” *Dalton Trans.* **2012**, *41*, 1792-1800.
9. Lo, W. S.; Kwok, W. M.; Law, G. L.; Yeung, C. T.; Chan, C. T. L.; Yeung, H. L.; Kong, H. K.; Chen, C. H.; Murphy, M. B.; Wong, K. L.; Wong, W. T. “*Impressive europium red emission induced by two-photon excitation for biological applications*” *Inorg. Chem.* **2011**, *50*, 5309-5311.